

THÈSE EN COTUTELLE PRÉSENTÉE  
POUR OBTENIR LE GRADE DE

**DOCTEUR DE  
L'UNIVERSITÉ DE BORDEAUX**

ÉCOLE DOCTORALE SCIENCES PHYSIQUES ET DE L'INGÉNIEUR  
Spécialité : Astrophysique, plasma, nucléaire

**ET DE L'INSTITUT NATIONAL DE LA RECHERCHE  
SCIENTIFIQUE**

PROGRAMME DE SCIENCES DE L'ÉNERGIE ET DES MATÉRIAUX

Par **Pilar PUYUELO VALDÉS**

***Laser-driven ion acceleration with high-density gas-jet  
targets and application to elemental analysis***

***Faisceaux d'ions accélérés par interaction d'un laser  
intense avec un jet de gaz dense et application à l'analyse  
élémentaire***

Sous la direction de : Fazia HANNACHI et Patrizio ANTICI

Soutenue le 05 octobre 2020 à l'Université de Bordeaux

Membres du jury :

<i>Rapporteurs :</i>	M. Luca VOLPE	Professeur	CLPU	Villamayor, Salamanca
	M. Alessandro FLACCO	Maître de conférences	LOA/ENSTA	Palaiseau, Ile de France
<i>Examineurs :</i>	M. Jean-Claude KIEFFER	Professeur	INRS	Varennes, Montreal
	Mme. Sophie KAZAMIAS	Professeure	LASERIX	Orsay, Ile de France
<i>Directeurs :</i>	Mme. Fazia HANNACHI	Directrice de recherche	CENBG	Gradignan, Bordeaux
	M. Patrizio ANTICI	Professeur	INRS	Varennes, Montreal
<i>Invité :</i>	M. Fabien DORCHIES	Directeur de recherche	CELIA	Talence, Bordeaux



*No hay mal que por bien no venga.*

Confinement 2020

A mis padres, por apoyarme siempre e incondicionalmente.



# ABSTRACT

---

In this joint thesis, performed between the French Institute CENBG (Bordeaux) and the Canadian Institute INRS (Varenes), laser-driven ion acceleration and an application of the beams are studied. The first part, carried out at CENBG and on the PICO2000 laser facility of the LULI laboratory, studies both experimentally and using numerical *particle-in-cell* (PIC) simulations, the interaction of a high-power infrared laser with a high-density gas target. The second part, performed at ALLS laser facility of the EMT-INRS institute, investigates the utilization of laser-generated beams for elementary analysis of various materials and artifacts. In this work, firstly the characteristics of the two lasers, the experimental configurations, and the different employed particle diagnostics (Thomson parabolas, radiochromic films, etc.) are introduced.

In the first part, a detailed study of the supersonic high-density gas jets which have been used as targets at LULI is presented, from their conceptual design using fluid dynamics simulations, up to the characterization of their density profiles using Mach-Zehnder interferometry. Other optical methods such as strioscopy have been implemented to control the dynamics of the gas jet and thus define the optimal instant to perform the laser shot. The spectra obtained in different interaction conditions are presented, showing maximum energies of up to 6 MeV for protons and 16 MeV for helium ions in the laser direction. Numerical simulations carried out with the PIC code PICLS are presented and used to discuss the different structures seen in the spectra and the underlying acceleration mechanisms.

The second part presents an experiment using laser-based sources generated by the ALLS laser to perform a material analysis by the Particle-induced X-ray emission (PIXE) and X-ray fluorescence (XRF) techniques. Proton and X-ray beams produced by the interaction of the laser with aluminum, copper and gold targets were used to make these analyzes. The relative importance of XRF or PIXE is studied depending on the nature of the particle-production target. Several spectra obtained for different materials are presented and discussed. The dual contribution of both processes is analyzed and indicates that a combination improves the retrieval of constituents in materials and allows for volumetric analysis up to tens of microns on  $\text{cm}^2$  large areas, up to a detection threshold of ppms.

# RESUME

---

Cette thèse en cotutelle entre la France et le Canada étudie l'accélération d'ions dans l'interaction laser-plasma. La première partie, réalisée au CENBG et sur l'installation PICO2000 du laboratoire LULI à l'École Polytechnique de Palaiseau, présente des études expérimentales, complétées par des simulations numériques de type Particle-In-Cell, portant sur l'accélération d'ions dans l'interaction d'un laser infrarouge de haute puissance avec une cible gazeuse de haute densité. La seconde, réalisée avec le laser ALLS de l'institut EMT INRS, concerne le développement d'une application des faisceaux générés par laser pour l'analyse élémentaire d'échantillons. Dans le manuscrit, les caractéristiques des deux lasers, des différents diagnostics de particules et d'X utilisés (paraboles de Thomson, films radiochromiques, CCD...) ainsi que les configurations expérimentales sont décrites.

Les jets de gaz denses supersoniques utilisés comme cibles d'interaction laser au LULI, sont présentés en détail; depuis leur conception grâce à des simulations de dynamique des fluides, jusqu'à la caractérisation de leurs profils de densité par interférométrie Mach Zehnder. D'autres méthodes optiques comme la strioscopie ont été mises en œuvre pour contrôler la dynamique du jet de gaz et définir l'instant optimal pour effectuer le tir laser. Les spectres obtenus dans différentes conditions d'interaction sont présentés. Ils montrent, dans la direction du laser, des énergies maximales allant jusqu'à 6 MeV pour les protons et 16 MeV pour les ions hélium. Des simulations numériques effectuées avec le code PICLS sont utilisées pour discuter les différentes structures observées dans les spectres et les mécanismes d'interaction sous jacents.

Des faisceaux de protons et d'X générés par le laser ALLS dans l'interaction avec des cibles solides d'aluminium, de cuivre et d'or ont été utilisés pour effectuer des analyses de matériaux par les méthodes Particle-induced X-ray emission (PIXE) et X-ray fluorescence (XRF). L'importance relative des deux techniques, XRF et PIXE, est étudiée en fonction de la nature de la cible d'interaction. Les deux diagnostics peuvent être implémentés simultanément ou individuellement, en changeant simplement la cible d'interaction. La double contribution des deux processus améliore l'identification des constituants des matériaux et permet une analyse volumétrique jusqu'à des dizaines de microns et sur de grandes surfaces ( $\sim\text{cm}^2$ ) jusqu'à un seuil de détection de quelques ppms.

# RESUMEN

---

En esta tesis doble, realizada entre el laboratorio francés CENBG y el Instituto canadiense INRS, se ha estudiado la aceleración de iones impulsados por un láser infrarrojo de alta potencia y una aplicación de los haces generados. En la primera parte, llevada a cabo en el CENBG y en la instalación láser PICO2000 del laboratorio LULI, se ha estudiado experimentalmente la interacción de este láser con un gas de alta densidad. En la segunda parte, realizada con el láser ALLS del instituto EMT-INRS, se ha investigado la utilización de haces generados por láser para el análisis elemental de diversos materiales y artefactos. En primer lugar, se presentan las características de los dos láseres, las configuraciones experimentales y los diferentes detectores empleados (parábolas de Thomson, RCF, etc.).

En la primera parte, se presenta un estudio detallado de los gases supersónicos de alta densidad que se han utilizado como blancos en el LULI, desde su diseño utilizando simulaciones de dinámica de fluidos, hasta la caracterización de sus perfiles de densidad utilizando interferometría Mach-Zehnder. Se han implementado otros métodos ópticos, como la estrioscopia, para controlar la dinámica del gas y, por lo tanto, definir el instante óptimo para realizar el disparo con láser. Se pueden encontrar los espectros obtenidos en diferentes condiciones de interacción. Muestran energías de hasta 6 MeV para protones y 16 MeV para iones de helio en la dirección del láser. Las simulaciones numéricas realizadas con el código PICLS son presentadas y utilizadas para discutir las diferentes estructuras vistas en los espectros y los mecanismos de aceleración subyacentes.

En la segunda parte se presenta un experimento utilizando los haces generados por el láser ALLS para realizar el análisis de distintos materiales mediante las técnicas de emisión de rayos X inducida por partículas (PIXE) y fluorescencia de rayos X (XRF). Los haces de protones y rayos X producidos por la interacción del láser con blancos de aluminio, cobre y oro se utilizaron para realizar estos análisis. La importancia relativa de XRF o PIXE ha sido estudiada según la naturaleza del blanco. En esta parte se presenta y discute varios espectros obtenidos para diferentes muestras. También se ha analizado la doble contribución de ambos procesos. La combinación de ambos mejora la recuperación de elementos en los materiales y permite el análisis volumétrico de hasta decenas de micras en grandes áreas, hasta un umbral de detección del orden de ppms.



# LIST OF PUBLICATIONS

---

This thesis is based on the following publications, which are referred to by their Roman numerals:

- I. *Optimization of critical-density gas jet targets for laser ion acceleration in the collisionless shockwave acceleration regime.*  
J.L. Henares, T. Tariesien, **P. Puyuelo**, J.R. Marquès, T. Nguyen-Bui, F. Gobet, X. Raymond, M. Versteegen and F. Hannachi.  
*J. Phys.: Conf. Ser.*, vol. 1079, 012004 (2018).
- II. *Laser-driven ion acceleration in high-density gas jets.*  
**P. Puyuelo-Valdes**, J.L. Henares, F. Hannachi, T. Ceccotti, J. Domange, M. Ehret, E. d'Humieres, L. Lancia, J.R. Marquès, J. Santos and M. Tariesien.  
*Proc. SPIE 11037, Laser Acceleration of Electrons, Protons, and Ions V*, 110370B, (2019).
- III. *The laser-driven ion acceleration beamline on the ALLS 200 TW for testing nanowire targets.*  
S. Vallieres, **P. Puyuelo-Valdes**, M. Salvadori, C. Bienvenue, S. Payeur, E. d'Humieres, and P. Antici.  
*Proc. SPIE 11037 Laser Acceleration of Electrons, Protons, and Ions V*, 1103703, (2019).

- IV. *Development of critical-density gas jet targets for laser-driven ion acceleration.*  
J.L. Henares, **P. Puyuelo-Valdes**, F. Hannachi, T. Ceccotti, M. Ehret, F. Gobet, L. Lancia, J.R. Marquès, J. J. Santos, M. Versteegen and M. Tarisien.  
*Rev. Sci. Instrum*, vol. 90, 063302, (2019).
- V. *Low-energy proton calibration and energy-dependence linearization of EBT-XD Radiochromic films.*  
S. Vallières, C. Bienvenue, **P. Puyuelo-Valdes**, M. Salvadori, E.d'Humières, and P. Antici.  
*Rev. Sci. Instrum.*, vol. 90, 083301, (2019).
- VI. *Proton acceleration by collisionless shocks using a supersonic H<sub>2</sub> gas-jet target and high-power infrared laser pulses.*  
**P. Puyuelo-Valdes**, J.L. Henares, F. Hannachi, T. Ceccotti, J. Domange, M. Ehret, E. d'Humieres, L. Lancia, J.-R. Marquès, X. Ribeyre, J.J. Santos, V. Tikhonchuk, and M. Tarisien.  
*Phys. Plasma*, vol. 26, 123109 (2019).
- VII. *Thomson Parabola and Time-Of-Flight Detectors Cross-Calibration Methodology on the ALLS 100 TW Laser-Driven Ion Acceleration Beamline.*  
S. Vallières, M. Salvadori, **P. Puyuelo-Valdes**, S. Payeur, S. Fourmaux, F. Consoli, C. Verona, E. d'Humières, M. Chicoine, S. Roorda, F. Schiettekatte, and P. Antici.  
*Rev of Sci Instrum.*, vol. 91, 103303 (2020).
- VIII. *Combined Laser based X-ray and Proton Induced Fluorescence: a versatile, fast, multi- element analysis tool for investigation of artifacts.*  
**P. Puyuelo-Valdes**, S. Vallières, M. Salvadori, S. Payeur, S. Fourmaux, J.-C. Kieffer, F. Hannachi, and P. Antici.  
Submitted (2020).

# ACKNOWLEDGE

---

I would like to acknowledge first the members of the jury for their careful reading and their suggestions.

Je souhaite également remercier le CENBG de m'avoir accueilli chaleureusement et plus particulièrement Nadine, parce que sans elle les choses ne se seraient pas si bien passées. Je remercie également tout le groupe ENL pour m'avoir fourni le pilier nécessaire pour ne pas me perdre en chemin. Un grand merci à Fazia pour son aide et ses précieux conseils qui m'ont guidés tout au long de la thèse. Merci aux collaborateurs, par exemple Vladimir, qui a été toujours disponible pour parler avec nous de théorie et il a eu la gentillesse de corriger mon chapitre théorique de thèse. Je remercie également les personnes qui m'ont accompagné dans les expériences, par exemple Jean Raphael et Livia, qui étaient mes premiers profs de manip. J'ai passé un si bon moment ces semaines à Paris, et ce n'était pas seulement grâce à la Tour Eiffel ! Je vous le garantie !

Un grand merci au groupe de l'INRS pour avoir rendu cette expérience universelle. Merci à Patrizio pour m'avoir aidé à élargir ma vision de la thèse ainsi que pour nous avoir offert des barres de chocolat dans le froid Canadien. De même à Simon, ta présence dans le groupe a été essentielle. Sans ton aide, je n'aurais pas pu faire tout le développement de la simulation et la boule rouge serait toujours un projet. Also thank you Martina, to bring calm and precision to the group. Je voudrais remercier Stéphane, Leo, Sylvain, François Vidal et toutes les personnes qui m'ont appris et aidé durant mon séjour à l'INRS. Dommage que le Canada ne soit pas plus proche, et que l'INRS-EMT soit si loin de Montréal. Les deux métros et le bus ne vont pas être faciles à oublier.

Je ne peux pas oublier tous ces gens qui, même s'ils n'appartenaient pas à mon groupe, m'ont diverti pendant les repas et même pendant quelques dîners : Ricardo, Ana, Herve, Jérémie, Yoandris, Elena, Uriel, Elissa, Angel et bien d'autres.

Gracias a mis profesores de toda la vida, de Zaragoza, en especial a Sebastián y a Pedro. Gracias Sebas por hacerme que me gustase el láser y gracias Pedro por soportar mis quejas durante toda la carrera. Seguidos de los profesores de Salamanca: Carlos, Iñigo, Julio, Ana, Enrique ... tenéis uno de los mejores másteres y no pude disfrutarlo más. También debo agradecer a mis compañeros de máster y amigos que me acompañaron en ese año maravilloso y que me siguen acompañando ahora también: Aurora, Alex, MA, JuanMi, Roberto, Laura, Mario etc.

Con especial hincapié, dar las gracias a José, a su pack Esther y a su gordita Muriel, por hacerme sentir como en casa tanto dentro como fuera del trabajo. Gracias José por tu paciencia y por todas las veces que me preguntabas si necesitaba ayuda, estos años no habrían sido iguales sin ti. Así como fuera, junto con Esther, habéis sido un apoyo grandísimo para superar estos años en la lluviosa Francia. No podría haber deseado una mejor familia.

No me puedo olvidar de personas que también han sido importantes en mi vida: ciclistas, Aimar, Barbara, amigos de Logroño y Zaragoza que cada vez veo menos pero que fueron muy importantes en su momento y a toda la gente que olvido pero que ha aportado su granito de arena en mi vida. También a Inés, por esas lecciones de inglés y pronunciación que me ayudaron para tener la confianza necesaria durante la presentación.

También agradecer a mi familia: abuela, tíos, primos; a mis seres más cercanos: mi madre y mi padre sobre todo, los que me creyeron capaces de hacer todo lo que quisiese y más. A mis hermanos, porque sé que los tengo allí para que lo que los necesite, aunque no tenga ni idea, ni la tendrán, de que va esta tesis. Y a mis dos personas favoritas: mi A y mi R. Quienes se hicieron relevo en estos años para soportarme y apoyarme. Porque sin esas cenas, sesiones de Netflix y discusiones por Skype no podría haber sobrevivido.

Gracias a todos por estar ahí cuando lo necesito. Por estar en los buenos y malos momentos de esta tesis. He aprendido mucho... no solo de física sino también de personas.

Merci à tous d'avoir été là quand j'en ai eu besoin, dans les bons et les mauvais moments de cette thèse. J'ai beaucoup appris ... pas seulement de la physique mais aussi des personnes.



# RESUME DE THESE EN FRANÇAIS

---

Depuis de nombreuses années, la communauté laser travaille au développement d'accélérateurs de particules compacts. Les accélérateurs conventionnels arrivent à des limites d'espace, et leur coût d'exploitation devient difficile à payer, en particulier pour ceux nécessaires à l'accélération des particules à haute énergie. En 1979, Tajima et Dawson [1979] ont introduit le concept d'accélération par champ de sillage laser (en anglais, *Laser wake field acceleration* (LWFA)). Ils ont prédit que l'accélération des électrons est possible avec une impulsion électromagnétique intense via une onde plasma. Les techniques basées sur le laser peuvent produire des champs accélérateurs, de l'ordre de centaines de GV/m. C'est trois ordres de grandeur de plus que le champ électrique maximum que les cavités résonantes des accélérateurs conventionnels peuvent supporter. Les électrons atteignent des énergies d'environ 8 GeV dans le vide en 20 cm. Cela réduit considérablement la quantité de blindage nécessaire.

L'accélération des particules à des énergies élevées est observée avec des impulsions laser de forte puissance d'une intensité  $\geq 10^{18}$  W/cm<sup>2</sup>. En 1985, la technique d'amplification d'impulsions pulsées (*chirped pulse amplification* (CPA)) était la clé pour obtenir des durées d'impulsions laser femto-seconde avec une puissance ultra-élevée allant du térawatt au pétawatt [Strickland 1985]. Cette invention a conduit Donna Strickland et Gérard Mourou à partager le prix Nobel de Physique en 2018. L'idée était d'étirer temporairement l'impulsion laser avant les étapes d'amplification et de la compresser en une courte impulsion par la suite. L'intensité de l'impulsion lors de l'amplification est réduite de plusieurs ordres de grandeur, permettant son amplification sans endommager le matériau d'amplification et sans produire d'effets non linéaires indésirables. La figure 1 montre l'évolution de l'intensité du

laser dans le temps depuis le début des années 60 d'après [Mourou and Tajima 2012]. Une fois la technique CPA apparue, l'intensité des lasers a augmenté de manière quasi-linéaire avec le temps. On observe que le régime relativiste, dans lequel la vitesse des électrons dans le champ laser est proche de la vitesse de la lumière, peut être obtenu avec des impulsions laser focalisées à une intensité minimale de  $10^{18}$  W/cm<sup>2</sup>.

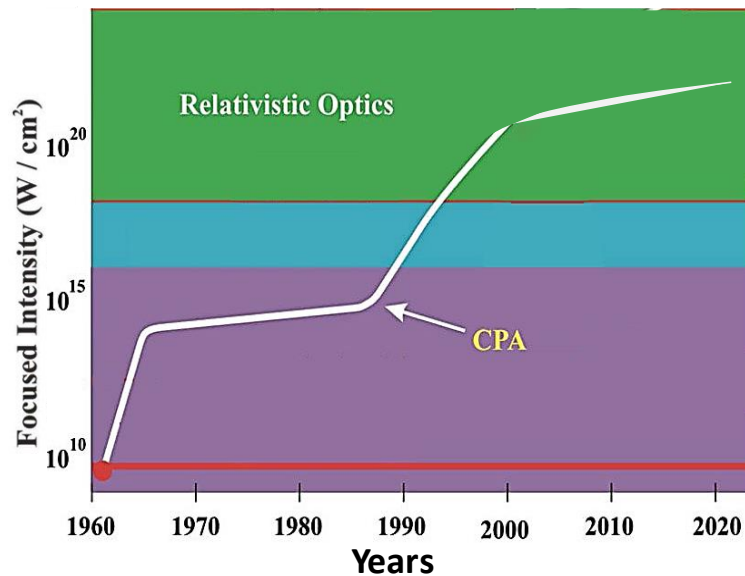


**Figure 1.** Évolution de l'intensité laser de 1960 à 2012. Modifié de [Mourou and Tajima 2012].

Avec de telles intensités, l'accélération des protons est possible. Certaines des caractéristiques du faisceau de protons produit par laser sont : de courtes durées de paquets (jusqu'à quelques picosecondes à la source), des flux de particules élevés (jusqu'à  $10^{13}$  protons/MeV/sr par tir) et de grandes plages d'énergie (jusqu'à 100 MeV). Un large éventail de domaines scientifiques, de la science fondamentale à la médecine, peut bénéficier de cette nouvelle génération d'accélérateurs compacts.

Pour des intérêts médicaux, par exemple, l'interaction de protons avec des énergies de quelques MeV avec certains matériaux peut produire des isotopes à courte durée de vie pour les diagnostics par tomographie par émission de positons (*positron emission tomography* (TEP)). Les principaux isotopes utilisés sont  $^{11}\text{C}$  ( $T_{1/2} = 20'$ ),  $^{13}\text{N}$  ( $T_{1/2} = 10'$ ),  $^{15}\text{O}$  ( $T_{1/2} = 2'$ ), et  $^{18}\text{F}$  ( $T_{1/2} = 110'$ ). Pour des utilisations pratiques, des isotopes à courte durée de vie doivent être produits à proximité des centres de thérapie médicale. Les accélérateurs d'ions par laser

peuvent être déployés facilement. Dans le même domaine, le dépôt d'énergie des protons dans la matière présente un intérêt pour la thérapie du cancer. La plupart de leur énergie est délivrée à la fin de leur trajet (dans le pic de Bragg), ce qui est différent du dépôt d'énergie continue des électrons ou des rayons X dans la matière. Les courbes de dépôt de dose correspondantes sont illustrées sur la figure 2. Le dépôt d'énergie localisé des ions permet de détruire les tumeurs mais limite la dose délivrée aux cellules saines.

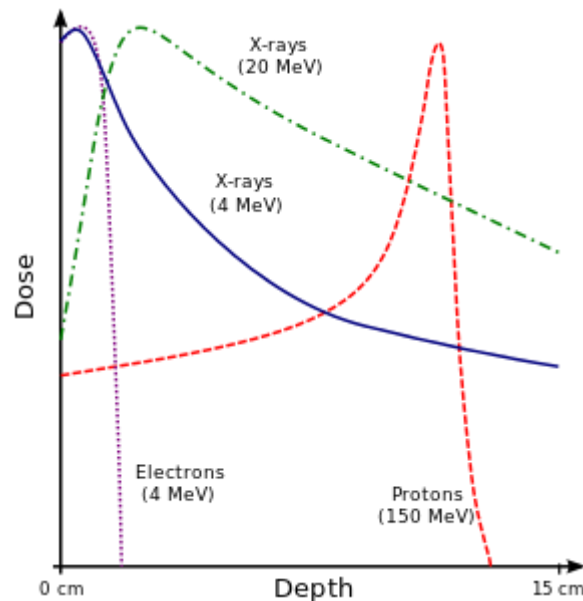


**Figure 2** Exemple de dépôt d'énergie pour les protons (150 MeV) dans l'eau par rapport aux rayons X (20 et 4 MeV) et aux électrons (4 MeV).

Cette dernière propriété est également utile pour la fusion nucléaire induite par laser. Roth et al. [2001] ont suggéré d'utiliser un faisceau de protons multi MeV produit avec un laser pétawatt comme faisceau d'allumage pour créer un point chaud dans le carburant.

Les faisceaux d'ions sont également utiles pour la caractérisation non destructive des matériaux, ce qui est important pour la recherche fondamentale et pour un large éventail d'applications, notamment l'analyse d'échantillons biomédicaux, les études du patrimoine culturel etc. Par exemple, la technique d'analyse par émission de rayons X induite par des particules accélérées par laser (*laser induced particle induced X ray emission*, Laser-PIXE) a été présentée par plusieurs groupes au cours des dernières années [Barberio 2017, Passoni 2019].

L'accélération des particules par laser est donc intéressante. Cependant, les faisceaux émis doivent être bien caractérisés, stables, avec des distributions d'énergie bien définies et être

produits à un taux de répétition élevé. Cela a déclenché une série de nouvelles installations laser produisant des impulsions courtes (ps-fs) de haute intensité ( $> 10^{18}$  W/cm<sup>2</sup>) avec des taux de répétition plus élevés (comme APOLLON en France, les piliers ELI en Europe, VEGA en Espagne, ALLS au Canada). Le taux de répétition de la génération précédente était d'environ un à deux coups par heure.

Cette thèse présente l'étude des mécanismes d'accélération d'ions basés sur les lasers, fournissant des énergies d'ions de l'ordre de quelques dizaines de MeV et facilement gérable à HRR et l'une de leurs applications. La structure de cette thèse est la suivante : Après un premier chapitre d'introduction.

Le chapitre 2 présente le contexte théorique qui permet de décrire l'interaction laser-plasma et les processus d'accélération des protons. Nous nous concentrons sur ceux qui intéressent ce travail de thèse.

Le chapitre 3 est dédié à la présentation des méthodes expérimentales développées ou utilisées dans ce travail de thèse : la description du laser, le développement de la cible d'interaction et les détecteurs. Les jets de gaz supersoniques à haute densité utilisés comme cibles d'interaction sont une alternative intéressante pour l'accélération de différentes espèces ioniques car ils peuvent être utilisés à HRR et sont exempts de débris. Cette partie du chapitre est basée sur les papiers I et IV.

Notre objectif était de produire des profils de densité de gaz avec une densité maximale d'environ  $10^{21}$  cm<sup>-3</sup> et une largeur à mi hauteur minimale (de l'ordre de 100 μm). Par conséquent, des buses à gaz supersoniques ont été conçues. Il est important de noter que les buses commerciales répondant à ces deux exigences ne sont pas faciles à trouver.

Trois types de buses supersoniques micrométriques ont été conçues à l'aide de simulations de dynamique des fluides : les buses coniques, les buses à choc et les buses asymétriques. Nous avons étudié en profondeur l'optimisation des paramètres des buses pour les deux premiers types. Une comparaison de leurs profils de densité transversale et longitudinale a également été effectuée. Les buses non axisymétriques sont plus difficiles à simuler car les simulations CFD 3D prennent du temps.

Afin de valider les résultats, les profils de densité de gaz délivrés par les buses coniques ont été mesurés avec un interféromètre Mach-Zehnder utilisant différents gaz. Des informations sur la tomographie 3D avec des buses non axisymétriques ont également été rapportées. Dans tous les cas, un bon accord a été trouvé entre les simulations et les mesures, ce qui a validé la procédure.

Une caractérisation rigoureuse de la dynamique du flux gazeux est obligatoire pour déclencher l'interaction laser à la densité maximale de la cible du gaz. L'évolution du flux gazeux a été mesurée par strioscopie. Nous avons observé l'évolution de l'écoulement des gaz d'hydrogène, d'azote et d'hélium pour différentes durées de temps d'ouverture des électrovannes. Il faut plusieurs ms (110 ms pour  $N_2$  et  $\sim 60$  ms pour  $H_2$  et He) pour remplir le volume du réservoir de la buse et atteindre la densité maximale. Afin d'utiliser ces cibles de gaz à haute répétition, la durée d'ouverture de la vanne ( $t_{open} = 40$  ms pour  $H_2$  et He et 80 ms pour  $N_2$ ) sera réduite à l'avenir en réduisant le volume du réservoir de la buse.

Le chapitre 4 décrit les résultats expérimentaux de l'interaction du laser infrarouge PICO2000 de haute puissance et des cibles à jet de gaz supersoniques conçues. Ce chapitre fait référence aux papiers [II](#) et [VI](#).

Deux campagnes expérimentales ont été réalisées. Dans la première campagne, nous avons étudié des buses coniques de différentes tailles et des buses asymétriques pour sélectionner les meilleurs paramètres pour l'accélération des ions. La plupart des interactions laser ont été réalisées avec de l'hydrogène pur.

Nous avons observé des pics intéressants dans les spectres dans le cas de buses asymétriques d'une énergie de 3,9 MeV à  $0^\circ$ . Cependant, la caractérisation de ces buses est plus difficile que pour les buses coniques et leur alignement n'était pas assez précis en raison de contraintes mécaniques. C'est pourquoi, bien que ces cibles puissent être prometteuses, les buses asymétriques n'ont pas été étudiées plus en détail.

Dans la 2ème campagne, de petites buses coniques ont été utilisées car elles ont donné des flux de protons élevés avec une bonne répétabilité dans la première campagne. Leur alignement et leur caractérisation étaient faciles et une petite quantité de gaz a été introduite dans la chambre à vide. La livraison de trop de gaz dans la chambre expérimentale a produit

plusieurs claquages électriques dans les *Thomson parabolas* (TP). Au cours de la deuxième campagne, des *imaging plates* MS-IP ont été utilisées comme détecteurs pour améliorer le rapport signal/bruit de la détection. Nous avons gagné un ordre de grandeur au niveau du fond. Cependant, les protons de basse énergie inférieures à 0,7 MeV n'étaient pas détectables puisqu'ils sont arrêtés dans la couche de protection avant de l'IP MS. Dans la première campagne, des dommages à la buse ont été observés après chaque tir. Pour la deuxième, nous avons modifié les buses coniques pour avoir un profil de densité similaire mais à une hauteur de tir de 400  $\mu\text{m}$  par rapport à la sortie de la buse (au lieu de 200  $\mu\text{m}$ ).

Dans cette campagne, nous avons constaté que la focalisation du laser sur la pente ascendante du profil de densité du jet de gaz fournit des protons plus énergétiques. Nous avons également constaté que la réduction du niveau ASE au minimum réalisable était un avantage pour l'accélération des protons dans la direction longitudinale. En résumé, une accélération isotrope a été observée avec un flux de  $10^{11}$  protons/MeV/sr à de faibles énergies jusqu'à 1,5 MeV. Des structures à flux constant de particules (plateau) ont été observées dans le sens transversal. Dans les meilleures conditions, une énergie maximale de 6 MeV a été rapportée dans la direction longitudinale. Auparavant, en utilisant des cibles  $\text{H}_2$  à haute densité, une énergie maximale de seulement 0,8 MeV était obtenue dans la direction longitudinale [[Chen 2017](#)].

Des simulations hydrodynamiques 3D ont été utilisées pour comprendre l'évolution du profil de densité du jet de gaz dû à l'interaction avec le laser ASE. Le profil de densité a été significativement modifié et n'était plus gaussien. Un côté du profil de densité a été radicalement transformé et un pic d'environ deux fois la densité d'origine s'est formé. L'emplacement exact de ce pic n'a pas été bien défini car il dépend de la durée ASE qui n'a pas été bien mesurée dans l'expérience.

Une fois que nous avons calculé la forme de la cible, des simulations PIC 2D ont été effectuées pour interpréter les spectres de protons mesurés et être en mesure d'expliquer les différents mécanismes d'accélération en jeu. L'auto-canalisation, l'auto-focalisation et la multi-filamentation ont été trouvées dans les premières picosecondes de la simulation lorsque le laser a interagi avec un plasma sous-dense. Ce fut l'origine des protons accélérés dans les directions transversales. Les protons dans la direction longitudinale ont été accélérés en

raison du processus RPA-HB, induit par un changement radical du profil de densité. Le processus a accéléré les protons à une énergie plus élevée et a créé des structures de plateau dans les spectres. Des structures pointues à haute énergie ont été observées à différents angles qui ont également été trouvés dans les simulations.

Certains tirs laser ont été réalisés avec une cible mixte de jet de gaz H<sub>2</sub> et He. Dans ces cas, des émissions de protons et d'hélium à tous les angles ont été observées. Environ 10<sup>12</sup> protons ont été mesurés aux trois angles les plus avancés, tandis que le nombre de particules émises à 90° est d'un ordre de grandeur inférieur. Au contraire, l'émission transversale He<sup>2+</sup> semblait plus importante que celle de 0°. De plus, presque aucun signal n'a été observé à 30°, ce qui indique une émission plus collimatée. Ces observations sont cohérentes avec les résultats rapportés dans les travaux précédents.

## Chapitre 5

Le chapitre 5 présente une expérience utilisant des sources générées par le laser ALLS pour effectuer une analyse de matériau par émission de rayons X induite par particules (PIXE) et de fluorescence X (*X ray fluorescence* (XRF)). Ceci se réfère aux papiers VII et VIII.

Nous avons montré, pour la première fois à notre connaissance, expérimentalement et numériquement (avec des simulations Geant4) que l'interaction d'un laser intense avec une cible solide peut produire XRF et PIXE. Nous avons constaté que les deux techniques d'analyse peuvent être mises en œuvre simultanément ou individuellement en quelques secondes en changeant simplement le type de cible d'interaction (numéros atomiques différents). Nous avons utilisé un échantillon d'acier inoxydable pour vérifier ce phénomène. Nous avons trouvé une augmentation de l'intensité du spectre lorsque la cible Cu était utilisée pour l'interaction laser par rapport au signal obtenu lorsque la cible Al (faible Z) était utilisée. Nous avons pu confirmer les contributions relatives XRF et PIXE avec des simulations Geant4, constatant que l'augmentation du signal était due à la contribution XRF. Les rayons X de l'aluminium ne produisent aucune XRF détectable par notre diagnostic.

Nous avons également étudié la taille minimale de l'échantillon avec différents échantillons de Ti pur. Cette technique permet d'analyser non seulement de grandes surfaces (le faisceau de protons peut avoir une taille de spot de plusieurs cm) mais aussi des petites (par exemple

jusqu'à 9 mm<sup>2</sup> dans le cas du Ti). Nous avons également constaté qu'il était possible de détecter l'arsenic dans un échantillon de silicium dopé à l'arsenic avec un niveau de dopage de 20 ppm, donnant le pourcentage de composition minimum détectable pour ce type d'élément. De plus, nous avons étudié des échantillons non métalliques, dont le spectre a été obtenu en une seule irradiation. Enfin, nous avons étudié le sondage volumétrique de différentes piles d'éléments métalliques et de différentes pièces métalliques. Dans ce dernier cas, nous avons pu identifier les pics liés à l'élément constitutif de chaque pièce.

## **Chapitre 6**

Le chapitre 6 résume les résultats de ces travaux et les défis futurs associés aux cibles de jet de gaz et aux techniques d'analyse dans les environnements laser.

# CONTENTS

---

CHAPTER 1. INTRODUCTION.....	29
CHAPTER 2. LASER-MATTER INTERACTION .....	35
2.1. Lasers: working principle.....	35
2.2. Plasma description.....	40
2.3. Single-electron interaction with an intense electromagnetic field in vacuum.....	40
2.3.1. Motion of a free electron in an electromagnetic plane wave .....	42
2.3.2. Ponderomotive force .....	44
2.4. Laser interaction with low-density plasmas .....	45
2.4.1. Critical density .....	45
2.4.2. Self-focusing.....	46
2.4.3. Multi filamentation.....	47
2.5. Laser interaction with high-density plasmas .....	48
2.5.1. Absorption mechanisms .....	48
2.5.1.1. <i>Collisional</i> absorption.....	49
2.5.1.2. Collisionless absorption.....	50
Resonant absorption and inverse bremsstrahlung .....	50
Vacuum plasma heating (Brunel mechanism) .....	51
Relativistic $\mathbf{J} \times \mathbf{B}$ heating .....	51
2.6. Hot electron generation.....	52

2.7. Generation of other particles and radiation .....	53
2.8. Ion acceleration mechanisms.....	54
2.8.1. Target Normal Sheath Acceleration (TNSA).....	54
2.8.2. Radiation pressure acceleration (RPA) .....	57
2.8.2.1. Thick targets: Hole boring regime (RPA-HB) .....	58
2.8.2.2. Thin targets: Light sail regime (RPA-LS).....	60
2.8.3. Collisionless shock acceleration (CSA) .....	60
2.9. Hydrodynamic simulations.....	62
2.10. Particle-In-Cell (PIC) simulation.....	63
<b>CHAPTER 3. EXPERIMENTAL METHODS.....</b>	<b>67</b>
3.1. Laser systems .....	67
3.1.1. PICO2000 laser system .....	68
3.1.2. ALLS 100 TW laser system .....	69
3.2. Targetry: development of gas-jet targets .....	71
3.2.1. Supersonic gas jets: definitions .....	74
3.2.2. Study and optimization of nozzle geometric parameters .....	80
Conical nozzles .....	82
Shock nozzles .....	85
Asymmetrical nozzles (AN).....	88
Remark concerning the gas reservoir design.....	88
3.2.3. Transversal and longitudinal density profiles.....	89
3.2.4. Remark concerning gas jets in air .....	91
3.2.5. Conclusion .....	92
3.2.6. Experimental characterization of the gas jet .....	94
Mach-Zehnder interferometer .....	94
3D tomography .....	97

Dynamics of the gas jet .....	100
3.3. Particle and X-ray diagnostics .....	103
3.3.1. Passive detectors .....	103
3.3.1.1. Radiochromic films (RCF) .....	103
3.3.1.2. Imaging plates (IP).....	105
3.3.2. Active detectors.....	107
3.3.2.1. Scintillators .....	108
3.3.2.2. Micro-channel plate (MCP) .....	108
3.3.2.1. CCD .....	109
3.3.2.2. Diamonds.....	109
3.3.3. Spectrometers .....	110
3.3.3.1. Time of flight (TOF).....	111
3.3.3.2. Thomson parabola (TP).....	112
<b>CHAPTER 4. GAS TARGET EXPERIMENT RESULTS .....</b>	<b>119</b>
4.1. Introduction .....	119
4.1. Experimental setup .....	119
4.2. Laser-beam alignment and plasma diagnostics.....	121
4.3. Results on proton acceleration .....	125
4.3.1. 1 <sup>st</sup> campaign .....	125
4.3.2. 2 <sup>nd</sup> campaign .....	129
4.3.3. Hydrodynamic and PIC simulations .....	132
4.3.3.1. Laser interaction with the under-dense plasma .....	135
4.3.3.2. Laser interaction with the over-critical plasma .....	137
4.3.3.3. Longer times: laser beam collapse.....	140
4.3.3.4. Discussion .....	141
4.4. Results on helium acceleration.....	143

**CHAPTER 5. Laser-based X-ray and Proton Induced Fluorescence (Laser-XPIF) analysis 147**

5.1. Introduction .....	147
5.1.1. Particle-matter interaction .....	148
5.1.1.1. Stopping power.....	148
5.1.2. Photon-matter interaction.....	149
5.1.2.1. X-ray beam attenuation coefficient.....	149
5.1.2.2. Interaction processes .....	150
5.2. PIXE and XRF techniques.....	151
5.2.1. Fluorescence yield and transition probability .....	154
5.2.2. Fluorescence cross-sections .....	155
5.2.1. Conventional PIXE and XRF sources and detectors .....	157
5.2.2. Background.....	158
5.2.3. Lower limits of detection .....	160
5.2.1. Penetration Depths .....	160
5.2.2. Flexibility.....	161
5.3. Laser-based analysis technique.....	161
5.4. Experimental setup .....	162
5.4.1. Spectrum reconstruction.....	163
5.4.2. Particle diagnostics .....	165
5.4.3. X-ray diagnostics.....	168
5.5. Results.....	170
5.5.1. PIXE and XRF contributions: XPIF technique.....	170
5.5.2. Metallic samples.....	173
5.5.3. Minimum sample size .....	173
5.5.4. XPIF background .....	174
5.5.5. Minimum detectable composition.....	175

5.5.6. Non-metallic samples .....	176
5.5.7. Volumetric probing.....	177
5.5.8. Real-setting application: coins.....	178
5.6. Conclusion.....	179
<b>CHAPTER 6. CONCLUSION AND PERSPECTIVES .....</b>	<b>181</b>
6.1. Ion acceleration with gas-jet targets .....	181
6.1.1. Future approaches .....	184
6.1.1.1. How to avoid nozzle damage .....	184
6.1.1.2. How to enhance the longitudinal proton acceleration: Plasma shaping .....	186
6.2. XPIF analysis technique .....	188
6.2.1. Future approaches .....	189
6.2.1.1. Quantitative analysis.....	189
6.2.1.2. Air XPIF.....	189
6.2.1.3. PIXE at high laser repetition rate.....	190



# INTRODUCTION

---

---

For many years, the laser community has been working on the development on compact particle accelerators. Conventional accelerators are running into space limits, as they are up to kilometer sizes, and their operating cost becomes difficult to afford, especially for those required for high-energy-particle acceleration. In 1979, Tajima and Dawson [1979] introduced the concept of *Laser-wake-field acceleration* (LWFA). They predicted that electron acceleration is possible with an intense electromagnetic pulse via a plasma wave. Laser-based techniques can produce high accelerating fields, of the order of hundreds of GV/m. This is three orders of magnitude higher than the maximum electric field that conventional accelerator resonant cavities can sustain. Electrons achieve energies of about 8 GeV in vacuum in 20 cm. Consequently, the radioactivity is only produced around the acceleration area, which is smaller than in conventional accelerators.

Particle acceleration at high energies is observed with high-power laser pulses of an intensity  $\geq 10^{18} \text{W/cm}^2$ . In 1985, the *chirped pulse amplification* (CPA) technique was the key to obtain down to femto-second laser pulse durations with ultra-high power from terawatt to petawatt [Strickland 1985]. This invention led Donna Strickland and Gérard Mourou to share the 2018 Physics Nobel Prize. The idea was to temporally stretch the laser pulse before the amplification stages and compress it to a short pulse afterward. The intensity of the pulse during the amplification is reduced by several orders of magnitude, allowing its

amplification without damaging the amplification material and without producing unwanted nonlinear effects. **Figure 1.1** shows the laser intensity evolution through time since the early 60s from [Mourou and Tajima 2012]. Once the CPA technique had emerged, the intensity of the lasers increased quasi-linearly with time. One observes that the relativistic regime, in which the electron quiver velocity in the laser field is close to the speed of light, can be achieved with laser pulses focused into an intensity of minimum  $10^{18}$  W/cm<sup>2</sup>.

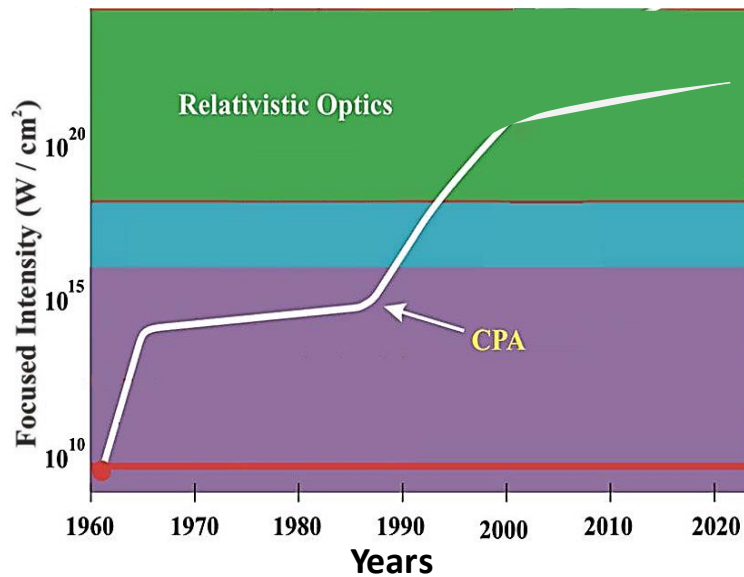


**Figure 1.1.** Laser intensity evolution from 1960 to 2012. Adapted from [Mourou and Tajima 2012].

With such high intensities, high-energy proton acceleration is possible. Some of the laser-driven proton beam characteristics are: short bunch durations (up to few picoseconds at the source), high particle fluxes (up to  $10^{13}$  protons/MeV/sr per shot) and large energy ranges (up to 100 MeV). A large range of science areas, from fundamental science to medicine, may benefit from these new generation of *compact* accelerators.

For medical interests, for example, the interaction of MeV protons with some materials can produce short-lived isotopes for *positron emission tomography* (PET) diagnostics. The principal isotopes used are  $^{11}\text{C}$  ( $T_{1/2} = 20'$ ),  $^{13}\text{N}$  ( $T_{1/2} = 10'$ ),  $^{15}\text{O}$  ( $T_{1/2} = 2'$ ), and  $^{18}\text{F}$  ( $T_{1/2} = 110'$ ). For practical uses, short-lifetime isotopes need to be produced close to medical therapy centers. Laser-driven ion accelerators represent a good alternative. In the same field, the proton energy deposition in matter is of interest for cancer therapy. Most of their energy is delivered

at the end of their path (in the so-called Bragg peak), which is at variance with the continuous energy deposition of electrons or X-rays. These are illustrated in **Figure 1.2**. This peak energy deposition allows to destroy tumors and limits the dose delivered to the surrounding healthy cells.

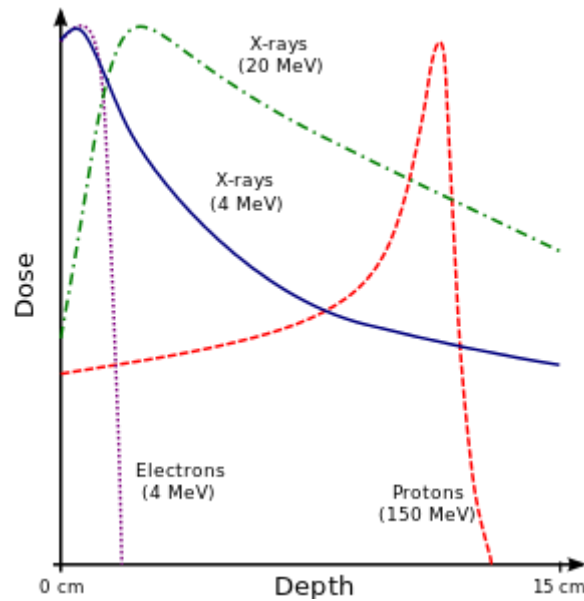


**Figure 1.2** Example of energy deposition for protons (150 MeV) in water compared with X-rays (20 and 4 MeV) and electrons (4 MeV). From wikicommons by Cepheden.

This later property is useful also for laser-induced nuclear fusion. Roth *et al.* [2001] suggested to use a multi-MeV proton beam produced with a petawatt laser as an ignitor beam to create a hotspot in the fuel.

Ion beams are also useful for non-destructive material characterization, which is important for basic research and for a wide range of applications, including analysis of biomedical samples, cultural heritage studies, forensic analysis and so on. For example, *Laser-based particle induced X-ray emission* (Laser-PIXE) analysis technique was presented by several groups in the last years [Barberio 2017, Passoni 2019].

Laser-driven particle acceleration is therefore of interest. However, the emitted beams need to be well-characterized, stable and with well-defined energy distributions and to be produced at *high repetition rate* (HRR). This has triggered a series of new laser facilities producing high-intensity ( $>10^{18}$  W/cm<sup>2</sup>) short pulses (ps-fs) with higher repetition rates. The previous generation's repetition rate was about one to two shots per hour. Nowadays, VEGA

laser in Spain or ALLS laser in Canada are capable to deliver around 5 J in several tens of femtosecond at 10 or 2.5 Hz respectively (200 TW). VEGA is expected to provide another laser line with 30 J of energy at 1 Hz (1 PW). In addition, ELI pillar project is already building 100 TW laser at 10 Hz, 1 PW laser at 1 Hz and 3 PW at 1 pulse per minute repetition rate in the Czech Republic, Hungary and Romania. In France, the APOLLON laser is as well under construction. The main laser pulse will deliver 150 J in 15 fs (10 PW) at 1 shot per minute.

This thesis presents the study of laser-based ion acceleration mechanisms providing ion energy of tens of MeV and easily manageable at HRR and one of their applications. The structure of this thesis is as follows:

### **Chapter 2**

Chapter 2 presents some theoretical background to describe laser-plasma interaction and the proton acceleration processes. We concentrate mainly in the ones of interest for this thesis work.

### **Chapter 3**

Chapter 3 is dedicated to the presentation of the experimental methods developed or used in this thesis work: the laser description, the interaction target development, and the detectors. The supersonic high-density gas jets employed as interaction targets are an interesting alternative for different ion species acceleration as they can be used at HRR and are debris free. We detail their design and characterization since they are not usually commercially available. This part of the chapter is based on **Papers I** and **IV**.

### **Chapter 4**

Chapter 4 describes the experimental results of the interaction of the PICO2000 laser and the designed supersonic gas-jet targets. The proton and He ion spectra obtained in different interaction conditions (laser parameters and gas-jet density profiles) are presented. Numerical simulations carried out with the hydrodynamic code FLASH and *particle-in-cell* (PIC) code PICLS are performed. Their results are used to enlighten the origin of the

different structures seen in the spectra and the underlying acceleration mechanisms. This chapter refers to **Papers II** and **VI**.

### **Chapter 5**

Chapter 5 presents an experiment using laser-based sources generated by the ALLS laser to perform a material analysis by the *Particle-induced X-ray emission* (PIXE) and *X-ray fluorescence* (XRF) techniques. Proton and X-ray beams produced by the interaction of the laser with aluminum, copper and gold targets were used to make these analyzes. The relative importance of XRF or PIXE is studied depending on the nature of the particle-production target. Several spectra obtained for different materials are presented and discussed. The dual contribution of both processes is also analyzed and discussed. This refers to **Papers VII** and **VIII**.

### **Chapter 6**

Chapter 6 summarizes the findings of this work and the future challenges associated with gas-jet targets and the analysis techniques in laser environments.



# LASER-MATTER INTERACTION

---

## 2.1. Lasers: working principle

Lasers are versatile tools that can be used in many fields: industry (cutting, welding), communication (optic fibers), medicine (cornea surgery, esthetic treatments), everyday life (scanning technology, laser pointers) and research. The working principle of the laser is based on three features: *population inversion*, *stimulated* emission in an amplifying medium and optical resonator.

When an electron from a low-lying atomic state is transferred to an excited one, after absorption of one or several photons, the electron in the excited state may spontaneously decay to the ground state by photon emission. The photon energy is the difference between the energies of the two states. This process is called *spontaneous* emission of fluorescence light, each excited atom emits a photon independently. However, if the population of the excited states is larger than the ground state ones, a *stimulated* emission is prominent. Hence, a first photon emitted by an excited atom passes by the neighbor excited atom and provokes emission of a second photon of the same frequency, in the same direction and in phase with the first one. The two photons are coherent: they have the same frequency, polarization, direction, and phase. This process proceeds in cascade. Namely, these two photons induce

emission of two more and so on. This is the so-called *stimulated* emission and it is at the origin of the optical amplification. **Figure 2.1** describes the different atom-photon interaction mechanisms presented above: **Figure 2.1a** describes the absorption. Some atoms in a media absorb photons and are transiting from the ground level 0 to a higher energy level 1. The emission processes are presented in **Figure 2.1b**, the *spontaneous* emission, and **Figure 2.1c**, the *stimulated* emission.

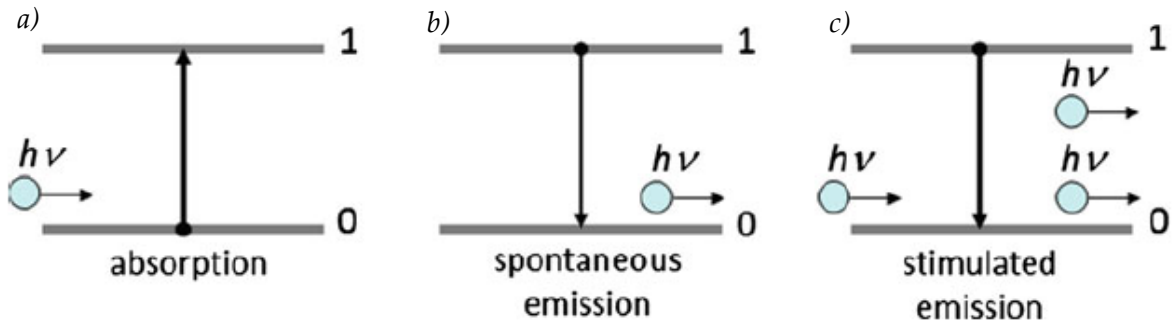


**Figure 2.1** Interaction mechanisms between an atom and a photon (the photon has an energy  $h\nu$  equal to the difference between the two atomic level energies) between levels 0 and 1. *a)* shows the absorption, *b)* the *spontaneous* emission and *c)* the *stimulated* emission. Figure taken from [Photonics 2016].

If the higher energy state has a greater population than the lower energy one, the *population inversion* is achieved. With the *population inversion*, amplifying a photon signal by *stimulated* emission is possible.

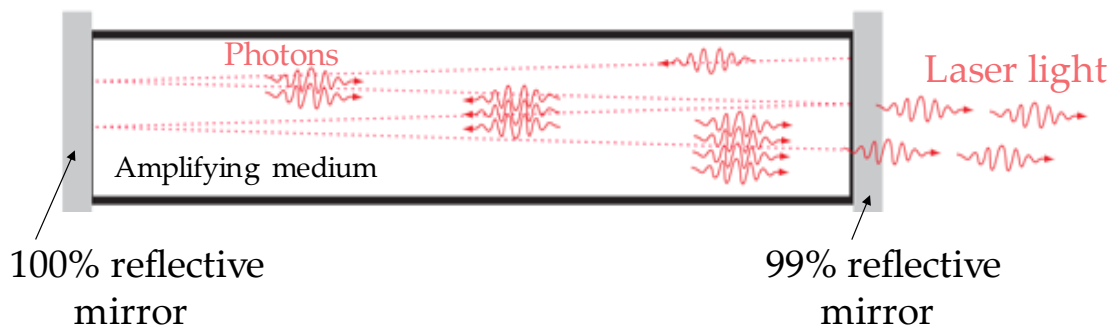


**Figure 2.2.** Scheme of multi-pass photon process in a laser cavity.

In a laser, the *stimulated* emission is produced spatially and temporally coherent in one direction while *spontaneous* emission is produced in all directions. To generate a strong signal, the amplifying medium is placed in an optical cavity equipped usually with two flat or concave mirrors, that reflect the photons back and forth (see **Figure 2.2**, photons are presented with red curvy arrows). The front mirror is made 99% reflective, hence some of the

laser light is transmitted by the mirror. The multi-pass process, illustrated in **Figure 2.2**, has a high gain.

Lasers can deliver continuous or pulsed light. Pulsed lasers concentrate their energy,  $E_L$ , in pulses of duration  $\tau_L$  at a repetition rate  $R_L$  to achieve the highest optical powers,  $P_L = E_L/\tau_L$ . This is achieved by the process of mode selection in lasing cavity. These parameters are represented in **Figure 2.3**, where the average intensity ( $I_{avg}$ ) is plotted as well.

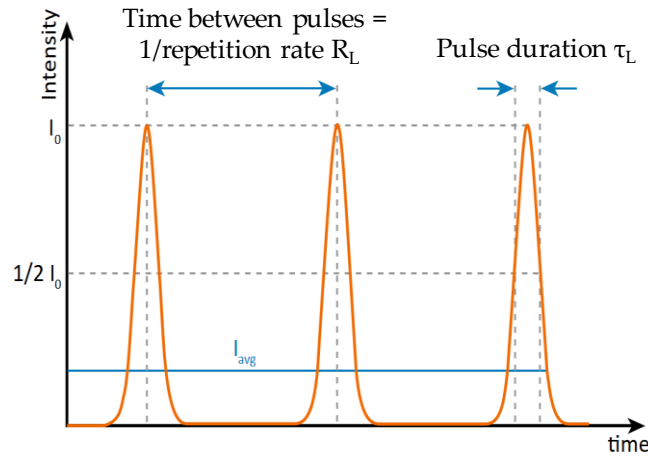


**Figure 2.3** Representation of the laser pulse intensity. The repetition rate  $R_L$  and the pulse duration  $\tau_L$  are represented in the image [the picture is taken from [www.silloptics.de](http://www.silloptics.de)].

The temporal and spatial distributions of the laser pulse can be described by the electric field of a monochromatic (and uniformly polarized) optical beam propagating at small angles (i.e. paraxially) along the  $x$ -direction of an  $xyz$  ( $\mathbf{r}$ ) Cartesian system of coordinates [LasersAndOpt 2012] (in the following, bold symbols represent vectors).

$\mathbf{E}(\mathbf{r}, t) = E_0 \mathbf{e}_y \mathbf{u}(\mathbf{r}) \exp(ik_L x - i\omega_L t)$  where  $\omega_L = 2\pi c/\lambda_L$  is the laser frequency,  $k_L = 2\pi/\lambda_L$  is the wavenumber,  $\mathbf{u}(\mathbf{r})$  is the complex field envelope,  $\mathbf{e}_y$  is the polarization vector and  $E_0$  is the maximum amplitude of the wave.

In the case of a Gaussian beam,  $\mathbf{u}(\mathbf{r})$  is expressed as:

$$\mathbf{u}(\mathbf{r}) = w_0/w(x) \exp(-(z^2 + y^2)/w^2(x)) \exp\left(ik_L(z^2 + y^2)/(2R(x))\right) \exp(i\varphi(x)) \quad (2.1)$$

where  $w(x) = w_0 \sqrt{1 + (x/z_R)^2}$  is the transverse size of the beam and  $w(x=0) = w_0$  (the minimum *spot size*) is the *beam waist*;  $R(x) = x(1 + (z_R/x)^2)$  is the radius of curvature of the

beam wave front,  $z_R = \pi w_0^2 / \lambda_L$  is the *Rayleigh length* and  $\varphi(x) = \tan^{-1}(x/z_R)$  is the beam Gouy phase.

It is important to notice that the scalar field  $\mathbf{u}(\mathbf{r})$  depends on:

an amplitude factor with a transverse Gaussian distribution

$$w_0/w(x) \exp\left(- (z^2+y^2)/w^2(x)\right) \quad (2.2)$$

a transverse phase factor

$$\exp\left(ik_L(z^2 + y^2)/(2R(x))\right) \quad (2.3)$$

and a longitudinal phase factor

$$\exp(i\varphi(x)) \quad (2.4)$$

The transverse size,  $w$ , which is called the *beam width*, changes along the propagation in the  $x$ -axis (See **Figure 2.4**). At  $x = z_R$ , the *beam width* has increased with respect to the *beam waist* by a factor of  $\sqrt{2}$ ,  $w = \sqrt{2}w_0$ . Because the beam tends to diffract, a new parameter is introduced: the divergence of the laser beam,  $\tan \theta_L = \lambda_L / (\pi w_0)$ , which is the ratio of the beam width to the distance from the focal plane  $w(x)/x$  at large distance,  $x \gg z_R$ . For real laser beams, an  $M^2$  factor is defined as  $M^2 = \theta_L \pi w_0 / \lambda_L$ , which characterizes the quality of the beam. If  $M^2 = 1$  the beam is perfectly Gaussian.

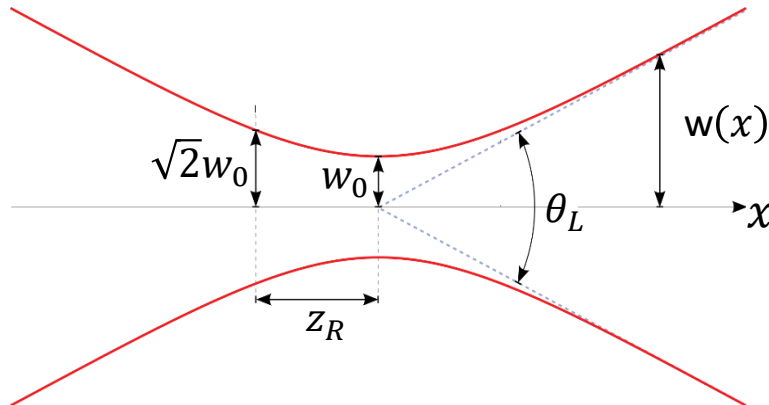


**Figure 2.4** Scheme of a laser beam propagation where  $w(x)$  is the beam *spot radius* and  $w_0$  is the *beam waist*,  $\theta_L$  is the divergence and  $z_R$  is the *Rayleigh length*.

Since we usually measure the intensity of a laser beam, it is useful to define the peak intensity of a Gaussian beam in the focal plane using the optical power and the *beam waist*:  $I_L \approx 0.5 P_L / (\pi w_0^2)$ . There is usually 40 or 50% of the laser energy in the central lobe due to diffraction effects.

After the invention of the CPA technique [Strickland 1985], ultra-high-power laser pulses could be produced without damaging the amplification material and the different optics involved in the amplification process. Since then, high-power laser facilities have been built all over the world. The characteristics of the lasers used in this thesis work are listed in **Table 2.1**.

	PICO2000	ALLS
<b>Laboratory</b>	LULI	EMT-INRS
<b>Country</b>	France	Canada
<b>Type</b>	Nd:Glass	Ti:Sapphire
<b><math>\lambda_L</math> [nm]</b>	1053	800
<b><math>\tau_L</math> [s]</b>	$1 \times 10^{-12}$	$20 \times 10^{-15}$
<b><math>T_{max}</math></b>	1 shot/h	2.5 Hz
<b><math>E</math> [J]</b>	60	2
<b><math>I</math> [W/cm<sup>2</sup>]</b>	$5 \times 10^{19}$	$1.3 \times 10^{20}$
<b>Parabola</b>	f/4	f/3
<b>Focal spot, FWHM [<math>\mu</math>m]</b>	12	5
<b>Contrast, 250 ps</b>	$10^{-6}$	$10^{-9}$

**Table 2.1** Characteristics of the PICO2000 and ALLS laser systems. FWHM means *full width at half maximum*.

The *spontaneous* emission that takes place in the laser process, limits the laser pulse temporal intensity contrast. After the pulse compression, the *amplified spontaneous emission* (ASE) results in a quasi-continuous pedestal which is partly located before the main pulse. This is the incoherent contribution. Laser operators measure the relation between the pulse intensity and the ASE by the so-called *contrast*. For example, ALLS laser has a ps *contrast* of  $10^{-9}$  and a ns *contrast* of  $10^{-11}$ . The PICO2000 laser has a ps *contrast* of  $10^{-6}$  and a ns *contrast* of  $10^{-8}$ . At high intensity, in relativistic laser-matter interactions, the ASE plays an important role as it modifies the target properties before the main pulse arrival.

## 2.2. Plasma description

In laser-based charged-particle acceleration, the interaction of the intense laser beam with a target (e.g. a micrometric foil) generates a plasma.

Plasma is the fourth fundamental state of matter. It is a gas of ions and electrons coupled with self-consistent electric and magnetic fields where free electrons screen the Coulomb potential of the ions by their own Coulomb potential. The plasma exhibits a collective behavior, and if a force (e.g. a laser) displaces a group of particles, the displacement will be felt by the whole plasma through the energy transfer by self-consistent fields. As the ions are ionized to different degrees, the number of free electrons in the plasma is larger than the number of ions. The electric and magnetic fields induced by the charged particles in movement affect their motion. The *Debye length*,  $\lambda_D$ , is defined as the characteristic length of a charge screening in a plasma. It is the distance at which the Coulomb potential created by one ion or electron is screened by the plasma electrons and ions. The *Debye sphere* is a volume whose radius is the  $\lambda_D$ .

$$\lambda_D[\text{cm}] = \sqrt{\epsilon_0 k_B T_e / (n_e e^2)} \approx 743 T_e^{1/2} [\text{eV}^{-1/2}] n_e^{1/2} [\text{cm}^{-3/2}], \quad (2.5)$$

where  $\epsilon_0$  is the vacuum permittivity,  $k_B$  the Boltzmann constant,  $T_e$  is the plasma electron temperature, and  $n_e$  is the plasma electron density. Plasma is considered as ideal if there are many charged particles, electrons and ions in the *Debye sphere*. Collective behavior of a plasma manifests itself in the time domain by oscillation of electrons with respect to ions at the electron *plasma frequency*  $\omega_p = \sqrt{n_e e^2 / m_e \epsilon_0}$ , where  $m_e$  is the electron mass (SI units). A similar oscillation frequency can be defined for ions  $\omega_i(n_i, m_i)$ .

The interaction of the laser beam with the plasma electrons is a complex phenomenon. Let us first describe the interaction of a single-electron with an intense electromagnetic field.

## 2.3. Single-electron interaction with an intense electromagnetic field in vacuum

The most known interaction process between a bound electron and a single photon is the *photoelectric effect* [Einstein 1905, Millikan 1916]. It is the process in which an electron is

ejected from an atom by a single photon. It occurs when the photon energy,  $\hbar\omega_L$  (where  $\hbar$  is the Planck constant) exceeds the height of the atomic potential barrier,  $E_{ion}$ , confining electrons in the atom. The energy  $E_{ion}$  for outer shells is several electron-volts, equivalent to photon wavelength into the ultraviolet range. For inner shells ( $\sim$ keV), hard X-rays are needed. However, with standard lasers (operating wavelengths  $0.25\ \mu\text{m}$ - $13.5\ \mu\text{m}$ ), the photoelectric effect is not possible because  $\hbar\omega_L \ll E_{ion}$ . As the intensity of the lasers incremented in the 60s (**Figure 1.1**), *multiphoton* ionization [Mainfray 1991] became possible when  $n\hbar\omega_L \geq E_{ion}$ . In this case, the electron absorbs  $n$  photons of moderate energy and then it is ejected. If the electron absorbs more photons than necessary for ionization, it acquires a residual kinetic energy  $E_e = n\hbar\omega_L - E_{ion}$ . This process is known as *above-threshold ionization* (ATI, [Agostini 1979]). The process of multi-photon ionization was theoretical described by L.V. Keldysh who established the *photoionization* probability of an electromagnetic wave [Keldysh 1964]. Keldysh's parameter,  $\gamma \sim \sqrt{E_{ion}/\phi_p}$ , is a measure of the ionization energy compared to the *ponderomotive* energy ( $\phi_p$ ) of a free electron oscillating in the laser electric field. The *ponderomotive* energy is defined as:

$$\phi_p[\text{eV}] = e^2 I_L / (2c m_e \epsilon_0 \omega_L^2) = 1.87 \times 10^{-13} I_L [\text{W}/\text{cm}^2] \lambda_L^2 [\mu\text{m}] \quad (2.6)$$

where  $c$  is the speed of light. If  $\gamma \gg 1.5$  (i.e. low-intensity and high-frequency lasers), *multiphoton ionization* occurs. The atomic binding potential remains undistorted by the laser field. However, if the laser ponderomotive energy gets close to  $E_{ion}$ , the laser field is able to distort the atomic Coulomb field. This is the case for  $\gamma \leq 1.5$  (high-intensity and low-frequency lasers) *tunnel ionization* takes place (**Figure 2.5**).

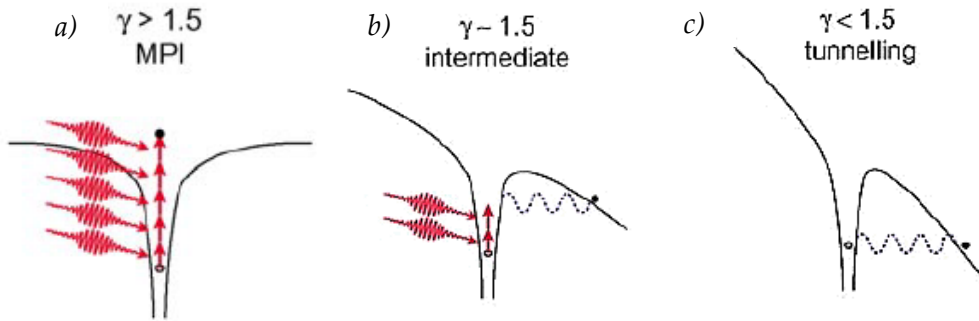


**Figure 2.5** Schematic picture of the Coulomb potential of an atom interacting with laser fields. *a)* *multiphoton* ionization when the Keldysh's parameter  $\gamma$  is bigger than 1.5 *b)* the intermediate case and *c)* when  $\gamma$  is smaller than 1.5 and *tunneling* of *barrier-suppression ionization* by a strong external electric field can take place.

<i>Ionization state</i>	$E_{ion}$ [eV]	$I_{ionization}$ [W/cm <sup>2</sup> ]
H <sup>+</sup>	13.61	$1.4 \times 10^{14}$
He <sup>+</sup>	24.59	$1.4 \times 10^{15}$
He <sup>2+</sup>	54.42	$8.8 \times 10^{15}$
C <sup>+</sup>	11.2	$6.4 \times 10^{13}$
C <sup>4+</sup>	64.5	$4.3 \times 10^{15}$
N <sup>5+</sup>	97.9	$1.5 \times 10^{16}$
O <sup>+</sup>	138.1	$4.0 \times 10^{16}$

**Table 2.2** Ionization threshold for different ions according to the *barrier-suppression ionization* model.

It can be explained qualitatively as a penetration of an electron through a potential barrier lowered by the laser field. In a very strong laser field where the Coulomb potential height falls below the ionization energy of the considered electron, the electron escapes spontaneously, and this is known as *over-the-barrier* or *barrier suppression ionization*. The threshold intensity is:

$$I_{ionization}[\text{W cm}^{-2}] \approx 4 \times 10^9 (E_{ion}[\text{eV}])^4 / Z^2 \quad (2.7)$$

where  $Z$  is the atomic number. The simplest example is the hydrogen, for which  $Z = 1$  and  $E_{ion} = 13.61$  eV. Other examples can be found in **Table 2.2**.

### 2.3.1. Motion of a free electron in an electromagnetic plane wave

A free electron oscillates in the electromagnetic field. A quantum mechanical description of an electron wave function in a monochromatic high-frequency electromagnetic field was proposed by Volkov [1935], who was one of the first to analyze a nonlinear electron behavior even before the laser invention. Later on, several papers were published on the same topic, e.g. Sarachik and Schappert [1970] who described the generation of higher harmonics of laser frequency by an oscillating electron. In particular, they defined the dimensionless parameter, or *normalized amplitude*, which can be considered as the ratio of electron quiver velocity to the speed of light.

$$a_0 = v_{osc}/c \text{ where } v_{osc} = eE_0/(m_e\omega_L) \quad (2.8)$$

In terms of  $I_L$  and  $\lambda_L$ :

$$a_0 = \sqrt{I_L [\text{W/cm}^2] \lambda_L^2 [\mu\text{m}^2] / 1.38 \times 10^{18}} \quad (2.9)$$

This means that the *relativistic regime*, characterized by  $a_0 \approx 1$ , is achieved when  $I_L \approx 1.4 \times 10^{18} \text{ W/cm}^2$  for  $\lambda_L = 1 \mu\text{m}$ .

The motion of an electron in an electromagnetic field  $\mathbf{E}$  and  $\mathbf{B}$  is described by the Lorentz equation:  $\mathbf{F}_L = d\mathbf{p}/dt = d(\gamma m_e \mathbf{v})/dt = -e(\mathbf{E} + \mathbf{v} \times \mathbf{B})$  where  $\gamma = (1 + p^2/m_e^2 c^2)^{1/2}$  is the Lorentz factor.

To illustrate the electron movement, let us assume that an elliptically-polarized wave packet is propagating in the  $x$ -direction. It can be represented by a wave vector with only  $y$  and  $z$  contributions which depend on the polarization, the phase of the wave and the normalized amplitude  $a_0$ . Following the book of Gibbon [2005], one finds that a free electron cannot gain energy from the laser. After the laser pulse, the electron energy is the same as before the laser arrival. However, a bound electron can gain an energy if it is liberated within the laser pulse. Then, there is a relation between the perpendicular ( $p_\perp$ ) and parallel ( $p_x$ ) components of the electron momentum following from the energy and momentum conservation. It can be expressed as  $p_x/m_e c = (1 - \alpha^2 + p_\perp^2/m_e^2 c^2)/(2\alpha)$  where  $\gamma - p_x/m_e c = \alpha$  is a constant of motion, which is equal to 1 for the electron being initially at rest. In this case, the electron position in a plane wave with an electromagnetic field propagating along  $x$  and linearly polarized along the  $y$  axis is defined as:

$$\begin{aligned} k_L x &= \frac{a_0^2}{4} \left( \phi + \frac{1}{2} \sin 2\phi \right), \\ k_L y &= a_0 \sin \phi, \\ z &= 0. \end{aligned} \quad \text{with } \phi = k_L x - \omega_L t \quad (2.10)$$

In the laboratory frame, the electron oscillates at the laser frequency along the laser polarization direction and moves in the laser propagation direction oscillating at the second harmonic frequency. In the drifting frame, along the  $x$ -axis, this movement corresponds to the famous *figure-of-eight* in the  $x$ - $y$  plane (**Figure 2.6**).

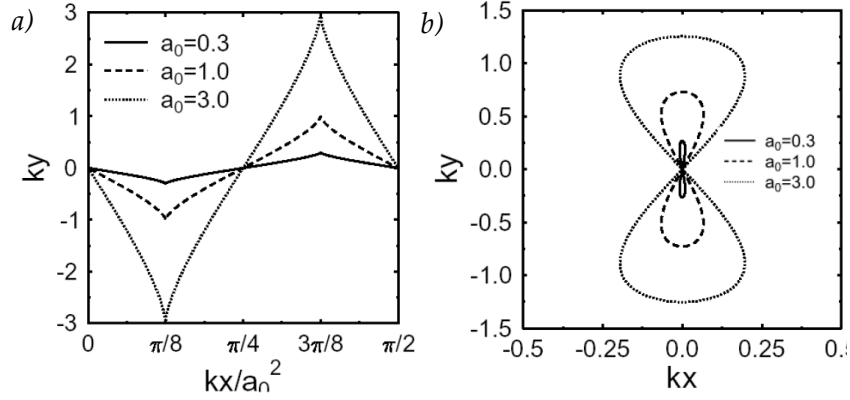


**Figure 2.6** Trajectories of a free-electron in a linearly polarized electromagnetic plane wave propagating in the  $x$ -direction in *a)* the laboratory frame, and *b)* the averaged rest frame. For a  $1\ \mu\text{m}$  laser wavelength, the chosen values of  $a_0$  correspond roughly to  $I_L = 10^{17}, 10^{18}$  and  $10^{19}$   $\text{W}/\text{cm}^2$  respectively. Taken from [Gibbon 2005].

### 2.3.2. Ponderomotive force

Short laser pulses are not plane waves because their tight focusing creates strong radial intensity gradients. That is why an electron in a focused laser beam can be accelerated.

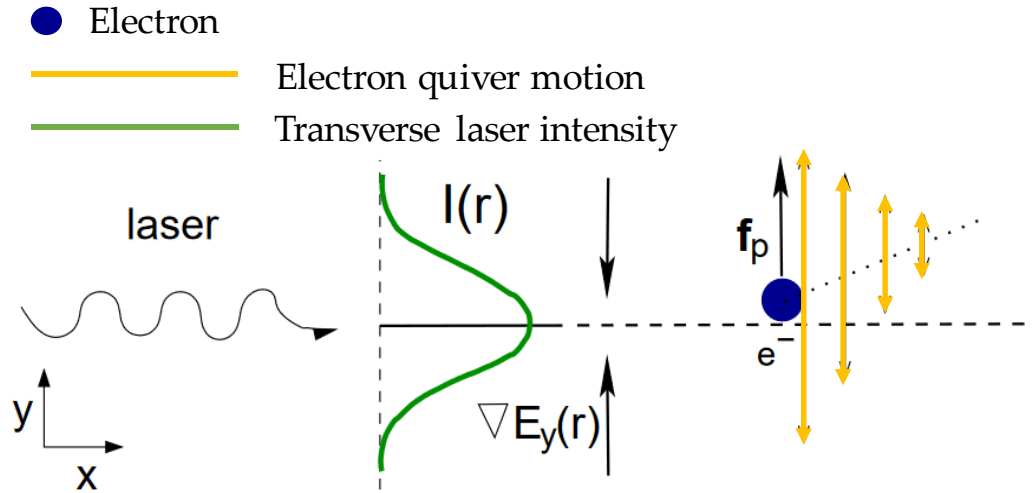


**Figure 2.7** Illustration of the *ponderomotive force* experienced by a non-relativistic electron initially sitting near the center of the beam in a spatially varying laser intensity profile. The electromagnetic wave propagates in the  $x$  direction. The laser electric field is assumed to vary in the  $y$ -direction and in time. Taken from [Gibbon 2005].

The force acting on the electron averaged over the laser period is defined as the *ponderomotive force* ( $f_p$ ) which can be represented as the gradient of the *time-averaged ponderomotive potential*  $\overline{\Phi_p}$ ,  $f_p(y) = -\nabla\overline{\Phi_p}(y)$ . It expels electrons away from region of higher intensity. A single electron drifts away from the center of the focused laser beam (**Figure 2.7**). The energy gained by the electron in a plane wave packet is equal to a difference of potential

$\overline{\Phi_p}$  at the beginning and the end of the pulse. Consequently, a free electron cannot gain energy in a plane wave. This fact is known as the theorem of Woodward. However, an electron can gain energy from the laser if it moves in two or three dimensions and its displacement is not parallel to the gradient of the ponderomotive force. Then, the kinetic energy gained by the electron reads as  $\nabla U = \int \mathbf{f}_p \, d\mathbf{S}$ , where  $d\mathbf{S} = \mathbf{v} \, dt$  is the displacement of electrons.

In the relativistic regime, the electron velocities approach the speed of light. Hence, the laser field magnetic component is non-negligible and the electron displacement has two components, parallel and perpendicular to the laser propagation direction.

## 2.4. Laser interaction with low-density plasmas

Once the interaction of a single electron with an intense electromagnetic field is explained, one can understand better the interaction of the laser with a whole plasma. For a given laser and depending on the plasma density, the interaction is different. To distinguish between low and high-density plasmas, the term *critical density* needs to be defined.

### 2.4.1. Critical density

The propagation of an electromagnetic wave in plasma depends on the plasma frequency:  $\omega_p$  (Section 2.2). A relation between the laser frequency and wavenumber in a plasma can be obtained from the Maxwell equations assuming small amplitude plane waves, cold electrons and ions, non-relativistic electron motion, and non-external magnetic fields. Then the classic dispersion relation for an electromagnetic wave in a plasma reads as:  $\omega_L^2 - \omega_p^2 = k_L^2 c^2$ . Here,  $k_L$  is the wave number, the electromagnetic wave is polarized perpendicularly to the propagation direction,  $\nabla \cdot \mathbf{E} = 0$ , and  $\mathbf{E}(x, t) = \mathbf{E}_0 \exp(ik_L x - i\omega_L t)$ . For  $k_L$  to be real, it is compulsory that  $\omega_L < \omega_p$ . The condition  $\omega_L = \omega_p$  defines the maximum plasma density that allows lasers to propagate into a cold, linear, non-relativistic plasma. This condition translates into an expression for a maximum electron density above which the laser cannot propagate further. For a given laser wavelength, the *critical density* is defined (in SI units) as:

$$n_e = n_{cr} = \frac{4\pi^2 m_e c^2}{\lambda_L^2 e^2} = 1.113 \times 10^{21} \left(\frac{1\mu\text{m}}{\lambda_L}\right)^2 [\text{cm}^{-3}] \quad (2.11)$$

$$\text{when } \omega_L = \omega_p = \sqrt{\frac{n_e e^2}{\epsilon_0 m_e}} = 5.64 \times 10^4 n_e^{1/2} \text{ [rad s}^{-1}\text{]} \quad (2.12)$$

If  $n_e < n_{cr}$ , the plasma is under-dense for a laser wavelength, and the laser can propagate. If  $n_e > n_{cr}$ , the plasma is over-dense. In this case,  $\omega_L < \omega_p$ , the wave number  $k_L$  is imaginary and the wave degenerates into an evanescent wave, consequently, at normal incident, the laser is reflected at the critical surface where  $n_e = n_c$ . For a laser wavelength  $\lambda_L \approx 1 \mu\text{m}$ , the *critical density* is  $n_{cr} \approx 10^{21} \text{ cm}^{-3}$ .

It is important to note that the phase velocity of the electromagnetic wave  $v_{ph} = \omega_L/k_L$  is bigger than the velocity of light and the index of refraction is smaller than 1, when  $\omega_L > \omega_p$ . However, the group velocity is always smaller than the velocity of light.

Electromagnetic wave of a relativistic amplitude,  $a_0 \geq 1$ , can propagate beyond the critical density. This effect is called *relativistic transparency*. The maximum plasma density where the wave can propagate is given by the expression:

$$n_{cr} = \gamma \frac{\omega_L^2 m_e c^2}{4\pi e^2} \quad (2.13)$$

where  $\gamma$  is given as,

$$\gamma = \left(1 + \frac{j a_0^2}{2}\right)^{\frac{1}{2}} \quad (2.14)$$

with  $j = 1$  and  $j = 2$  for linear and circular polarization, respectively.

In the following sections, the two main interaction mechanisms between laser pulses and under-dense plasmas are explained.

### 2.4.2. Self-focusing

When a laser amplitude propagates in an under-dense plasma, the self-focusing process may take place because the wave induces changes in the local plasma refractive index, which becomes depending on the laser intensity. Consequently, an effective *plasma lens* is formed that focuses the laser beam. This happens due to thermal, ponderomotive or relativistic effects. The first two result in the expulsion of plasma from regions of high laser intensity, creating local increase of the plasma refractive index [Krushelnick 1997]. The last one is due

to a change in the refractive index caused by a reduction in plasma frequency from induced relativistic electron motion in the laser field. A similar effect in non-ionized transparent materials, due to non-linear polarization of atoms and molecules in a strong laser field, is called the optical *Kerr effect*. [Hecht 2002].

In a uniform and fully ionized plasma, laser relativistic self-focusing [Litvak 1970, Max 1974, Sprangle 1987] depends on the total laser beam power. It is characterized by a power threshold named the *critical power*:

$$P_c \approx 17 \left( \frac{\omega_L}{\omega_p} \right)^2 \text{ [GW]} \quad (2.15)$$

The self-focusing condition becomes  $P_L \geq P_c$ . If  $P_L \leq P_c$ , the beam diverges and if  $P_L = P_c$ , the beam propagates indefinitely with a constant radius. If  $P_L \geq P_c$ , the beam collapses and the distance,  $z_c$ , where the laser beam width decreases formally to zero is given by:

$$z_c = \frac{z_R}{(P_L/P_c - 1)^{1/2}} \quad (2.16)$$

However, as the beam power is conserved, this condition implies that the intensity becomes infinite in a zero-width collapse. In reality, additional defocusing forces take place before that happens or the paraxial approximation breaks down for some reason, for example, if the spot size becomes smaller than the laser wavelength.

Other nonlinear effects such as filamentation or self-modulation may affect also the propagation of the laser in plasmas.

### 2.4.3. Multi filamentation

Laser beams with power significantly larger than the critical power, instead of global self-focusing may undergo multi-filamentation, that is a spontaneous splitting of the whole beam into multiple smaller beamlets, each of them carrying approximately a critical power. The characteristic size of the beamlets is set by the dynamic balance between the self-focusing and the diffraction. Therefore, multi-filamentation can be observed during the process of self-focusing if the laser beam power is greater than the critical power of

self-focusing. This process of spatial modulation of the laser beam front can be considered as an instability of the high-intensity light field [Bespalov 1966]. Consequently, multi-filamentation of laser propagating in plasma is seeded by uncontrolled small-amplitude perturbations. Hence this process is fundamentally stochastic [Kandidov 2009].

## 2.5. Laser interaction with high-density plasmas

The interaction between a high-intensity laser pulse and an over-dense plasma is complex. First, the ion charge-state distribution in plasma created by a short laser pulse changes with the time due to the rapid change of the interaction conditions. After the ionization, the plasma becomes opaque for the laser, so one must estimate how much laser energy can be coupled to an over-dense plasma during this transient process. This interaction is quite different from the one with under-dense plasmas (**Section 2.4**). For plasmas created with solid non-transparent targets, the laser pulse is initially partially absorbed in a skin layer and reflected like on a mirror. The absorbed fraction of light induces plasma creation at the target surface and its expansion. The subsequent interaction of laser with this expanding plasma depends on the laser intensity and the plasma properties. Efficient coupling the laser energy to a solid target has always posed a problem and requires an appropriate choice of the target material and interaction conditions.

### 2.5.1. Absorption mechanisms

Plasmas are called *relativistic* when a large number of plasma electrons are accelerated up to relativistic velocities [Bulanov 1992]. In this case, plasmas are essentially *collisionless* (particles interact through the mutually induced collective space-charge field, the binary collision frequency strongly decreases with the particle relative velocity and becomes negligible at relativistic conditions) [Pegoraro 2005]. Electrons submitted to the laser magnetic and electric fields move due to the Lorentz force. They can be accelerated in all directions, preferentially in the direction of the laser propagation.

The laser light absorption mechanisms can be classified as *collisional* or *collisionless* depending on the nature of the plasma. First, theoretical works were focused on laser

absorption in expanding over-dense plasmas. The laser intensities were low compared with today's ones (less than  $10^{14}$  W/cm<sup>2</sup>), so collisions in the plasma were important. For short and intense laser pulses (sub-picosecond relativistic regime), *collisional* absorption is less important and *collisionless* absorption dominates.

### 2.5.1.1. Collisional absorption

However, even on the sub-picosecond timescale, if the laser profile is steep, the laser can access high densities where the plasma is highly *collisional*. The Helmholtz equation has been used to calculate the *collisional* absorption coefficient. Two cases of polarization in the plane of incidence (*p*) or out of incidence plane (*s*) have been studied. The absorption fraction of both *s*- and *p*-polarization light is summarized in **Figure 2.8** from [Gibbon 2005]. For *p*-polarization the absorption is higher than for *s*-polarization because of the additional resonance transformation of laser radiation into plasma waves in the former case. The maximum absorption for *p*-polarization is at an incidence angle that depends on the ratio of the *density scale-length*  $L$  and the laser wavelength  $\lambda_L$ .

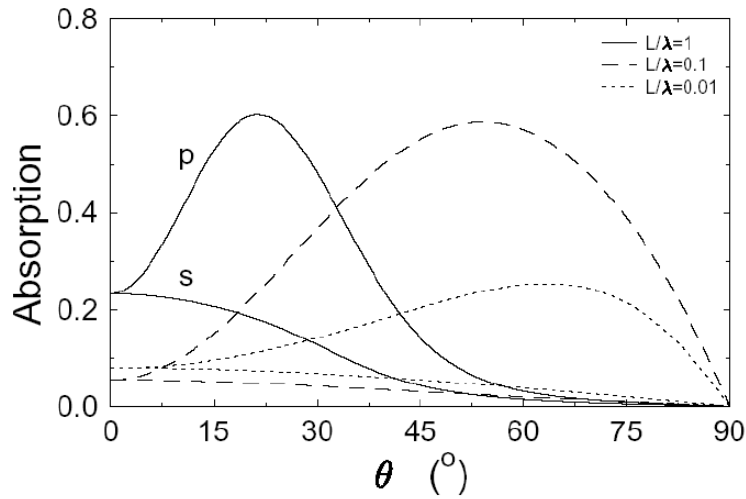


**Figure 2.8** Numerical solution of angular absorption coefficients for various *density scale-lengths* ( $L/\lambda$ ). Taken from [Gibbon 2005].

In the case of an *s*-polarized wave normally incident onto a density step of modest height ( $n_0/n_c = 5$ ) the electromagnetic field is presented in **Figure 2.9**. The electromagnetic field is reflected, but there is a small fraction that penetrates the over-dense plasma in a *skin-layer* (the laser penetration depth) and deposits its energy.

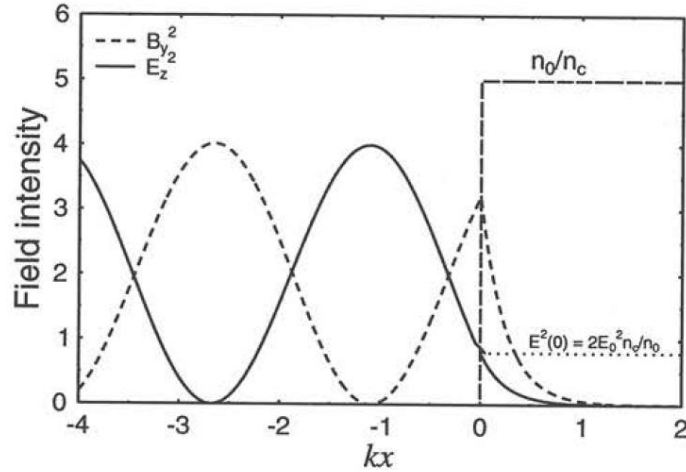


**Figure 2.9** Normally incident electromagnetic fields in an over-dense plasma *skin-layer* with  $n_0/n_c = 5$  and  $E_0 = 1$ . Taken from [Gibbon 2005].

### 2.5.1.2. Collisionless absorption

There are several *collisionless* processes which can couple laser energy to the near-critical or over-dense plasma ( $n_e \geq n_{cr}$ ). The best-known is the *resonance absorption* that explains the origin of fast electrons generated in nanosecond laser-plasma interactions. For short pulses and steep plasma densities  $L/\lambda_L \leq 1$ , resonance absorption is much less efficient. For ultra-high-intensity and ultra-short laser pulses, other absorption mechanisms (e.g. *Brunel absorption* [Brunel 1987] or  $J \times B$  heating [Gibbon 2005]) are important. Their contributions depend on the angle of incidence and on the laser polarization.

### Resonant absorption and inverse bremsstrahlung

These absorption processes, the *resonant absorption* and the *inverse bremsstrahlung* [Wilks 1997], dominate at low intensity ( $10^{12} - 10^{17} \text{ W/cm}^2$ ) corresponding to the laser pulse ASE or the laser *wings*. In the case of the *resonant absorption*, the electromagnetic wave excites the electron plasma wave resonantly, at the same frequency. The plasma wave is absorbed in the plasma and its electrostatic energy is converted into electron kinetic energy. This mechanism occurs near the critical surface. In the case of *inverse bremsstrahlung*, the laser energy is deposited to the electrons in an under-dense plasma. Electrons oscillate with the laser electric field and lose their energy by collisions with the plasma ions. This mechanism is efficient in long density scale lengths and at low temperatures. As the electron transit time

through the plasma is much longer than the laser period, the energy in the dense plasma is transferred by the electron heat conduction.

### **Vacuum plasma heating (Brunel mechanism)**

Brunel [1987] showed that *resonant absorption* mechanism, after a few modifications, operates also at steep highly over-dense plasma profiles. It is called the *Brunel* absorption mechanism or *vacuum plasma heating*. A significant absorption could be achieved under oblique incidence for *p*-polarized laser pulses despite the total absence of plasma resonance. In this mechanism, the energy absorbed by the surface electrons, which are ejected from a dense plasma, accelerated by the laser field in vacuum and then transported back into the target, is deposited in the plasma. This mechanism is similar to the *inverse bremsstrahlung absorption*. The electrons near the edge of an abrupt change in the plasma-vacuum interface are exposed directly to the laser field. If the electron arrives near the edge at the right moment in the laser cycle, it may be dragged out violently into the vacuum. As the field reverses its direction, the same electron is accelerated back into the plasma. The plasma is already over-dense, and the electric field cannot penetrate further, but the electron can travel through the target until its energy is absorbed by collisions. Since the laser pulse repeats this process every cycle, the effect is that bunches of electrons are accelerated into the target at the frequency of the incident laser pulse,  $\omega_L$ .

### **Relativistic $\mathbf{J} \times \mathbf{B}$ heating**

At high-laser intensities, electron motion becomes relativistic and the  $\mathbf{v} \times \mathbf{B}$  component of the Lorentz force is comparable with the electric field contribution to the electron motion. Considering the Lorentz force equation  $\mathbf{F}_L = e(\mathbf{E} + \mathbf{v} \times \mathbf{B})$ , the main driving force is the  $\mathbf{v} \times \mathbf{B}$  component, which is the origin of the electron oscillation at twice the laser frequency. Similarly to the Brunel effect, the electrons are ejected from the plasma in vacuum by the Lorentz force, gain kinetic energy from the laser field, return then into the over-dense plasma and deposit their energy there. The  $\mathbf{J} \times \mathbf{B}$  heating works for any linear polarization (but not for circular one) and it is most efficient for normal incidence. It dominates laser absorption at relativistic intensities [Gibbon 2005].

## 2.6. Hot electron generation

In the under-dense plasma, with the appropriate pulse length and plasma density, the laser ponderomotive force can induce an electron plasma wave, i.e. oscillations in the electron density inside the plasma. If the wave amplitude is high enough, electrons in the wake field can be accelerated to relativistic energies. This acceleration is the so-called *Laser wake field acceleration* (LWFA). In **Figure 2.10** we can observe the density perturbation behind the laser pulse. An electron propagating with a velocity close to the wake field phase velocity can gain additional energy from the electric field of a plasma wave. This acceleration process can accelerate electrons up to energies of above hundreds of MeV [Malka 2002].

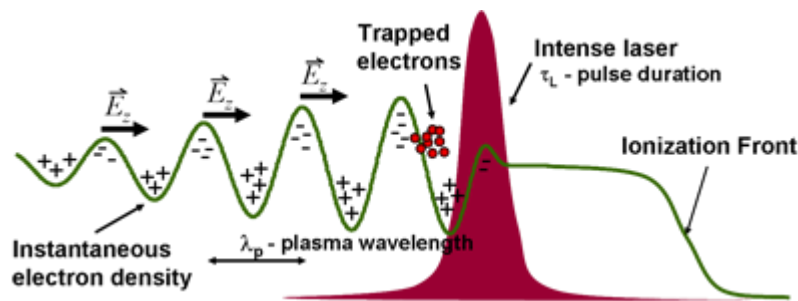


**Figure 2.10** Schematic of a laser pulse interacting with a low-density gas (e.g. hydrogen or helium). This image is taken from [Michigan engineering website].

Laser cannot penetrate into over-critical density plasmas. The energy is transported to these regions by the energetic (or hot) electrons that are produced in an under-dense plasma by *collisionless* absorption mechanisms. More information can be found in the reviews by Gibbon [2005], Mulser and Bauer [2010] or Roth *et al.* [2016].

As explained in Roth *et al.* [2016], the hot-electron component has an exponential energy distribution that can be characterized by an effective temperature that is approximately equal to the ponderomotive potential of the high-intensity laser beam,  $T_{hot}[\text{MeV}] = (I_L \lambda_L^2 / 10^{19} [\text{W} \mu\text{m}^2 / \text{cm}^2])^{1/2}$ . The hot electrons are directed mainly in the forward direction. An example of electron distribution is shown in **Figure 2.11**, taken from [Gibbon 2005] and obtained in PIC simulations. It comprises thermal electrons with a Maxwellian distribution of temperature  $T_e \approx 5 \text{ keV}$  and a hot electron tail with a characteristic temperature  $T_{hot} \gg T_e$ . The electron distribution has not just a single-temperature because of several collective heating mechanisms at play during the

interaction. The difficulty of isolating a single absorption mechanism, either experimentally or in simulations, is present in laser-plasma interactions.

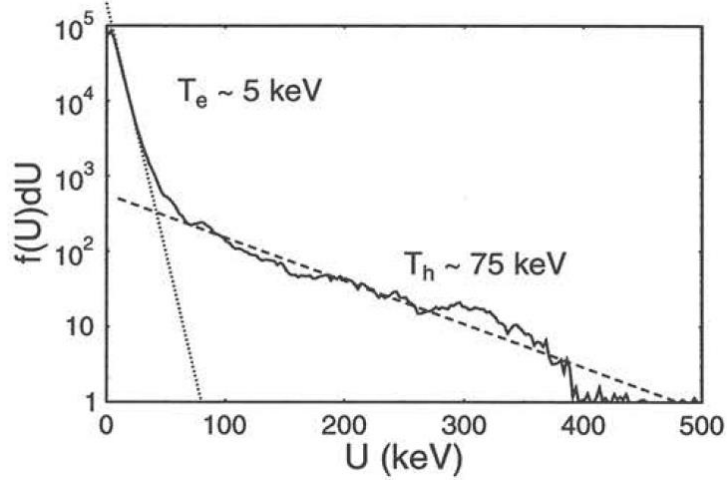


**Figure 2.11** Typical bi-Maxwellian electron distribution resulting from collisionless heating by a laser. This example taken from [Gibbon 2005]; it was obtained from a 1D PIC simulation with a laser irradiance  $5 \times 10^{16} \text{W}/(\text{cm}^2 \mu\text{m}^2)$  incident at  $45^\circ$  onto a plasma with  $n_e/n_c = 3$ .

The electron beam is divergent because of self-generated electric and magnetic fields generated on the target surface and electron-ion collisions as they propagate into the target. The full-cone angle of the electron distribution depends on the laser energy and intensity, as well as on the target thickness. For thick targets ( $> 40 \mu\text{m}$ ) the value is around  $30^\circ$  (FWHM); for thin targets ( $< 10 \mu\text{m}$ ) the value is  $16^\circ$  (FWHM) [Roth 2016].

## 2.7. Generation of other particles and radiation

When an ultra-high-intensity laser pulse interacts with plasma, electrons are preferentially accelerated forwards, in the direction of the laser propagation (Section 2.6). The ions can be also accelerated in a strong electric field generated by hot electrons (Section 2.8). Relativistic plasmas may emit coherent high-order harmonics up to the X-ray spectral region as well as incoherent X-rays. Free electrons interacting with the Coulomb potential of the ions radiate continuous electromagnetic spectrum (Bremsstrahlung emission) and the electron transitions between the discrete levels of ionized atoms induced by hot electrons can produce line spectra. [Daido 2012 and references therein].

## 2.8. Ion acceleration mechanisms

If the intensity of the laser is high enough, large electric fields induced by the hot electrons may accelerate a fraction of ions to energies up the multi-MeV range. They are several ion-acceleration mechanisms depending on the laser intensity and plasma density and thickness. These acceleration mechanisms, in a *real* laser-plasma experiment, may operate separately or jointly. In the following sections, we will describe the most important or useful for this thesis.

### 2.8.1. Target Normal Sheath Acceleration (TNSA)

Solid targets are widely used for ion acceleration in many experiments for their simple fabrication and ability to produce high-quality ion beams. The developments in laser technology allowed experimentalists to explore the properties of ultra-high intensity ( $I > 10^{18}$  W/cm<sup>2</sup>) laser-produced plasmas. In 2000, with micrometric-thickness targets, Clark *et al.* [2000], Maksimchuk *et al.* [2000] and Snavely *et al.* [2000] independently reported an intense emission of multi-MeV protons. Snavely observed  $10^{13}$  protons with energy up to 58 MeV, using a laser intensity of  $3 \times 10^{20}$  W/cm<sup>2</sup> on a 100  $\mu$ m thickness CH polymer target. The rather collimated proton beam was produced at the rear side of the target, opposite to the interaction side, and propagated in the direction normal to the target surface. The protons observed were attributed to the thin layer of impurities, water, or hydrocarbons, present on the backside of the target.

In 2001, Wilks *et al.* [2001] presented the TNSA model by applying the Poisson's equation and assuming a Boltzmann distribution. Later, in 2005, Mora [2005] presented an isothermal and adiabatic model that agreed with the experimental results. This ion acceleration mechanism TNSA relies on the electrons accelerated in the plasma plume at the front surface of the target. The intense laser beam ionizes material at the front target surface and transfers its energy to the electrons as it was explained in the sections above dedicated to the *collisionless* laser absorption. The electrons are accelerated into the bulk of the target, causing further ionization. The typical hot electron beam parameters are: divergence between 5° and 15°, density of the order of the *critical density* and effective temperature of several MeV [Passoni 2010]. The mean free path of these electrons is much larger than the target thickness,

so they easily cross it. However, only a small part of the highest energy electrons may escape far from the target, the majority is retained by the electric field of a positively charged target. The high-density negatively charged electron layer remains at the target rear surface interface, with a thickness of the order of a *Debye length* [Section 2.2]. The electrostatic field formed within this very thin sheath of confined electrostatic potential is extremely strong. The value is in the order of some TV/m (or MV/ $\mu\text{m}$ ) [Borghesi 2014]. This field accelerates ions from the target rear surface perpendicularly to the target. The acceleration is most effective for light ions (protons, carbon, and oxygen ions) than for heavier ions (the element of the target) because of the higher charge-to-mass ratio. The heaviest ion population can be accelerated on a longer time scale and to lower energies, but their presence is essential to provide a positive charge for the charge separation at the rear surface. Protons, with the highest charge-to-mass ratio, are the dominant component of TNSA ion beams unless the target is treated before the laser interaction to remove the impurities present on its surface [Hegelich 2002]. The TNSA acceleration process is represented in Figure 2.12 from [Schwoerer 2006]. The laser in oblique incidence hits the front surface of the target, presented in grey. A hot electron cloud is detached from the target surface, presented in green, and a bunch of ions, in red, are consequently accelerated.

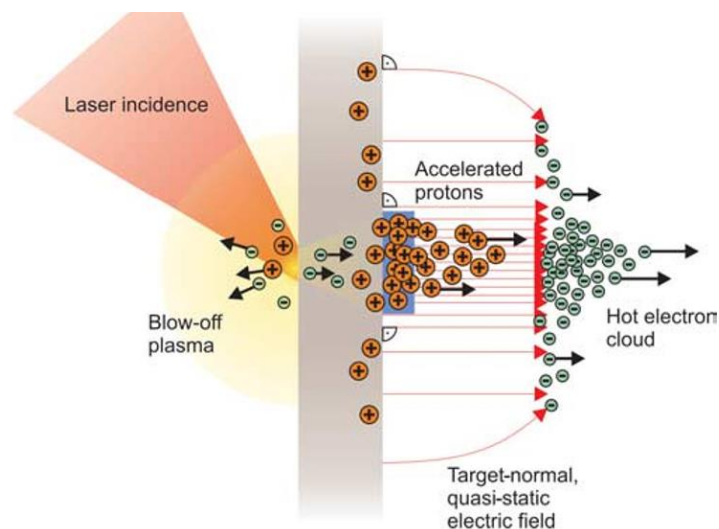


**Figure 2.12** Scheme of TNSA. The laser irradiates the front surface on a thin foil and the laser field ionizes and heats electrons. Hot electrons cross and scatter through the target and ionize the rear side. A hot electron cloud remains at the target rear surface interface that creates a confined electrostatic steep potential with a value in the order of some TV/m. This electric field accelerates ions from the impurities. This figure is taken from [Schwoerer 2006].

Under the right combination of target thickness and pulse duration, hot electrons recirculate through the target during the ion acceleration process which can lead to an enhancement of the ion energy [Mackinnon 2002]. The possibility of TNSA at the front surface has been experimentally demonstrated. In this case, the efficiency may be reduced if a pre-plasma is present [Ceccotti 2007].

The energy spectra of the ion beams are typically broadband, with an exponential energy distribution up to a high-energy cut-off. TNSA energies of the order of 80 MeV, were reported in experiments with a high-power laser, PHELIX, ( $10^{20}\text{W}/\text{cm}^2$ ) and a 900  $\mu\text{m}$  thickness plastic target [Wagner 2016]. It is observed that for equal intensities, longer pulses (order of ps) accelerate ions more efficiently than pulses with a duration of tens of fs [Borghesi 2014]. However, it was reported, with only a few J of laser energy on a 0.8  $\mu\text{m}$  thick Al target, a maximum energy of 40 MeV [Ogura 2012].

The beams are also characterized by low transverse emittance (0.004 mm mrad according to [Cowan 2012]) and ultrashort (ps) duration at the source. The beams contain up to  $10^{13}$  protons per shot with energies  $>\text{MeV}$ , corresponding to currents in the kA range. However, ions with higher energies have a lower flux ( $10^8$  protons/MeV/sr) with a divergence of a few degrees. This leads to a conversion efficiency of laser to ion beam energy of up to 9% [Roth 2016]. The half opening angle of the ion beam depends on the ion energy. The opening angle decreases with increasing energy. A parabolic dependency has been found in the LULI experiments [Roth 2016]. As it is described, protons with the highest energy are emitted in a cone of  $5^\circ$  half-angle, and protons with less energy are emitted in cones with larger opening angles.

**Figure 2.13**, taken from [Borghesi 2014], shows how the cut-off energies of TNSA spectra increase with the laser intensity on target. However, more factors affect the cut-off energy: ASE energy, laser pulse duration or target thickness. Information about the scaling laws can be found in [Fuchs 2005] and [Robson 2006].

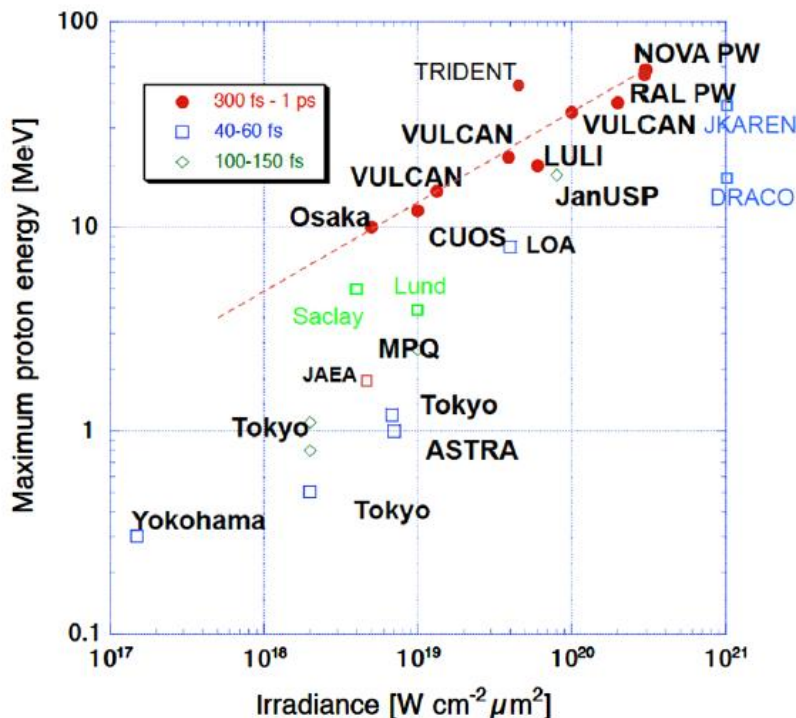


**Figure 2.13** Survey of TNSA cut-off energies measured in experiments before 2014, plotted vs irradiance and labeled according to the pulse duration. This picture was taken from [Borghesi 2014].

Other types of solid targets, for example, nanostructured surfaces, have attracted the attention of many scientists for their anti-reflection and light-trapping properties. The reduction of the surface reflection can increase the optical absorption and improve ion acceleration by the so-called *enhanced-TNSA* [Paper III]. It was observed in PIC simulations (Section 2.10) that it is possible to increase the cut-off energy by using target with an array of nanowires attached to the target front surface. However, the target manufacturing is costly and the target manipulation is more complicated and targets are very sensitive to the laser pulse contrast.

In 2018, near-100 MeV protons were reported by [Higginson 2018] produced by a combination of two different mechanisms: TNSA and *radiation pressure acceleration* (RPA). This was successfully performed using a thin plastic target foil (90 nm) with the Vulcan laser.

### 2.8.2. Radiation pressure acceleration (RPA)

As it has already been explained, the momentum carried by electromagnetic waves when they penetrate into the medium can be transferred to the charged particles. The *radiation*

pressure (RP) is the result of this momentum transmission, whose expression for a plane, monochromatic electromagnetic wave of an intensity  $I_L$  and frequency  $\omega_L$  normally incident on a plane surface of a medium is  $P_{rad} = I_L (1 + R - T)/c = I_L (2R + A)/c$  where  $R$ ,  $T$  and  $A$  are the reflection, transmission, and absorption coefficients respectively (with  $R + T + A = 1$ ). These coefficients depend on the medium refractive index and thus on the wave frequency.

### 2.8.2.1. Thick targets: Hole boring regime (RPA-HB)

If the laser is intense enough, the RP of the laser pulse may push the surface of the over-dense plasma, steepening the density profile (see **Figure 2.14a** and **b**). As the density profile is modified, the laser pulse penetrates further into the target creating a hole. This regime was first studied by Wilks *et al.* [Wilks 1992] using 2D PIC simulations (**Section 2.10**). They found that a laser pulse, tightly focused and normally incident to the surface can bore a hole several wavelengths deep into a moderate over-dense plasma on a sub-ps timescale. In the ideal case, shown in **Figure 2.14c**, the entire laser pulse is reflected by the electrons at the surface. The laser pressure at relativistic intensities is much bigger than the thermal plasma pressure, and the plasma is pushed inwards at the center of the focal spot.

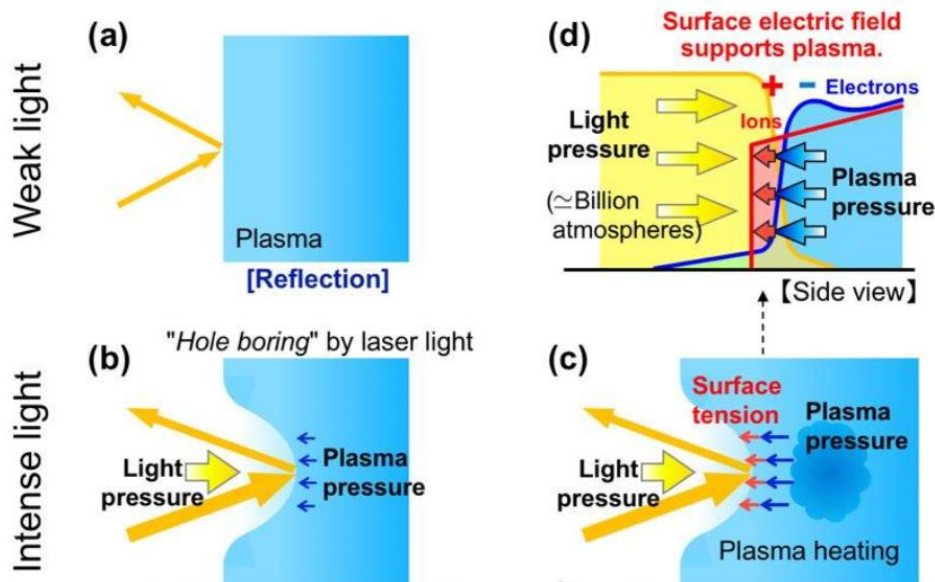


**Figure 2.14** Scheme of the *hole boring* process by laser. *a*) The light of the laser is weak, and the laser is reflected by the over-dense plasma. *b*) If the laser is intense enough, the laser is reflected. However, in this case, the light pressure is higher than the plasma pressure, and it deforms the surface acting like a *piston*. *c*) If the pulse is long enough (several fs), the plasma heats and the plasma pressure increase. There is a balance between the surface tension and the light pressure, so the velocity of the *piston* is constant. *d*) In the side view, the piston pushes the electrons by radiation pressure and forms an electric field that accelerated ions. This picture was taken from [Osaka University].

The laser pulse acts as a piston, it moves into the plasma with a constant velocity,  $v_{HB}$ , compresses it and accelerates ions. Inside the laser *piston* the electrons are separated from ions (see **Figure 2.14d**). Hence ions are accelerated there in the charge separation electric field. Such a structure, the laser *piston* and the ions accelerated in front of it, corresponds to the RPA process. An electrostatic shock is formed due to the density discontinuity that travels through the target with a constant velocity. Ions can be accelerated to a velocity twice the piston velocity,  $2v_{HB}$ , propagating ahead the *piston*.

According to Macchi *et al.* [2013], the piston velocity can be estimated by equating the electromagnetic and mass momentum flows in a planar geometry. Assuming that the plasma in front of the piston moves at a constant velocity, the plasma momentum flux per unit surface is  $n_i m_i v_{HB}^2$  (here, we neglected the electron contribution as  $m_e \ll m_i$ ). Equating it to the laser momentum flux,  $2R I_L / c$ , one finds the expression of the HB velocity,  $v_{HB} = \sqrt{(2R I_L / m_i n_i c)}$ . Defining as Macchi *et al.*, a *dimensionless pistoning* parameter  $\Pi = I / (m_i n_i c^3)$ , one can write  $v_{HB} = c\sqrt{2R\Pi}$ . This expression is valid in the non-relativistic regime, where  $\Pi \ll 1$ . In the relativistic regime and assuming total laser reflection,  $R = 1$ , the expression for the energy of accelerated ions reads:

$$E_{\max} = 2m_i c^2 \Pi / (1 + 2\Pi^{1/2}) \quad (2.17)$$

As this equation shows, high ion energies may be obtained via RPA-HB acceleration for large  $\Pi$ , hence if the plasma density is reduced but still higher than  $n_c$ , so the plasma is opaque and reflects the laser pulse. This regime was experimentally demonstrated by using a CO<sub>2</sub> laser for which *critical density* is  $10^{19} \text{ cm}^{-3}$  [Palmer 2011]. Using a laser with an intensity of  $I_L = 6 \times 10^{15} \text{ Wcm}^{-2}$ , they observed protons with energies up to 1.2 MeV and with a narrow energy spread (4%). They studied the dependence of the maximum ion energy with the ratio  $I_L / n_e$  and stated a linear scaling fairly consistent with the theoretical formula 2.16. In fact, the ion energies were even larger than expected, which was suggested to be due to self-focusing in the under-dense region.

This mechanism generates a *shock* because there is a perturbation of the plasma and this shock has a Mack number,  $M < 1$  (see **Chapter 3** for a precise definition of a M). In the case of *collisionless shock acceleration* (CSA), mechanism that will be described later in **Section 2.8.3**,

$M$  gets values greater than 1. The two shocks are different, and in the second case the electrostatic shock wave is formed after the laser interaction. In the literature, we must notice that, for example, in references [Zhang 2007, Schlegel 2009, Zhang 2009, Palmer 2011, Antici 2017] the acceleration mechanism is very probably RPA-HB as the electrostatic shock is sustained by the laser pressure.

### 2.8.2.2. Thin targets: Light sail regime (RPA-LS)

When the target is thin enough, in the range of a few tens of nanometers, all ions in the laser focal spot can be accelerated before the end of the laser pulse. A complete *hole boring* process, when laser *piston* traverses the target before the end of the laser pulse, is called *light sail regime*. In this case, the ions can be accelerated to even higher energies since the same number of ions is accelerated by the laser pulse for a longer time [Macchi 2013].

### 2.8.3. Collisionless shock acceleration (CSA)

This acceleration mechanism is different from the others. The ions are not accelerated in a charge separation electric field created by hot electrons, and the plasma does not need to be over-dense. CSA occurs when a shock wave is formed in plasma. It happens on a time scale larger than the pulse duration. Ions can be directly reflected by the shock front, whichever process generates it. CSA shock can propagate in plasma as a blast wave even if the laser pulse is no longer present. This is the main difference with the RPA-HB, where the presence of the laser is compulsory in order to push the piston which will stop if the light pressure is no longer there.

In the frame moving at the shock velocity  $v_{shock}$ , ions are reflected if the electrostatic potential barrier in the shock front  $\Phi_{max}$  is larger than the kinetic energy of ions upstream the shock in the shock frame,  $Ze\Phi_{max} > m_i v_1^2/2$ . Assuming the upstream ions are at rest in the laboratory frame,  $v_1 = 0$ , reflected ions acquire a velocity equal to  $2v_{shock}$ . Silva *et al.* [2004] studied this mechanism in PIC simulations (Section 2.10), in the case of an intense laser pulse interaction with an over-dense plasma. They show that the laser *piston* may produce a shock with a high Mach number  $M = v_{shock}/c_s \gg 1$ , where the sound speed  $c_s$  was estimated using the hot electron energy as the temperature.

If a shock is generated at the front surface with a velocity close to  $v_{HB}$ , it can evolve to a supersonic (CSA) one if  $\sqrt{2}a_0 > n_e/n_c$ . Haberberger *et al.* [2012] reported on monoenergetic (energy spread of 1%) acceleration of protons up to 22 MeV by CSA in the interaction of CO<sub>2</sub> laser pulses with hydrogen gas jets at intensity up to  $6.5 \times 10^{16}$  W/cm<sup>2</sup> corresponding to  $a_0 = 2.5$ . The temporal structure of the laser pulse, 100 ps train of 3 ps pulses, was essential for the shock formation in the experiment. However, they obtained only  $\sim 3 \times 10^5$  ions in the narrow spectral peak at 22 MeV for a 60 J pulse energy. The laser energy conversion efficiency was only of  $10^{-8}$ .

Fiuza *et al.* [2013] have deeply studied the CSA mechanism in more detail and described it with the following diagram:

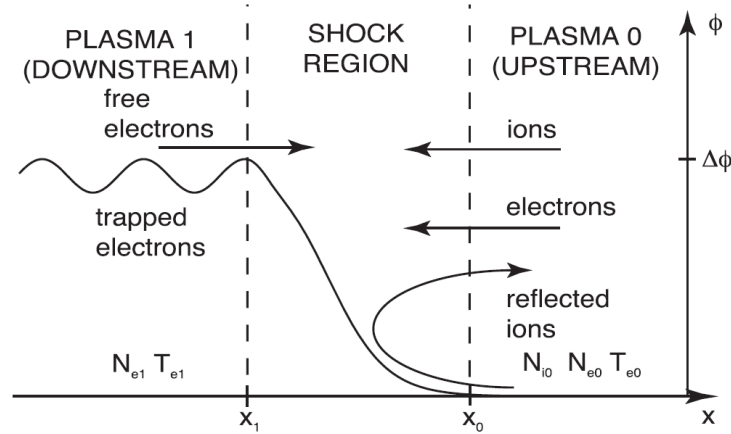


**Figure 2.15** Steady-state electrostatic shock structure as seen from the shock frame. Electrons from the upstream region are free while electrons from the downstream region are free or trapped. Ions are slowed down by the electrostatic potential and reflected back into the upstream for strong shocks. Figure extracted from [Fiuza 2013].

We observe in **Figure 2.15** that the shock front separates two different plasma regions. The first one, *plasma 1*, downstream plasma, is moving to the right, it is characterized by two electron population: trapped electrons with energies smaller than the shock electrostatic potential  $\Phi_{max}$ , and free electrons with a higher energy that penetrate through the shock front. The second upstream plasma, *plasma 0*, is at rest and it is characterized by the two populations of ions: free ions with energies larger than the shock potential, which are moving through the shock front, and the ions reflected from the shock front and propagating upstream with a velocity higher than the shock velocity. The electrostatic potential inside the shock front increases from  $\phi = 0$  at  $x = x_0$  to  $\phi = \Phi_{max}$  at  $x = x_1$  as illustrated in **Figure 2.15**.

If  $\Phi_{\max}$  is large enough, almost all upstream ions are reflected by the shock. More information about this model can be found in [Fiuza 2013].

To understand the processes at play during laser-matter interactions, simulations are needed in addition to the experiments. Two types of simulations are usually performed for preparation and interpretation of experiments: Hydrodynamics ones are used for modeling the interaction of the laser ASE with the target on a ns time scale and characterization of the plasma before the arrival of the main laser pulse. Particle-in-cell simulations are used for modelling the interaction of the main laser pulse with the plasma on a <sub-ps time scale and particle acceleration.

## 2.9. Hydrodynamic simulations

In laser-matter experiments, first the laser ASE arrives to the target and ionizes it if its intensity is high enough (see **Table 2.2**). This means that the target is modified before the main pulse arrival. Interferometric instruments to measure electron number densities in the pre-plasma are often unavailable, or too complicated, or the target geometry does not allow probe beams to directly access the pre-plasma. In this case, simulations are the only way to have important information about the *real* target density profiles.

The hydrodynamic codes can describe plasma as a single species fluid with two temperatures, for electrons and ions. They include the following physics processes: the ionization of atoms, the laser propagation and collisional absorption of laser energy in plasma, the energy transport into a dense plasma with electrons and ions, the plasma equation of state, and optional bits of physics such as nuclear burn rate, soft X-ray emission and energy transport [Gibbon 2005]. They can simulate the target heating, plasma expansion, radiation emission from laser-irradiated plasmas on a time scale of several nanoseconds and predict the properties of the generated pre-plasma. In this thesis, the pre-plasma formation has been simulated with the hydrodynamic code FLASH [Fryxell 2000].

FLASH is a finite-volume Eulerian code that operates on a block-structured mesh using *adaptive mesh refinement* (AMR) [MacNeice 2000]. In the code, laser propagation is modeled within the geometrical optics. Laser beam is split into rays that propagate in plasma and

deposit energy on the grid according to the *inverse bremsstrahlung* process. This energy is absorbed by the electrons and transferred to ions. A deeper description of the physics induced in FLASH and comparison with other hydrodynamic codes can be found in [Orban 2013]. Non-linear laser plasma interactions, for example, the ponderomotive force, are not included in FLASH. However, the intensity of the laser pre-pulse is sufficiently low and nonlinear laser plasma interactions are not too much important.

With the initial target density and the laser ASE properties as inputs, FLASH simulates the interaction to obtain the pre-plasma density profile.

## 2.10. Particle-In-Cell (PIC) simulation

After the target is already ionized by the laser ASE, the main pulse arrives. To understand the interaction between the main pulse and the plasma (which happens on a time scale of less than a picosecond), detailed kinetic simulations are needed along with the experiments. The PIC codes [Birdsall 1985, Chen 1984, Lieberman 2005] use the set of Maxwell's equations along with equations for the electron and ion dynamics permitting to study the collective effects in plasma and charged particle acceleration.

The PIC simulations have as input the charged particle distribution, according to the density, temperature and velocity distributions calculated with hydrodynamic codes. The charge of the particles is distributed among the cells and the electric and magnetic fields are evaluated at the nodes of the cells (that is why the name *Particle-in-cell*). The number of particles in each cell is much smaller than in real plasma. However, these *macro-particles* consisting of several real particles. The charge-to-mass ratio of these macro-particles is the same as in real particles and their sizes are of the order of the *Debye length*. Before running the code, the number of plasma cells, the time step and the number of particles per cell must be specified.

The position and velocity of each particle are updated at each time step with the Newton's second law according to the Lorentz force and collisions between particles may be accounted by the Monte Carlo method. The different steps in the loop are represented in **Figure 2.16**. In addition to solving the equations of particle motion, it includes evaluation of the charge and

current densities needed for Maxwell equations, solution of Maxwell equations on the grid and evaluation of the electric and magnetic fields on the particle positions. After the particles have moved to new positions, it is necessary to verify if there are still in the computational domain. Two boundary conditions are possible: the particles can either exit the domain or can be re-injected by using specular or diffuse reflection laws. So computational boundaries are either *open* (absorbing, allowing particles to leave), *reflective* (elastically returning particles into the domain) or *periodic* (particles are transported to the opposite side of the box). The outputs can be obtained at selected times.

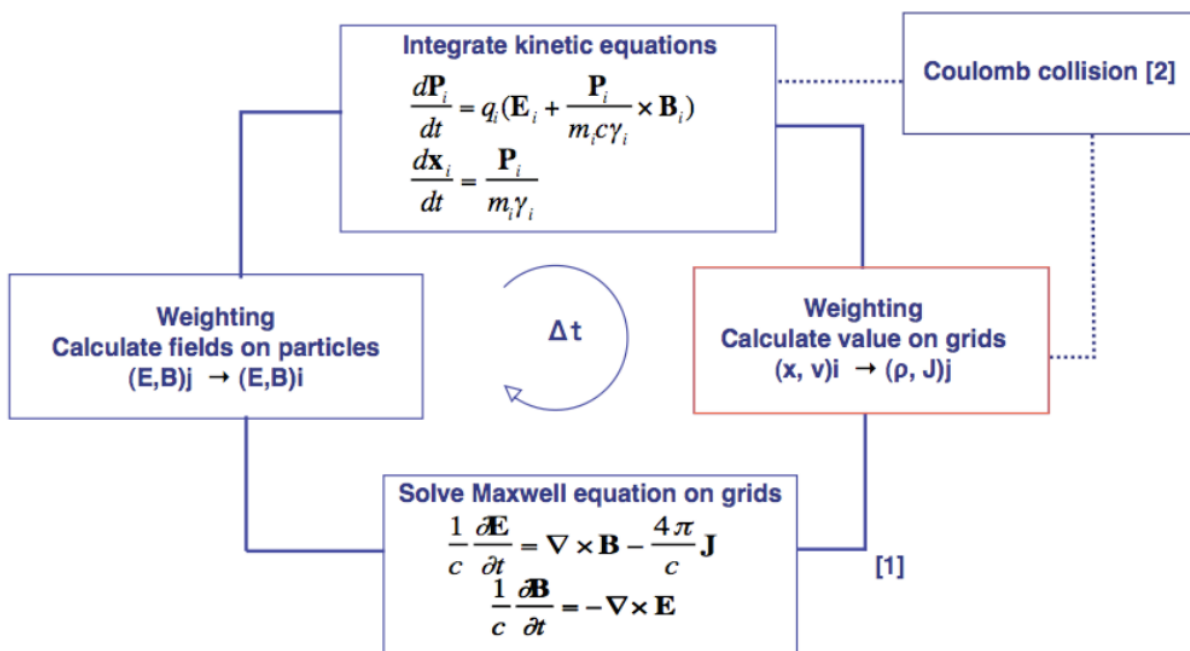


**Figure 2.16** Time loop in a PIC code. Time is increased in steps of  $\Delta t$  so that  $t = t_0 + n \times \Delta t$  where  $n$  is the number of loops of the simulation. Taken from [PICLS Handbook].

In the case of laser-matter interaction, the laser pulse input is prescribed as an incident electromagnetic wave at the boundary of the simulation box. The laser inputs are the laser electric and magnetic field amplitudes as a function of time and the laser wavelength.

In this thesis work, the relativistic PIC code, PICLS [Sentoku 2008] is used. The code includes electron and ion collisions, which are important to determine the characteristics of hot electron transport [PICLS handbook]. The code features a perfect energy conservation in individual collisions and momentum conservation on average even if the use of macro particles has significant consequences for the binary collision model. It is based on the

Monte-Carlo method accounting for the energy and momentum transfer in collisions. In **Figure 2.17** one can find the different processes taken into account in the simulations.

From PICLS simulations, one can obtain the following information about the laser-plasma interaction: the distribution of the density averaged over several cells, a snapshot of the distribution of  $p$ - and  $s$ - polarized electromagnetic fields averaged over several cells, the distribution of the energy density averaged over the cells, the distribution of the ions and electrons in the phase space, a snapshot of the current density distribution averaged over the cells and so on.

Computer simulations can be performed in one-, two- or three-dimensions (1D, 2D, and 3D respectively). 1D and 2D simulations are widely used because of the relatively low request for computational resources and their ability to capture the main physics. However, multi-dimensional effects appear when the laser is tightly focused. Here, 3D simulations may be needed [Fiuza 2011]. As stated by Liu *et al.* [2013] for thick targets, electrons spread almost uniformly along with two transverse directions, while in the case of ultra-thin targets electrons spread more quickly along the direction orthogonal to the laser polarization direction. This spreading decreases the hot electron density (See **Section 2.6**) which affect the ion acceleration process. That is why the maximum proton energy observed in 3D simulations is smaller than the one observed in 1D or 2D simulations.

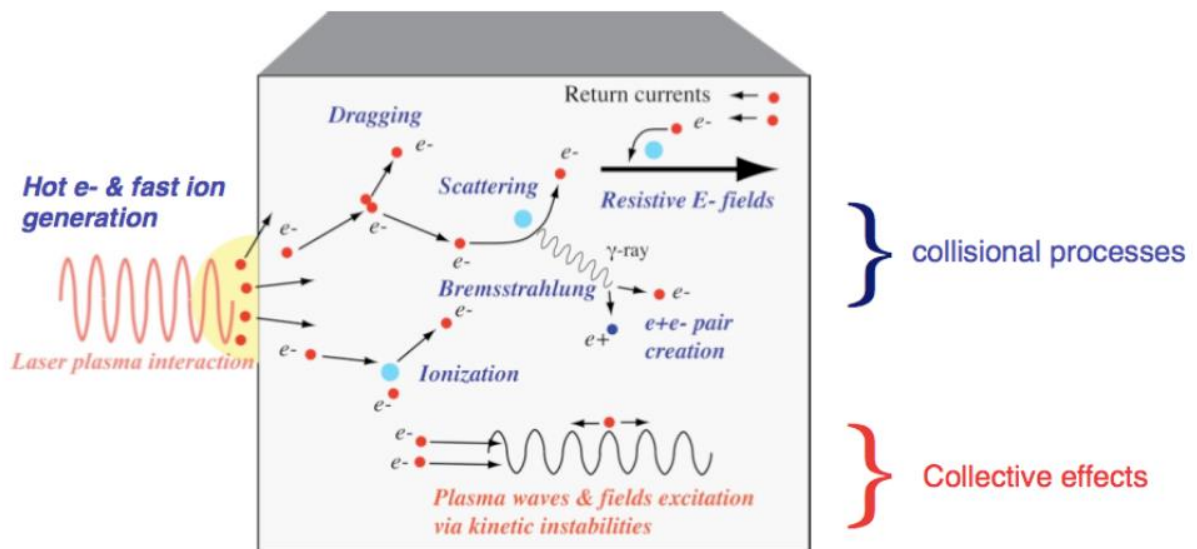


**Figure 2.17.** Different processes taken into account in the PICLS simulations. Extracted from [PICLS handbook].



---

# EXPERIMENTAL METHODS

---

## 3.1. Laser systems

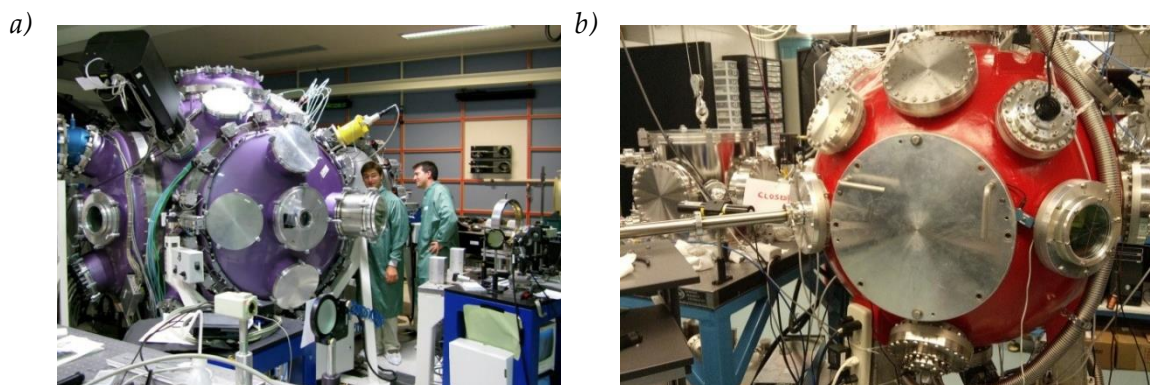


**Figure 3.1** *a)* Picture of the MILKA chamber at LULI Research Infrastructure in France. [Taken from *FuseNet Association*]. *b)* Picture of the *Boule rouge* at EMT-INRS center in Canada. On the left, one can observe the small vacuum chamber coupled to the main one, where a spectrometer is placed. The KF 40 tube visible between the principal door and the secondary chamber is part of another spectrometer.

In this work, the experiments have taken place at two different laser facilities: the *Laboratoire pour l'Utilisation des Lasers Intense (LULI)* Research Infrastructure at *Ecole Polytechnique* in Palaiseau, near Paris, France, and the *Energie Materiaux Telecommunications (EMT)* Research Centre from the *Institut National de la Recherche Scientifique (INRS)* in Varennes, near Montreal, Canada. Both experimental chambers are shown in **Figure 3.1**. The MILKA chamber at LULI and the *Boule rouge* at EMT-INRS have diameters of 2 m and 1 m

respectively. In the last case, some detectors are placed in smaller vacuum chambers coupled to the main chamber.

### 3.1.1. PICO2000 laser system

The LULI laser system consists of two high-power (1 kJ) neodymium-glass laser chains ( $\lambda_L = 1053$  nm). The repetition rate is limited to 1 shot every 90'. One of the chains can operate in the ps regime due to CPA implementation. In order to avoid grating damage, the laser energy is limited to 100 J in 1 ps (150 TW). This laser is sent into the MILKA chamber in which the vacuum can reach  $10^{-5}$  mbar. The PICO2000 laser beam (180 mm of diameter) is focused at the *target chamber center* (TCC) with an f/4 parabola.

During our experiment, the energy on the target was around 60 J and the focal spot diameter about  $12 \mu\text{m}$  *full width at half maximum* (FWHM) providing an intensity of  $\sim 5 \times 10^{19} \text{ W/cm}^2$  ( $a_0 \approx 6$ ). The first *Airy disk* was found at  $27 \pm 3 \mu\text{m}$  from the center. The laser *Rayleigh length* was of the order of  $100 \mu\text{m}$ .

An optimized interaction between the main laser pulse and the target depends strongly on the nanosecond pedestal (the ASE) that comes before the main pulse. The ASE level can be reduced by changing *Pockel cell delays* (PD). A *Pockel cell* is a device that consists of an electro-optic crystal through which a light beam can propagate. The refractive index of this type of crystal can be modulated by applying a variable electric voltage and consequently, the phase delay changes.

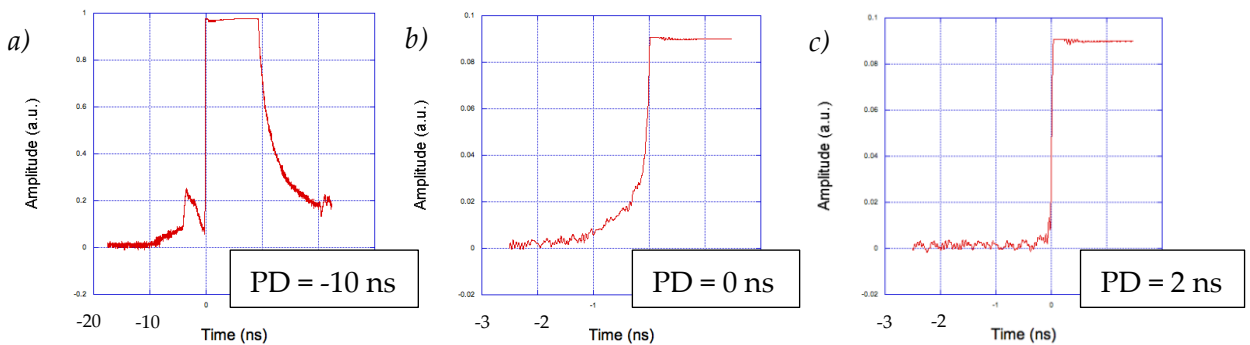


**Figure 3.2** Time spectra for PICO2000 laser for different *Pockel cells delays* (PD). The figures are provided by LULI. The main pulse, on the right of each figure, is saturated. *a)* PD = -10 ns: no delay is applied. The nanosecond ASE is present before the main pulse. *b)* PD = 0 ns: the ASE level is reduced *c)* PD = 2 ns: the level of ASE is further decreased but the duration of the main pulse starts to increase.

If no delay is applied ( $PD = -10$  ns), a high ASE level is measured before the main pulse maximum amplitude (**Figure 3.2a**). An increase of the *Pockel* cell delay (e.g.  $PD = 0$  ns) reduces the ns ASE level (**Figure 3.2b**). This procedure affects the laser bandwidth and the pulse duration. Hence, a compromise has to be found. E.g., in **Figure 3.2c**, ( $PD = 2$  ns), the level of ASE is decreased but the laser bandwidth is also decreased. Thus, the duration of the pulse starts to increase and the interaction between the laser pulse and the target changes drastically. During the experiment, the ns contrast of the laser system was around  $10^{-8}$  for the minimum level of ASE and pulse duration.

### 3.1.2. ALLS 100 TW laser system

The ALLS 100 TW laser is a solid-state Ti:Sapphire system ( $\lambda_L = 800$  nm) which delivers  $\sim 5$  J in 20 fs (100 TW) running at 2.5 Hz. The compression of the pulse is achieved due to double CPA and the contrast is improved by a *cross-polarized wave generation* (XPW) system placed before the second CPA. That allows a contrast of  $10^{-8}$  at 100 ps before the main pulse, along with a steep power rise with a *contrast* of  $< 10^{-6}$  at 3 ps before the main pulse. The temporal spectrum is shown in **Figure 3.3**. The mean laser pulse is at  $t = 0$  ps, on the right.

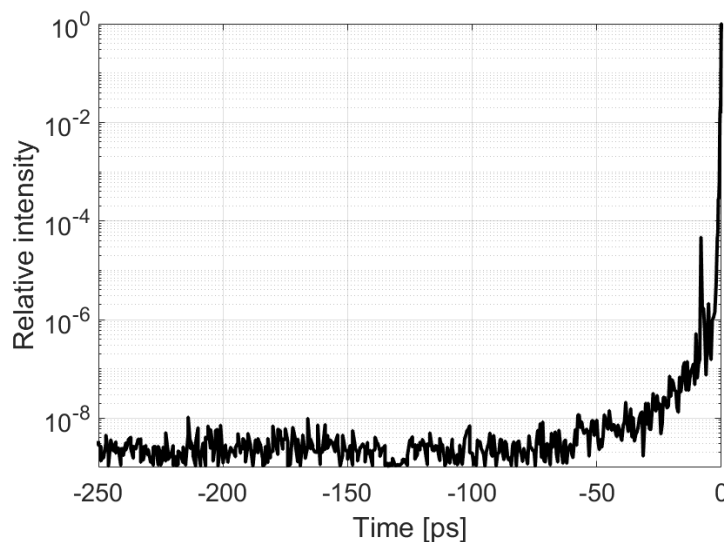


**Figure 3.3** ALLS 100 TW laser system temporal spectrum. On the right, the main laser pulse. The smaller peak on the left (at  $t = 15$  ps) is not real, it is just an artifact of the auto-correlation measurement. The figure shows a contrast of  $< 10^{-8}$  at 100 ps before the main pulse.

A focal spot image system has been developed. It works at full laser energy where the optical distortions and aberrations are maximal [Avizonis 1978]. The laser-driven ion acceleration beamline has an  $f/3$  off-axis parabola which focus the 100 mm diameter beam (at  $e^{-2}$ ) to a spot of about 5  $\mu\text{m}$  (FWHM) (see **Figure 3.4**) with the *Airy* disk at 15  $\mu\text{m}$  from the center. The Rayleigh length is about 48  $\mu\text{m}$ . The energy on target is about 2 J corresponding to an intensity of  $\sim 1.3 \times 10^{20} \text{ W/cm}^2$  ( $a_0 \approx 9$ ). ALLS laser optical aberrations are well controlled and compensated at full power by a thermalization system, which makes this laser very stable.

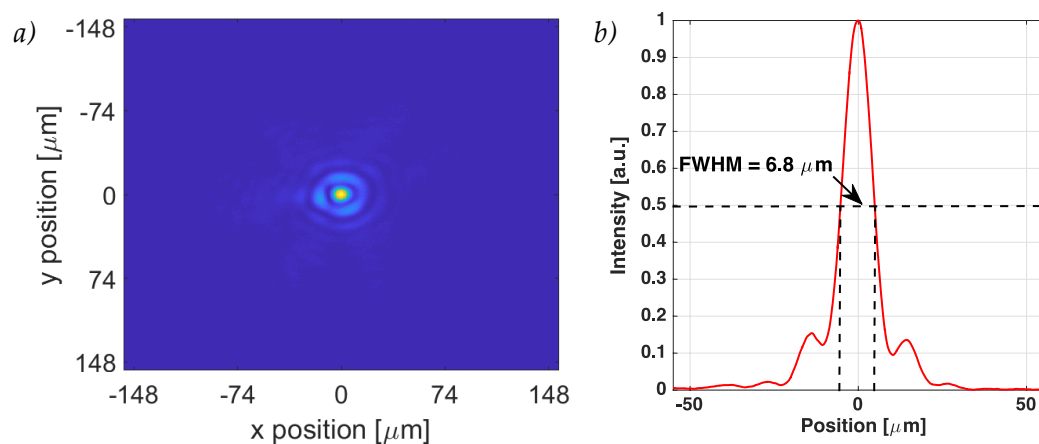


**Figure 3.4** Focal spot imaging system designed to work at full power (2 J at TCC). *a*) Picture taken from a CCD *b*) Reconstructed spot size. The intensity as a function of the position is plotted. Picture taken from [Paper III].

## 3.2. Targetry: development of gas-jet targets

Laser-driven ion acceleration can be achieved with high-power laser systems. The laser pulse parameters have a strong impact on ion acceleration, however access or modifications over large ranges are not always possible. Thus, the optimization of the target is often the simplest way to enhance ion acceleration with a given laser.

Solid targets are mostly used for ion acceleration in many experiments for their high density, simplicity of fabrication, and ability to produce high-quality ion beams using TNSA acceleration mechanism.

In this thesis work, solid targets are used at the EMT-INRS installation. The acceleration mechanism is well known (TNSA). With the previous beam line, protons with energies up to  $11 \pm 1$  MeV were found using 120 nm thickness etched silicon nitride membranes and using a plasma mirror [Fourmaux 2013]. In the current beamline, protons with a maximum energy of  $8 \pm 0.5$  MeV were found using 5  $\mu\text{m}$  thickness copper targets [Paper VI]. This last result could be improved by using thinner targets and a plasma mirror. In the last campaign, concentrated on the laser-based source applications (Chapter 5), Al, Cu, and Au commercial foils (purity 99.9%, purchased from Goodfellow) of 3 and 5  $\mu\text{m}$  thicknesses of mm dimensions were used. A multi-target holder, which contain several solid targets, is utilized with a capacity of 14 targets. A compact *target alignment bench* (TAB) is designed for our holder outside the vacuum chamber (See Figure 3.5).

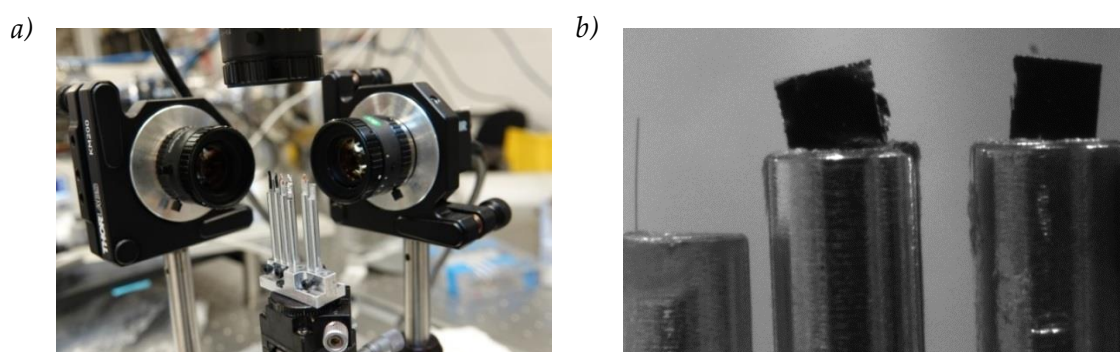


**Figure 3.5** a) *Target alignment bench* (TAB) to pre-align the solid targets outside the vacuum chamber b) Picture is taken with one of the cameras of the multi-holder target. A 20  $\mu\text{m}$  diameter tungsten pin is in one holder target to do a first precise alignment. 5  $\mu\text{m}$  thickness copper targets are on the right of the picture, displayed from the front.

The TAB is calibrated to follow the same direction as the translation axis of the central motors inside the vacuum chamber at TCC. Inside the vacuum chamber, the targets are aligned by a shadowgraphy imaging system along with two cameras on each side of the top part of the chamber. Along with good laser stability, the shot-to-shot repeatability of the target alignment is important for ensuring a reliable proton source.

However, the replacement of the destroyed target and the realignment of the new one are mandatory after each laser shot. Moreover, the interaction generates debris that could damage the surrounding optical elements. A large effort has been made to develop fast-moving, HRR (up to 0.5 Hz [Gao 2017]) target holders. A considerable improvement has been achieved, but no-debris deposition and multi-target-holder replacement after several shots still represent a challenge. A particular kind of solid targets, that can be regenerated *in situ*, are cryogenic ribbons [Margarone 2016, Obst 2017]. These could be clean sources of protons, free of contaminants and could operate at HRR; but their operation is extremely costly and complex. The acceleration mechanism is again TNSA producing broad energy distributions. For instance, a flux of  $10^9$  protons/MeV/sr with a maximum energy of 18 MeV was reported at the 150 TW ultra-short pulse laser Draco, HZDR with a planar ( $20 \times 2 \mu\text{m}$ ) cryogenic hydrogen jet [Obst 2017].

Another option consists in using liquid targets as water droplets [Karsch 2003, Ter-Avetisyan 2004, Schnurer 2005, Hilz 2018] or liquid crystal films [Poole 2014], which are difficult to align. Recently, Hiltz *et al.* [2018] observed proton bunches with energies between 20 and 40 MeV using the PHELIX PW laser at GSI delivering 500 fs pulses with an energy of 150 J. The acceleration mechanism reported is Coulomb repulsion. The laser impinges onto the target, the atoms are ionized and the positive charges accumulate until the moment that the ions are accelerated by the repulsive electrostatic field and emitted from the irradiated target.

Gas-jet targets are an interesting alternative for different ion species acceleration as they can be used at HRR and are debris free. Under-dense ones have been studied for helium acceleration and first results were published in 1999 by Krushelnick *et al.* [1999]. They used the VULCAN laser (50 J and 0.9 ps pulse duration) at *Rutherford Appleton Laboratory* with a gas jet target of  $n_e \sim 5 \times 10^{19} \text{ cm}^{-3}$ . Later, in 2004, Wei *et al.*, [2004] used the same installation

but with the Petawatt laser beam of 180 J and a He target of density equal to  $1.4 \times 10^{20} \text{ cm}^{-3}$ . In 2006, Willingale *et al.*, [2006] an experiment was done at the same installation with 340 J and with He target of density equal to  $4 \times 10^{19} \text{ cm}^{-3}$ . More recently, near-critical-density gas-jet targets have been studied. The acceleration scheme at play involving collisionless-shock waves has been first introduced by Silva *et al.* [2004] for over-dense plasmas and expanded by d’Humières *et al.* [2010] for under-dense plasma targets. In **Section 4.4**, we will detail their results.

With near-critical-density plasmas using a CO<sub>2</sub> laser ( $\lambda_L \approx 10 \text{ }\mu\text{m}$ ), Haberberger *et al.* [2012] demonstrated that laser-driven collisionless shocks can accelerate proton beams up to 20 MeV with a narrow energy spread of about 1% and low emittance. Several results were published using CO<sub>2</sub> lasers with near-critical gas-jet targets ( $n_{cr} [\lambda_L=10 \text{ }\mu\text{m}] = 10^{19} \text{ cm}^{-3}$ ) [Harberberger 2012; Palmer 2011; Helle 2016]. However, the development of near-critical-density supersonic gas-jet targets for near-infrared lasers is still very challenging ( $n_{cr} [\lambda_L=1 \text{ }\mu\text{m}] = 10^{21} \text{ cm}^{-3}$ ). Only a few experiments testing near-critical gas-jet targets for near-infrared lasers have been performed so far: in 2013, Sylla *et al.* [2013] carried out one with the *Salle Jaune* laser at LOA ( $\tau_L = 35 \text{ fs}$ ,  $E_L = 810 \text{ mJ}$ ,  $\lambda_L = 820 \text{ nm}$ ,  $R_L = 10 \text{ Hz}$ ) using a submillimetric supersonic  $0.95 n_{cr}$  density helium jet from a conical nozzle. They observed a maximum energy of 250 keV in the transverse direction. In 2017, Chen *et al.* [2017] used a supersonic  $2.5 n_{cr}$  density hydrogen gas-jet from a rectangular nozzle at the TITAN laser facility (LLNL) ( $\tau_L = 5 \text{ ps}$ ,  $E_L = 210 \text{ J}$ ,  $\lambda_L = 1054 \text{ nm}$ ,  $R_L = 2 \text{ shot/h}$ ) and observed protons with energies up to 0.8 MeV in the longitudinal direction.

Gas jets as laser-driven ion acceleration targets are promising tools in view of HHR operation. The challenge is to build nozzles capable to generate the required gas density and shape. E.g., subsonic or supersonic gas flows have different density profiles. Laser-driven ion acceleration requires supersonic micrometric nozzles that are not often commercially available. These nozzles are used in conjunction with fast electro-valves triggered by an electric signal delivered by the laser system. They are fed by high-pressure gas boosters.

In the following, we recall the flow properties of supersonic gas jets and introduce some related definitions. Then, we discuss the results of the *computational fluid dynamics* (CFD) simulations with the code FLUENT [ANSYS FLUENT] used to design different supersonic

nozzles and study the properties of their density profiles. The density profiles obtained by simulations are compared later with the measured ones to validate the simulation parameters. The dynamics of the flow is experimentally studied as well to define the properties of the gas jet impinged by the laser pulse. These gas-jet targets have been tested at the LULI laser facility (see **Figure 3.6**). The results are described in **Chapter 4**.

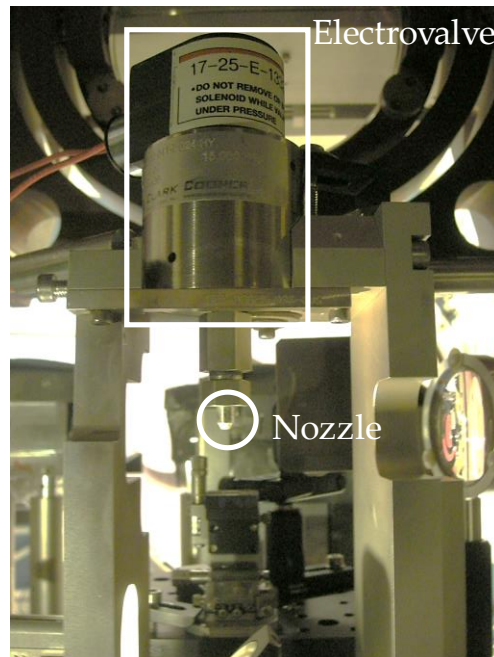


**Figure 3.6** Picture of the nozzle and the electro-valve at the LULI laser facility. The nozzle is upside down.

### 3.2.1. Supersonic gas jets: definitions

Anderson [1990] has explained the different properties of subsonic and supersonic flows in Laval nozzles, which are *convergent-divergent* nozzles. A subsonic flow is a flow that has a velocity smaller than the velocity of sound, so the fluid has a Mach number  $M < 1$ .

Supersonic flows ( $M > 1$ ) are related to supersonic shock waves of different types: *normal shock waves*, *oblique shocks* or *expansion waves*. The first one is an example of *one-dimensional* flow, in which the flow properties vary only in one direction. The *oblique shocks* and *expansion waves* are *two-dimensional* phenomena.

A *normal shock* is an abrupt and finite variation of temperature, pressure, density, and velocity perpendicular to the free stream of the fluid. The shock is a very thin region, usually of the order of a few molecular mean free paths  $\sim 10^{-5}$  cm for air at standard conditions

(273 K and 1 bar). A simple diagram of a *normal shock* is presented in **Figure 3.7**, taken from [Anderson 1990]. When  $M_1$  and  $M_2$  are equal to 1, the *normal shock* is infinitely weak and it is defined as a *Mach wave*.

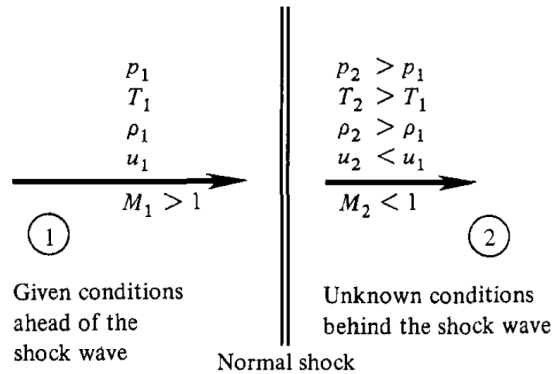


**Figure 3.7.** Diagram of a *normal shock*. From [Anderson 1990].

*Oblique shocks* and *expansion waves* occur when supersonic flows bend their trajectories due to a change in the surface direction. Diagrams of these two types of shocks are presented in **Figure 3.8**, figure also taken from [Anderson 1990].

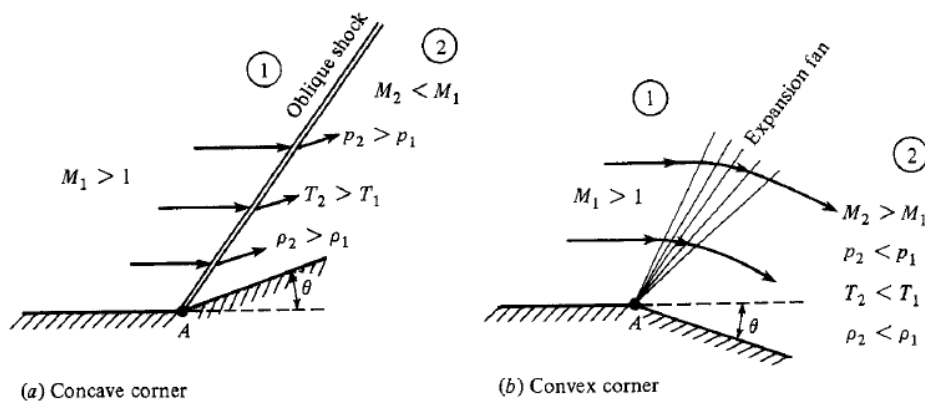


**Figure 3.8.** Diagrams of supersonic flow over a corner. From [Anderson 1990].

In **Figure 3.8a**, at point A, the slope of the surface changes by an angle  $\theta$ . Hence, the flow streamlines are deflected upwards, following the surface direction. An *oblique shock* is formed in the free-stream direction. Across the *oblique shock*, the Mach number decreases and the pressure, temperature, and density increase. The weak oblique shocks correspond to *Mach waves* in a *two-dimensional* flow.

In the case of a convex corner, **Figure 3.8b**, the flow streamlines are deflected downward, towards the surface. The change of flow direction takes place across an expansion wave

centered at point A. Basically, the expansion wave is a continuous succession of Mach waves. In contrast with the *oblique shock*, the flow properties change smoothly and continuously. The  $M$  value increases and the pressure, temperature, and density decrease. If the convex corner is sharp, the expansion fans are called *centered* or *Prandtl-Meyer* (who first worked out a theory for this supersonic flow).

These different kinds of flows are at play in supersonic nozzles. A nozzle is a duct with a throat connected at its inlet to a very large reservoir with total *reservoir* pressure  $p_r$ . (**Figure 3.9a**). The exit of the duct has an *exit static* pressure  $p_e$ . As  $p_e$  is gradually reduced from  $p_r$ , air flows from the reservoir to the exit with a mass flow  $\dot{m}$ . The mass flow through any elemental surface arbitrarily oriented in a flowing fluid is defined  $\dot{m} = \rho \mathbf{u} \cdot d\mathbf{S}$ , where  $\rho$  is the density,  $\mathbf{u}$  the velocity and  $d\mathbf{S} = \mathbf{n} dS$  where  $\mathbf{n}$  is the unit vector normal to the surface  $S$ . As  $p_e$  is reduced,  $\dot{m}$  increase, until it remains constant even if  $p_e$  is reduced all way to vacuum (**Figure 3.9b**). The local Mach number increases through the convergent portion of the nozzle, reaching the minimum area with a  $M = 1$ , a sonic flow. When  $\dot{m}$  no longer increases with the reduction in  $p_e$ , the duct is called to be *choked*. As the flow achieves the sonic flow in the throat, in the convergent portion nothing happens.

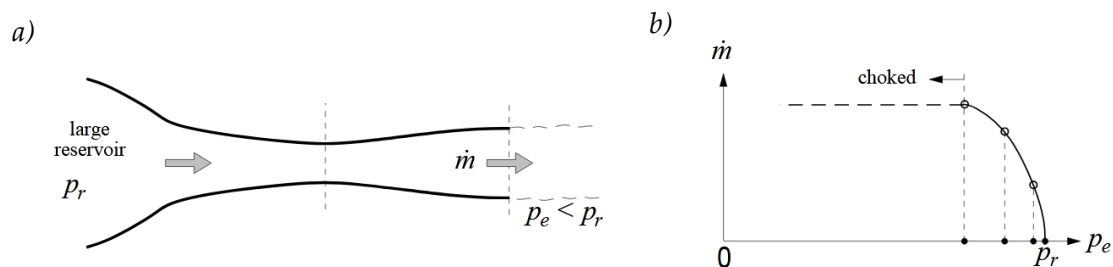


**Figure 3.9** a) Diagram of a nozzle, considering a duct with a throat, connected at its inlet to a very large reservoir with total pressure  $p_r$ . The *exit static pressure* is defined as  $p_e$  and the mass flow as  $\dot{m}$ . b)  $\dot{m}$  is presented as a function of  $p_e$ . As  $p_e$  decreases,  $\dot{m}$  increases. Until the duct is *choked* and the mass flow no longer increases. The figure was taken from [Anderson 1990].

When the *exit* pressure is reduced below the level required to reach choking, a new flow emerges which is called the *Laval nozzle flow*. In the divergent duct, the flow becomes supersonic, its velocity increases, the pressure decreases as the area increases.

A *normal shock* is formed inside the duct. As the *exit* pressure is reduced, the *normal shock* wave moves downstream, closer to the nozzle exit. Behind the shock, the flow is subsonic, its Mach number decreases, and density, temperature, and static pressure increase as we

observed in **Figure 3.7**. The shock produces a total pressure loss and the Mach number behind the shock is lower than what they would be.

If the exit pressure is low enough, the exit flow becomes fully supersonic as the shock can be moved outside the duct. There are three types of exit flows: *over-expanded*, *Matched* and *under-expanded*, depending on the *exit* pressure  $p_e$  and the *back* pressure  $p_B$  of the surrounding air. The first type, *over-expanded* flow, is when  $p_B > p_e$ : the flow must adjust to a higher pressure, see **Figure 3.10a**. An oblique shock attached to the nozzle exit is formed but outside the duct. The second type of flow, *Matched*, is when  $p_B = p_e$  and the duct nozzle flow comes out at the same pressure and no turning takes place in **Figure 3.10b**. The third one, *under-expanded* flow, is when  $p_B < p_e$  and the nozzle flow must expand to match  $p_B$  (**Figure 3.10c**). In this case, the flow is equilibrated due to *expansion waves* outside the nozzle.

A fourth type, more complicated than the others, is the *jet shock diamonds*, a combination of *under-expanded* and *over-expanded* nozzle flows (see **Figure 3.10d**). The gas jet is propagating through the atmosphere, which has boundary surfaces. Several *oblique shocks* are produced, and their reflections at the boundaries are characteristic of this flow. The various reflected waves form a diamond-like pattern.

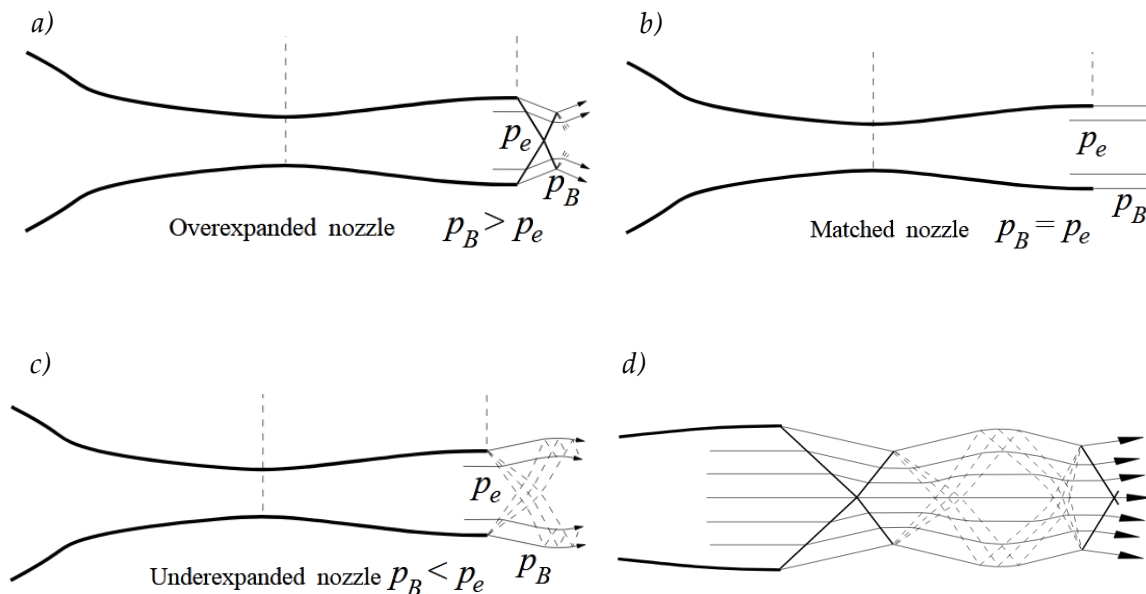


**Figure 3.10** Scheme representation of the flow of a) an *over-expanded* nozzle, b) a *matched* nozzle, c) an *under-expanded* nozzle and d) a *jet shock diamond*. In this last picture, only the nozzle exit is presented on the left. Taken from [Anderson 1990].

This is a *quasi-one-dimensional* consideration and it does not tell anything about the *contour* of the duct. For *real* supersonic nozzles, the shock depends on the wall shapes, the thermal conduction, the viscosity and so on. E.g. *oblique shocks* can occur inside the nozzle. We are not going to describe in detail the numerical techniques for a steady supersonic flow, however, **Figure 3.11** shows a schematic of supersonic nozzle design in a *two-dimensional* consideration.

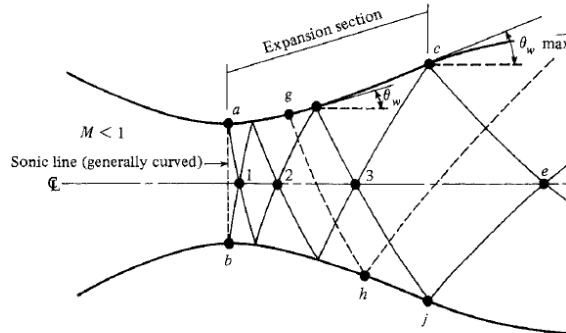


**Figure 3.11** Schematic of a supersonic nozzle design in two dimensions. From [Anderson 1990].

In the expansion section of the nozzle, *expansion waves* are generated and propagate. The solid lines present the weak *expansion waves*, i.e., the *Mach waves*. Multiple reflections are observed from the nozzle throat to the exit of the nozzle. We can observe that due to the geometry symmetry, the waves generated from the top wall seems to be *reflected* from the centerline. That is why the calculation can be simplified and one can only calculate the flow above the centerline.

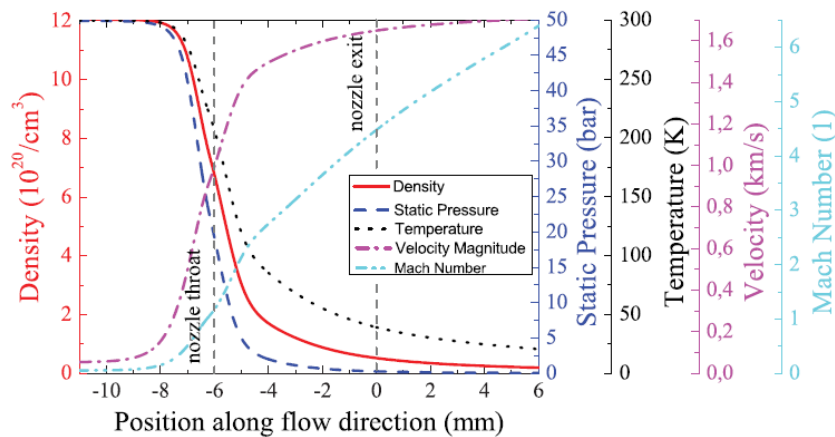


**Figure 3.12** Density, static pressure, temperature, velocity, and Mach number obtained at the center of a helium gas flow through a Laval nozzle obtained from *computational fluid dynamics* simulations from [Schmid 2012].

**Figure 3.12** shows the behavior of the different flow properties of a simulated *under-expanded* nozzle. The figure is taken from [Schmid 2012]. It is possible to observe how the M number (flow velocity) increases and it is equal to 1 at the throat of the nozzle (light-blue dashed line). Meanwhile, the density (red solid line), the static pressure (dark-blue dashed line), and the temperature (black dashed line) decrease from the reservoir to the nozzle exit.

In this thesis work, three types of supersonic micrometric nozzles have been designed: *conical nozzles*, *shock nozzles*, and *asymmetrical nozzles*. In **Figure 3.13**, a 3D presentation of these nozzles is made with an *artistic program* [Sketchup]. The simplest one is the *conical nozzle*, close to the *Laval nozzle*. This nozzle is modified with an edge at its exit to form a *shock nozzle* (**Figure 3.13b**).

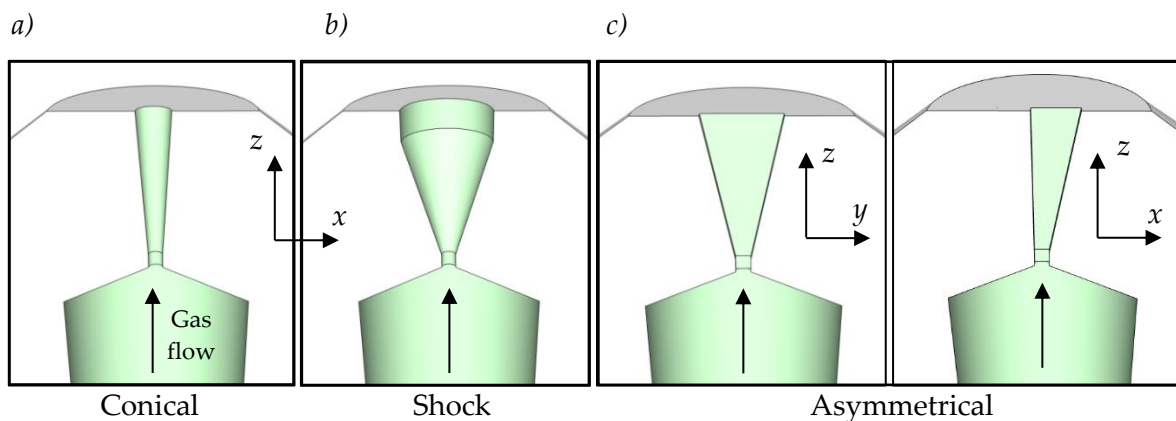


**Figure 3.13** 3D presentation of different types of nozzles. *a)* convergent-divergent nozzle similar to the *Laval nozzle*: *conical nozzle*. *b)* Divergent-convergent nozzle with an edge at the exit of the nozzle: *shock nozzle*. *c)* A more complex nozzle as a rectangular one: *asymmetrical nozzle*.

In the laboratory conditions, these nozzles produce *under-expanded* flow at the exit of the nozzle. The edge of the *shock nozzle* produces a thin peaked density profile at a certain distance of the nozzle exit due to the formation of *oblique shocks*. Its fabrication is not simple, and the edge increases the manufacturing cost of the nozzle.

More complex nozzles can be interesting, e.g., *asymmetrical nozzles*. They may have rectangular shapes at the throat and exit but the convergent-divergent shape is still present. It is also possible to have one side convergent-divergent and the other convergent-straight (see **Figure 3.13c**) and so on. As *shock nozzles*, their fabrication is more difficult and more expensive than *conical nozzles*. Moreover, the non-axisymmetric nozzle experimental

characterization is more complex (see **Section 3.2.6**). 3D CFD simulations, which are extremely time-consuming, are needed.

### 3.2.2. Study and optimization of nozzle geometric parameters

In this thesis work, gas jets with an electronic density of around  $10^{21} \text{ cm}^{-3}$  are developed. As seen in **Chapter 2**, the lasers are mostly absorbed around their critical densities. Such high densities can be achieved with supersonic gas jets. The objective is to obtain a high density at a certain distance from the nozzle exit under vacuum conditions, while controlling other parameters such as the gas-jet divergence, transversal density profile, and longitudinal shape. A proper understanding of the nozzle geometry is essential because it strongly impacts the conditions mentioned above. E.g., the maximum density variation depends the inlet pressure, exit nozzle diameters, and throat diameters. CFD simulations have been performed to design different kinds of nozzles.

FLUENT simulations numerically solve the Navier-Stokes equations [[Constantin 1988](#)] on a discrete grid. An implicit *density-based coupled solver* (DBCS) is used with double-precision accuracy *green-Gauss* node-based gradients of solution variables, to solve the stationary fluid flow, using a *real-gas Peng-Robinson* solution. The standard *k-omega* model is used to model the turbulence [[Wilcox 2006](#)]. For symmetric nozzles, a 2D axisymmetric grid with quadrilateral cells has been employed, which typically consists of  $2 \times 10^5$  cells with  $2 \times 10^{-2}$  average skewness ratio and minimum orthogonal quality of  $8.5 \times 10^{-1}$ . The grid is adapted to the surfaces and it has been verified that further refinements do not change the simulation results.

The nozzle is composed of a reservoir, a convergent section, a throat, and an expansion section giving to a chamber under vacuum. The geometrical parameters of the simulation are the throat diameter  $d$ , the nozzle exit diameter  $D$ , and the cone length  $L$ . **Figure 3.14a** shows all these parameters. For *shock nozzles*, the length of the edge is denominated as  $E$ , as one can see in **Figure 3.14b**. To facilitate the reading of this chapter, a schematic drawing of the nozzle with its parameters is included as a foot note in some pages.

The simulation also takes into account a wall roughness of about  $1 \mu\text{m}$ , that micrometric nozzles machined by electroerosion usually show. The boundary conditions of the

simulation are a high pressure at the inlet and two low pressures at the outlets in the vacuum chamber outside the nozzle. The distance from the nozzle exit is represented by  $z$ . The medium is diatomic hydrogen unless otherwise indicated.

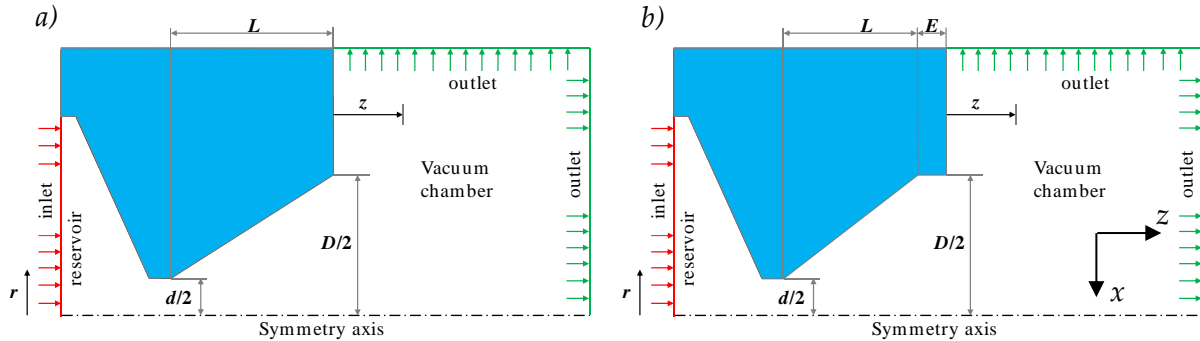


**Figure 3.14** Scheme of the 2D axisymmetric nozzle geometries for a) *conical nozzles* and b) *shock nozzles* used in CFD simulations (see text for details).

The density evolution as a function of the *reservoir* pressure (or *inlet* pressure),  $p_r$ , is well known to fit a linear progression [Couperus 2016]. **Figure 3.15** shows the linear evolution of the density as a function of the  $p_r$  for three *conical nozzles* exit sizes  $D$  in the pressure range between 50 and 1000 bar at a distance of  $z = 500 \mu\text{m}$  from the nozzle exit. This range of pressures can be achieved with commercial gas boosters. In order to provide a bigger density than the critical one, the minimum reservoir pressure is 400 bar. A  $p_r$  of 1000 bar allows to access a density close to the critical density almost independently of the nozzle parameters and over-critical densities can be reached with optimized geometries.  $p_r = 1000$  bar is chosen to work with and optimize the nozzles with respect to their density profiles and shapes.

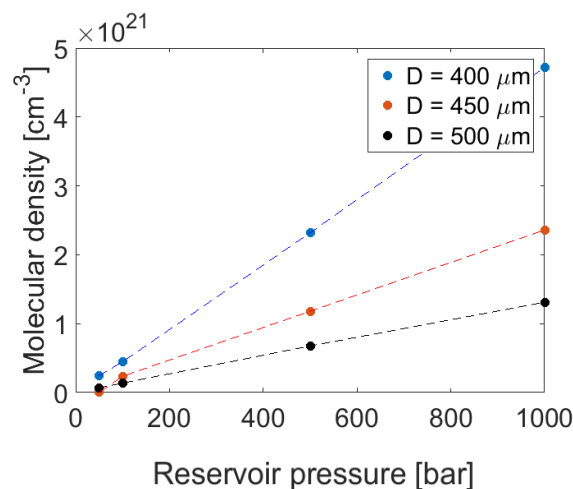


**Figure 3.15** Evolution of the molecular density as a function of the *reservoir* pressure at a distance of  $500 \mu\text{m}$  from the *conical nozzle* exit for different exit sizes ( $400 \mu\text{m}$ ,  $450 \mu\text{m}$  and  $500 \mu\text{m}$ ).

The laser-gas-jet interaction must take place at a certain distance  $z$  from the nozzle exit, where the wanted density profile is achieved.  $z$  should be large enough to minimize the nozzle damage during the laser-plasma interaction.

### Conical nozzles

A detailed study is carried out to design *conical nozzles* capable to deliver more than  $10^{21} \text{ cm}^{-3}$  of diatomic hydrogen far from the nozzle exit. In order to find the optimum parameters, density contour maps are made. The distance from the nozzle exit  $z$  is presented as a function of the exit size  $D$  for different values of  $d$  and  $L$ .

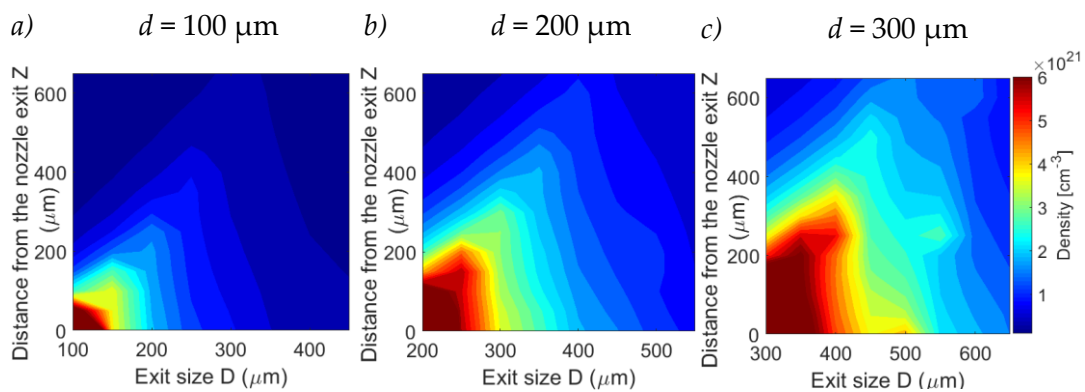
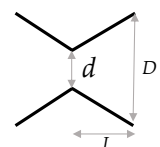


**Figure 3.16** Interpolated contour maps of the molecular density at 1000 bar of hydrogen at different distances from the nozzle exit  $z$  as a function of the exit size  $D$  for three throat diameters ( $L$  is fixed) a)  $d = 100 \mu\text{m}$ , b)  $d = 200 \mu\text{m}$  and c)  $d = 300 \mu\text{m}$ .

**Figure 3.16** shows density contour maps comparing three throat diameters  $d = 100 \mu\text{m}$ ,  $200 \mu\text{m}$ , and  $300 \mu\text{m}$ . The exit size  $D$  was varied from 100-200-300  $\mu\text{m}$  to 450-550-650  $\mu\text{m}$  respectively. Distances  $z$  from the nozzle exit,  $z = 0$ , up to 650  $\mu\text{m}$  by 50  $\mu\text{m}$  steps are investigated. For each figure,  $L = 1 \text{ mm}$  is fixed while  $D$  is scanned.

A given density can be reached using different couples of exit sizes  $D$  and different distances to the nozzle  $z$ . We can compare the three images and observe that a larger throat diameter  $d$  induces an increase of the *molecular density*  $\rho$  and a decrease of the optimum distance from the nozzle,  $z$ . Some of the results are summarized in **Table 3.1**.



	$d = 100 \mu\text{m}$	$d = 200 \mu\text{m}$	$d = 300 \mu\text{m}$
	$\rho = 4.4 \times 10^{20} \text{ cm}^{-3}$	$\rho = 3.2 \times 10^{21} \text{ cm}^{-3}$	$\rho = 1.1 \times 10^{22} \text{ cm}^{-3}$
$D = 300 \mu\text{m}$	$z = 600 \mu\text{m}$	$z = 300 \mu\text{m}$	$z = 100 \mu\text{m}$
	<b>Figure 3.16a</b>	<b>Figure 3.16b</b>	<b>Figure 3.16c</b>

**Table 3.1** Molecular densities,  $\rho$ , and the optimum interaction distances from the nozzle exit,  $z$ , achieved for a nozzle exit  $D = 300 \mu\text{m}$  and different  $d$  values.

**Figure 3.17** shows the FWHM contour maps performed with the same parameters as in **Figure 3.16**. One observes that the maximum density corresponds to the minimum FWHM as a result of the converging waves.

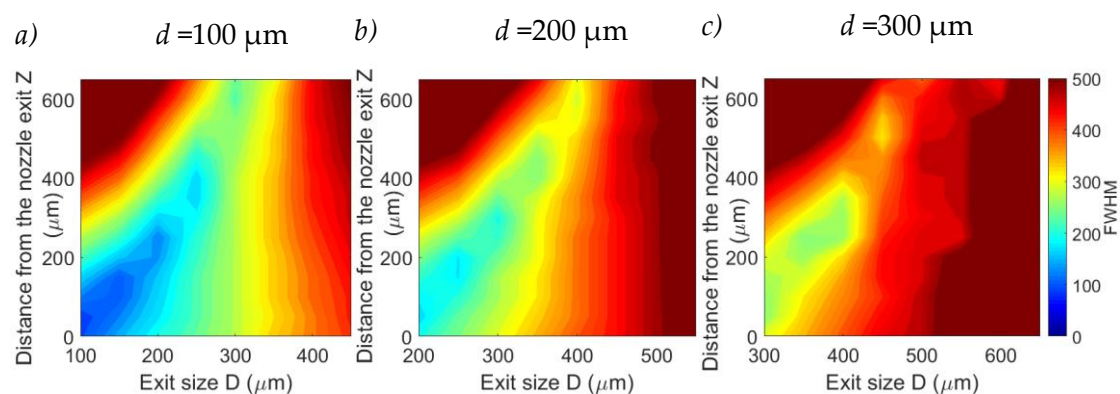
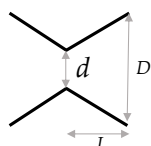


**Figure 3.17** The FWHM interpolated contour maps at 1000 bar of hydrogen at different distances from the nozzle exit  $z$  as a function of the exit size  $D$  for three throat diameters ( $L$  is fixed) *a*)  $d = 100 \mu\text{m}$ , *b*)  $d = 200 \mu\text{m}$  and *c*)  $d = 300 \mu\text{m}$ .

We can compare the three images and observe that a larger throat diameter  $d$  induces an increase of the FWHM and a decrease of the optimum distance from the nozzle,  $z$ . Some of the results are summarized in **Table 3.2**.

	$d = 100 \mu\text{m}$	$d = 200 \mu\text{m}$	$d = 300 \mu\text{m}$
	$FWHM = 230 \mu\text{m}$	$FWHM = 200 \mu\text{m}$	$FWHM = 257 \mu\text{m}$
$D = 300 \mu\text{m}$	$z = 600 \mu\text{m}$	$z = 300 \mu\text{m}$	$z = 100 \mu\text{m}$
	<b>Figure 3.17a</b>	<b>Figure 3.17b</b>	<b>Figure 3.17c</b>

**Table 3.2** FWHM and the optimum interaction distances,  $z$ , achieved for a nozzle exit  $D = 300 \mu\text{m}$  and different  $d$  values.



In **Table 3.2**, the FWHM for  $d = 100 \mu\text{m}$  is larger than the one  $d = 200 \mu\text{m}$ . This is because  $D = 300 \mu\text{m}$  is not an optimized value for a small throat diameter. For example, for  $D = 150 \mu\text{m}$  a FWHM of  $110 \mu\text{m}$  can be achieved.

**Figure 3.17** also represents the divergence of the flow for a chosen exit size  $D$  value. We can observe from **Figure 3.17a** that a further distance from the nozzle exit,  $z$ , induces an increase of the FWHM. Some of the results are summarized in **Table 3.3**. A study of the gas jet longitudinal profile is made further in **Section 3.2.3**.

$D = 200 \mu\text{m}$	$z = 200 \mu\text{m}$	$z = 300 \mu\text{m}$	$z = 400 \mu\text{m}$	$z = 500 \mu\text{m}$
$d = 100 \mu\text{m}$	$FWHM = 140 \mu\text{m}$	$FWHM = 170 \mu\text{m}$	$FWHM = 270 \mu\text{m}$	$FWHM = 370 \mu\text{m}$

**Figure 3.17a**

**Table 3.3** FWHM achieved for a throat diameter  $d = 100 \mu\text{m}$  and nozzle exit  $D = 200 \mu\text{m}$  at different  $z$  values.

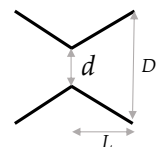
The exit size,  $D$ , dependence can be observed in **Figure 3.16** and **Figure 3.17**. Comparing the two images we observe that a larger nozzle exit  $D$  induces a decrease of the density,  $\rho$ , an increase of the FWHM and an increase of the optimum distance from the nozzle,  $z$ . Some of the results are summarized in **Table 3.4**.

	$D = 150 \mu\text{m}$	$D = 250 \mu\text{m}$	$D = 300 \mu\text{m}$
$d = 100 \mu\text{m}$	$\rho = 3.8 \times 10^{21} \text{ cm}^{-3}$	$\rho = 9.3 \times 10^{20} \text{ cm}^{-3}$	$\rho = 4.5 \times 10^{20} \text{ cm}^{-3}$
<b>Figure 3.16a</b>	$FWHM = 110 \mu\text{m}$	$FWHM = 170 \mu\text{m}$	$FWHM = 250 \mu\text{m}$
<b>Figure 3.17a</b>	$z = 100 \mu\text{m}$	$z = 350 \mu\text{m}$	$z = 550 \mu\text{m}$

**Table 3.4** Densities,  $\rho$ , FWHM and the optimum interaction distances from the nozzle exit,  $z$ , achieved for a throat diameter  $d = 100 \mu\text{m}$  and different  $D$  values.

**Figure 3.18** shows the change of the density contour maps for different nozzle lengths  $L$ . In the three images we observe that for different nozzle lengths  $L$  (in a small range between 1 and 3 mm), the density does not change dramatically. Some of the results are summarized in **Table 3.5**.

However, if  $L$  is larger, Mach waves will dissipate inside the cone (see **Figure 3.11**) and a shorter nozzle ( $< 0.5 \text{ mm}$ ) will not confine the flow, with a consequent decrease of density of the gas jet produced and increase of its flow divergence [[Schmid 2012](#)].



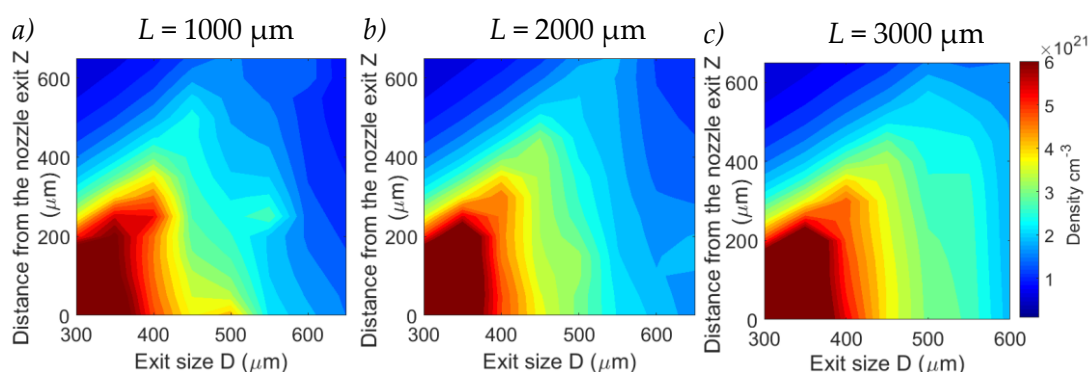


**Figure 3.18** Contour maps of the density at 1000 bar at different distances from the nozzle exit  $z$  as a function of the exit size  $D$  for three lengths ( $d=300\ \mu\text{m}$  fixed): a)  $L=1000\ \mu\text{m}$  b)  $L=2000\ \mu\text{m}$  and c)  $L=3000\ \mu\text{m}$ .

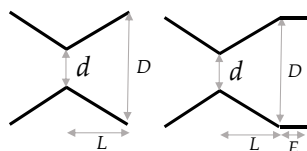
$z = 250\ \mu\text{m}$	$L = 1000\ \mu\text{m}$	$L = 2000\ \mu\text{m}$	$L = 3000\ \mu\text{m}$
$D = 350\ \mu\text{m}$	$\rho = 5.6 \times 10^{21}\ \text{cm}^{-3}$ <b>Figure 3.15a</b>	$\rho = 5.5 \times 10^{21}\ \text{cm}^{-3}$ <b>Figure 3.15b</b>	$\rho = 5.4 \times 10^{21}\ \text{cm}^{-3}$ <b>Figure 3.15c</b>

**Table 3.5** Densities achieved at  $z = 250\ \mu\text{m}$  for a nozzle exit  $D = 350\ \mu\text{m}$  and different  $L$  values.

### Shock nozzles

The *shock nozzle* exit flow is different from the *conical nozzle* one because of its edge at the nozzle exit. The other nozzle parameters are the same as in the previous case (throat diameter  $d$ , exit diameter  $D$ , and cone length  $L$ ) with the addition of an edge of length  $E$ . This edge acts as a *concave corner*, forming an *oblique shock* at a fixed distance in the longitudinal direction ( $z$ -axis). In this section, density flow side view images are presented to optimize the nozzle parameters to reach the furthest interaction point.

The first parameter studied is the throat diameter,  $d$  (see **Figure 3.19**).  $D$  ( $480\ \mu\text{m}$ ) and  $E$  ( $200\ \mu\text{m}$ ) are fixed. An increase of  $d$  induces an increase of the density and of the focal spot size. This behavior has been already observed with *conical nozzles*, however, for *shock nozzles*, we avoid the term FWHM and introduce the term focal spot size. This will be explained in **Section 3.2.3**. In **Figure 3.19**, we can also observe how the shock formation distance,  $z_{shock}$ , decreases with the throat size. These results are summarized in **Table 3.6**. For the following parameters,  $d$  will be fixed at  $100\ \mu\text{m}$ . This is the minimum diameter possible that electroerosion can produce.



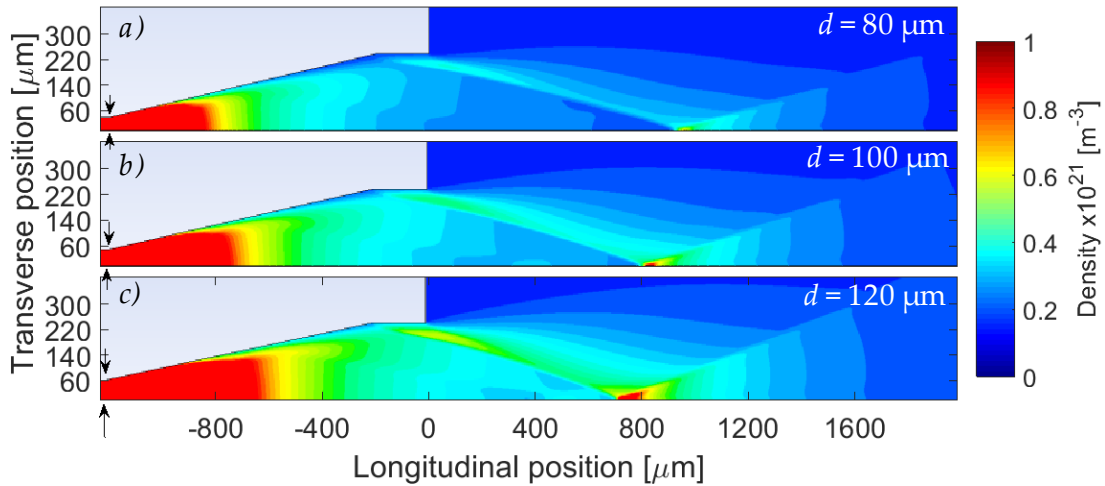


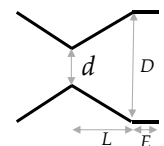
**Figure 3.19** Molecular density maps at 1000 bar of hydrogen for different throat diameters  $d$ . The longitudinal position is normalized to  $z = 0$  at the exit of the nozzles. *a)*  $d = 100 \mu\text{m}$ , *b)*  $d = 200 \mu\text{m}$  and *c)*  $d = 300 \mu\text{m}$ . The red color at the entrance of the nozzle can represent molecular densities larger than  $1 \times 10^{21} \text{cm}^{-3}$ .

$d = 80 \mu\text{m}$	$d = 100 \mu\text{m}$	$d = 120 \mu\text{m}$
$z_{shock} \approx 960 \mu\text{m}$	$z_{shock} \approx 840 \mu\text{m}$	$z_{shock} \approx 750 \mu\text{m}$
<b>Figure 3.19a</b>	<b>Figure 3.19b</b>	<b>Figure 3.20c</b>

**Table 3.6** Optimum interaction distances,  $z_{shock}$ , achieved for  $D = 480 \mu\text{m}$ ,  $E = 200 \mu\text{m}$  and different  $d$  values.

The second parameter studied is the exit diameter  $D$ , as observed in **Figure 3.20**.  $d$  ( $100 \mu\text{m}$ ) and  $E$  ( $150 \mu\text{m}$ ) are fixed. When the exit diameter increases, the shock is created further from the nozzle exit (the results are summarized in **Table 3.7**), and the density and the size of the focal spot are decreased.

We can analyze the edge  $E$  variation, keeping  $d = 100 \mu\text{m}$ ,  $D = 500 \mu\text{m}$  fixed. **Figure 3.21** shows how a larger edge induces a focal spot area closer to the exit of the nozzle. These results are summarized in **Table 3.8**. The dimensions of the spot size and density are increased.



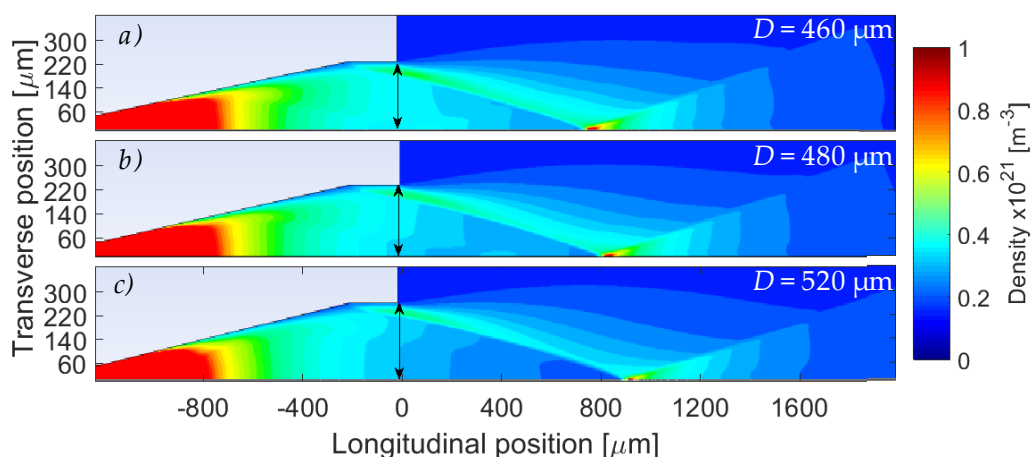


**Figure 3.20** Molecular density maps at 1000 bar for different exit diameters  $D$ . The longitudinal position is normalized to  $z = 0$  at the exit of the nozzles. *a)*  $D = 460 \mu\text{m}$ , *b)*  $D = 480 \mu\text{m}$  and *c)*  $D = 520 \mu\text{m}$ . The red color at the entrance of the nozzle can represent densities larger than  $1 \times 10^{21} \text{cm}^{-3}$ .

$D = 460 \mu\text{m}$	$D = 480 \mu\text{m}$	$D = 520 \mu\text{m}$
$z_{shock} \approx 770 \mu\text{m}$	$z_{shock} \approx 840 \mu\text{m}$	$z_{shock} \approx 920 \mu\text{m}$
<b>Figure 3.20a</b>	<b>Figure 3.20b</b>	<b>Figure 3.20c</b>

**Table 3.7** Optimum interaction distances,  $z_{shock}$ , achieved for  $d = 100 \mu\text{m}$ ,  $E = 150 \mu\text{m}$  and different  $D$  values.

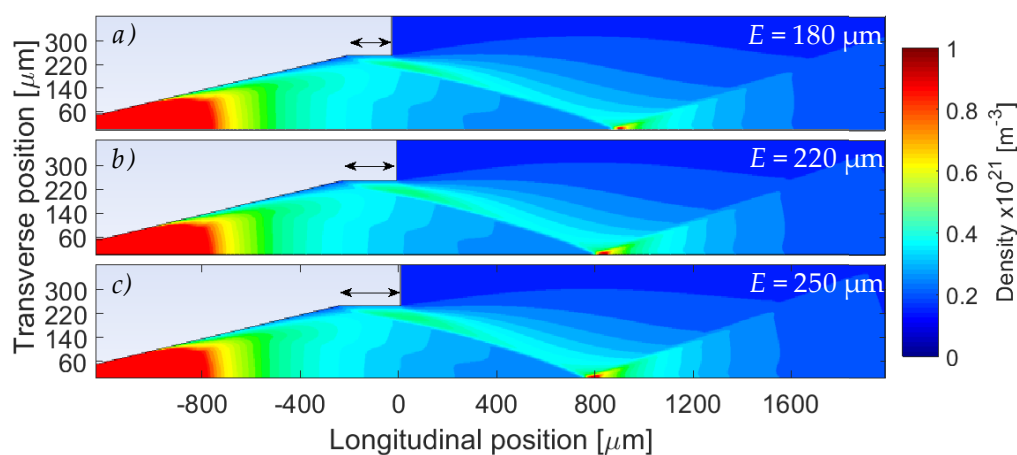
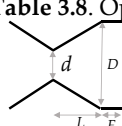


**Figure 3.21** Molecular density maps at 1000 bar for different edge size  $E$ . The longitudinal position is normalized to  $z = 0$  at the exit of the nozzles. *a)*  $E = 180 \mu\text{m}$ , *b)*  $E = 220 \mu\text{m}$  and *c)*  $E = 250 \mu\text{m}$ . The red color at the entrance of the nozzle can represent densities larger than  $1 \times 10^{21} \text{cm}^{-3}$ .

$E = 180 \mu\text{m}$	$E = 220 \mu\text{m}$	$E = 250 \mu\text{m}$
$z_{shock} \approx 920 \mu\text{m}$	$z_{shock} \approx 845 \mu\text{m}$	$z_{shock} \approx 800 \mu\text{m}$
<b>Figure 3.20a</b>	<b>Figure 3.20b</b>	<b>Figure 3.20c</b>

**Table 3.8.** Optimum interaction distances,  $z_{shock}$ , achieved for  $d = 100 \mu\text{m}$ ,  $D = 500 \mu\text{m}$  and different  $E$  values.



If only the nozzle length,  $L$ , varies, fixing  $D = 350 \mu\text{m}$  and  $d = 100 \mu\text{m}$ , the distance at which the shock is formed and its density do not drastically change (see **Figure 3.22**).

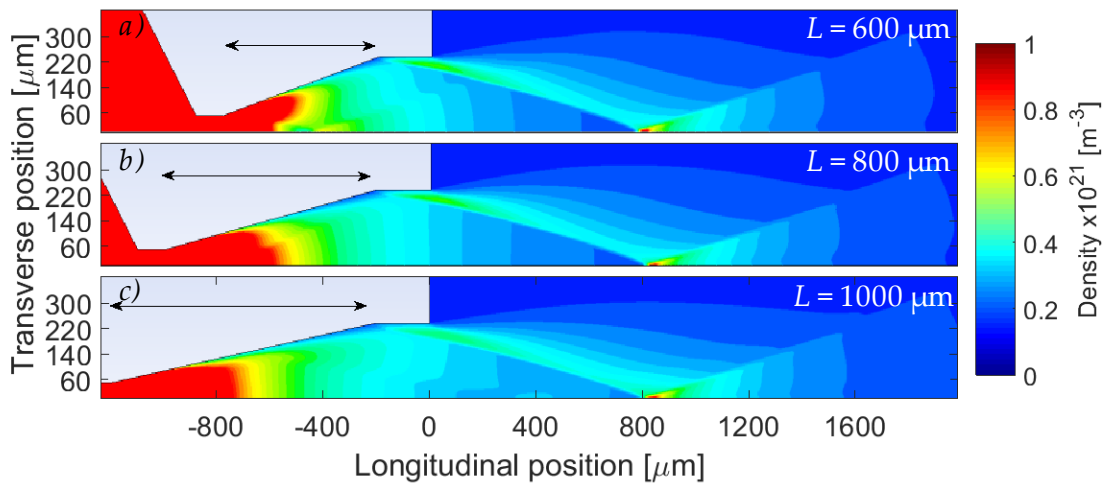


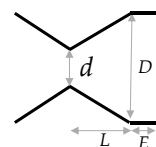
**Figure 3.22** Molecular density maps at 1000 bar for different nozzle lengths  $L$  with  $D$  and  $d$  constant. The longitudinal position is normalized to  $z = 0$  at the exit of the nozzles. *a)*  $L = 600 \mu\text{m}$  nozzle length, *b)*  $L = 800 \mu\text{m}$  nozzle length and *c)*  $L = 1000 \mu\text{m}$  nozzle length. The red color at the entrance of the nozzle can represent densities larger than  $1 \times 10^{21} \text{cm}^{-3}$ .

### Asymmetrical nozzles (AN)

*Asymmetrical nozzles* require 3D simulations. Some have been performed, but their computational *cost* did not allow a detailed study. The interest of *asymmetrical nozzles* is to provide with a single nozzle two different transversal target profiles for laser interaction. These are shown in **Section 3.2.6**.

### Remark concerning the gas reservoir design

The nozzle geometrical parameters are essential for finding the optimum density profile. However, one cannot forget about the design of the gas reservoir. As explained in **Paper I**, an occasional formation of a supersonic flow section inside the transport system can generate instabilities in the flow that lead to turbulences and flow-blocking zones. **Figure 3.23** compares the effect of a conical transition (**a**) and a sharp transition (**b**). A sharp transition leads to a perturbed flow propagation in the subsequent sections of the nozzle. The flow is blocked and mass conservation cannot be reached due to the instabilities of the fluid flow. The general rule is to avoid relatively big gas reservoir areas before the nozzle throat, to use



conical profiles between sections of different diameters, to avoid sharp discontinuities or surface irregularities and to propagate the flow from big diameters to lower diameters.

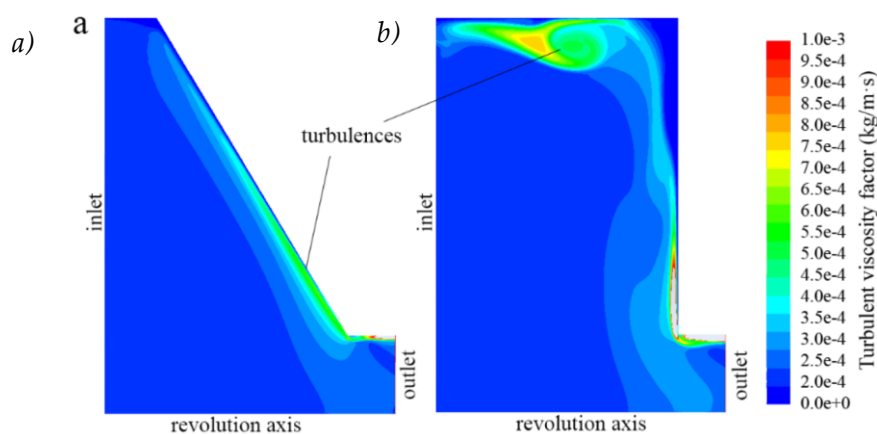


**Figure 3.23** Effect of the sharp discontinuity in the converging region on the turbulent viscosity factor. The figures represent half of the axisymmetric nozzle view where the lower line is the revolution axis. The inlet is in the left and the outlet is in the right of each figure: a) a 59° convergent cone and b) a 90° transition.

### 3.2.3. Transversal and longitudinal density profiles

The gas-jet transversal density profile is fundamental to optimize the laser-driven ion acceleration. **Figure 3.24a** shows *conical nozzles* density profiles with molecular densities up to  $\sim 1 \times 10^{21} \text{ cm}^{-3}$  (it is assumed that all hydrogen atoms are ionized by the laser pulse, therefore the free electron density is twice the molecular density) at  $z \geq 200 \text{ }\mu\text{m}$ . The FWHM at a distance of the nozzle exit from  $z = 300$  to  $400 \text{ }\mu\text{m}$  is less than  $150 \text{ }\mu\text{m}$ .

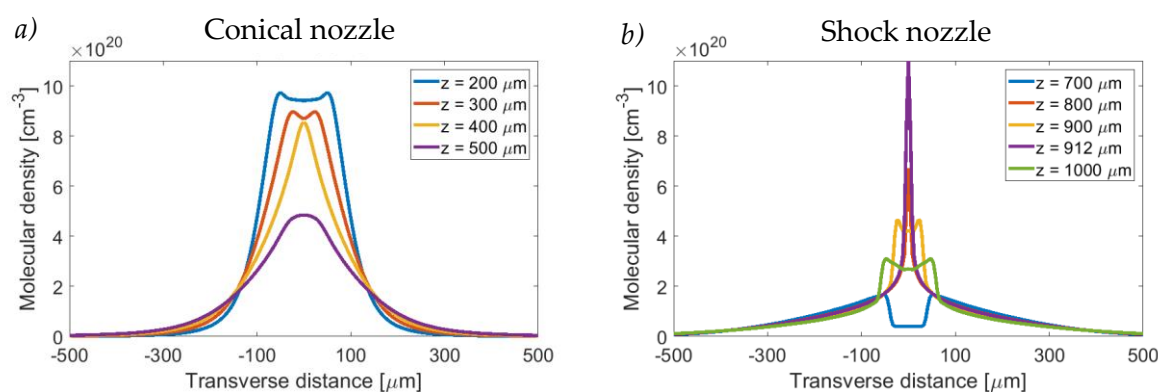


**Figure 3.24** Transversal density profiles at 1000 bar for different distances from the nozzle exit *a)* conical nozzles *b)* shock nozzles. A comparison of both can be found in **Figure 3.25b** in logarithmic scale.

For further distances, the densities drop down to  $4 \times 10^{20} \text{ cm}^{-3}$  and the FWHM increase. For smaller distances, the densities are higher, but the profiles become flat-tops. Flap-top

profiles can be inhomogeneous depending on how the Mach waves converge and can present dips or wavy structures. In the region of space where Mach waves converge, Gaussian-like profiles with a minimum FWHM are found [Schmid 2012]. In this case, the optimal distance is  $z = 400 \mu\text{m}$ .

**Figure 3.24b** shows the density profile for *shock nozzles*. It is important to notice how the transverse density profiles change drastically with  $z$ . The optimum distance from the exit of the nozzle is  $z = 912 \mu\text{m}$  with a molecular density of  $1.1 \times 10^{21} \text{cm}^{-3}$ . However, only  $12 \mu\text{m}$  below the density drops to  $4.5 \times 10^{20} \text{cm}^{-3}$  and the profile shape is lost. In this particular case, the density profile is formed by the combination of a Gaussian background due to the flow propagation and a sharp peak that stands over it due to the shock formation. The Gaussian background forms two *wings* in both sides of the sharp peak. From the center of the transversal density profile, the *wings* start before  $100 \mu\text{m}$  with a molecular density of around  $2 \times 10^{20} \text{cm}^{-3}$  and continues even further than  $500 \mu\text{m}$  with a molecular density of  $10^{19} \text{cm}^{-3}$ . This is why we avoid the use of FWHM to characterize the density profiles of this type of nozzles.

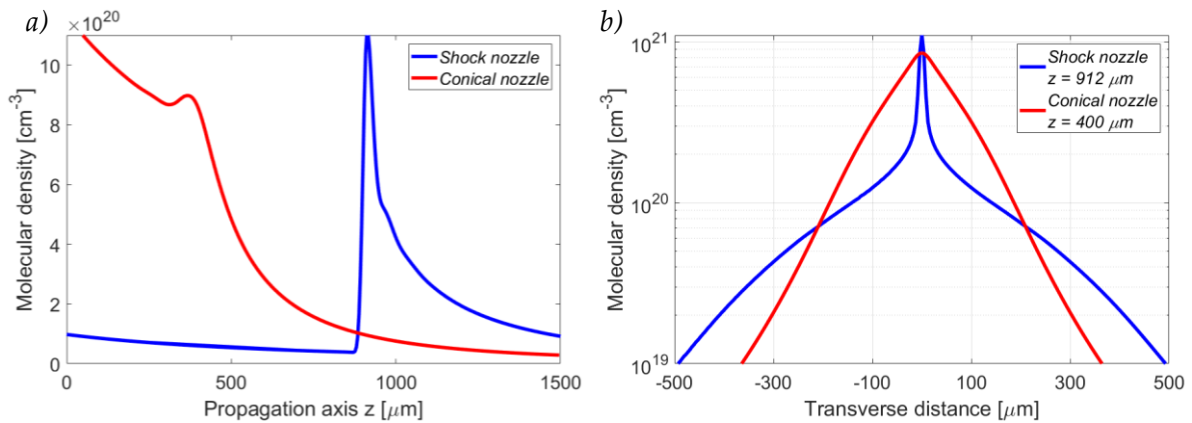


**Figure 3.25** a) Comparison of the downstream propagation of the flow from the nozzle exit for *shock nozzles* and *conical nozzles*. b) Comparison of both transversal density profiles in logarithmic scale at the optimal  $z$  where maximal density is reached.

In **Figure 3.25a**, the comparison between both nozzle longitudinal density profiles is presented. The *shock nozzle* shock converges further than the *conical nozzle* ones. For *shock nozzles*, the achievement of the same density but at a further distance from the exit nozzle is its main advantage. Before the converging point, the longitudinal density profile is different, i.e., while *conical nozzle* density decreases with  $z$ , *shock nozzle* density slowly decreases until

there is an abrupt change and the density increases in several  $\mu\text{m}$  (at the *shock nozzle* focal point). That is why the transversal profile presented in **Figure 3.24b** changes dramatically with  $z$ . After the shock, the density decreases faster than in the *conical nozzle* case.

The comparison of the transverse density profiles is shown in **Figure 3.25b**. The shapes of these density profiles are different, i.e., even if the reached maximum density is similar, one must notice that the *wings* of *shock nozzles* are higher.

In the experiment, a laser pulse will first interact with the *wings*. If the density of the *wings* is too high, the laser pulse may not be able to penetrate and interact with the high-density peak as it will lose all its energy during this first interaction. From **Figure 3.25b** one can observe that the interaction with the laser starts at least  $100\ \mu\text{m}$  before in the case of *shock nozzles* compared with *conical nozzles*.

### 3.2.4. Remark concerning gas jets in air

During the experiment, the gas jets are always under vacuum (e.g.  $p_B = 10^{-3}\text{-}10^{-7}$  mbar) and their flow propagation is *under-expanded* (**Section 3.2.1**). However, if there is an increment of pressure in the chamber, the supersonic jet becomes *over-expanded*. The behavior of an *over-expanded* jet is experimentally observed in **Figure 3.26** with the designed *conical nozzles*. After the first *oblique* shock, the pressure increases and there is a typical behavior of *diamond jet* flows [**Section 3.2.1**].

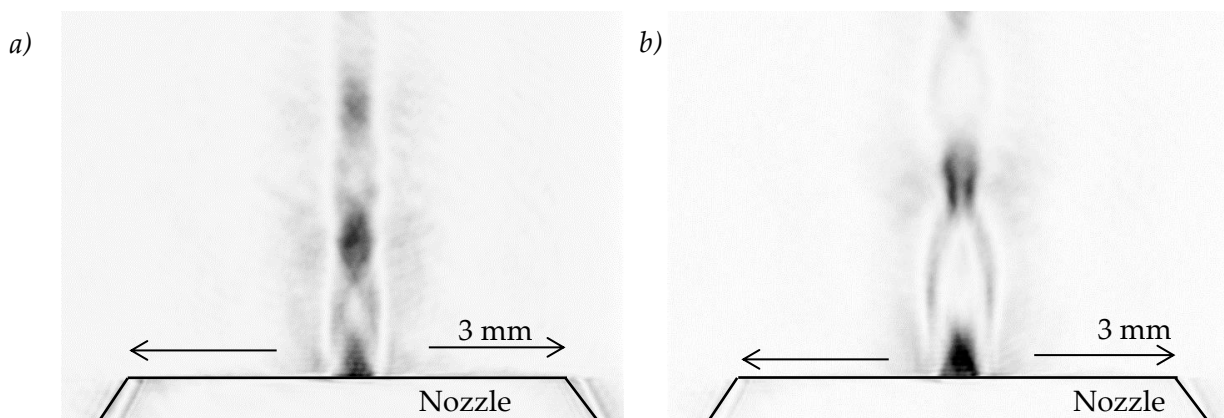


**Figure 3.26** Mach waves generated by the designed *conical nozzle* fed with a) 10 bar and b) 20 bar of nitrogen propagating through 1 bar air. Mach waves are formed at different distances and propagate until they collapse.

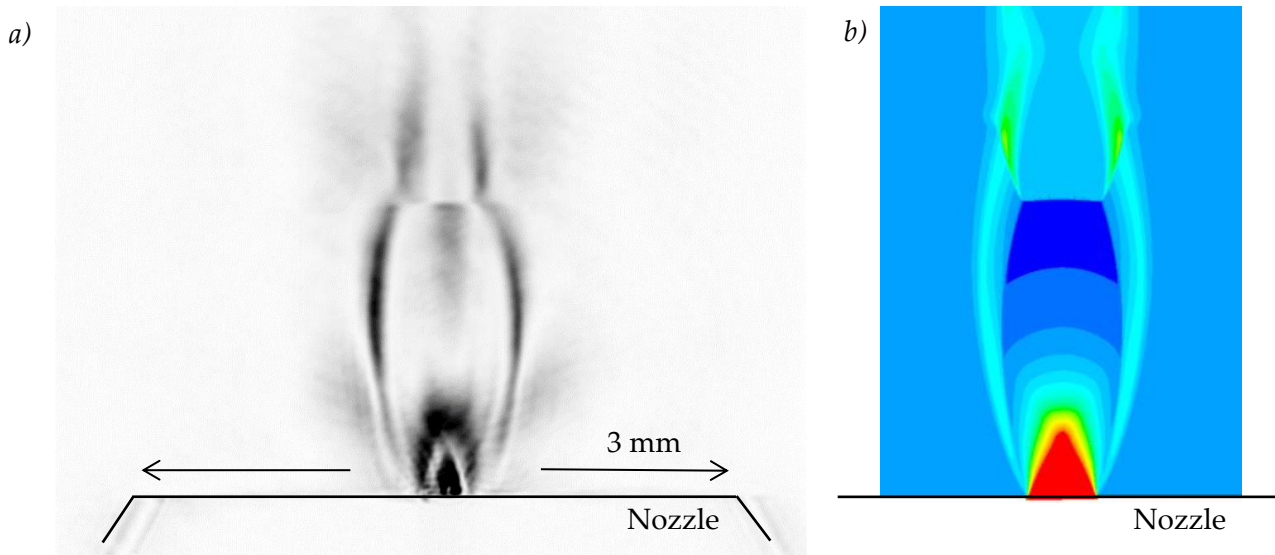


**Figure 3.27** Propagation in air at 1 bar pressure for Mach waves generated by the designed *conical nozzle* fed with 50 bar  $N_2$  a) measurement and b) simulation. Shock fronts are observed in both cases at the same distance of the nozzle exit.

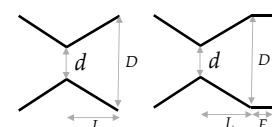
Shock fronts are reproduced by simulations with an inlet pressure of 50 bar of nitrogen (see **Figure 3.27**). The nozzle parameters are the same as the one used in the experiment and the outside pressure is around 1 bar, the atmospheric pressure. The shock front is measured at  $z = 1500-1700 \mu\text{m}$  (the error is due to the uncertainty of the nozzle exit position) and the simulation gives a shock front at  $1620 \mu\text{m}$ . A good agreement between the experiment and the simulation is observed.

### 3.2.5. Conclusion

In this section we recall the main conclusions of the parametrical study of the nozzle geometries for *conical nozzles* and *shock nozzles* in **Table 3.9**.

Among all parameters, FWHM one is not easy to define for *shock nozzle* (which transversal profile is not a Gaussian distribution). If one characterizes the *shock nozzles* with the FWHM of the sharp profile edge, the wings contribution is neglected, and this is a problem since it plays a major role in the laser-matter interaction. Thus, for *shock nozzles*, we prefer to talk about the spot size defined by the entire density profile.

The increase of  $d$  implies an increase of the maximum density and of the FWHM/spot size. The focal distance decreases. A balance between the maximum density, small FWHM/spot size, and far focal distance must be found.



	Conical nozzle	Shock nozzle
$d \uparrow$		$\uparrow \rho_{\max}$ $\uparrow$ FWHM / spot size $\downarrow z$
$D \uparrow$	$\uparrow$ FWHM	$\downarrow \rho_{\max}$ $\downarrow$ spot size $\uparrow z$
$L \uparrow$		$\approx z$ $\approx \rho_{\max}$
$E \uparrow$	-	$\uparrow \rho_{\max}$ $\uparrow$ spot size $\downarrow z$

**Table 3.9** Summary of the behavior of *conical* and *shock* nozzles with the different nozzle parameters. Note that  $d$  is the throat diameter,  $D$  the nozzle exit diameter,  $L$  the cone length and for *shock nozzles*,  $E$  is the length of the edge.  $\rho_{\max}$  is the maximum molecular density at the distance  $z$  from the exit of the nozzle.

An increase of  $D$  means a decrease in the maximum density. For *conical nozzles*, the FWHM increases while for *shock nozzles* the spot size decreases and the focal point is further from the nozzle exit.

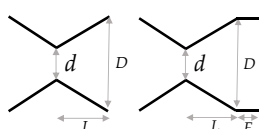
A slide modification of  $L$ , if  $L \approx 1$  mm, does not play an important role.

Last, only for *shock nozzles*, an increase of  $E$  implies higher density, bigger focal spot size and a closer shock formation from the exit of the nozzle.

We calculate the dependence on the focal distance of each parameter. We conclude that, for *conical nozzles*, both parameters ( $d$  and  $D$ ) have the same importance for the optimum focal distance. For *shock nozzles*, the most critical parameters are  $E$  and  $D$ . These results are summarized in **Table 3.10**.

Conical nozzles	Shock nozzles
-	$E [\mu\text{m}] = -0.58 z [\mu\text{m}] + 711$
$D [\mu\text{m}] = 0.34 z [\mu\text{m}] + 121$	$D [\mu\text{m}] = 0.4 z [\mu\text{m}] + 147$
$d [\mu\text{m}] = -0.39z [\mu\text{m}] + 332$	$d [\mu\text{m}] = -0.19 z [\mu\text{m}] + 260$

Table 3.10 Dependence on the focal distance of each parameter.



### 3.2.6. Experimental characterization of the gas jet

In order to validate the CFD simulations, the real density profile delivered by the gas-jet *conical nozzles* is measured with a Mach-Zehnder interferometer using different gases. The gas-jet flux dynamics are studied as well.

#### Mach-Zehnder interferometer

In **Figure 3.28a**, the scheme of the interferometer is presented. An overview can be seen in **Figure 3.29**. The light radiation source of 20 mW Melles-Griot HeNe (632.8 nm) is employed and a Kepler beam expander is installed to increase the beam diameter in order to cover all gas-jet volume. With this configuration, it is possible to add a pinhole in its focus, which spatially filters the laser beam, to remove noise from modes other than the Gaussian one and to obtain a homogeneous beam. The system is formed by an  $f_1 = 40$  mm lens (N-BK7, biconvex, 350-700 nm antireflection coated) and  $f_2 = 200$  mm lens (N-BK7, plano-convex, 633 nm coated) separated 240 mm, which gives a magnification of x5. The beam diameter is 0.96 mm at the entrance of the beam expander and at the exit is 4.8 mm. The spot size at FWHM where the pinhole is placed is around 70  $\mu\text{m}$ , and the pinhole is 75  $\mu\text{m}$  of diameter.

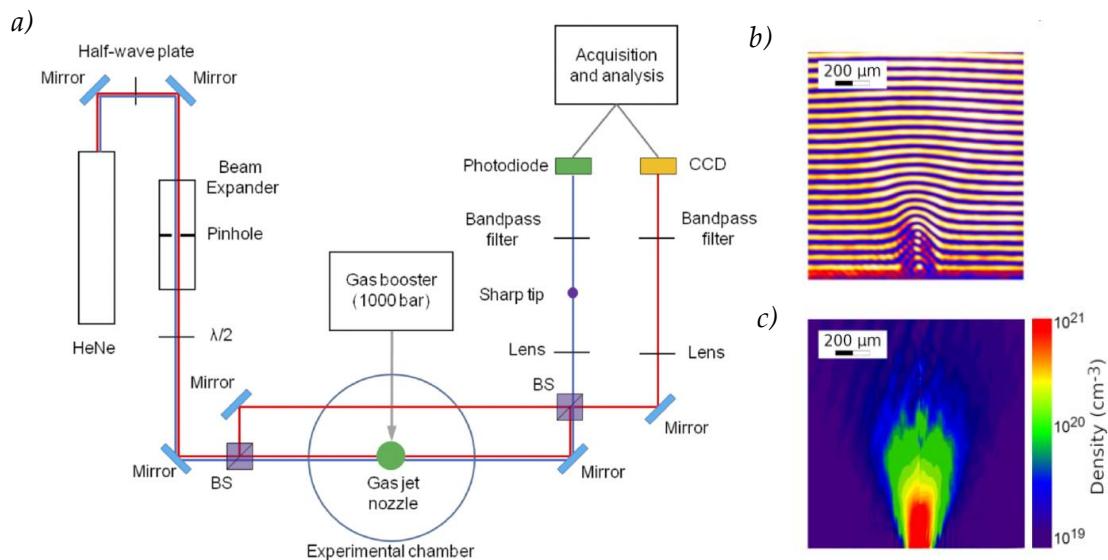


**Figure 3.28** *a)* Scheme of the Mach-Zehnder interferometer (red line). Strioscopy (blue line) is set up by blocking the reference ray in the interferometer and by including a sharp object in the focus of the imaging lens. The signal is detected by a photodiode. *b)* Interferogram obtained with  $\text{N}_2$  at 1000 bar reservoir pressure and *c)* density reconstruction considering an axisymmetric nozzle.

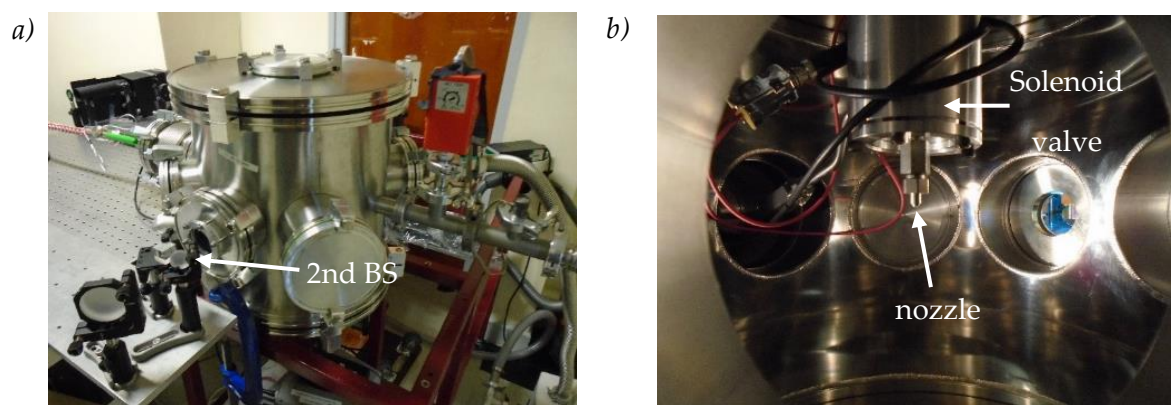


**Figure 3.29** a) General view of the interferometer chamber, b) view from the inside of the chamber.

The laser beam is divided by a *beam splitter cube* (BS) into reference and probe rays, with the probe ray passing through the gas jet. The two laser beams are recombined by another BS to obtain a phase shift image. BS are made to split and recombine the laser light between 420 and 680 nm. A halfwave plate is also installed to control the relative intensity of polarized light that goes to each arm of the interferometer. The gas-jet nozzle is mounted on a Clark-Cooper solenoid valve EX30 that can provide continuous or pulsed gas flux. The high density is reached by using 1000 bar inlet pressure delivered by a Haskel gas booster model AGT-62/152. A lens images the phase shift interferogram onto a linear CCD camera PixelFly whose magnification allows to get approximately 3 microns/pixel. An  $f_3 = 500$  mm lens (N-BK7, plano-convex, 633 nm coated) is used. The object is at 735 mm from the lens, giving an image with an enlargement of  $\times 2.12$  at around 1563 mm. The image has a size of  $\sim 10$  mm. The background noise of the interferometric image is reduced by subtracting the reconstructed image without gas (unperturbed condition). A good shot-to-shot stability and reproducibility is observed.

The phase shift induced by the gas flow is obtained by the fringe displacement from the unperturbed position in vacuum (**Figure 3.28b**). A phase shift measurement allows the reconstruction of the gas-jet density profile by means of the variation of the refractive index  $n$ . Assuming a cylindrical symmetry of the gas jet (which is the case with axisymmetric nozzles) the reconstruction of the density profile along one direction is possible from a single-phase shift image (**Figure 3.28c**). The radial distribution of the refraction index is deduced using Abel inversion. A description of the mathematical extraction of the phase shift variation and the Abel inversion can be found in [Malka 2000]. The phase shift

calculation and the reconstruction of the density profile from the refractive index variation are performed by the analysis program [Neutrino]. The gas molecule number density  $\rho$  is calculated from the general form of the Lorentz-Lorentz equation [Born 1999],

$$\rho = \frac{3}{4\pi\alpha} \frac{n^2 - 1}{n^2 + 2} \quad (3.1)$$

where  $\alpha$ , the mean polarizability of the gas molecule, is defined as

$$\alpha = \frac{3A}{4\pi N_A} \quad (3.2)$$

where  $A$  is the molar refractivity and  $N_A$  is Avogadro's number. Last two equations can be combined to obtain

$$\rho = \frac{N_A}{A} \frac{(n^2 - 1)}{n^2 + 2} \quad (3.3)$$

The molar refractivities for hydrogen and nitrogen are calculated using the last equation and refractive indices of gases from [Peck 1977] (see **Table 3.11**). It is known that they remain constant even at high pressures when  $n$  differs from unity [Born 1999].

Hydrogen [m <sup>3</sup> /mol]	$2.094 \times 10^{-6}$
Nitrogen [m <sup>3</sup> /mol]	$4.506 \times 10^{-6}$

**Table 3.11** Calculated values of molar refractivity of hydrogen and nitrogen using refractive index values from [Peck 1977].

Experimental measurement of nitrogen molar refractivity is described in [Stone 2004] giving a value of  $4.445 \times 10^6$  m<sup>3</sup>/mol. With this value and the one calculated for hydrogen (no experimental value was found), the density profiles are reconstructed in **Figure 3.30**.

Due to the opacity of the gas jet at high densities, reconstruction of the density is only possible in a moderate-density region ( $10^{19}$  -  $10^{20}$  cm<sup>-3</sup>). For this reason, the measurements are performed away from the exit of the nozzle ( $z > 500$   $\mu$ m). The density profiles obtained by interferometry (blue solid line) are compared to the ones obtained by CFD simulations

(red dashed line) with diatomic hydrogen at 50 bar and 100 bar, and diatomic nitrogen at 100 and 1000 bar.

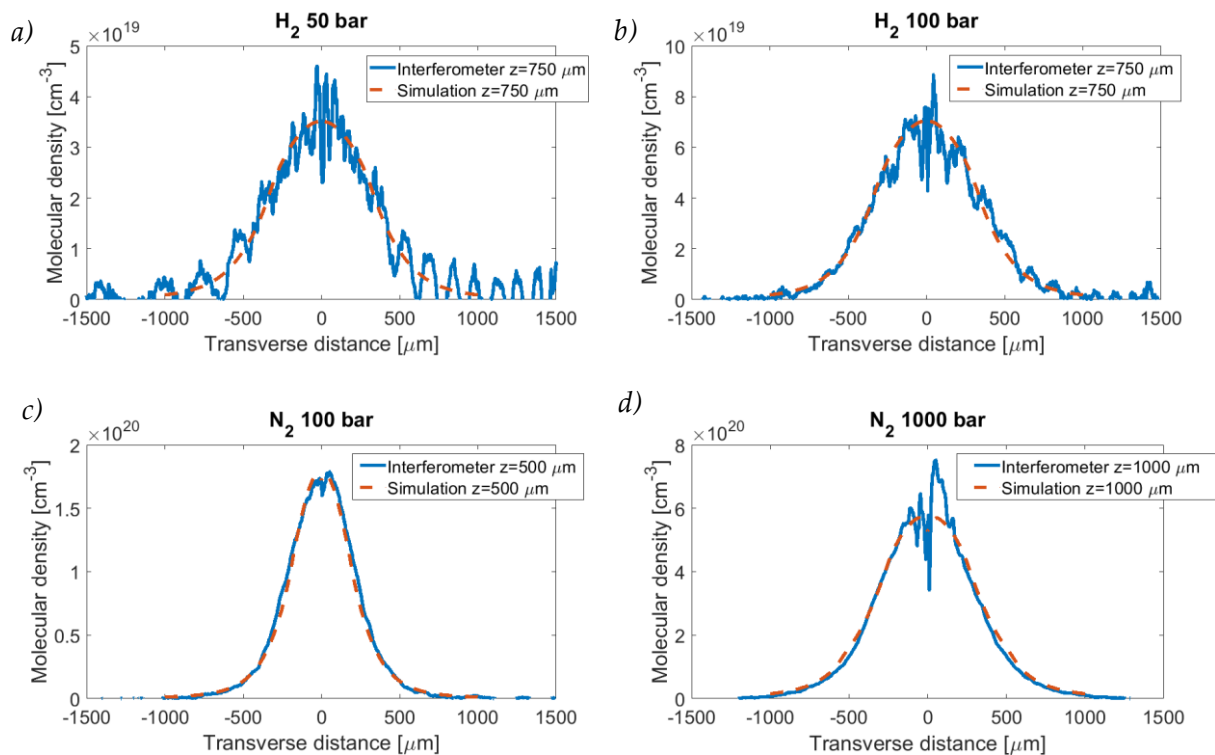


**Figure 3.30** Comparison of simulation results with interferometry reconstructions for *a)* 50 bar diatomic hydrogen at  $z = 750 \mu\text{m}$  *b)* 100 bar diatomic hydrogen at  $z = 750 \mu\text{m}$  *c)* 100 bar diatomic nitrogen at  $z = 500 \mu\text{m}$  *d)* 1000 bar diatomic nitrogen at  $z = 1000 \mu\text{m}$ .

The fluctuations in the central region of the profiles are artifacts due to the inherent noise of the Abel inversion close to the axis of symmetry and the imprecision of the symmetry axis position. The overall good agreement validates our simulations and gives us confidence in their results at 1000 bar with diatomic hydrogen.

The hydrogen interferogram is more difficult to obtain due to its small refractive index (1.0001493) compared to the one of nitrogen (1.0002984) [Peck 1977]. That is why the fluctuations obtained with hydrogen are bigger (See **Figure 3.30**).

### 3D tomography

3D characterization by tomography is needed for nozzles without cylindrical symmetries (e.g. *asymmetrical nozzles*). Abel inversion is no longer possible in those cases and this complicates the characterization process. To measure the density profile of a non-cylindrical nozzle, several images of the phase shift displacement have to be taken at different angles

(see **Figure 3.31**). This study was made with nitrogen at 100 bar. This step can be developed with *neutrino*. In our case, a rotation plate is placed around the nozzle to allow the acquisition of phase shift images at controlled angles.

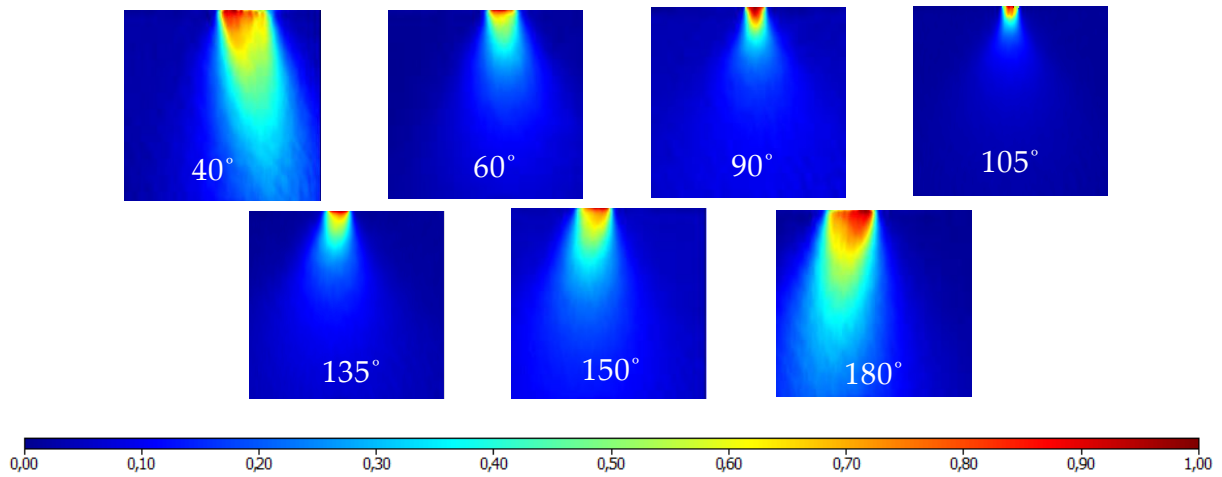


**Figure 3.31** Images of the phase shift taken at different rotation angles with *asymmetrical nozzles*. These pictures are produced with [*Neutrino*] and the phase shift is normalized to one.

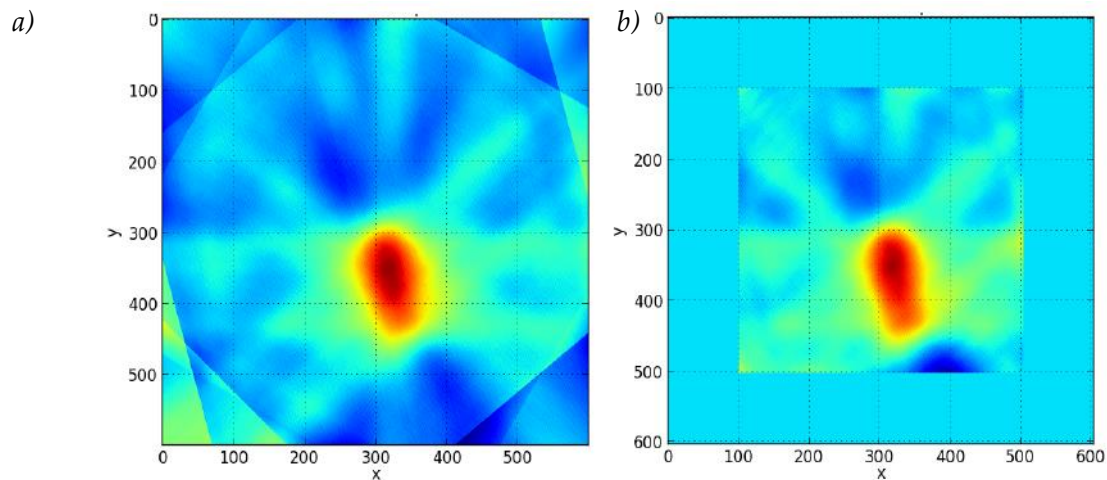


**Figure 3.32** Reconstruction of the phase shift at 200  $\mu\text{m}$  of the *asymmetrical nozzles* exit with TomoRaw program. *a)* Using one iteration series between each pair of images *b)* Using two interaction series and a mask to avoid the erroneous interferences of the reconstruction from the overlapping borders. Both images are normalized to 1.

Each phase-shift matrix from each angle is normalized and used as input into a tomographic reconstruction code (TomoRaw) developed at LULI. It extracts the matrices between each measure by different iteration series. To precisely measure the density profile at all angles, a high quantity of images is needed. In our case, as a motorized rotation plate was not available, images for only 7 angles are taken. **Figure 3.32** shows the reconstruction of

the phase shift with one iteration series between two angles (**Figure 3.32a**) or using two iterations and a square mask (**Figure 3.32b**).

The superposition of different images at different angles may affect the signal at the borders where not all images contribute to the signal. A square or circular mask is recommended to avoid interferences from the unclear borders.

In **Figure 3.33**, the density reconstruction of **Figure 3.32b** is shown. The angle of the figure is corrected in order to observe the nozzle in a *straight* position.

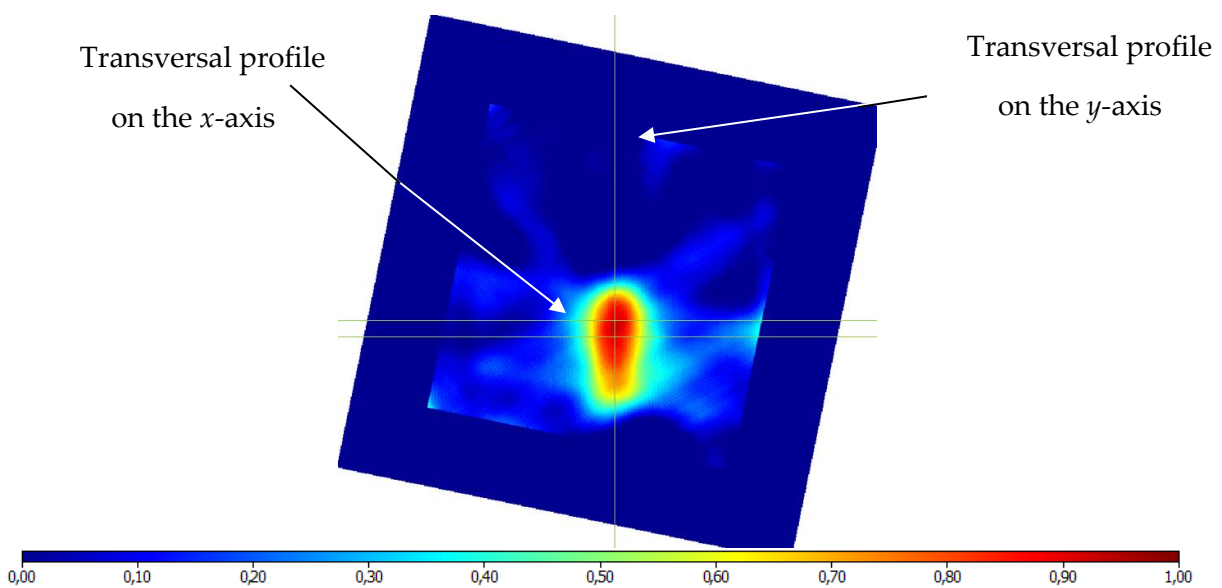


**Figure 3.33** Density reconstruction of **Figure 3.32b**. The image is normalized. The color bar is proportional to the density by a factor of  $10^{21} \text{ cm}^{-3}$ . The lines are at  $x = 360 \text{ } \mu\text{m}$  and  $y = 400$  and  $420 \text{ } \mu\text{m}$ .

The transversal density profiles following each line of **Figure 3.33** are plotted in **Figure 3.34** and compared with the simulated ones. The horizontal line on the figure indicates the position of the transversal profile on the  $x$ -axis, and the vertical line, the one on the  $y$ -axis.

The transversal density profile on  $x$ -axis for *asymmetrical nozzles* is different from the transversal density profile on  $y$ -axis and their FWHM are proportional to the nozzle exit  $x$  and  $y$  dimensions respectively. The density profile on the  $x$ -axis (**Figure 3.34a** black line) looks like a *conical nozzle* one. A Gaussian curve can be fitted with a measured maximum density of  $9 \times 10^{19} \text{ cm}^{-3}$  and FWHM of  $261 \text{ } \mu\text{m}$ . The measured  $x$  profile (**Figure 3.34a** black line) is wider: the same maximum density is reached but with an FWHM of  $482 \text{ } \mu\text{m}$ . A high

background is found on the  $x$ -axis line, which may explain why the measure and the simulated FWHM differ.

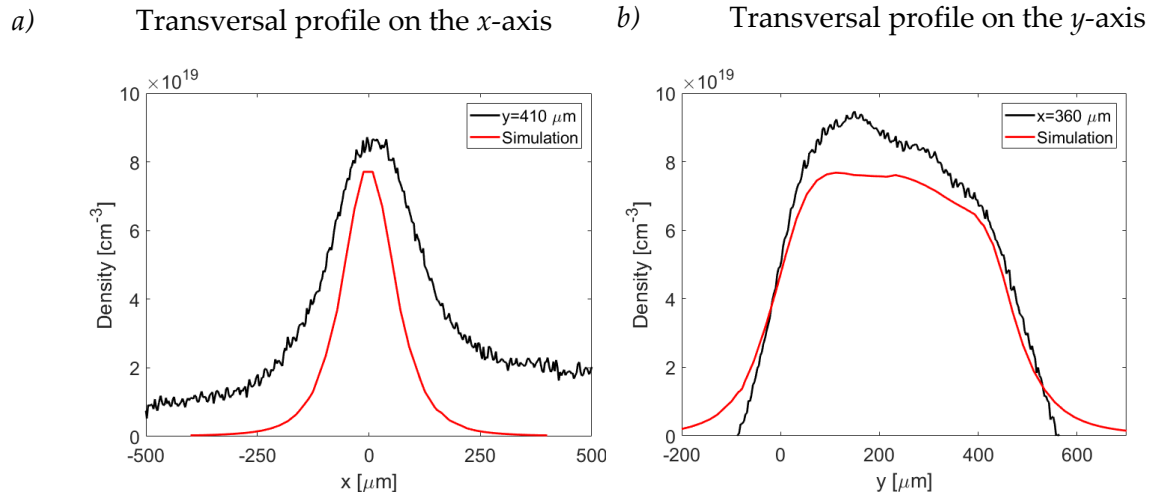


**Figure 3.34** Density profile measured by TomoRaw (black) and compared with FLUENT simulations (red) for a) the transversal profile on the  $x$ -axis b) the transversal profile on the  $y$ -axis.

The simulated  $y$  profile matches with the measured one (**Figure 3.34b**). However, we observe that the density at  $\pm 250 \mu\text{m}$  is bigger in the case of the experimental results.

### Dynamics of the gas jet

During the experiment, a solenoid valve is used to produce pulsed gas jets. Perfect characterization of the dynamics of the gas flux is mandatory to synchronize it with the incoming laser pulse. The goal is to trigger the laser interaction when the maximum density of the gas jet is reached. The evolution of the gas flow is measured by strioscopy (based on the Schlieren effect). Strioscopy is an optical Fourier process in which the light diffused from an object is filtered by an obstacle and the diffracted light is measured (**Figure 3.28a**). The refractive index gradient of the object deflects the light in different optical path lengths and the turbulences generated by the density gradient can be detected with a photodetector [Hirschberg 2002]. This method allows finding the precise moment of flow stabilization for different gases, pressures, and opening time durations of the solenoid valve.

In **Figure 3.35a, c and e**, one can see the gas flow evolution for different opening time durations. The rising time of the gas jet corresponds to the time needed to completely fill the nozzle reservoir volume (about  $230 \text{ mm}^3$ ), and it is also affected by the size of the throat ( $100 \text{ mm}$ ). The time needed to reach the maximum density may be reduced using smaller

reservoirs. The dimension of the reservoir and throat also affect the time needed to completely evacuate the gas once the solenoid valve is closed. In the following work, mechanical constraints related to the solenoid valve did not allow to reduce the reservoir size.

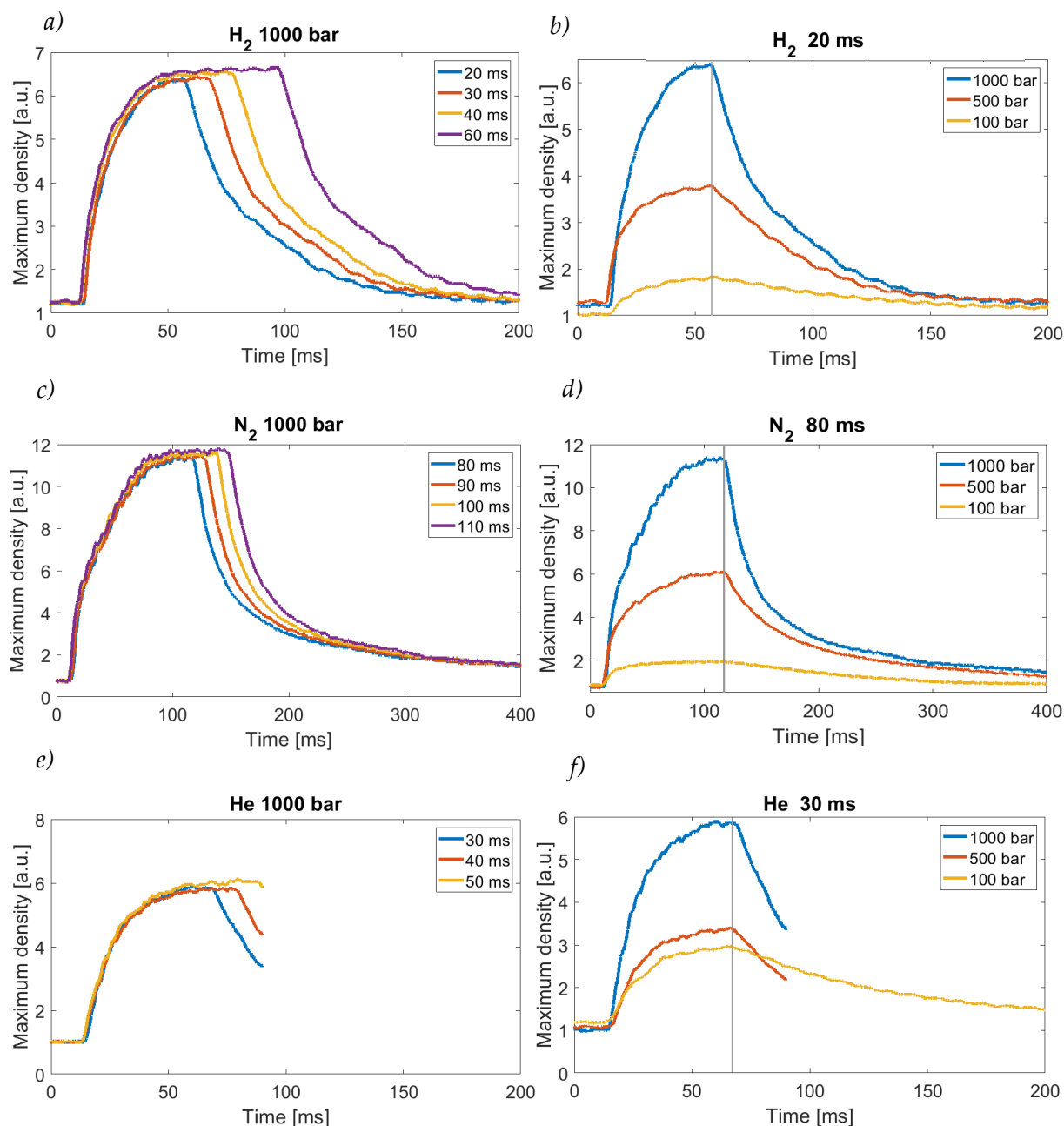


**Figure 3.35** Gas flow evolution of a) b) diatomic hydrogen c) d) diatomic nitrogen e) f) helium as a function of time for a) c) e) different solenoid valve opening durations b) d) f) different pressures. When the solenoid valve is triggered (at  $t = 0$  ms) is about 12 ms before the gas flow.

**Figure 3.35a** shows the diatomic hydrogen flow dynamics for different valve opening durations. For the experiment, it is important to achieve the maximum density with the

minimum quantity of gas in the vacuum chamber. The maximum of the density for diatomic hydrogen gas jet is reached after a  $time = 70$  ms with a larger valve opening duration of  $t_{open} = 40$  ms. To minimize the gas quantity in the vacuum chamber, this time should be carefully chosen. In the case of diatomic nitrogen, the gas flow takes  $time = 110$  ms to reach the maximum density with a larger valve opening duration  $t_{open} = 80$  ms (**Figure 3.35b**). The dynamics of nitrogen is slower than the one of hydrogen, and more gas flows inside the vacuum chamber. This is due to the different gas molecular weights. For helium gas, the strioscopy and interferometry are more complicated to perform because of its smaller refraction index (1.000036 vs 1.000149 for hydrogen gas [Peck 1977]). The stabilization takes place at  $time = 70$  ms for an opening duration of  $t_{open} = 40$  ms.

For the three gases, a comparison of the flux dynamics with the inlet pressure is made (**Figure 3.35b, d, and f**). As observed with the FLUENT simulations, the gas-jet density evolution as a function of the inlet pressure displays a linear progression (**Figure 3.15**). However, one observes that the stabilization time does not depend on the reservoir pressure. **Figure 3.35b** shows the flux evolution for hydrogen gas for an opening duration of  $t_{open} = 20$  ms. Even if this is not the optimum opening duration, the maximum density is achieved at the same time,  $time = 57$  ms at all reservoir pressures. The linear progression can be obtained again with the maximum densities ( $maximum\ density\ [a.u.] = 0.0051\ reservoir\ pressure\ [bar] + 1.32$ ).

**Figure 3.35d** shows the nitrogen flux dynamics for an opening duration of  $t_{open} = 80$  ns. The maximum density is reached at  $time = 110$  ms for all pressures as well. In this case, the equation is  $maximum\ density\ [a.u.] = 0.0104\ reservoir\ pressure\ [bar] + 0.89$ . It is still linear but the slope has a different value. The constant factor is not relevant, as the measurements are not done with the same exact conditions from one gas to the other.

**Figure 3.35f** presents the case of helium for an opening duration,  $t_{open} = 30$  ms. The time at which the maximum density is reached is 68 ms. As mentioned above, strioscopy measurements are more difficult to perform with helium, so the flux dynamics cannot be compared in height between the different pressures since the experimental conditions had to be modified during the measurements.

### 3.3. Particle and X-ray diagnostics

The laser interaction with a target generates different radiations and accelerates electrons and ionized particles. There are several ways to detect ionizing particles and these can be divided into two groups: one based on passive detectors and the other one on active detectors. In experimental setups, these detectors can be used alone or as parts of more complex systems, e.g. spectrometers. In this section, the most common detectors and spectrometers are described. With them, it is possible to characterize the energy, number, and the divergence of the accelerated ion/electron beams, or X-ray spectra.

#### 3.3.1. Passive detectors

Three types of passive detectors are mostly used: *Columbian resin #39* (CR-39) films, *radiochromic films* (RCF), and *imaging plates* (IP). They are 2D detectors without magnetic or electric fields. They are not sensitive to electromagnetic noises, unlike electronic devices. They are mostly used in stacks to analyze the ion beam energy distribution and its divergence. In this thesis, RCF and IP were used as passive detectors.

##### 3.3.1.1. Radiochromic films (RCF)

These films consist of a single or double radiation-sensitive layer on a thin polyester base with a transparent coating. The RCF are sensitive to ionizing particles under which their active layer (dye) turns from white to blue. The resulting optical density is directly related to the absorbed dose. The advantage of this simple detector is that no complex processing is required since they are easily readout with standard scanners. However, for quantitative analysis, it is important to allow the chemical reaction in the sensitive layer to take place during some hours after their irradiation and scan them afterwards with the scanner used for their calibration and using the same *digitalization* parameters (resolution, wavelengths and so on). The resulting digitized maps of optical density are translated into energy deposits in the films using dose to *optical density* (OD) response functions.  $O.D. = -\log(I_t/I_{ref})$  where  $I_t$  is the intensity transmitted by the irradiated RCF and  $I_{ref}$  the reference intensity transmitted by a virgin film. The modification of the optical density is proportional to the deposited dose

in the RCF by the ionizing particles or radiation. An example is shown in **Figure 3.36**. The energy deposit in the RCF cannot be measured when the films are saturated.

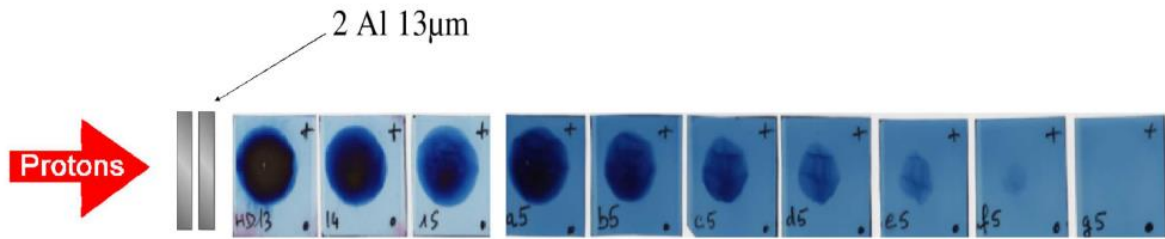


**Figure 3.36** Example of an RCF stack irradiated by a proton beam at LULI laser installation. The proton beam traverses the stack from the left to the right. The proton beam has 2 cm spot size at 3.5 cm from the production source where it is almost punctual. The energy of this shot was 23 J, the pulse duration 300 fs, i.e. an intensity of  $2 \times 10^{19}$  W/cm<sup>2</sup>. [Plaisir 2010]

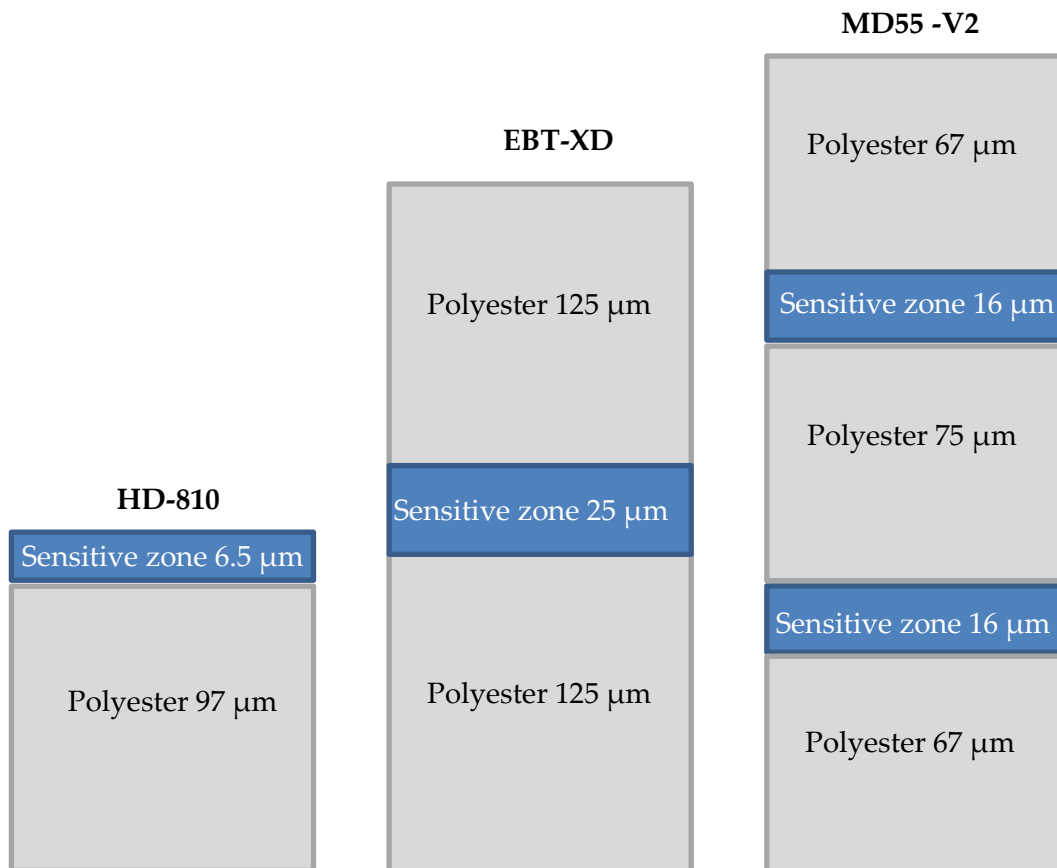


**Figure 3.37** Schematic view of the layers of three different RCF (HD 810, EBT-XD and MD55-V2). In a laser-plasma experiment, protons come from the top to the bottom.

The proton beam generates also nuclear reactions in the RCF films since they are composed of light elements such as carbon, oxygen and nitrogen on which nuclear reactions are induced. Radioactive isotopes are produced, and the activity of the films can be measured

and studied. Hence the proton beam properties (energy distribution and number of particles) can be inferred from the activities measured in the RCF stack [Plaisir 2010].

Several types of films have been manufactured by Gafchromic™ and each type of film has a different composition (HD-810, EBT, MD-55 ...) with different updates (MD-55-V2, EBT1-3, ... , EBT-XD). E.g. HD-810 films have one sensitive zone of 6.5 μm thickness. EBT-XD films contain a 25 μm layer between two polyester layers of 125 μm. MD-55-V2 films consist of two sensitive layers of 16 μm each (see **Figure 3.37**). These last films are more sensitive than the first ones.

### 3.3.1.2. Imaging plates (IP)

IP are detectors sensitive to ionizing radiation and particles, e.g., photons, electrons, and ions. After irradiation, these films must be processed by a scanner. A spatially resolved 2D image is obtained, in which the content of each pixel (or intensity) is related to the number of electron-holes (metastable states) created in the film by the ionizing radiation. They can be reused as white light recombines the formed electron-holes. They are more sensitive than RCF and their good spatial resolution (25 μm) makes them good detectors for spectrometers such as *Thomson parabolas* (TP) (see **Section 3.3.3**).

Fuji Photo Film Co. Ltd provides three different types of IP: BAS-SR, BAS-MS and BAS-TR. They have up to four different layers: protective, sensitive, support, and magnetic layer. The ionizing particles traverse the IP from the protection layer to the magnetic one. Both BAS-SR and BAS-MS films have a 6 and 9 μm protective layer respectively which stops protons with energies lower than 600 keV, while BAS-TR films are protective layer-free. The sensitive one for BAS-MS and BAS-TR is composed of  $\text{BaFBr}_{0.85}\text{I}_{0.15}:\text{Eu}^{2+}$  of 115 and 50 μm respectively and the support one of  $\text{C}_2\text{H}_2\text{O}$  of 190 and 250 μm thicknesses respectively. The magnetic layer is  $\text{ZnMn}_2\text{Fe}_5\text{NO}_{40}\text{H}_{15}\text{C}_{10}$  and have 160 μm thickness. These values are summarized in **Table 3.12**.

The physics process inside an IP has been presented by H. von Seggern [1992]. An ionizing particle traverses the sensitive layer and forms an electron-hole, ionizing the dopant  $\text{Eu}^{2+}$ . The electron is captured by the  $\text{FBr}^-$  or the  $\text{FI}^-$  to form a metastable complex. The information of the ionizing particle is stored as number of electron-holes. The deexcitation can occur

spontaneously, by a process called *fading*. On the other hand, the recombination can be stimulated by photons. This last process is interesting to measure the IP signal. The stimulated recombination generates a *photostimulated luminescence* photon (PSL) (see **Figure 3.38**). It can be by electron transport in the valence band or by tunnel effect if the  $\text{FBr}^-$  or the  $\text{FI}^-$  are close to the  $\text{Eu}^{3+}$ . The deexcitation by *fading* is a loss of information. That is why the IP must be scanned as soon as possible after the irradiation [[Bonnet 2013](#)].

		SR	MS	TR
<b>Protection</b>	<b>Composition</b>	$\text{C}_2\text{H}_2\text{O}$		-
	<b>Thickness [<math>\mu\text{m}</math>]</b>	6	9	
<b>Sensitive</b>	<b>Composition</b>	$\text{BaFBr}:\text{Eu}^{2+}$	$\text{BaFBr}_{0.85}\text{I}_{0.15}:\text{Eu}^{2+}$	
	<b>Thickness [<math>\mu\text{m}</math>]</b>	120	115	50
<b>Support</b>	<b>Composition</b>	$\text{C}_2\text{H}_2\text{O}$		
	<b>Thickness [<math>\mu\text{m}</math>]</b>	188	190	250
<b>Magnet</b>	<b>Composition</b>	$\text{ZnMn}_2\text{Fe}_5\text{NO}_{40}\text{H}_{15}\text{C}_{10}$		
	<b>Thickness [<math>\mu\text{m}</math>]</b>	160		

**Table 3.12** Composition and thickness of the different layers in SR, MS and TR imaging plates.

During the experiment, IP were analyzed using a FUJIFILM FLA-7000 reader after each shot. They were scanned  $\sim 20'$  after the laser-matter interaction. The *fading* can be neglected in these conditions [[Bonnet 2013](#)]. The scanner has a laser wavelength optimized for  $\text{FBr}^-$  or  $\text{FI}^-$  stimulation and a photomultiplier that counts the luminescence photons. Once the measurement is done, it is possible to *delete* the information in the IP by using intense white light. After  $5'$  the films are erased and can be reused. After irradiation with the signal to be measured and before placing the IP in the scanner, they must not be exposed to light, so every manipulation is to be done in darkness. The scanner generates a matrix with numerical

values per pixel which are coded in 2 octets (*quantum level (QL)*). Each *QL* from each IP pixel is converted to *PSL* by the function:

$$PSL = \left(\frac{Res}{100}\right)^2 \frac{400}{S} 10^{L\left(\frac{QL}{2^D-1} - \frac{1}{2}\right)} \quad (3.4)$$

where *PSL* is the *photostimulated luminescence* photons in one pixel, *Res* is the resolution (size of a pixel), *S* the sensibility, *L* the latitude, *D* the lecture dynamic (8 or 16 bits) and *QL* the numerical value of the pixel (from 0 to  $2^D - 1$ ). In our case, the resolution was 50  $\mu\text{m}$ , the sensibility 4000, the latitude 5 and it was coded on 16 bits.

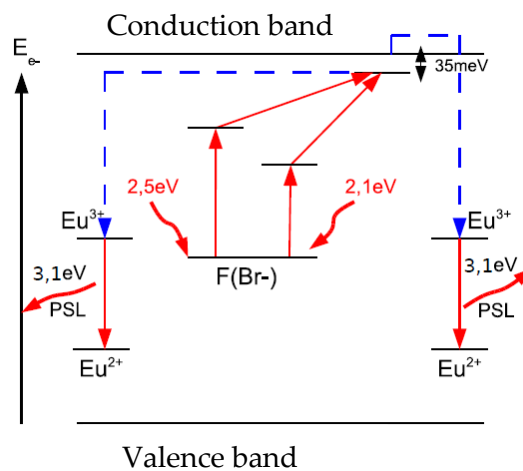


**Figure 3.38** Levels of BaFBr crystal doped with Europium in the SR IP sensitive layer. The figure is taken from [Bonnet 2013].

### 3.3.2. Active detectors

More complex detectors, but important for HRR experiments, are 2D electronic detectors that provide short (few seconds) readout times. Fast scintillators coupled to a CCD or a *photomultiplier tube* (PMT), a *micro-channel plate* (MCP) coupled to a phosphor screen and complex CCD are examples of active detectors (e.g. for plasma images or X-rays detection). Recently, diamond detectors are also being used in laser-plasma experiments.

The detection acquisition time can be optimized to discriminate signals produced by protons, ions, electrons and X-rays. The signal from electrons is usually suppressed by magnetic fields placed in front of the detector entrance.

### 3.3.2.1. Scintillators

A scintillator is a material that produces light when it is excited by ionizing radiation. The material may absorb the particle energy and scintillate, or if metastable excited states are populated, the light produced by the deexcitation of the electrons from the excited states to lower states is delayed from the input signal.

Sometimes the scintillator is coupled to an electronic light sensor (PMT, photodiode or silicon photomultiplier). The PMT absorbs the light emitted by the scintillator and generates electrons by the photoelectric effect. The multiplication of electrons amplifies the input signal and results in an electrical signal that can be analyzed.

In addition, nuclear techniques can be useful for particle characterization. Tarisien *et al.*, designed and built the *nuclear activation technique for analysis of laser induced energetic particles* (NATALIE) system [Tarisien 2011]. It can quantify precisely laser-accelerated particles by simultaneous counting several activated samples. NATALIE is a set of 32 NaI scintillator detectors assembled in pairs that measure the two 511 keV coincident photons following a nuclear  $\beta^+$  decay. This system can be operated for particle energies above a few MeV up to several tens of MeV with very accurate measurement of the energy and angular distribution of the particle beams.

### 3.3.2.2. Micro-channel plate (MCP)

An MCP is a 2D detector that amplifies electron signal in several million of channels which act as independent electron multipliers, as presented in **Figure 3.39**. If an ionizing particle enters into a channel and hits its walls, electrons are emitted and accelerated by the electric field generated by a high voltage applied on both sides of the MCP (In our case, -2000 V). These electrons are multiplied until a cascade emerges from the rear of the plate. The electrons then are attracted by the +5000 V of the phosphor plate placed at some mm away from the MCP. The phosphor is excited and generates light in some ms. An image can be taken by a CCD placed behind the phosphor.

The operation of an MCP is not straightforward, e.g. in the case of needed manipulation in air, a maximum time of 2h is recommended since little dust affects the measurement of the signal. However, HRR ion beam characterization is possible with this kind of detector,

problems with breakdowns between *Thomson parabola* (TP) electrodes are less important than in the IP case and the detection efficiency is high.

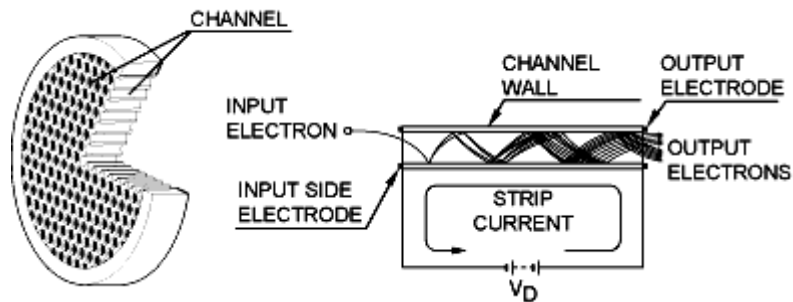


**Figure 3.39** Schematic of a *microchannel plate* (MCP) detector. At the left, a single channel electron multiplier. At the right, with electron multiplication dynamics [dm photonics].

### 3.3.2.1. CCD

In all laboratories, common CCDs are used for optical alignment of laser beams or even coupled to an MCP. They have good resolutions for small prices.

More complex cameras are used for X-ray detection. E.g., in this thesis, a deep-depletion X-ray CCD was used (model PI-LCX:1200 cooled with liquid nitrogen) to detect X-rays produced by the interaction of protons and photons with a sample. The quantum camera efficiency extended above 20 keV, allowing us to count X-ray photons around 8 keV. A thin beryllium window is always present to seal the deep cooling, protect de CCD from visible light and reduce the background (more information is given in **Chapter 5**).

### 3.3.2.2. Diamonds

*Chemical vapor deposition* (CVD) diamonds are wide-bandgap intrinsic semi-conductors that have outstanding intrinsic properties such as low leakage currents, fast time response or radiation hardness. The energy of a charged particle is deposited in the material creating a free electron-hole pair (energy gap = 13.6 eV). A voltage is applied to the electrodes of the detector to allow the charged particle collection. The voltage amplitude is chosen such to have an electric field  $E > 1$  MV/m in order to operate in electron holes pairs velocity saturation regime. Their radiation hardness allows them to tolerate high radiation doses without degradation of their properties. The energy necessary to create a free electron-hole pair guarantees a very low dark current and prevents IR and visible light from contributing

to the signal. Their small sizes make them interesting for laser-driven acceleration experiments. There are two different electrodes configuration of CVD diamond detectors: planar or transverse. [Verona 2015]. Both structures are presented in **Figure 3.40**.

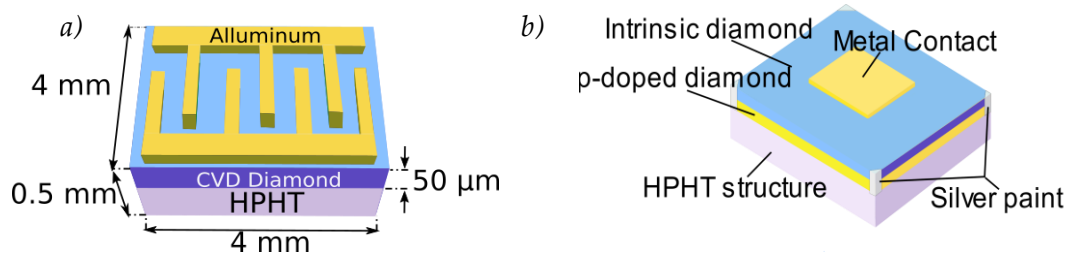


**Figure 3.40** Two different types of electrodes layout: *a)* the interdigital configuration, *b)* sandwich configuration. They are both mounted inside a cylindric metallic enclosure designed to minimize the EMP effects. [Verona 2015]

These types of detectors have been developed and optimized together with a readout system to operate in critical environments (laser-plasma interaction ones) [Marinelli 2013, De Angelis 2016]. At the ALLS installation thanks to the contribution of M. Salvadori [2020], two CVD diamond detectors were used for proton *time of flight* (TOF) measurements. Both have an active layer of thickness 50  $\mu\text{m}$  grown on a commercial 4 $\times$ 4 $\times$ 0.5 mm *high pressure high temperature* (HPHT) substrate but are presenting two different electrode layouts. The signal collected by the CVD diamond detector is sent to a Tektronix DPO 7104 scope (1 GHz bandwidth and 5 Gs/s sample rate) through 15 m long RG 223 cables. The detectors are triggered by a signal correlated to the laser pulse arrival on target. They are shielded for a good reduction of the EMP noise which affects all the electronic devices placed nearby the experimental chamber.

### 3.3.3. Spectrometers

Spectrometers are useful tools to measure the number of ions as a function of their energy. In laser-plasma experiments, the TOF and TP spectrometers are commonly used. While the TOF cannot distinguish different ion species, TP allows splitting and steering the ions to separate the contribution of each ion species and its energy.

### 3.3.3.1. Time of flight (TOF)

A TOF spectrometer consists of a long vacuum tube connected to a detector. Ion beams can spread out temporally because of the velocity dispersion. It is simple and has fast readout for HRR lasers. However, no distinction between different ions is possible. Other particles, e.g. electrons, can be easily deviated by small magnets.

The detector can be a plastic scintillator placed far (several meters) from the interaction point. The protons arrive at different times at the scintillator depending on their energy. The scintillation light is converted into electrons by a photocathode and multiplied by a PMT. The signal is read by an oscilloscope. However, the signal of the PMT is not linear which makes impossible the measurement of the absolute number of protons with different energies. Moreover, the scintillator must be placed far away from TCC to have a good resolution (see **Figure 3.41**).

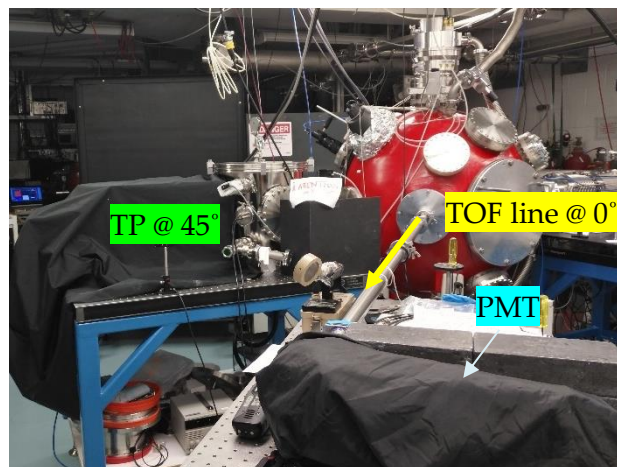


**Figure 3.41** The first ALLS configuration. TOF line coupled with an PMT at 0°. On the left, at 45°, the TP spectrometer.

The replacement of the plastic scintillator by a diamond is interesting because of its fast response. The diamond detector can be closer to the interaction point and still have a good time resolution, even if there is no possibility to split the different accelerated ions. Moreover, diamond detectors have a small size which is always an advantage (e.g. there is the possibility of using several detectors in the same chamber).

This type of spectrometer was used at EMT-INRS center in a second configuration and they were placed in almost symmetrical positions (-6 and +9 degrees). In **Figure 3.42**, it is possible to see the experimental chamber with the KF40 pipes leading to the diamond detectors.



**Figure 3.42** Second ALLS configuration: TOF lines at -6° and 9°. One can observe the small size of the diamond detectors. The line in the middle is for the TP (@ 0°).

### 3.3.3.2. Thomson parabola (TP)

TP is a useful spectrometer: it is capable to disperse, in energy and in mass-to-charge ( $A/Z$ ) ratio, different ion species. A traditional TP scheme is shown in **Figure 3.43**. It consists of pairs of rectangular magnets and electrodes that produce uniform magnetic and electric fields respectively. A particle passes through the magnetic and electric field and its trajectory is steered by the Lorentz force ( $m\mathbf{a} = q(\mathbf{E} + \mathbf{v} \times \mathbf{B})$ ). The electric and magnetic fields are parallel to each other and perpendicular to the ion initial momentum. The particle trajectory is deviated as a function of its energy by the magnet in the longitudinal axis and then deflected as a function of its  $A/Z$  ratio in the vertical axis by the electric field. If particles have different energies, a parabola is formed for each ion species.

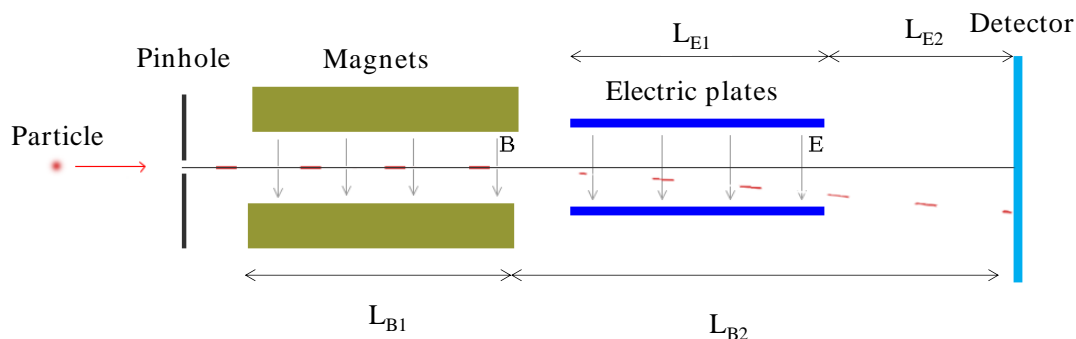


**Figure 3.43** Schematic of a Thomson parabola TP spectrometer.  $L_{B1}$  and  $L_{E1}$  is the magnet and electric plates length and  $L_{B2}$  and  $L_{E2}$  the distance from the magnet or the electric plates to the detector.

TP are usually shielded (e.g. by lead walls) for signal-to-background ratio improvement and equipped with pinholes at their entrances for better energy resolution.

Considering uniform electric and magnetic fields without fringe field effects, the ion displacement at the detector for non-relativistic cases along the vertical direction ( $Y$ , as the electric field) and horizontal direction ( $X$ , as the magnetic field) is:

$$\begin{aligned} X &= \alpha B \left( \frac{L_{B1}^2}{2} + L_{B1}L_{B2} \right) \\ Y &= \alpha^2 E \frac{m}{q} \left( \frac{L_{E1}^2}{2} + L_{E1}L_{E2} \right) \end{aligned} \quad (3.5)$$

Where  $\alpha = q/mv_z$  and  $v_z$  is the longitudinal speed of the ion (of mass  $m$  and charge  $q$ ) at the pinhole,  $L_{B1}, L_{B2}, L_{E1}, L_{E2}$  correspond to the distance shown in **Figure 3.43**, and  $E$  and  $B$  are the electric and magnetic field strengths, respectively. The distance  $X$  and  $Y$  are derived using equations of motion for the particles and the Lorentz force neglecting the change of  $v_z$ . More information in [Gwynne 2014].

The displacement has a linear dependence on the magnetic ( $B$ ) and electric ( $E$ ) field strengths and a stronger dependence on the length of the magnets and electric plates. Since electrons have an opposite charge compared to protons, they are deflected inside the magnetic field in the opposite direction.

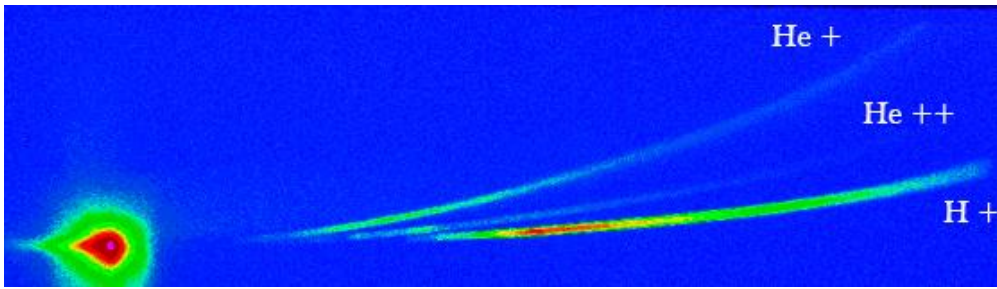


**Figure 3.44** Scanned BAS-TR IP that shows the three different parabolas from the helium-hydrogen gas mixture used as a target. The spot at the left indicates the initial position of the particles before being deflected by the electric and magnetic fields. The X-rays and UV light from the laser reach the IP at this spot.

For the gas-jet experiments, TP were used coupled to IP. **Figure 3.44** shows a scanned BAS-TR IP after the PICO2000 laser interaction with a helium-hydrogen mixture gas-jet target. The parabolas from protons ( $H^+$ ), and helium ions ( $He^{++}$  and  $He^+$ ) are shown on the

right. The spot on the left indicates the initial position of the particles before being deflected. For the analysis, once the logarithmic response of the detector ( $QL$ ) is linearized ( $PSL$ ) [Dorias 2015], one must sum vertically the  $PSL$  of a parabola trace (e.g, the one for protons). An example is shown in **Figure 3.45**. For each ion species, a parabola trace and a background trace were isolated, and the background was carefully subtracted. In the case of several parabolas, the maximal energy may be probably underestimated because of parabola trace overlaps.

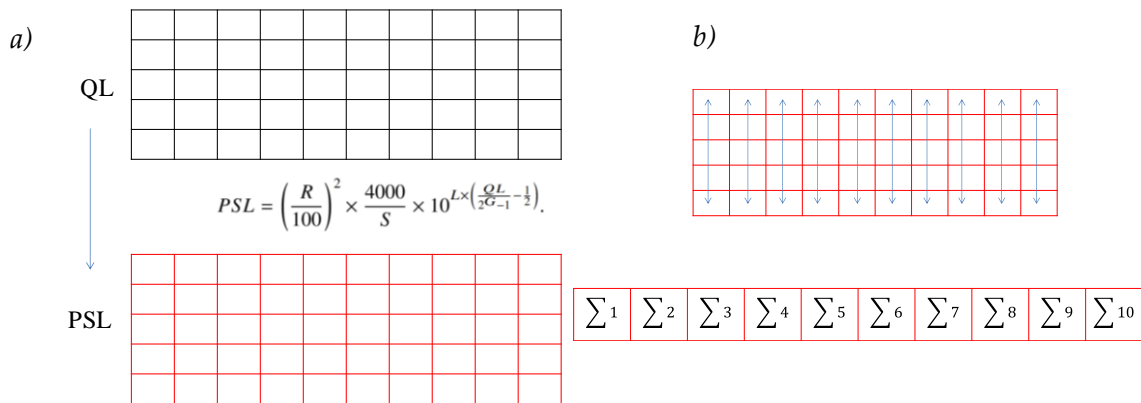


**Figure 3.45** Making the assumption that the parabola trace is just in 10x10 pixels (represented as squares) *a*) QL must be converted in PSL before any manipulation. *b*) Then one can sum the PSL for each column.

The conversion  $PSL$  position to energy can be calculated with the TP geometry and/or its magnetic field map. All TP used during the experiment campaigns have been calibrated in energy at the AIFIRA accelerator facility at CENBG, in the energy range from 500 keV to 3.5 MeV. **Figure 3.46** shows the PSL position as a function of the energy.

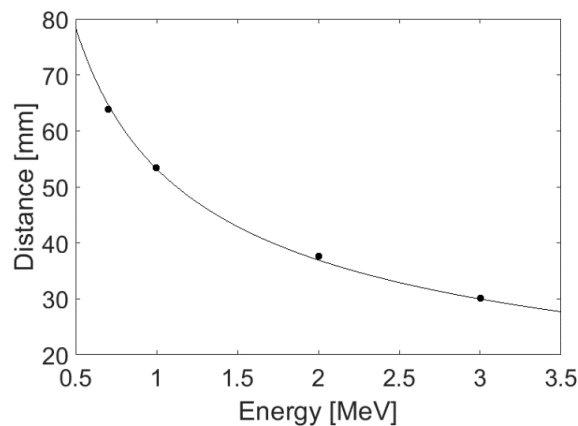


**Figure 3.46** Four different ion beam energies were analyzed in AIFIRA accelerator. 0.7 MeV, 1 MeV, 2 MeV and 3 MeV. A fit was done to relate the position of the beam spot to its energy. This process was performed for all the TPs used in the gas-jet experiment.

The number of protons at each pixel position (or ion energy) is extracted from the number of PSL using the response functions shown in **Figure 3.47** taken from [Bonnet 2013]. However, before using this response function, one must check if the scanner conditions are similar to the one use in [Bonnet 2013]. The number of protons/MeV/sr is obtained dividing the number of protons by the solid angle of the parabola pinhole (in steradian) and by the value of the energy bins in the spectra.

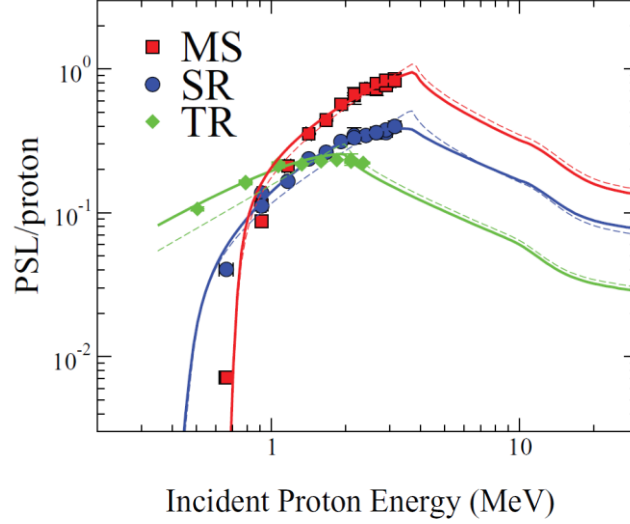


**Figure 3.47** Response function  $R(E)$  of BAS-MS, BAS-SR, and BAS-TR IPs. The symbols represent the data from [Bonnet 2013]. For more information [Bonnet 2013].

The uncertainties in the energy value and in the number of protons/MeV/sr ( $N_p/\text{MeV}/\text{sr}$ ) were calculated assuming that all variables (solid angle  $\Omega$ , response function, number of PSL, energy calibration) are statistically independent and summing their variances.

$$N_{p/\text{MeV}/\text{sr}} = \frac{N_p}{\Omega E} \left\{ \begin{array}{l} N_p = \frac{\text{signal}_{NB}}{N_{p-PSL}} = \frac{\text{signal}_T - \text{signal}_B}{N_{p-PSL}} \\ \Omega = \frac{\pi \left(\frac{\phi}{2}\right)^2}{d_{TCC}^2} \\ E = \text{diff}(E) \end{array} \right. \quad (3.6)$$

where  $N_{p/\text{MeV}/\text{sr}}$  is the number of protons/MeV/sr,  $N_p$  the number of protons,  $\text{signal}_T$  the signal obtained in the IP detector,  $\text{signal}_B$  the background signal,  $\text{signal}_{NB}$  the actual signal with background subtracted,  $\phi$  the pinhole diameter,  $d_{TCC}$  the distance from the target to

the pinhole,  $E$  the energy binning. As the uncertainties are statistically independent, the total uncertainty can be calculated as:

$$\delta N_{p-sr} \approx |N_{p-sr}| \left( \frac{\delta N_p}{N_p} + \frac{\delta \Omega}{\Omega} + \frac{\delta E}{E} \right) \quad (3.7)$$

The energy is measured with an accuracy of about 3%. The accuracy of  $N_p/\text{MeV}/\text{sr}$  is about 50% at low energies and about 20% at high energies.

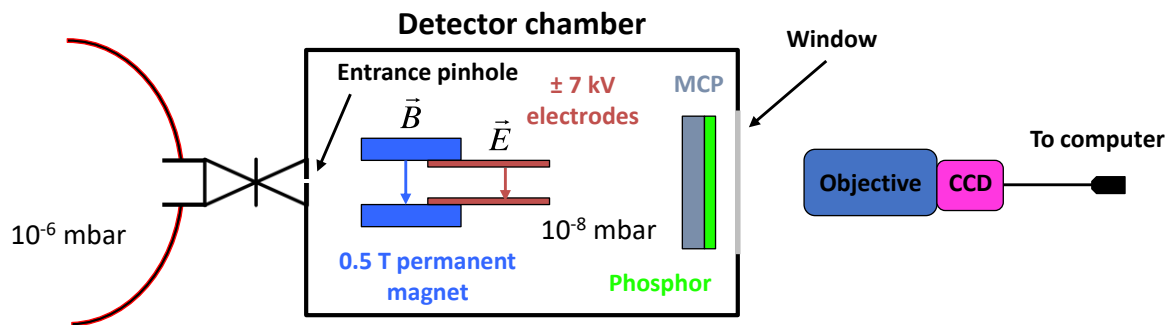


**Figure 3.48** Schematic of the TP-MCP used at the EMT-INRS center. The detector is in a different vacuum chamber allowing a differential vacuum and the possibility of opening the main chamber without breaking the vacuum in the detector chamber. The real photo is in **Figure 3.49** [Paper III].

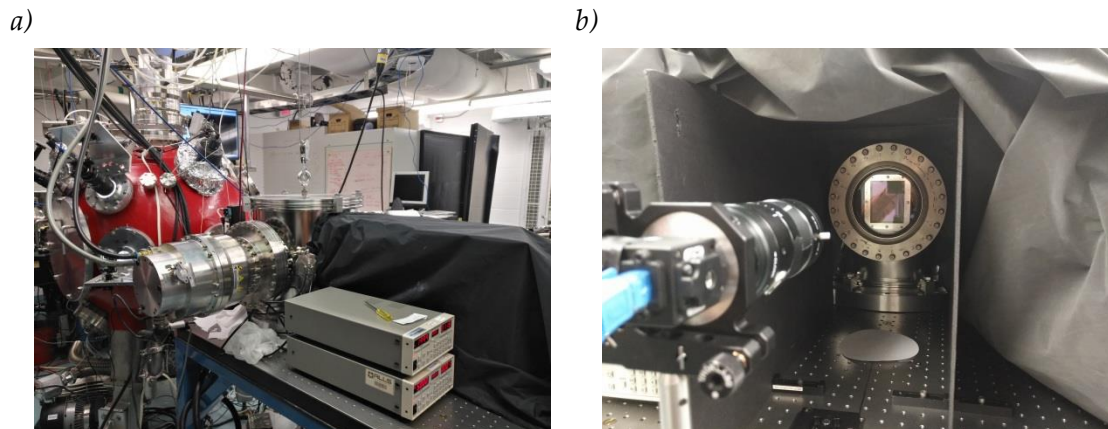


**Figure 3.49** a) Picture of the detector chamber connected to the *boule rouge* at EMT-INRS center. b) Picture of the CCD pointed at the MCP inside the detector chamber. The picture is taken under the black blanket on the right of picture a).

The TP at the EMT-INRS was used with an MCP as detector ( **Figure 3.48** and **Figure 3.49**). The TP-MCP is placed in a separate chamber in a high-quality vacuum. The TP was calibrated in intensity on the 2x6 MV Tandem linear accelerator from University of Montreal (UdM). A cross-calibration was performed between the TOFs and the MCP to

calibrate the relevant parameter of the TP spectrometer required to find the proton kinetic energy. More information about this calibration can be found in [Paper VII].

Figure 3.50 shows a typical MCP image obtained from the TP spectrometer with a Cu target. One can see the parabola from the light species: protons,  $H^+$ , and different carbon ion species ( $C^{4+}$ ,  $C^{3+}$  and  $C^{2+}$ ). A less intense copper ion parabola is observed as well.

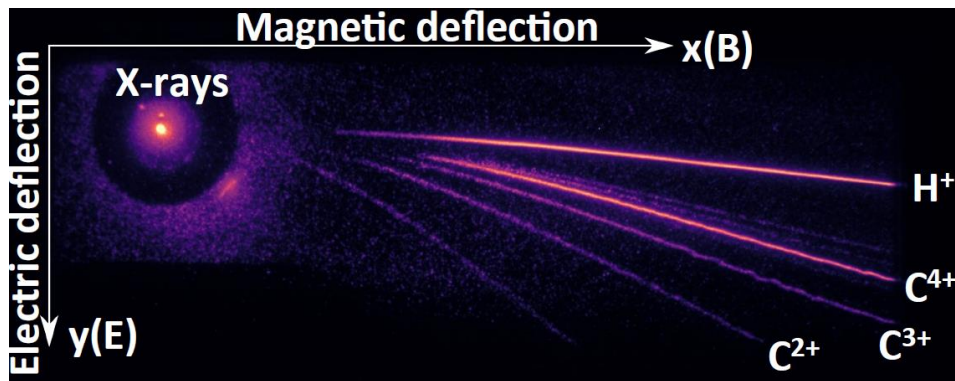


Figure 3.50 MCP image obtained from the TP spectrometer with a Cu target. Taken from [Paper VII].

The manipulation of the MPC is more complicated than the IP, however, they are suitable for HRR. Moreover, breakdown problems are less important in the case of MCPs. Both detectors are sensitive to UV so the breakdowns are detected. In the case of IP, the breakdowns marked the IPs and they could not be used for that shot.



# GAS TARGET EXPERIMENT RESULTS

---

## 4.1. Introduction

The designed gas-jet nozzles presented in **Section 3.2** are tested in two different experimental campaigns with the PICO2000 laser system. In the experiment, proton acceleration is studied using hydrogen gas and different types of nozzles: *big* and *small conical nozzles*, and *asymmetrical nozzles*. *Shock nozzles* were designed after the experiment. The parameters of each type of nozzle are summarized in **Table 4.1**. Moreover, helium acceleration is studied with a mix of hydrogen and helium gases using an asymmetrical gas-jet target. These results are discussed in **Section 4.4**.

## 4.1. Experimental setup

Four TPs with their respective IP are used to detect and resolve in charge and energy the accelerated ions. They are placed at  $0^\circ$ ,  $30^\circ$ ,  $60^\circ$ ,  $90^\circ$  with respect to the laser axis in the first campaign, and at  $0^\circ$ ,  $30^\circ$ ,  $70^\circ$ ,  $80^\circ$  in the second campaign (**Figure 4.1**) due to space constraints. They are shielded by lead walls for signal-to-background ratio improvement and equipped with pinholes at their entrances for better energy resolution. The pinhole diameters are smaller than  $500\ \mu\text{m}$ .

	<i>Big conical nozzle</i>	<i>Small conical nozzle 1</i>	<i>Small conical nozzle 2</i>	<i>Asymmetrical nozzle</i>	
<b>Shape</b>	Conical	Conical	Conical	Rectangular	
<b><math>d</math> [<math>\mu\text{m}</math>]</b>	300	100	100	100 x 100	
<b><math>D</math> [<math>\mu\text{m}</math>]</b>	400	200	240	500 x 100	
<b><math>L</math> [mm]</b>	1	1	1	1	
<b><math>z_{\text{opt}}</math> [<math>\mu\text{m}</math>]</b>	200	200	400	200	
<b><math>\rho_{\text{max}}</math> [<math>\text{cm}^{-3}</math>]</b>	$3.54 \times 10^{21}$	$1.53 \times 10^{21}$	$8.95 \times 10^{20}$	$7.22 \times 10^{20}$	$4.31 \times 10^{20}$
<b>FWHM [<math>\mu\text{m}</math>]</b>	347	140	148	480	139

**Table 4.1** Parameters of the nozzles used in the experiments ( $d$  is the throat diameter,  $D$  the nozzle exit diameter and  $L$  the cone length). The optimal interaction distance  $z_{\text{opt}}$ , the maximum molecular density delivered  $\rho_{\text{max}}$  and the FWHM of the density profile are given in the two last rows.

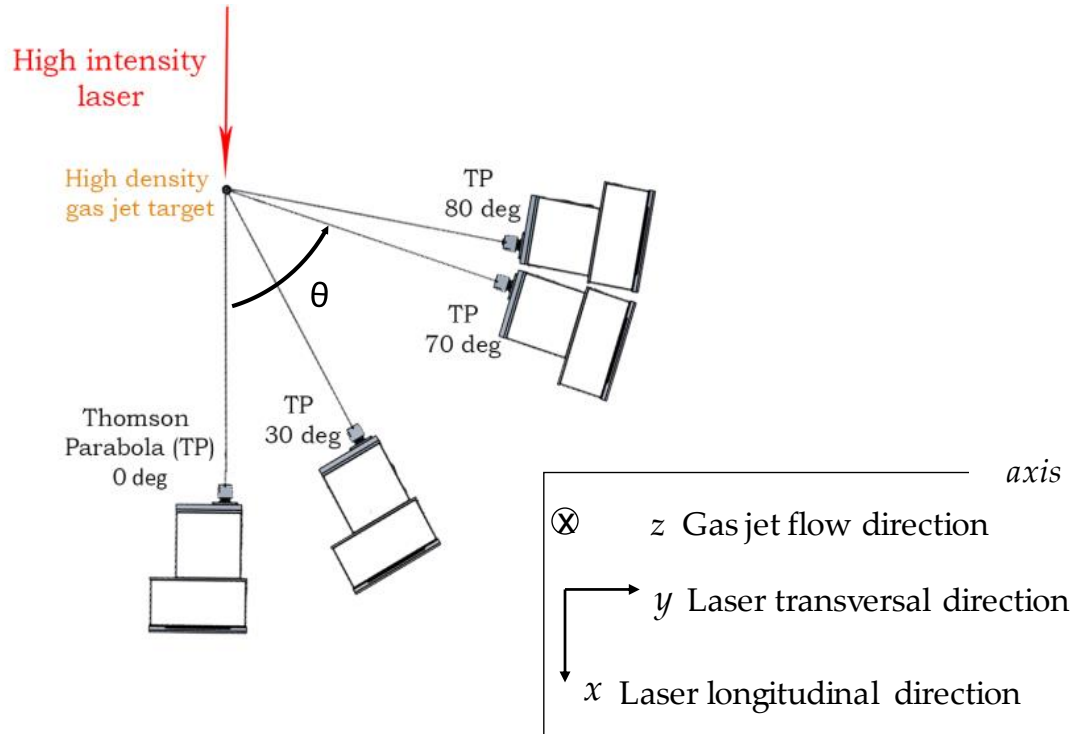


**Figure 4.1** Experimental setup at the LULI facility. PICO2000 high-power laser is impinging on the high-density gas-jet target. Four TPs equipped with IPs are placed at 0°, 30°, 70°, and 80° with respect to the laser axis, 50 cm away from the gas-jet target.

The gas-jet target alignment is achieved using bottom and side views placed in the chamber. During the interaction, both views are also used as plasma detectors. The  $2\omega$  emission in the interaction is recorded in the *bottom view* camera. During the second campaign, 500 ps after each shot, a shadowgraphy picture is saved using the *side view* CCD.

## 4.2. Laser-beam alignment and plasma diagnostics

For the laser beam alignment, a tip at TCC is the reference ( $x = 0$ ,  $y = 0$  and  $z = 0$ ). **Figure 4.2a** shows the laser shining on it. The red cross indicates TCC. In **Figure 4.2b** a nozzle is placed at the same place. Its illumination and the magnification of the image were not optimal in the first campaign, both parameters are improved in the following one (**Figure 4.4**).

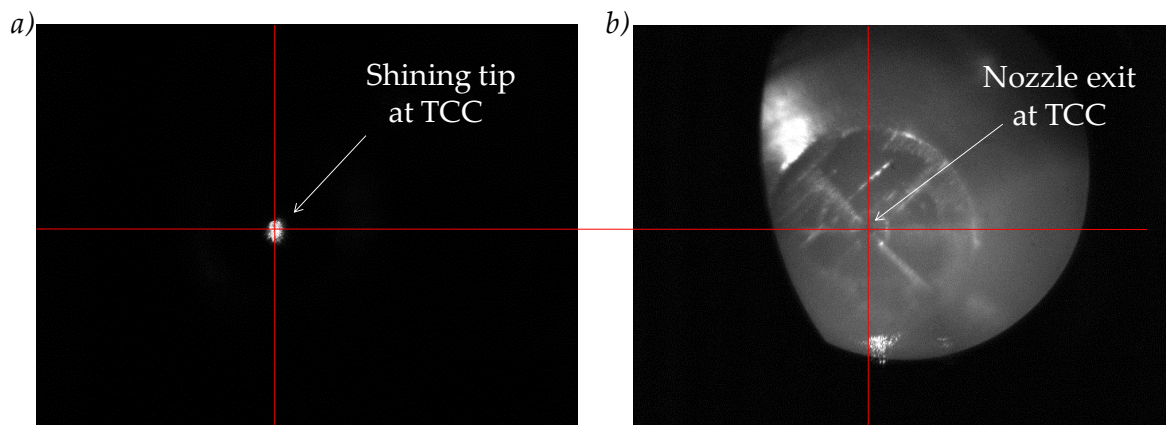


**Figure 4.2** First experiment bottom view. The red cross represents TCC. *a)* The illuminated tip at TCC. *b)* The nozzle at the same place.

The same optical path is used to observe the second-harmonic ( $2\omega$ ) emission of the plasma during the laser-gas interaction. In this case, a band-pass filter is placed in front of the CCD. Second-harmonic generation is an important indicator of nonlinear laser-plasma interaction. Its characteristics can provide information about e.g. the laser energy absorption mechanisms. Images of second-harmonic generation induced by a ponderomotive force have been presented in [Mori2002]. Stronger second-harmonic generation was observed in [Zhizhan 1983; Stamper 1985]. It was usually due to self-focusing, filamentation or stimulated Raman scattering. In this work, the laser ponderomotive force sweeps the

electrons away from the laser beam path inducing a change of the refractive index which may probably be at the origin of the  $2\omega$  emission.

In the experiment, the  $2\omega$  emission is observed when the laser interacts with the different types of gas targets. **Figure 4.3a** and **b** show the  $2\omega$  emission from the bottom view for a *big conical nozzle* and a *small conical nozzle 1* respectively. **Figure 4.3c** shows the comparison of the gas density profile of each nozzle at the interaction distance  $z = 200 \mu\text{m}$ . The laser is always focused at TCC, as indicated on the figures with a red cross. The red arrows indicate the laser direction, along the longitudinal position ( $x$ -axis). To modify the relative position between the center of the nozzle and the laser focus, the nozzle is displaced in the laser's longitudinal position. In the picture, the grey circle indicates the position of the nozzle at the time of the shot.

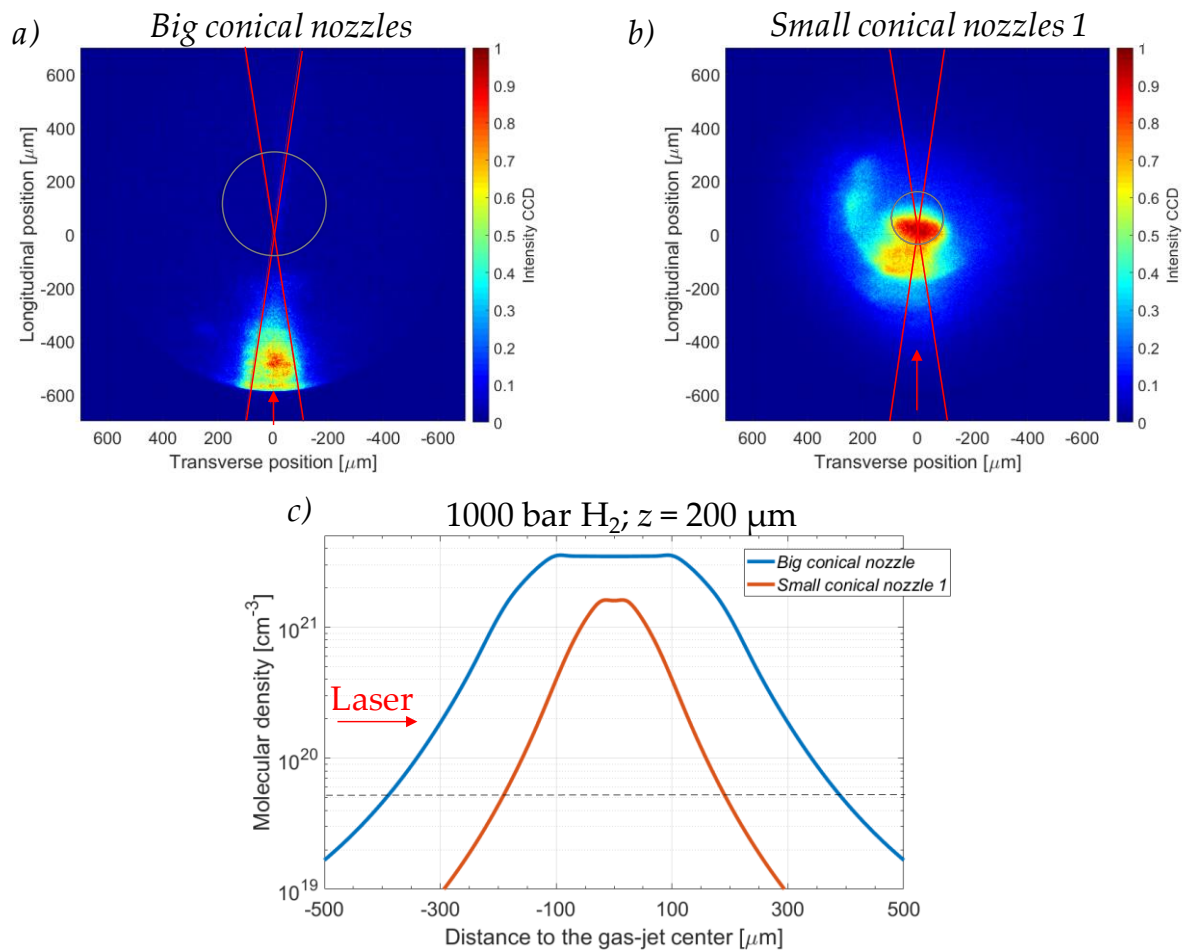


**Figure 4.3** Capture of the  $2\omega$  emission of the plasma during 250 ps after the laser-gas interaction on *a) a big conical nozzle b) a small conical nozzle 1* . *c) The gas density profile for these different types of gas targets.*

With a *big conical nozzle* (see **Figure 4.3a**), even if the laser focus is planned at the entrance of the nozzle, the generation of the second harmonic is observed before. That could mean that the plasma in the *wings* of the gas density profile (**Chapter 3**) is too dense and the laser is not capable to traverse it, i.e., the laser interacts with a plasma before the maximum density, losing its energy. The interaction seems to start before  $x = -600 \mu\text{m}$  from the focal point, where the density of the plasma is of the order of  $10^{19} \text{ cm}^{-3}$  (see **Figure 4.3c**). The start of the interaction was too far to be observed.

In the second case, for a *small conical nozzle 1* (**Figure 4.3b**), the second-harmonic generation is observed closer to the focal point. The density profile is thinner so the laser starts the interaction closer to the nozzle entrance, at  $x \simeq -300 \mu\text{m}$ , where the density of the gas jet is also about  $10^{19} \text{ cm}^{-3}$ . The maximum signal is observed at the center of the nozzle exit.

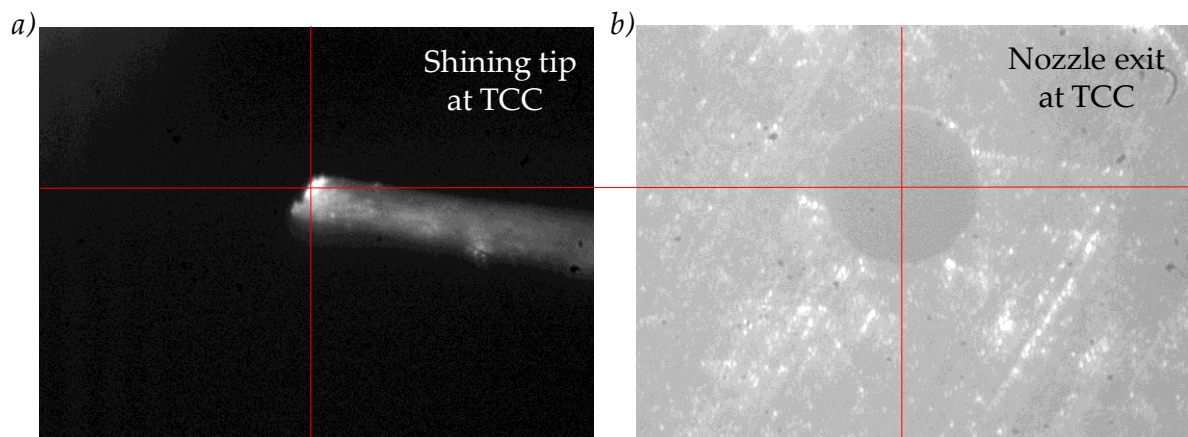


**Figure 4.4** Pictures from the bottom view CCD in the second experiment *a)* of the illuminated tip at TCC *b)* of the nozzle at TCC. The red cross represents TCC.

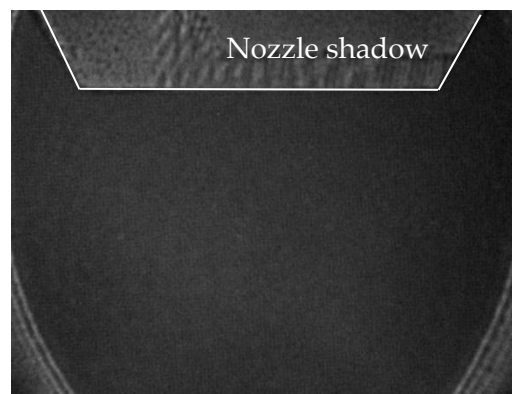


**Figure 4.5** Picture from the side view CDD. The nozzle is upside down.

In the second campaign, the resolution and illumination of the nozzles are improved (**Figure 4.2** vs. **Figure 4.4**). An additional CCD is placed at one side of the nozzle which is used to observe the shadowgraphy of the plasma enlighthed by a Quanta-Ray laser (ns) (**Figure 4.5**). The precision of our alignment in the second campaign is therefore better.

Nozzles are always *small conical nozzles 2* and the interaction point is at  $z = 400 \mu\text{m}$  from the nozzle exit. In **Figure 4.6a**, the focus is made at the center of the gas jet while in **Figure 4.6b** the laser is focused at the rising slope of the jet density profile. In both cases, the main interaction at the focal point is observed. However, it is difficult to explain the different shapes observed. Proton energy spectra from those shots are plotted in **Figure 4.12b** and **Figure 4.13a** respectively.

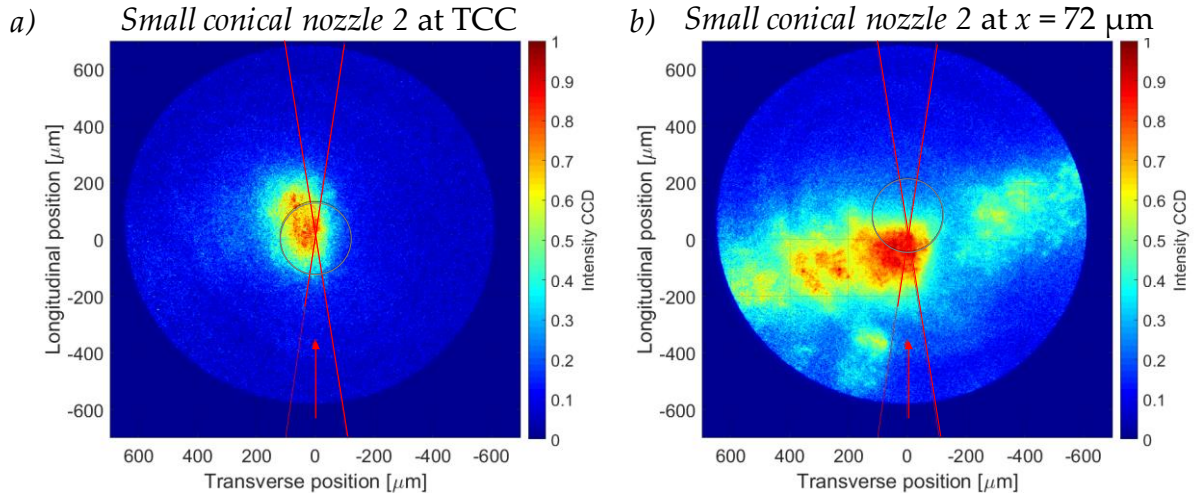


**Figure 4.6** Capture of the  $2\omega$  emission of the plasma during 120 ps after the laser-gas interaction on a conical nozzle. *a)* The nozzle is placed at TCC *b)* The rising slope of the jet density profile is placed at TCC.

On the side view, the plasma expansion is recorded with a *small conical nozzle 2*. In **Figure 4.7**, a dense plasma (dark blue) is observed on both sides of the interaction point, at  $z = 400 \mu\text{m}$  from the nozzle exit. This plasma expands and follows the rest of the gas. A dense plasma is also formed at the surface of the nozzle. Nozzle damage was observed in both campaigns after one laser shot. The nozzles were more damaged in the first campaign (when the laser was focused  $200 \mu\text{m}$  from the nozzle exit) compared to the second one ( $z = 400 \mu\text{m}$ ). As a consequence of this damage, in the experiment, the nozzles were changed after each shot. We can conclude that, for no damage to the nozzle, much higher interaction distances should be used.

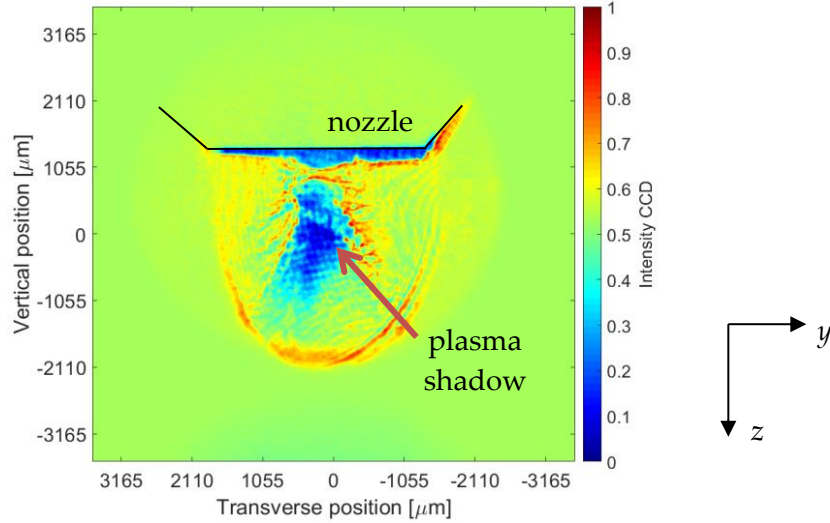


**Figure 4.7** Shadowgraphy of the plasma by a Quanta-Ray laser (ns) during 500 ps after the laser-gas interaction.

## 4.3. Results on proton acceleration

### 4.3.1. 1<sup>st</sup> campaign

The first campaign objective is the study of different nozzle types (*big conical nozzles*, *small conical nozzles 1* and *asymmetrical nozzles*) to test the best design for ion acceleration. Most of the shots are performed with hydrogen for protons acceleration. The detector used in the TP is BAS-TR IP.

Firstly, proton acceleration is obtained using *big conical nozzles*. The laser is focused at 200  $\mu\text{m}$  from the nozzle exit (in the  $z$  direction) and the nozzle is placed 150  $\mu\text{m}$  away from TCC in the  $x$  direction (for better understanding of the nozzle displacement, seen **Figure 4.3a**). The laser interacts with the gas-jet target 18 ms after the release of the gas. The electro-valve allows the gas flow during 20 ms ( $t_{open} = 20$  ms). During some shots, the effect of the ASE on the proton spectra is studied. We modified the ASE level tuning the *Pockels* cell delay (PD), as explained in **Section 3.1.1**.

**Figure 4.8** shows typical spectra obtained with the laser ( $E_L \approx 75$  J) focused at the rising slope of the gas-jet density profile and with the ASE level defined as PD = 0. The spectrum in **Figure 4.8a** shows that about  $10^{12}$  protons in a continuous energy distribution up to 1.5 MeV are emitted in all directions. The signal in the laser's transversal direction seems higher,

however, micro breakdowns in the 90° TP introduce a big uncertainty on the number of protons ( $\pm 80\%$ ). In **Figure 4.8b**, when the ASE was reduced to PD = 1.05 ns, higher energy protons in the laser's longitudinal direction ( $x$ -axis) are reported. Small second structures (shown in red circles) at 2.8 MeV and 5 MeV at 0° are observed. At 30°, a second structure (plateau) with a constant number of  $10^{10}$  protons with energies from 1 MeV up to 2.5 MeV is noticed. The ASE is more reduced in order to obtain a higher signal in the laser's longitudinal direction. However, the ASE is *too* reduced (PD = 1.25 ns, **Figure 4.8c**) and the laser pulse wavelength spectrum starts to decrease; with the consequence of larger pulse duration. The signal in the laser's longitudinal direction is not improved. The relative delay between the *Pockels* cells is then determined as 1.05 ns for the following laser-plasma interactions with the minimum ASE level achievable.

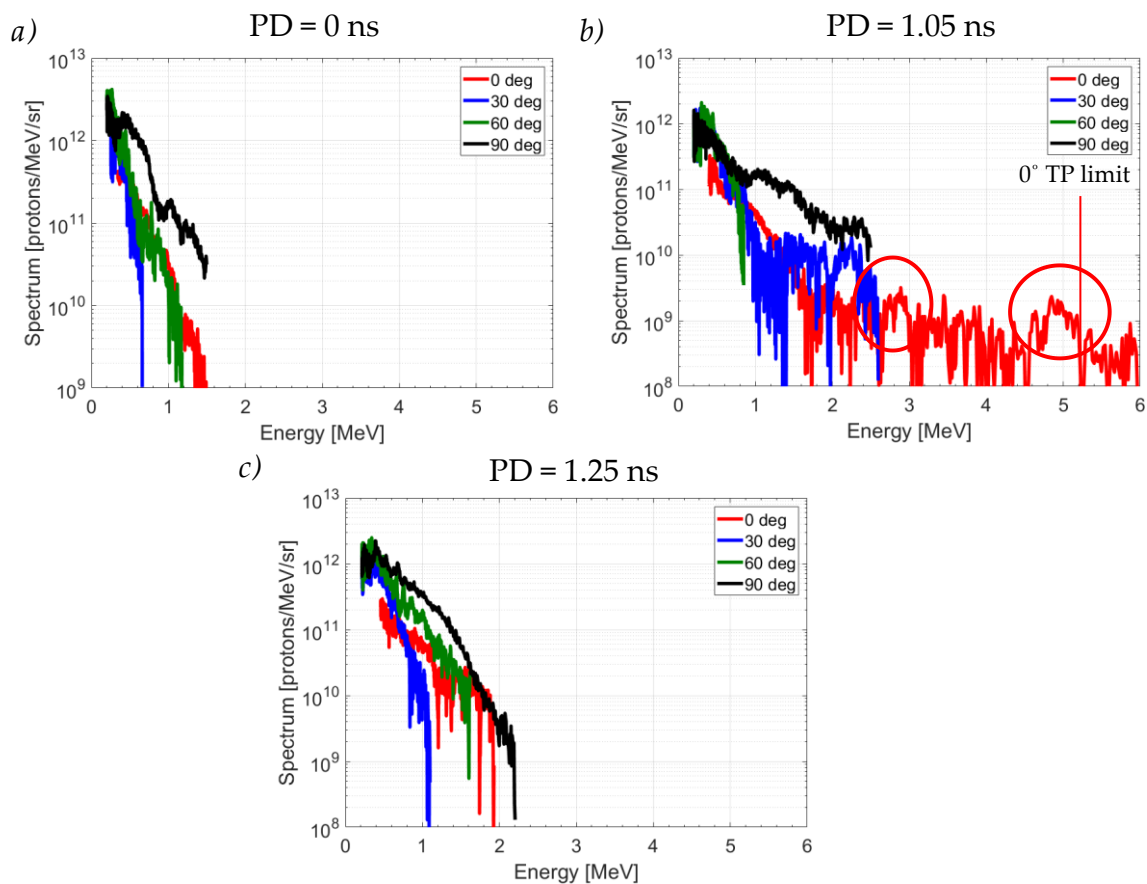


**Figure 4.8** Proton energy spectra at 0° (red), 30° (blue), 60° (green) and 90° (black) obtained with the laser focused at the rising slope of the *big conical nozzle* density profile at  $z = 200 \mu\text{m}$ . The ASE is continuously reduced from one shot to the other.

Proton acceleration is also achieved using *small conical nozzles 1*. The laser was focused at 200  $\mu\text{m}$  and 250  $\mu\text{m}$  from the nozzle exit ( $z$ -axis). The molecular density profiles are shown in

**Figure 4.9a.** On the  $x$ -axis, the nozzle was placed  $60\ \mu\text{m}$  away from TCC. The laser interacts with the gas-jet target  $64\ \text{ms}$  after the gas release ( $t_{\text{open}} = 30\ \text{ms}$ ).

First, the same interaction conditions are performed two times, with the small difference that the laser energy on the target is  $66.5\ \text{J}$  in the first shot and  $75.5\ \text{J}$  in the second one. **Figure 4.9b** and **c** show about  $10^{13}$  protons with energies up to  $2.5\ \text{MeV}$  at all angles but  $30^\circ$ . A good repeatability is observed. Secondly, the interaction distance from the nozzle is modified, so that the laser interacts with a different density profile. The spectra is shown in **Figure 4.9d**. A thinner density profile seems to improve the acceleration in the longitudinal direction of the laser.

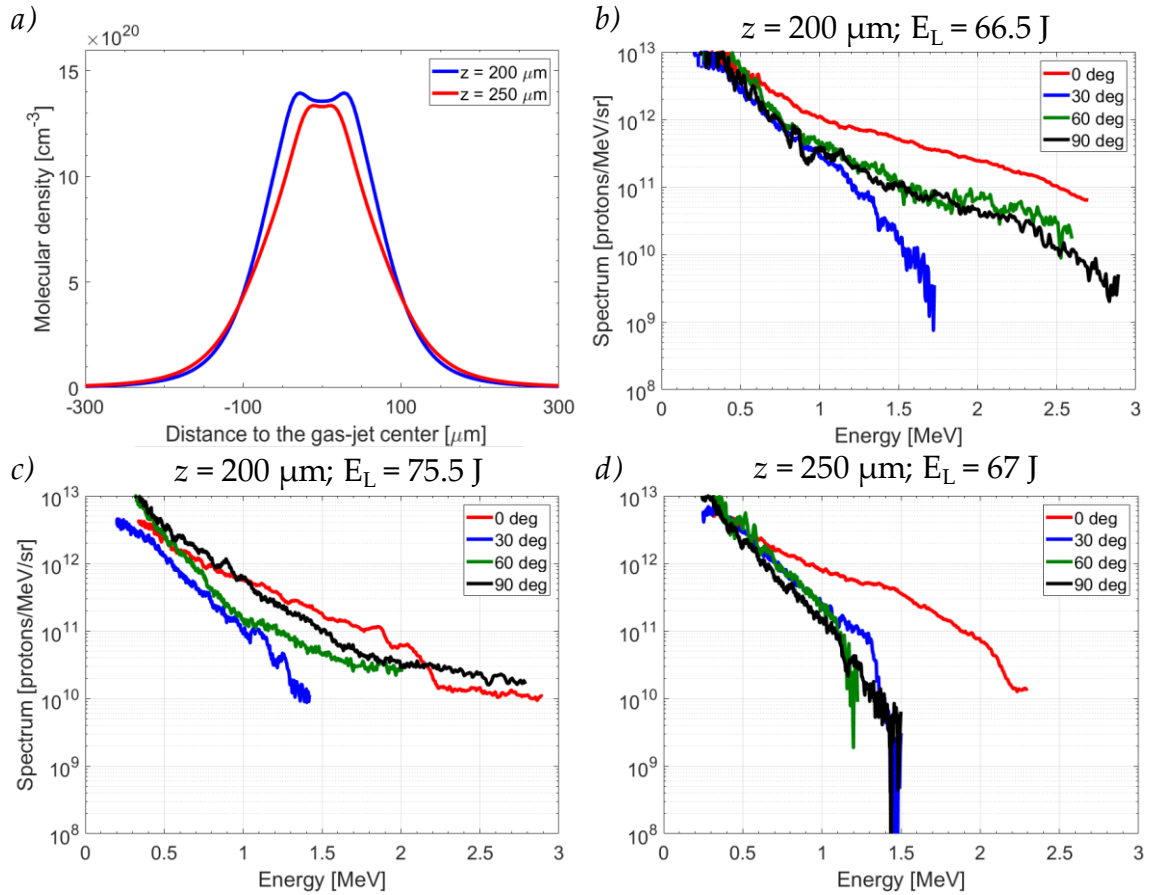


**Figure 4.9** Proton energy spectra at  $0^\circ$  (red),  $30^\circ$  (blue),  $60^\circ$  (green) and  $90^\circ$  (black) obtained with the laser focused at the rising slope of the *small conical nozzle 1* jet density profile at *c*) and *d*)  $200\ \mu\text{m}$  *b*)  $250\ \mu\text{m}$ . A comparison between the density profiles at  $z = 200\ \mu\text{m}$  and  $z = 250\ \mu\text{m}$  is shown in *a*).

Protons are also accelerated using *asymmetrical nozzles*. The laser focus is at  $200\ \mu\text{m}$  from the nozzle exit and the nozzle was placed at TCC. The laser interacts with the gas-jet target  $64\ \text{ms}$  after its release ( $t_{\text{open}} = 30\ \text{ms}$ ). Two shots are done with this type of nozzle, with a possibly

slightly different orientation for one to the other due to a bad *bottom view* resolution in the first campaign. The corresponding gas density profiles are shown in **Figure 3.24**. Other parameters are similar with a small difference in the laser energy ( $E_L = 66.5$  J vs 75.5 J). In the first shot, proton acceleration is mainly observed at  $0^\circ$  and  $90^\circ$  with a maximum energy of 2 MeV (**Figure 4.10a**). In the second shot, (**Figure 4.10b**) protons are more isotropically accelerated. However, a peaked structure at 3.9 MeV is observed in the laser's longitudinal direction.

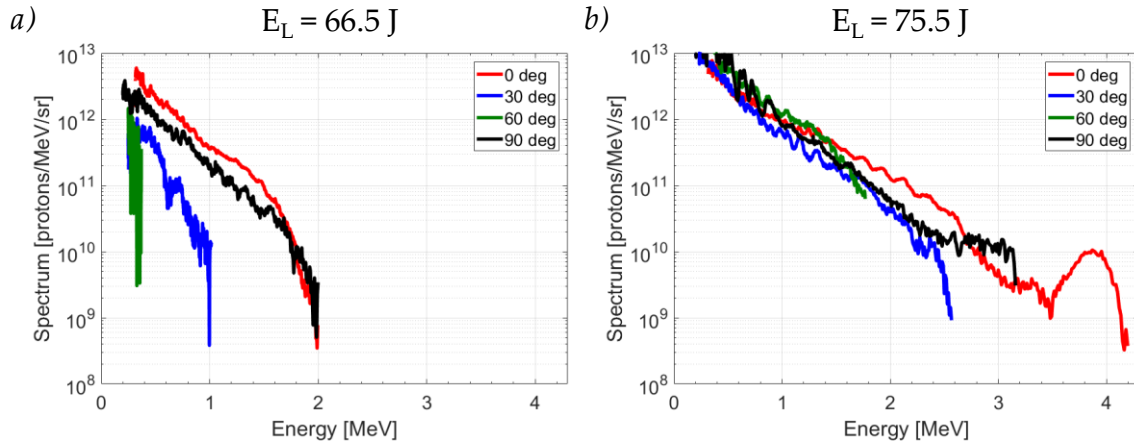


**Figure 4.10** Proton energy spectra at  $0^\circ$  (red),  $30^\circ$  (blue),  $60^\circ$  (green) and  $90^\circ$  (black) obtained with the laser focused at the rising slope of the *asymmetrical nozzle* jet density profile at  $z = 200$   $\mu\text{m}$ . The orientation is probably different in figure *a*) and *b*).

In summary, proton acceleration with *asymmetrical nozzles* is interesting because longitudinal acceleration to high energies (up to 4 MeV in **Figure 4.10b**) is obtained. However, the alignment is not precise and the characterization as shown in **Section 3.2.6** is harder than for other nozzles. This is why we did not use this type of nozzle in the second campaign. Comparing *big* and *small conical nozzles 1*, the maximum energy is similar, but more protons are accelerated with *small conical nozzles 1* (**Figure 4.9**). The laser cannot penetrate into the gas target delivered by *big conical nozzles* due to its thick density profile, so it does not interact with the target maximum density. This phenomenon was also observed in **Figure 4.3a**, where we could see that, even if the laser focus was planned at the entrance of the nozzle, the generation of the second harmonic was observed before. Moreover, more gas is delivered into the vacuum chamber with the *big conical nozzles* which usually produced TP breakdowns. The amount of background present on the IP, in this case, is therefore higher. As a consequence, the statistical fluctuations of the spectra are bigger.

### 4.3.2. 2<sup>nd</sup> campaign

In the 2<sup>nd</sup> campaign, we used only one type of nozzle, *small conical nozzles 2*, and we improved the detection setup. As mentioned before, *small conical nozzles* are chosen because they provide the biggest flux of protons with good repeatability, easy alignment, and characterization. In order to improve the *small conical nozzle 1* used in the first campaign and try to avoid the nozzle damage, some modifications were performed to achieve a similar density profile but at a further distance from the nozzle exit. 400  $\mu\text{m}$  from the nozzle exit is achieved. Moreover, BAS-MS IP are used as detectors, gaining one order of magnitude on the background level. That is also why the signal at energies smaller than 0.7 MeV is not present on the following spectra. Examples of proton spectra with BAS-TR and BAS-MS IPs from Fuji Photo Film Co. Ltd are shown in **Figure 4.11**.

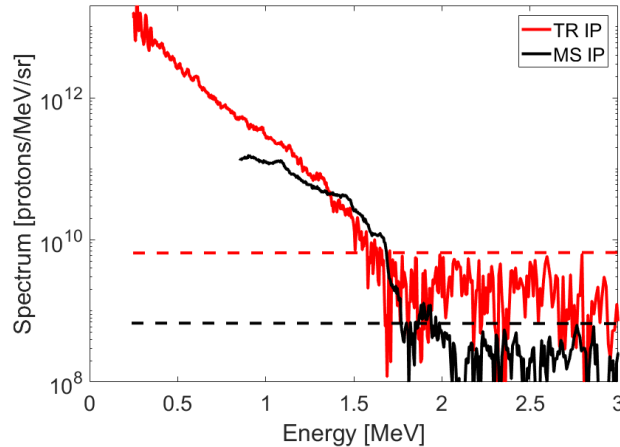


**Figure 4.11** Proton energy spectra recorded at 30° in two similar shots using both types of IPs. The one in red is from a BAS-TR IP while the black one is from BAS-MS IP. Dashed lines indicate the detection limit corresponding to the mean value of the background level plus two times its variance.

BAS-TR IP display a background of  $(1.9 \times 10^9 \pm 1.4 \times 10^9)$  protons/MeV/sr while for BAS-MS IP it is  $(0.25 \times 10^9 \pm 0.22 \times 10^9)$  protons/MeV/sr. This is probably due to their different sensibility to UV light. Note that the energy is measured with an accuracy of about 3%. The accuracy of  $N_p/\text{MeV}/\text{sr}$  is about 50% at low energies and about 20% at high energies.

**Figure 4.12** shows typical spectra obtained with the laser focused at the center of the gas jet. With no modification of the *Pockels* cell delay (PD = 0 ns, **Figure 4.12a**),  $\sim 10^{11}$  protons/MeV/sr in a continuous energy distribution up to 1.5 MeV are observed in all directions. By reducing

the ASE at half of the minimum achievable (PD = 0.8 ns, **Figure 4.12b**) a second structure up to 2.5 MeV is observed in the laser transverse direction containing  $10^{10}$  protons/MeV/sr. Unfortunately, the TP at  $80^\circ$  was not in place in some shots.

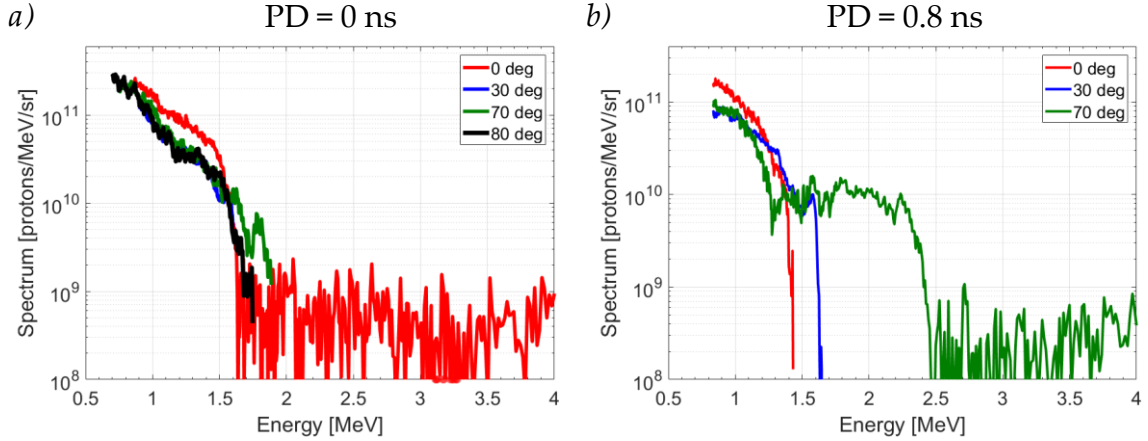


**Figure 4.12** Proton energy spectra at  $0^\circ$  (red),  $30^\circ$  (blue),  $70^\circ$  (green) and  $80^\circ$  (black) obtained with the laser focused at the center of the gas jet *b*) and reducing the ASE at half of the minimum achievable.

**Figure 4.13** shows typical spectra obtained with the laser focused at the rising slope of the gas-jet density profile. With and without modification of the ASE, about  $10^{11}$  protons/MeV/sr in a continuous energy distribution up to 2 MeV are observed at  $0^\circ$  and  $30^\circ$ . A similar distribution in a larger energy range is also observed in the other directions ( $70^\circ$  and  $80^\circ$ ). When the ASE is reduced (PD = 0.8 ns), the contribution of a second structure from 2 MeV to 3 - 4 MeV is larger, containing  $5 \times 10^{10}$  protons/MeV/sr. Besides the structures already presented, an additional peak at 2.3 MeV is observed at  $0^\circ$  in **Figure 4.13a**.

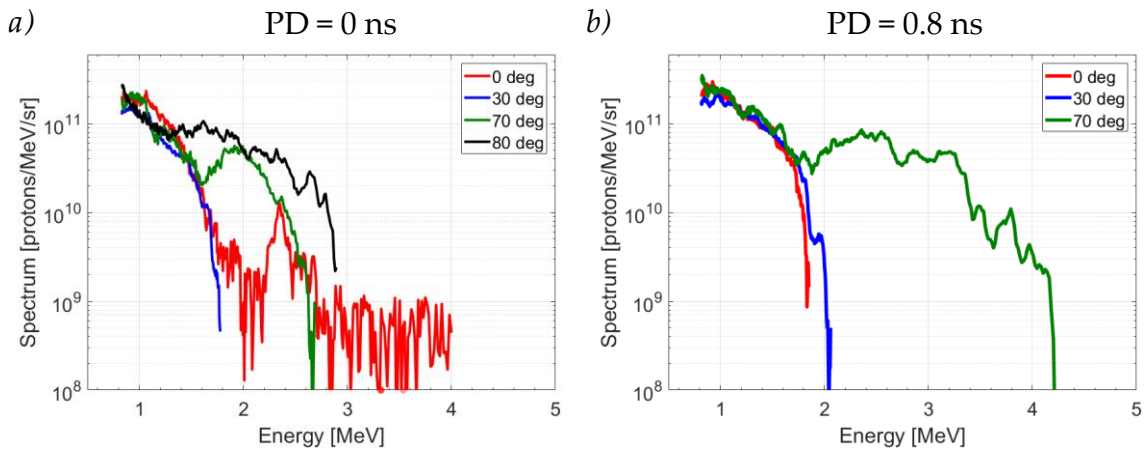


**Figure 4.13** Proton energy spectra at  $0^\circ$  (red),  $30^\circ$  (blue),  $70^\circ$  (green) and  $80^\circ$  (black) obtained with the laser focused at the rising slope of the jet density profile *b*) and the ASE is reduced.

In conclusion, the laser focus at the rising slope of the gas-jet density profile provides more energetic protons and even additional peaked structures.

It is worth noting that the angular position and energy of the peaked structure at  $0^\circ$  in **Figure 4.13a** is highly dependent on the laser and target parameters. Small variations of these (e.g., the lower maximum density of the gas jet and laser fluctuations) can shift the peak to the transverse directions ( $70^\circ$  and  $80^\circ$ ) and to different energies (3.3 MeV), as seen in **Figure 4.14**. In **Figure 4.14b**, a clear plateau structure in the energy range 2-3 MeV is also observed at  $30^\circ$ . Similar features in the laser transverse direction can be seen in **Figure 4.15a** or **Figure 4.12b** at  $70^\circ$ .

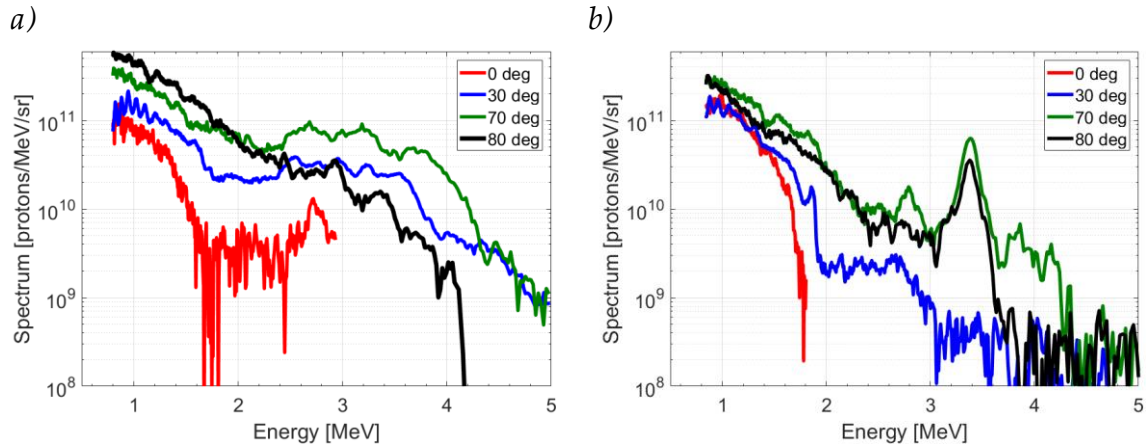


**Figure 4.14** Proton energy spectra at  $0^\circ$  (red),  $30^\circ$  (blue),  $70^\circ$  (green) and  $80^\circ$  (black) obtained with the laser focused at the rising slope of the jet density profile.

**Figure 4.15a** presents the proton energy distribution measured with the laser focused at the rising slope of the gas-jet density profile and the ASE level reduced at minimum achievable. The spectra display more complex structures. The proton flux at  $80^\circ$  is smaller than in previous shots, while the maximum energy at  $0^\circ$  is higher. Three particular features can be seen on the spectrum in the laser's longitudinal direction. The proton flux drops from  $10^{11}$  to  $10^9$  in the energy range between 0.5 MeV and 2 MeV. Then it increases up to  $10^{10}$  between 1.7 MeV and 3 MeV and the third peak with a flux of  $5 \times 10^9$  is observed in the range of 4.3 MeV to 5.3 MeV. Another peak at the energy of 3.4 MeV can also be seen at  $70^\circ$ . **Figure 4.15b** presents the proton energy distribution with a worse contrast. This time the complex structures appear at  $30^\circ$  up to 5 MeV of energy.

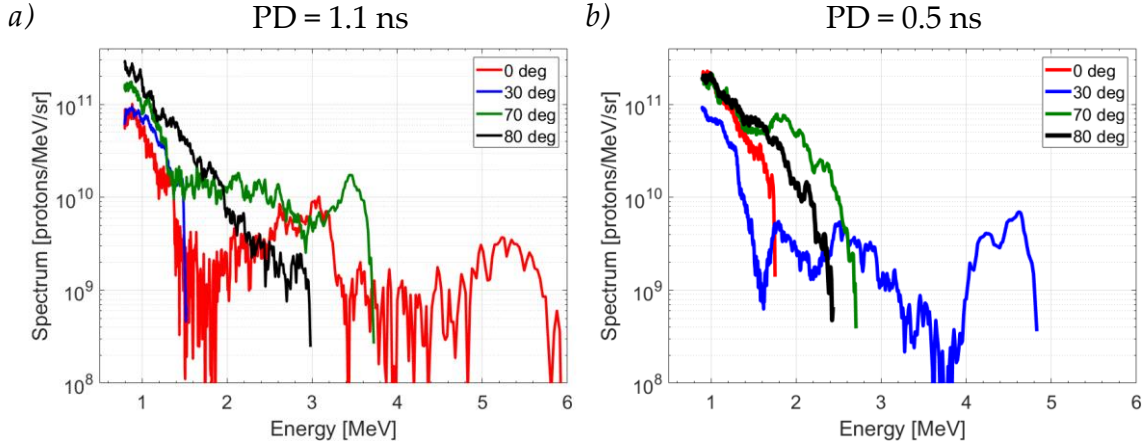


**Figure 4.15** Proton energy spectra at  $0^\circ$  (red),  $30^\circ$  (blue),  $70^\circ$  (green) and  $80^\circ$  (black) obtained with the laser focused at the rising slope of the jet density profile and the ASE level was reduced at the minimum achievable.

These results are discussed in the following section, 4.3.3, and compared with hydrodynamics and PIC simulations.

### 4.3.3. Hydrodynamic and PIC simulations

PIC simulations with the PICLS code are used for interpretation of the measured proton spectra. The PICO2000 laser parameters at normal incidence and  $s$ -polarization are utilized as inputs (Section 3.1.1). The temporal and spatial laser intensity profiles are described by truncated Gaussian functions. The laser temporal pulse is truncated at 2 ps. The pulse is injected at the left side of the simulation box ( $600 \times 160 \mu\text{m}^2$ ) at a time  $t = 0$ . Assuming that the high-intensity laser pulse fully ionizes the gas; the target is described as a  $380 \mu\text{m}$  length plasma of electrons and protons. The mesh size is 80 nm and 15 particles of each species are used in each cell. Physical processes are simulated during 3.6 ps with a time step of 0.267 fs. Absorbing boundary conditions for the fields and the particles are applied.

The plasma density profile in the PIC simulations accounts for the interaction of the laser ASE with the initial gas density profile. In the experiment, it was not possible to measure the pre-plasma created by the laser ASE so the pre-plasma properties have been modeled with the 3D hydrodynamic code FLASH.

In these simulations performed by X. Ribeyre at CELIA, the gas jet is contained in a cylinder of  $200 \mu\text{m}$  diameter centered on the maximum of its radial density profile. The

dimensions of the simulation box are  $560 \times 120 \times 120 \mu\text{m}^3$  and the center of the cylinder is at  $x' = 290 \mu\text{m}$  from the laser arrival side. The prepulse radial distribution is the same as the main pulse one with the maximum intensity reduced by a factor of  $10^6$  (corresponding to the cut of PD  $\simeq 1$  ns on the *Pockels* cell timing).

For example, **Figure 4.16** shows the initial Gaussian density profile of the gas jet (dashed line) and the calculated density profile (solid line) in the laser propagation direction 240 ps after the start of the simulation, which is of the order of the ASE duration in the experiment. The left part of the initial density profile is dramatically modified and a shock is formed with a peak of approximately twice the original density. The exact location of the peak and its magnitude depends on the ASE duration which has not been precisely measured in this experiment. The consequences of a different density profile are discussed at the end of **Section 4.3.3.4**. A low-density plasma remains in the left part of the density profile.

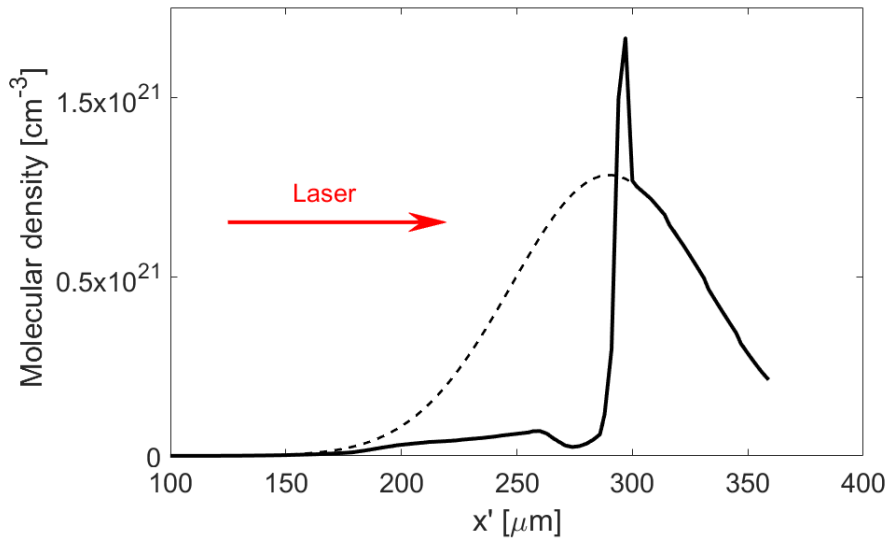


**Figure 4.16** Dashed line: initial density profile of the gas jet based on measurements. Solid line: density profile calculated with the FLASH code taking into account the laser ASE and used as input in the PIC simulations.

In **Figure 4.17**, a 2D slice of the 3D electron density calculated with the code FLASH at  $t = 240$  ps is represented. It shows that the laser penetrates up to the critical density and produces a density channel in the gas jet. It is worth noting that the density on the  $y$ -axis is constant over the focal spot diameter of  $12 \mu\text{m}$ , therefore a constant  $y$  density is introduced in the PIC simulations.

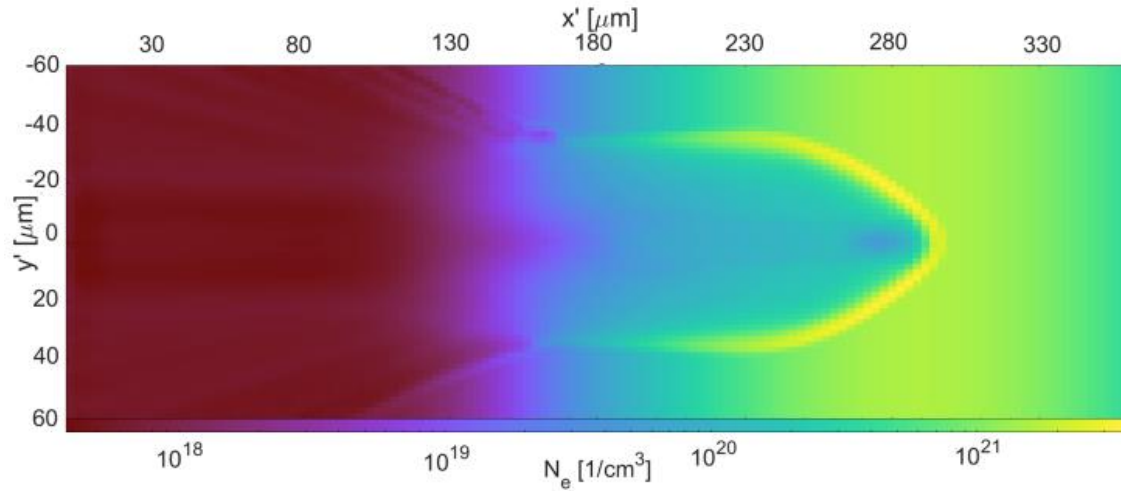


**Figure 4.17** 2D slice of the 3D electron density in the FLASH simulation at  $t = 240$  ps, the time of the main pulse arrival.

The plasma density profile used as input in the PIC simulations is shown in **Figure 4.18(1)**. To simplify the calculations, the plasma density on the  $x$ -axis is assumed to be constant ( $\sim 10^{19} \text{ cm}^{-3}$ ) for  $x < 185 \mu\text{m}$  and increases to the maximum molecular density value of  $\sim 1.7 \times 10^{21} \text{ cm}^{-3}$  over a distance of  $5 \mu\text{m}$ , ( $x = 190 \mu\text{m}$  in the PIC simulation corresponds to  $x' = 297 \mu\text{m}$  in FLASH simulations since the left edge of the plasma was defined as  $x = 0$  in the PIC simulations). For  $x > 200 \mu\text{m}$  the initial Gaussian profile has been used without any modification. Sharp plasma borders generate artifacts in the PIC simulation. Since real gas edges are not sharp, a slope of 15% of the plasma length was used at each border of the plasma in order to minimize this effect. Particles accelerated in these parts are not considered in the analysis. The initial plasma temperature is set to zero.

The PIC simulation results are presented in **Figure 4.18** for particle energy density at four consecutive instants and are discussed in detail in the following sections:

$t = 1$  ps, the laser penetrates to the density  $\sim 10^{19} \text{ cm}^{-3}$  (**Figure 4.18a**).

$t = 1.8$  ps, laser attains the maximum plasma density  $> n_c$  (**Figure 4.18b**).

$t = 2.3$  ps, soon after (**Figure 4.18c**).

$t = 3.6$  ps, at the end of the simulation (**Figure 4.18d**).

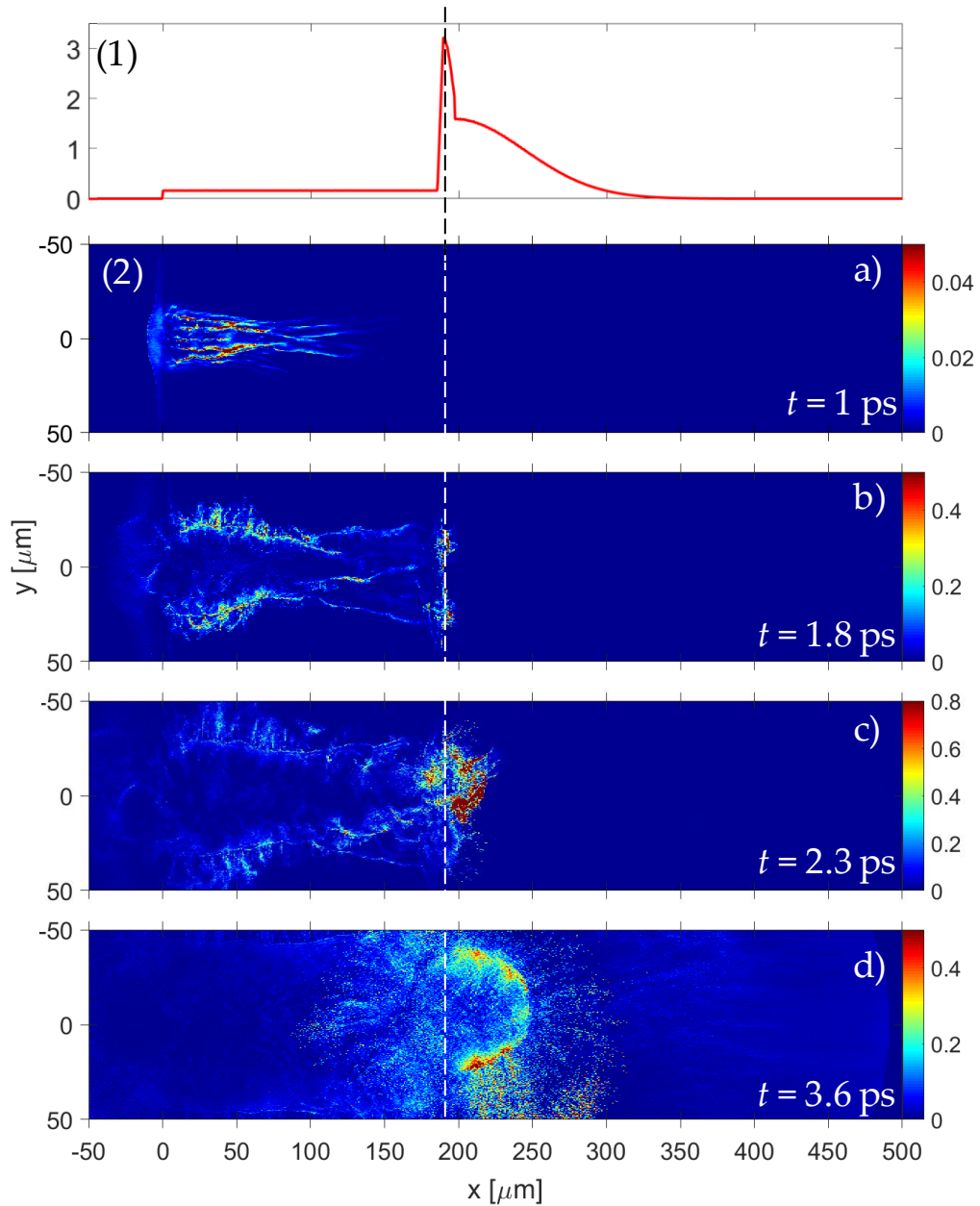


**Figure 4.18** (1) Proton density profile [in  $n_c$  units] at  $t = 0$  ps (2) Evolution of the proton energy density [in relativistic units,  $n_c m_e c^2$ ] in the PIC simulation: a)  $t = 1$  ps b) 1.8 ps c) 2.3 ps d) 3.6 ps

#### 4.3.3.1. Laser interaction with the under-dense plasma

As the laser penetrates in the under-dense plasma, electrons are heated and expelled radially by the laser ponderomotive force. A channel is formed and the protons are accelerated radially by the charge separation electric field. At  $t = 1$  ps, self-focusing and filamentation of the laser pulse are observed. As the laser pulse power is larger than the critical power of self-focusing, multiple filaments are formed (Figure 4.18a).

The proton phase spaces at  $t = 1$  ps are shown in **Figure 4.19**. At first, the protons are accelerated at the plasma edge  $x = 0$ . However, the radial acceleration dominates: the transverse momentum,  $p_y$ , displayed in **Figure 4.19b** is much bigger than the longitudinal one,  $p_x$ , shown in **Figure 4.19a**.

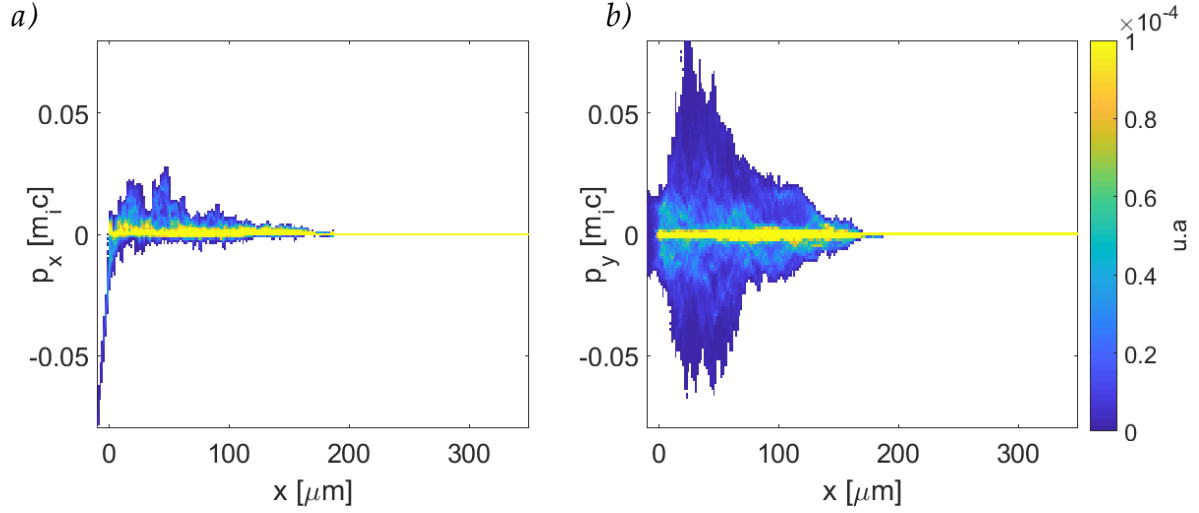


**Figure 4.19** Proton phase space histogram at time  $t = 1$  ps: *a)* longitudinal and *b)* transverse momentum as a function of the longitudinal coordinate.

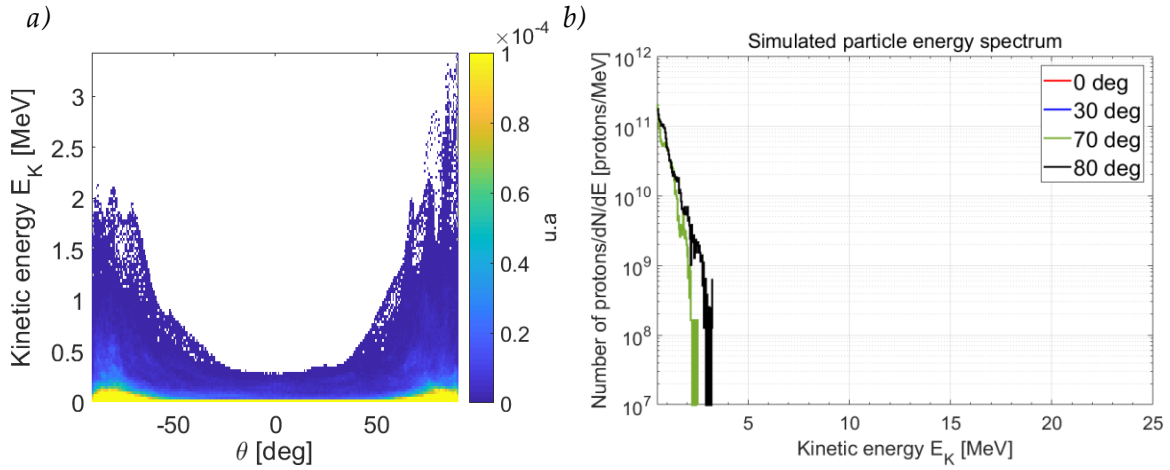


**Figure 4.20** *a)* Angular energy distribution of forward ( $p_x \geq 0$ ) accelerated protons at  $t = 1$  ps. *b)* Particle energy spectrum  $p_x \geq 0$  at  $t = 1$  ps.

The proton angular energy distribution in the forward ( $p_x \geq 0$ ) direction is displayed in **Figure 4.20a**. Most of the protons are accelerated in the transverse direction during the laser filamentation in the under-dense plasma. This particular feature of gas-jet experiments has been reported even in the case of helium acceleration. [Sylla 2013; Krushelnick 1999; Sarkisov 1999; Wei 2004; Willingale 2006]. The particle energy spectra, calculated within  $10^\circ$  wide

angular windows, are presented in **Figure 4.20b** at the angles where TPs were set in the experiment. Only spectra in the transverse directions are observed with energies up to 2 MeV for  $70^\circ$  and 3 MeV for  $80^\circ$ . The number of protons decreases smoothly with the energy.

### 4.3.3.2. Laser interaction with the over-critical plasma

At  $t = 1.8$  ps when the laser pulse reaches the maximum target density, one observes more complex interaction processes. **Figure 4.21a** evidences a collisionless shock formed at  $x = 185 \mu\text{m}$  which accelerates protons both forward and backward (see the red box). This shock is the result of the laser intensity profile steepening: the increased radiation pressure pushes the plasma density forward and the so-called *hole boring* process, presented in **Chapter 2**, takes place (**Figure 4.21b**). The proton acceleration in the shock is essentially longitudinal. However, there is a small component in the transverse direction as shown in **Figure 4.21b**. The contribution at  $x < 185 \mu\text{m}$  from the under-dense plasma, as explained in the last section, is still present.

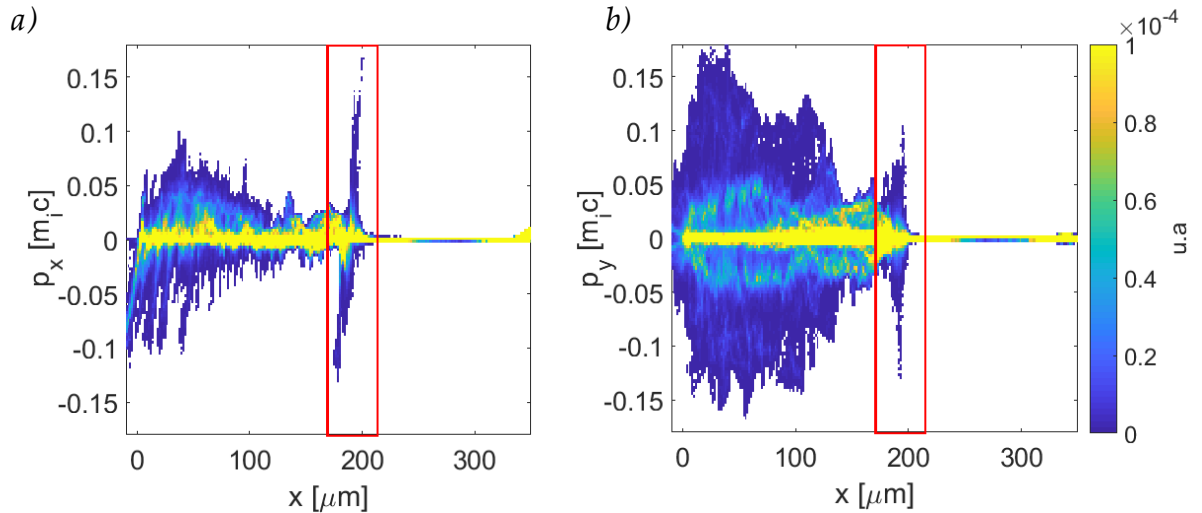


**Figure 4.21** Proton phase space histogram at time  $t = 1.8$  ps: *a*) longitudinal and *b*) transverse momentum as a function of the longitudinal coordinate.

The angular energy distribution of protons accelerated in the forward direction is presented in **Figure 4.22a**. Similar to the previous instant shown in **Figure 4.20a**, the majority of protons are accelerated in the transverse direction. However, there is a small fraction of the protons that are accelerated in the longitudinal direction due to the HB process. **Figure 4.22b**

confirms their origin: the angular energy distribution of the protons accelerated in the interval  $x = 185 \mu\text{m}$  and  $x = 210 \mu\text{m}$  presents a forward energetic component as shown in the phase space in the red square in **Figure 4.21**. The particle energy spectrum is as well presented in **Figure 4.22c**. The spectra in the transverse directions contains the majority of protons; however, there is a small contribution in the longitudinal directions that was not observed in **Figure 4.20b**.

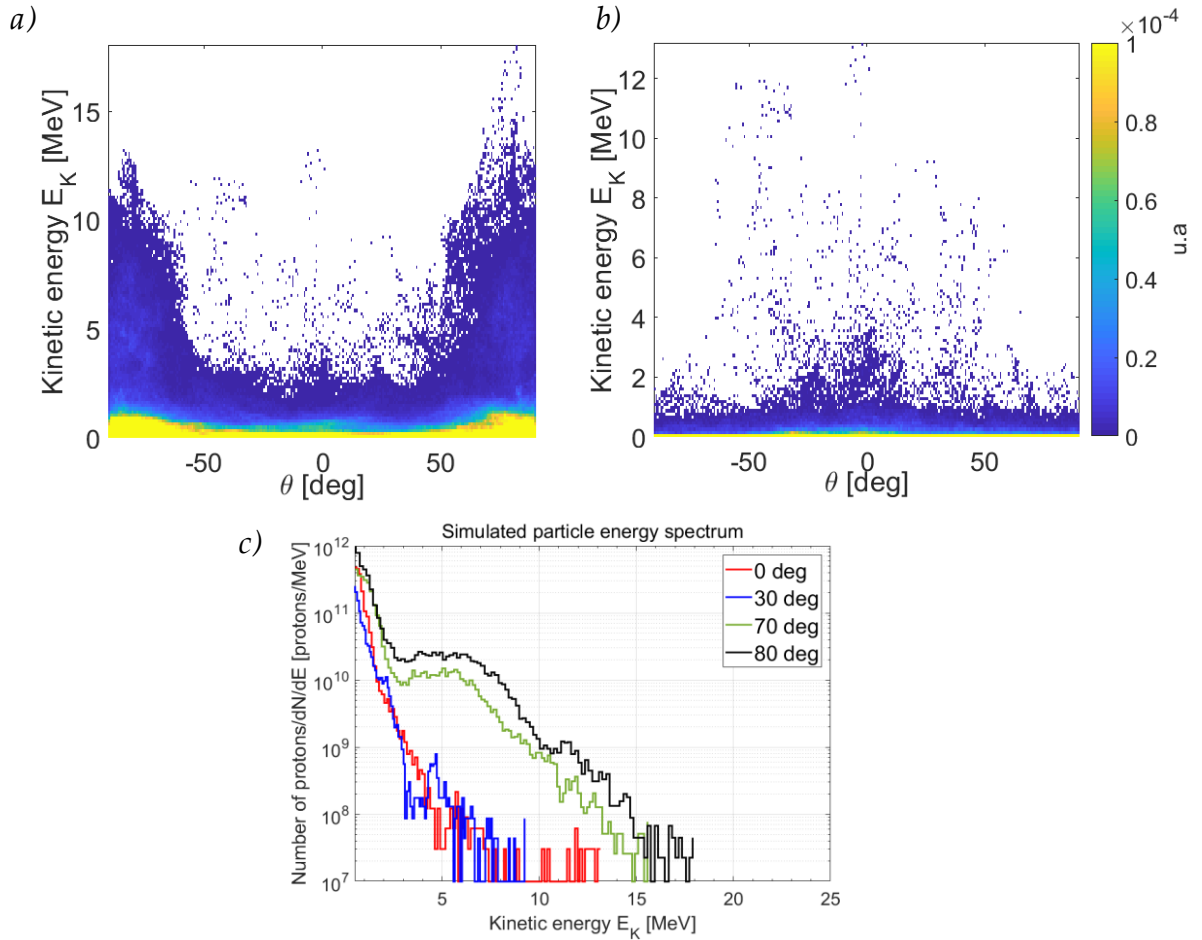


**Figure 4.22** Angular energy distribution of *a)* all forward accelerated protons and *b)* forward protons accelerated between  $x = 185 \mu\text{m}$  and  $x = 210 \mu\text{m}$  at  $t = 1.8 \text{ ps}$ . *c)* Particle energy spectrum.

In the HB process, the details of the shock instability strongly depend on the interaction conditions: the initial plasma temperature and the density profile. **Figure 4.23a** presents the angular energy distribution at  $t = 2.3 \text{ ps}$ . **Figure 4.23b** shows the shock accelerated protons in the direction of  $50^\circ$  with energies up to 25 MeV higher than those accelerated by laser channeling (up to 15 MeV). Furthermore, in **Figure 4.23c**, which represents the spatial distribution of the period-averaged electromagnetic laser energy at  $t = 2.3 \text{ ps}$ , one can see that

most part of the laser is reflected at  $x = 185 \mu\text{m}$ , except for a small part which direction is also bent.

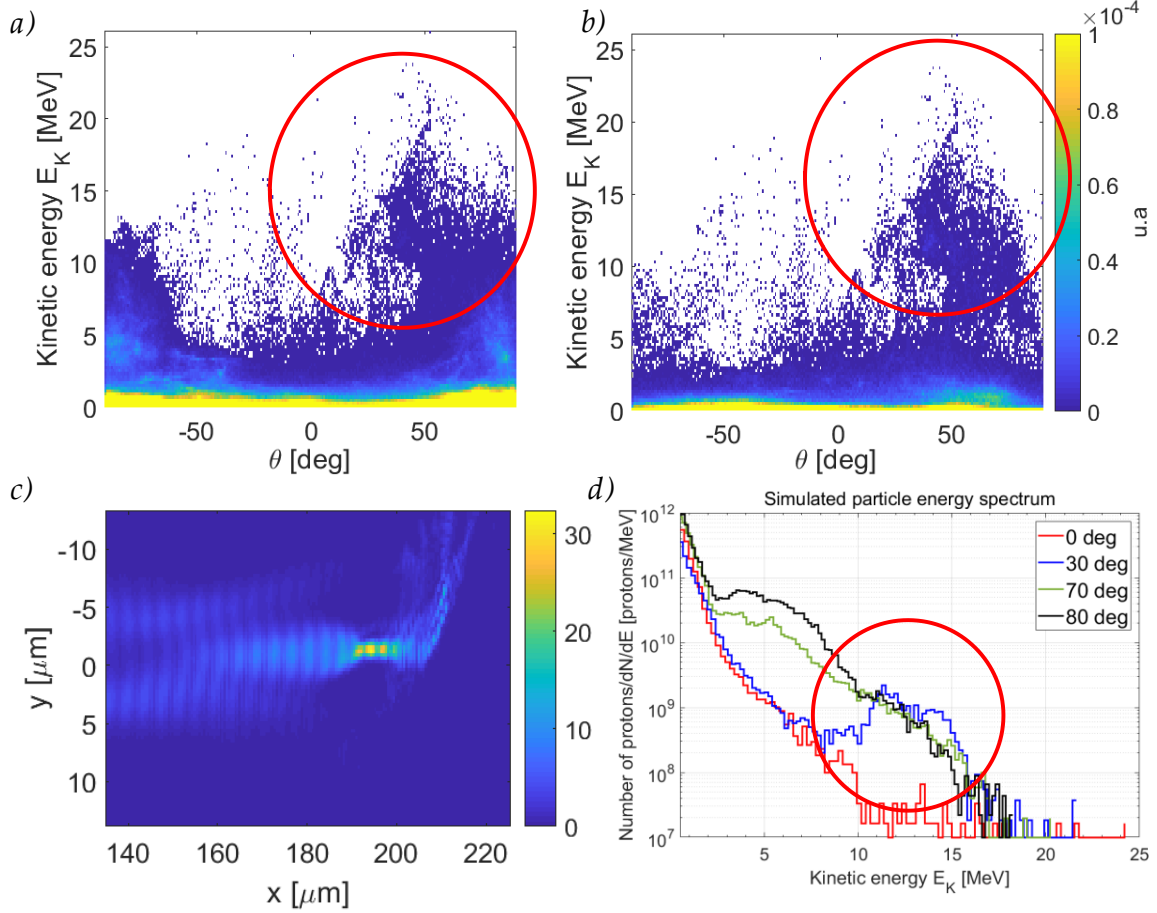


**Figure 4.23** Angular energy distribution of *a)* all forward accelerated protons and *b)* forward shock protons accelerated in the interval  $x = 185 \mu\text{m}$  to  $x = 250 \mu\text{m}$  at  $t = 2.3 \text{ ps}$ . *c)* Period-averaged electromagnetic laser energy  $E_z^2 + E_y^2 + (c B_z)^2$  at  $2.3 \text{ ps}$ . *d)* Particle energy spectrum at the same simulation time.

**Figure 4.23d** shows the spectra at  $t = 2.3 \text{ ps}$ . The proton contribution in the transversal direction is high, with energies up to  $17 \text{ MeV}$ . In the longitudinal direction, the number of protons decreases with energies up to  $10 \text{ MeV}$ . However, at  $30^\circ$  and  $10 \text{ MeV}$ , there is a change of slope in the spectra, creating a plateau structure. This structure is due to the HB process, that accelerated the protons to higher energies. A red circle helps to localize the HB contribution in the spectra and in the angular energy distributions.

### 4.3.3.3. Longer times: laser beam collapse

The laser beam, which has deviated from its initial propagation direction, cannot penetrate further in the plasma. For  $t > 2.5$  ps in the simulation (**Figure 4.18d**, **Figure 4.24a**), we observe the laser beam collapses as previously reported in Sylla [2013] and shown in **Figure 4.24b**.

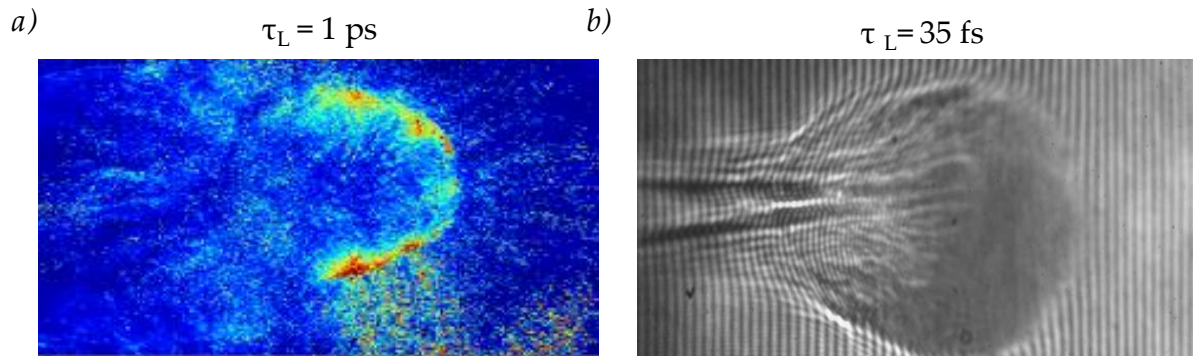


**Figure 4.24** *a)* Laser collapse at 3.6 ps shown in our PIC simulation, with a laser pulse of 1 ps FWHM *b)* Laser collapse from electron density interferogram with a laser pulse of 35 fs FWHM taken from [Sylla 2013].

**Figure 4.25** shows the forward proton energy distribution at  $t = 3.6$  ps. The spectra at all angles are continuously decreasing while at the angles of  $0^\circ$  and  $30^\circ$  there is a second plateau structure at high energy (from 10 MeV to 20 and 25 MeV respectively). The latter is due to the particles accelerated by HB, already analyzed in **Section 4.3.3.2** and observed in **Figure 4.23**.

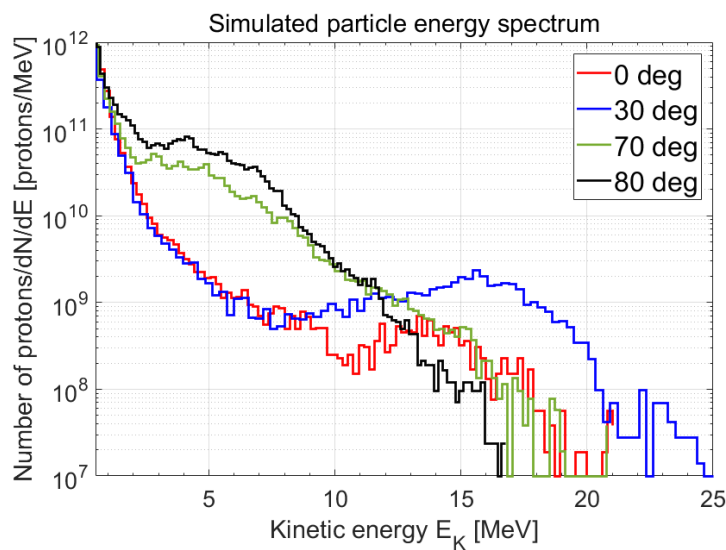


**Figure 4.25** Forward proton energy distributions at  $t = 3.6$  ps from PIC simulations. A  $10^\circ$  wide angular window was taken for each spectrum.

#### 4.3.3.4. Discussion

The goal of these simulations was to interpret the measured proton spectra and understand their origins. **Figure 4.25** allows to compare the simulated energy distributions with the measured ones (**Section 4.3.2**). However, it is worth noting that the maximum energies and higher particle fluxes are found at  $50^\circ$  in the simulation (**Figure 4.23**).

Isotropic acceleration with an average flux of  $10^{11}$  protons/MeV/sr in the energy range up to 1.5 MeV, observed in the experiment, is well reproduced in the PIC simulation. The energy range is higher than in the experiment, which can be explained by the fact that proton energies can be overestimated in 2D simulations, as explained in **Section 2.10**. This broad angle acceleration is present because the laser interacts first with a smooth plasma density profile. Its maximum energy depends on the length of the laser path before the collapse.

We also succeeded to identify the collisionless shock produced in the HB process as the origin of the plateau in the proton energy distribution at near forward directions. The energy range of the plateau and direction of the proton propagation depend on the initial conditions: the characteristics of the laser pulse and the ASE level. It is observed that the initial shock direction is the longitudinal one. However, the deviation of the laser beam affects the angular distribution of the energy plateau at longer times. In particular, it is influenced by the laser self-focusing in the under-dense plasma. The subsequent filaments of the laser beam interact separately with the steepest part of the density profile producing their deflection. In the experiment, the laser interacts with the gas before  $x = 0$  due to the smooth border of the gas profile. This means that the laser may not, in fact, focus at the simulated focal point and the curvature of its trajectory can be different from the simulated one. It is highly probable that the laser beam bends to higher angles inducing a plateau structure in the transverse direction as seen in the experiment. Concerning the ASE level, the worst contrast may generate a less steep density slope at  $x = 185 \mu\text{m}$ , leading to smaller plateau structures.

A striking feature of the experimental energy spectra is the peaked structures. They are measured at different angles depending on the laser shot. In the simulation spectrum shown in **Figure 4.26**, a high energy particle bunch separated from the principal structure is also

observed at 12 MeV in the  $22^\circ$  direction. These types of features are highly dependent on the initial parameters of the simulation and in this case, are not predicted at the angles where the parabolas were placed in the experiment.

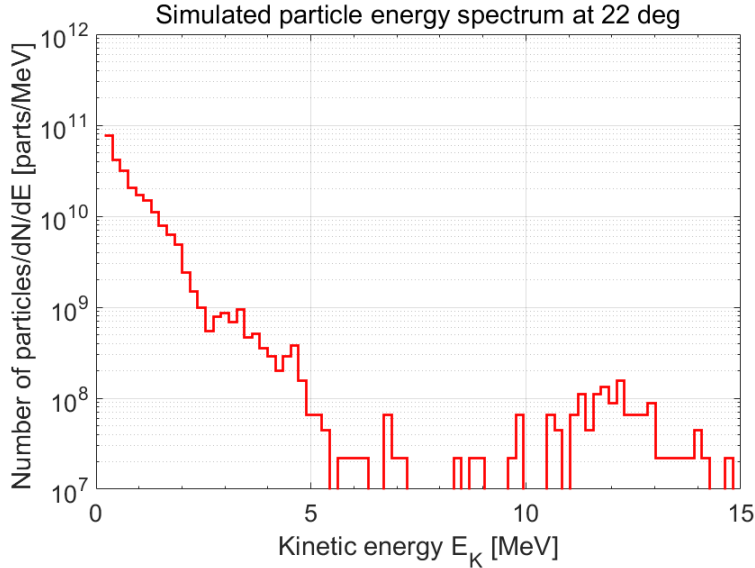


**Figure 4.26** Forward proton energy distribution at  $t = 3.6$  ps from PIC simulations from  $21^\circ$  to  $23^\circ$ .

We can compare as well the measured results with the RPA-HB theory presented in **Chapter 2. Equation (2.17)** allows to calculate the maximum energy per nucleon in the laboratory frame in a planar geometry. If we use the maximum molecular density in the density profile obtained by FLASH,  $1.7 \times 10^{21} \text{cm}^{-3}$  and the PICO2000 laser pulse intensity,  $5 \times 10^{19} \text{W/cm}^2$ , we obtain  $E_{\text{max}} \approx 6$  MeV. Even if this is a rough calculation and the experiment is much more complicated, we find a similar value for the maximum energy.

The simulations were running during  $\sim 3$  ps, and we know that the CSA mechanism could play a role after longer times due to the laser piston perturbation. To do a rough estimation, we calculate the HB velocity in our case:  $v_{HB} = 1.7 \times 10^7 \text{m/s}$  which means that the Mach number is  $M = 0.06$ . We confirm that this velocity is too small to produce the CSA mechanism after the laser interaction and therefore the PIC simulations do not need to be prolonged in time.

## 4.4. Results on helium acceleration

Protons and helium ions are accelerated using *asymmetrical nozzles* at 200  $\mu\text{m}$  from the nozzle exit ( $z$ -axis). For every shot and at each angle, the spectra of protons,  $\text{He}^{1+}$  and  $\text{He}^{2+}$  are analyzed. The high-intensity laser fully ionizes both gases during the interaction. Charge-exchange/recombination of He ions in the gas jet is responsible for the  $\text{He}^{1+}$  spectra observed [Wei 2004]. In all shots, similar ion spectra are observed. **Figure 4.27** displays typical ones obtained with an *asymmetrical nozzle*.

**Figure 4.27a** shows  $\text{He}^{1+}$  spectra. The distributions are very similar at all angles but at  $30^\circ$ , reaching maximal energy of 3-4 MeV. The monotonic shapes of the distributions change above 2 MeV. At  $0^\circ$ , up to  $10^{12}$  ions/MeV/sr are collimated in a beam with a divergence angle smaller than  $30^\circ$ , while at  $90^\circ$  the divergence is bigger. **Figure 4.27b** presents  $\text{He}^{2+}$  spectra which display very different behaviors. The maximum ion energy reaches 16 MeV at  $60^\circ$  and  $90^\circ$  and 7.5 MeV at  $0^\circ$ . Up to  $10^{11}$  ions/MeV/sr are detected at  $0^\circ$ , while at  $60^\circ$  and  $90^\circ$  one order of magnitude more is reported. The signal recorded at  $30^\circ$  is too weak to be significant.

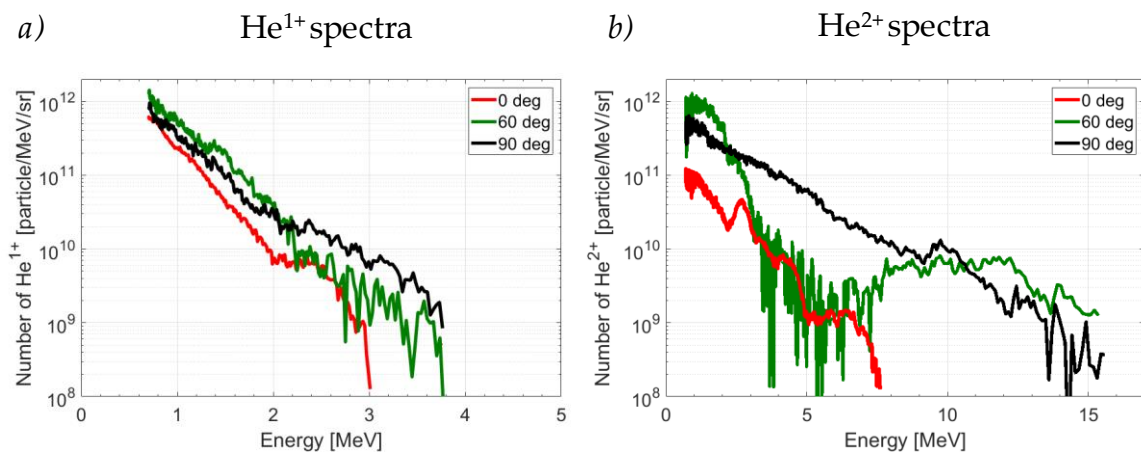


**Figure 4.27** Particle energy spectra at  $0^\circ$  (red),  $30^\circ$  (blue),  $60^\circ$  (green) and  $90^\circ$  (black) obtain with a mixed of helium and hydrogen gas-jet target.

The results of other experiments with gas-jet targets can be summed up:

Krushelnick *et al.* [1999]: They observed a continuous distribution of  $\text{He}^{2+}$  with a superimposed small peaked structure at about 2 MeV. The maximum energy reported is about 3.6 MeV at  $90^\circ$  with respect to the laser axis.

Wei *et al.* [2004]: They reached more than 10 MeV for He<sup>2+</sup> and 3.5 MeV for He<sup>1+</sup> detected at 100° with respect to the laser axis. A plateau structure was reported in the He<sup>2+</sup> spectrum.

Willingale *et al.* [2006]: They observed He<sup>2+</sup> ions at all angles, with up to 40 MeV (10 MeV for He<sup>1+</sup>) at 0°. Transverse ions had 7.8 MeV for He<sup>2+</sup> ions and 3.4 MeV He<sup>1+</sup> ions and no plateau was observed on their spectra.

Sylla *et al.* [2013]: They observed He<sup>+</sup> ions with energies up to 250 keV in the transverse direction.

Unlike Krushelnick *et al.* [1999], Wei *et al.* [2004], and Sylla *et al.* [2013], we observe ions accelerated at 0°. However, the maximum particle energy at 0° is not as high as Willingale *et al.* To our knowledge, no other experiment was done to confirm this high maximum energy.

The comparison is not straight forward because the laser and target parameters are different. Sylla *et al.* laser parameters diverge from PICO2000 laser, so even if supersonic nozzles were used in both experiments, it is difficult to compare the results. On the other hand, Krushelnick *et al.*, Wei *et al.*, and Willingale *et al.* used sub-dense targets ( $n_e \sim 5 \times 10^{19} \text{ cm}^{-3}, 1.4 \times 10^{20} \text{ cm}^{-3}, 4 \times 10^{19} \text{ cm}^{-3}$  respectively). The energy of the laser is higher than PICO2000 for the two last ones.

Krushelnick *et al.*, and Willingale *et al.* used the same target parameters, but the laser energy changed from 50 J to 340 J. That may be why another acceleration mechanism was involved on the second experiment which accelerated ions in the longitudinal direction.

Kruskhenick *et al.* relied the accelerated protons on the *Coulomb explosion* of the high-intensity laser-produced plasma [Burnett and Enright 1990]. The same year, Sarkisov *et al.* [1999] investigated the dynamics of the interaction using interferometry. A stable plasma channel was observed and a kinetic model to describe the plasma channel formation and the ambient gas excitation and ionization related to it was developed.

Willingale *et al.* reported that the balance between transverse and longitudinal acceleration is dependent on plasma density (always working with under-dense plasmas). Above

$n_e = 2 \times 10^{19} \text{ cm}^{-3}$ , they observed clear and reproducible signal of ions in the  $0^\circ$  and  $10^\circ$  spectrometers. It is noticeable that the maximum energy at  $45^\circ$  was less than both the transverse and longitudinal directions. They attributed the transverse acceleration to the *Coulomb explosion* as well. The acceleration in the longitudinal direction is due to the back surface sheath field created by hot electrons leaving the target. D'Humières *et al.* [2010] detailed a description of shock-like accelerating mechanism that could explain the previous results using PIC simulations. They explain that *shock-like mechanism starts as a strong asymmetrical Coulomb explosion and evolves into wave breaking driven by the strong electric field presented*. It depends strongly on the characteristics of the density gradient, it is for intermediate density gradients when the shock-like mechanism starts to show in the decreasing density ramp.

What is relevant is that their spectra were continuous and no plateau structures were found. On the other side, Wei *et al.* [2004] used a denser target and some structures are present on the spectrum. The plateau was interpreted as due to electrostatic shocks generated by the laser transverse ponderomotive force. They varied the density of their targets and observed that this mechanism did not occur in low-density plasma. They reported a strong dependence of the additional radial (transverse) shock acceleration on plasma density. In this thesis, with a near-critical target (denser than their gas targets), more complex structures are observed.

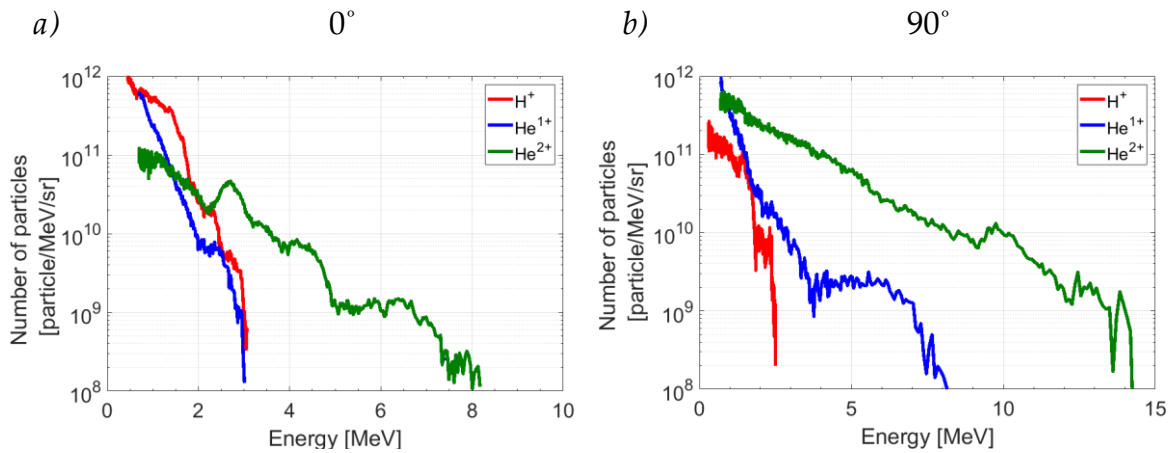


**Figure 4.28** Particle energy spectra of protons (red),  $\text{He}^{1+}$  ions (blue) and  $\text{He}^{2+}$  ions (green) obtained with a mixture of helium and hydrogen gas-jet target on the same shot at a)  $0^\circ$  b)  $90^\circ$ .

Moreover, the mixture of hydrogen and helium allowed to observe and compare the proton and helium ion acceleration in the same shot in our experiment. **Figure 4.28a** displays all ions spectra at  $0^\circ$ .  $\text{He}^{2+}$  ions reach the highest energy, up to 8 MeV (2 MeV per nucleon),  $\text{He}^{1+}$  ions and protons up to 3 MeV. As reported by Wei *et al.*, one may conjecture that the weaker signal below 3 MeV in the  $\text{He}^{2+}$  ion spectrum is due to the recombination into  $\text{He}^{1+}$  ions which is more probable for low energy ions ( $\sigma \sim 1/E^3$ ). On the  $\text{He}^{2+}$  ion distribution, a peaked structure is visible starting from 2.5 MeV.

**Figure 4.28b** displays all ion spectra at  $90^\circ$ .  $\text{He}^{2+}$  ions reach the highest energy, 14 MeV (4 MeV per nucleon).  $\text{He}^{1+}$  ions reach 8 MeV and protons 3 MeV. A flat  $\text{He}^{1+}$  ion spectrum is measured between 4 MeV and 7 MeV and a small peak is probably present at 10 MeV in  $\text{He}^{2+}$  ion spectrum.

As it was already observed in 2D PIC simulations in the proton acceleration case, when a high-intensity laser pulse propagates through an under-dense plasma, the relativistic ponderomotive force pushes the electrons away from high to low intensity regions. Ions react slowly due to their larger mass and are accelerated by the electric field induced by the charge separation created by the electrons. Self-focusing of the laser pulse may take place during its propagation until the collapse in a small section due to electron expulsion and the relativistic increase of the electron mass. The refractive index of the plasma increases and focuses the laser pulse. When the laser does not focus strongly, this force compensates the diffraction of the beam and a laser filament is formed. In this case, electrons are pushed away in radial directions. The ponderomotive force will, therefore, distribute the ions perpendicular to the laser beam direction. This behavior was also probed and diagnosed by Sylla *et al.*, [2013] and Sarkisov *et al.*, [1999] in a helium gas jet target. These different acceleration mechanisms are likely at play in our helium and protons experiment. Plateau structures characteristic of acceleration due to laser-driven laminar shock waves and peak structures are observed as well as in [Wei 2004] and in our 2D simulations. The HB mechanism is also probably at play in these experiments.

# Laser-based X-ray and Proton Induced Fluorescence (Laser-XPIF) analysis

---

Particle and radiation sources (generated by lasers, conventional accelerators, or radioisotope sources) are widely employed in many applications as mentioned in **Chapter 1**, more specifically for analytical techniques. Hereinafter, some of these techniques are briefly introduced. Two of them, laser-driven PIXE and XRF were implemented on the EMT-INRS ALLS beamline to analyze different kinds of samples. The results of this study are presented.

## 5.1. Introduction

*Ion beam analysis* (IBA) is a group of modern analytical techniques that characterize the composition of samples and their surface structures with MeV ion beams. These methods are based on the nuclear and atomic interactions of ions and the detection of the induced radiation or characteristic particles. Within this group, we can find the *Particle induced X-ray emission* (PIXE), *Particle induced gamma-ray emission* (PIGE), *Induced ion beam luminescence* (IBIL), *Nuclear reaction analysis* (NRA), *Elastic recoil detection analysis* (ERDA), or *Rutherford back scattering* (RBS) [[Williams 1989](#)].

Other spectroscopy techniques use electron or X-rays instead of ion beams to analyze the samples: e.g., *X-Ray fluorescence* (XRF), *Energy dispersive X-ray spectroscopy* (EDX) based on electron sources, or *X-ray photoelectron spectroscopy* (XPS) [[Verma 2007](#)].

All these techniques, when used wisely, do not cause any damage to the sample. Before describing the techniques used in this work, we recall hereinafter the main processes involved in ion, photon, and electron interactions with matter.

### 5.1.1. Particle-matter interaction

When bombarding a sample, electrons and ions interact with electrons and the nuclei that are present in the sample. The interaction probability is characterized by their cross-sections of all the processes involved,  $\sigma$ , which mainly depends on the particle energy and on the matter atomic number,  $Z$ .

While RBS and ERDA are based on elastic collisions between ions and atoms, NRA and PIGE are based on the interaction between the ion and the nuclei; PIXE method is based on the interaction between ions with the atomic electrons. EDX is based on the interaction of atomic electrons with the sample.

#### 5.1.1.1. Stopping power

Particles transfer their energy to the matter through ionization all along their trajectory. The particle energy loss per unit path length is defined as:

$$S(E) = -dE/dx \quad (5.1)$$

and named as *stopping power*.

The way of electrons and ions deposit their energy is very different, as observed in **Figure 1.2**. E.g., the ion energy deposited increases toward the end of the trajectory and reaches a maximum in the Bragg peak, just before the ion energy drops to zero.

The range of a particle is defined as the distance traveled before a particle loses all its energy. The amount of energy that these particles lose per distance in a sample depends on the projectiles, their velocity, the elements in the sample and the density of the sample material. The Bethe-Bloch formula for the *stopping power* is written as

$$S \propto K \frac{Z_1^2 Z_2}{A_2 \beta^2} \quad (5.2)$$

$$\text{where } K = 4\pi N_A r_e^2 m_e c^2 = 0.307 \text{ MeV g}^{-1} \text{cm}^2$$

Where  $Z_1$  are the atomic number of the projectile,  $Z_2$ ,  $A_2$  are the atomic number and the atomic weight of the sample.  $N_A$  is the Avogadro constant.  $\beta$  is the velocity  $v/c$  and  $r_e = e^2/(4\pi\epsilon_0 m_e c^2) = 2.8 \text{ fm}$  is the classical electron radius.

The Bethe-Block formula needs to be multiplied by the density of the sample for heavy particles.

The process by which charged particles lose their energy in matter is mostly by ionization in which electron vacancies are created in the atoms. The atom will return to its initial state and the arrangement of electrons in the orbitals is accompanied by X-ray photon or by Auger electron emissions. The competition between these two emissions is characterized by the *fluorescence probability*,  $\omega$ .

In the case of electrons, Bremsstrahlung process is also very important due to its light mass. As a consequence, ion trajectories are quasi-straight lines while electrons trajectories are much less well defined.

## 5.1.2. Photon-matter interaction

Photon-matter interaction depends on the photon energy and the matter atomic number of the sample,  $Z$ . The interaction can be with atomic electrons or the nucleus. The most important interaction processes are the photoelectric effect and Rayleigh scattering, the Compton and the pair production.

### 5.1.2.1. X-ray beam attenuation coefficient

As a consequence of these interactions, a photon beam loses its intensity while penetrating through the material. The X-rays attenuation in matter can be described by

$$I = I_0 e^{-\mu/\rho \cdot \rho \cdot x} \tag{5.3}$$

where  $I$  is the beam intensity after attenuation,  $I_0$  is the incident intensity,  $\mu/\rho$  [ $\text{cm}^2/\text{g}$ ] is the mass attenuation coefficient of the sample,  $\rho$  [ $\text{g}/\text{cm}^3$ ] its density and  $x$  [ $\text{cm}$ ] its thickness.

The intensity of the photon beam decreases exponentially while penetrating in the matter. The attenuation coefficient  $\mu$  decreases with increasing photon energy so a low energy X-ray beam is more attenuated than a high energy one in a given sample. Depending on the energy and the sample atomic number, several interaction processes can take place.

### 5.1.2.2. Interaction processes

The three major processes of photon-matter interaction are the photoelectric effect, the Compton scattering and the pair production. A minor process is the Rayleigh scattering.

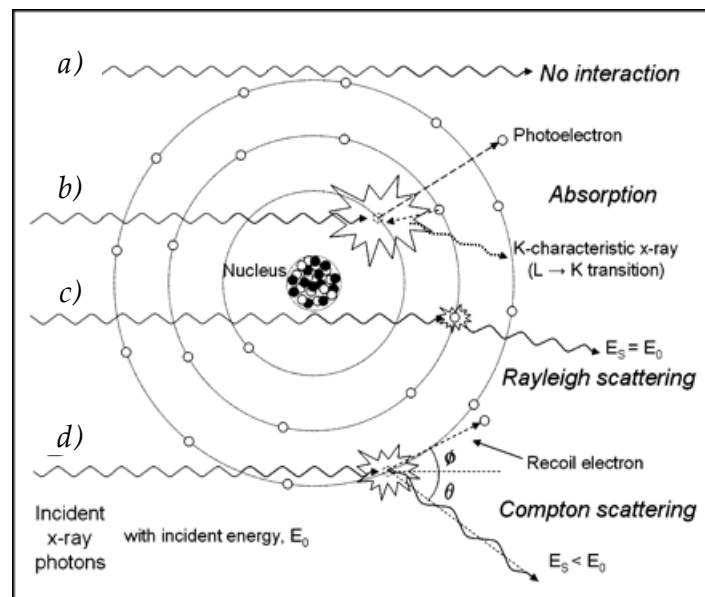


**Figure 5.1** Illustration of three X-ray interactions. *a)* unattenuated beam. *b)* the photoelectric effect, *c)* the Rayleigh scattering and *d)* the Compton effect. The figure is taken from [Seibert and Boone 2005].

The photoelectric effect corresponds to the total absorption of the photon by the atom. The XRF technique is based on this phenomenon. The atom is ionized: an electron (photoelectron) is ejected with a kinetic energy equal to the difference between the photon energy and the electron binding energy (see **Figure 5.1b**).

Compton effect occurs when an inelastic collision takes place between the incident photon and an electron (See **Figure 5.1d**). There is a transfer of momentum and energy to the electron and so a change of the diffused photon wavelength. This diffused photon is emitted in all directions and the energy transferred to the electron will depend on the diffusion angle of the photon. Since the scattered X-ray has less energy, therefore it has a longer wavelength than the incident photon. This is also known as incoherent scattering.

The pair production process occurs only when the energy of the photon is greater than 1.02 MeV. It interacts with the Coulomb field of a nucleus and produces a pair of electron and positron. In this thesis, the photons are not energetic enough to produce this process.

The Rayleigh scattering is an elastic diffusion without any loss of energy. This occurs when the X-ray photon interacts with the atomic electrons and the photon is scattered without transfer in energy to the scattering atom. It is mainly produced in the specular angle. This process is illustrated in **Figure 5.1c**.

For low photon energy, the most dominant effect is the photoelectric one while for high energies is the pair production (see **Figure 5.2**). Rayleigh contributes in the low X-ray energy domain.

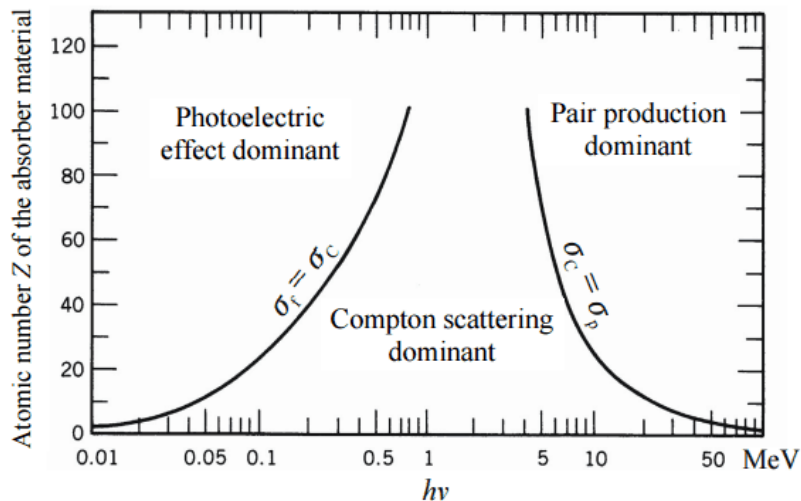


**Figure 5.2** Diagram of the different effects between photons and matter depending on the atomic number of the matter and the energy  $h\nu$  of the incident photon.

## 5.2. PIXE and XRF techniques

Among the analysis techniques presented at the beginning of this chapter that allow the study of an unknown material, we will focus on XRF and PIXE, two well-established, multi-element analysis techniques, which provide the most complete information about the elements of materials.

Both techniques are routinely used in a variety of fields like biology, environmental, medicine, archaeology, and forensic science. They can analyze rocks [Guerra 1998], metals [Lekki 2017], paintings [Neelmeijer 2000], coins [Cruz 2020], atmospheric aerosols [Reyes-

[Herrera 2015] etc. Most works agree that they are complementary, depending on the sample matrix and the atomic number of the studied element [Malmqvist 1986, Cruz 2020]. A detailed study of the advantages and disadvantages of each technique is found in [Verma 2017].

In both cases, the fundamental approach is similar with the difference that the XRF is based on the interaction of high-energy X-ray photons with the inner-shell electrons and while PIXE the interaction with the inner-shell electrons is performed by protons or other charged particles. The X-rays transfer their energy by the photoelectric effect. The protons transfer some of their energy by Coulomb interaction. As the atom rearranges the electrons in the orbital, it emits an X-ray (see **Figure 5.3**) or an Auger electron.

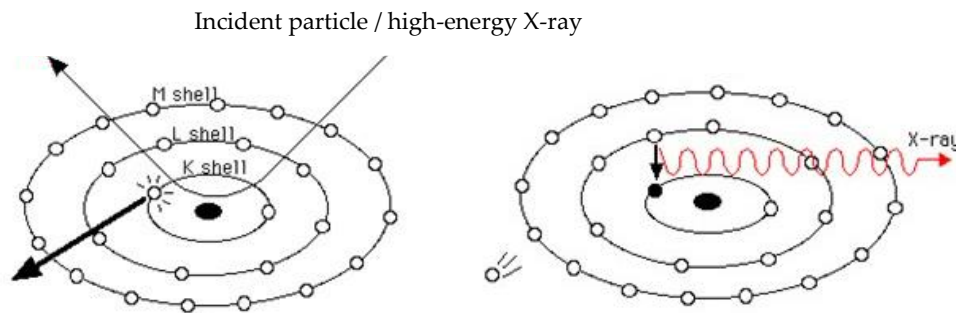


**Figure 5.3** Scheme of the inner-shell atoms when they are perturbed by an incident particle or a high-energy X-ray ( for PIXE and XRF respectively). An electron is ejected and a vacancy is formed. Then an electron from an upper level drops down and the atom emits an X-ray.

The X-ray spectrum is determined by the energy levels of the electrons in the atom. **Figure 5.4** shows a level diagram of an example element. The transitions going to the K-shell are denoted *K* X-rays. If the electrons filling the vacancy come from the L-shell to the K-shell, the transition is denoted  $K_{\alpha}$ , and if they come from the M-shell to the K-shell,  $K_{\beta}$ . The transitions to the L-shell are denoted *L* X-rays and these have many components, especially in heavy elements.

Even if the total X-ray spectrum can be quite complicated, several components appear in single peaks in the experimental spectrum. E.g., the transitions from the  $L_3$  and  $L_2$  shell to the K-shell ( $K_{\alpha_1}$  and  $K_{\alpha_2}$  respectively) cannot usually be distinguished in the experimental spectra. The **Table 5.1** presents some of the X-ray transition energies for elements of interest for this work.

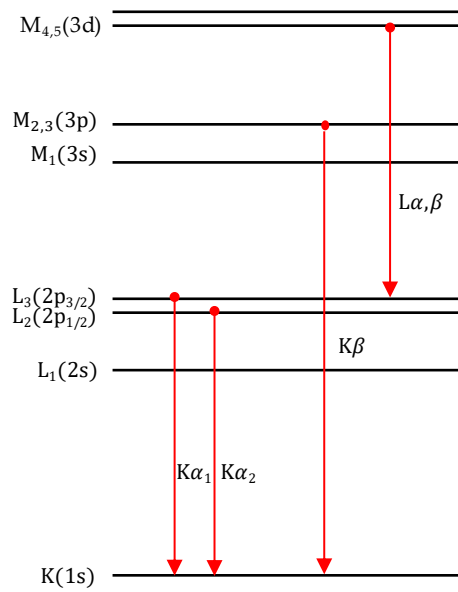


**Figure 5.4** Energy level diagram and the possible transitions from L and M to K shell, from M to L shell and their denotations.

The quantitative analysis with XRF and PIXE techniques generally requires calibration of the experiment with known reference standards (NBS, IAEA, *Micromatter*). These reference standards should have the same thicknesses as the analyzed samples. However, absolute quantitative analytical methods without external standards have been developed for well-characterized sources [Gil 1989, Verma 2007].

In the case of PIXE and thin samples (the energy loss of the particle beam in the target is negligible and the attenuation of the lowest energy photon of interest emerging from the sample is negligible as well) with a monoenergetic proton beam of energy  $E$ , the number of photons produced in a transition  $N_x$  is proportional to the number of incident particles. The following equation applies to all transitions. For example, for the K transition:

$$N_x = N_a N_p \sigma_K^x(E) \quad (5.4)$$

where  $N_a$  is the number of atoms per unit of surface,  $N_p$  the number of incident particles and  $\sigma_K^x(E)$  the X-ray production cross-section for the K-shell:  $\sigma_K^x(E) = \sigma_K^i(E) \omega_K k$  where  $\sigma_K^i$  is the probability to produce a vacancy (hole) in the K-shell,  $\omega_K$  the fluorescence yield and  $k$

the relative X-ray transition probability. The same equation can be used for XRF where the number of incident particles is the intensity of the photon beam.

Element		$K_{\alpha_1}$	$K_{\beta_1}$	$L_{\alpha_1}$	$L_{\beta_1}$
Z	Name	(keV)			
20	Ca	3.69	4.01	0.34	0.35
22	Ti	4.51	4.93	0.45	0.46
24	Cr	5.42	5.95	0.57	0.58
25	Mn	5.90	6.49	0.64	0.65
26	Fe	6.41	7.06	0.71	0.72
28	Ni	7.58	8.27	0.85	0.87
29	Cu	8.15	8.90	0.93	0.95
30	Zn	8.64	9.57	1.01	1.04
41	Nb	16.62	18.63	2.17	2.26
42	Mo	17.48	19.61	2.29	2.39
47	Ag	22.16	24.94	2.98	3.15

**Table 5.1**  $K_{\alpha_1}$  and  $K_{\beta_1}$ ,  $L_{\alpha_1}$  and  $L_{\beta_1}$  energies for some elements in their natural forms.

### 5.2.1. Fluorescence yield and transition probability

**Figure 5.5a** presents the variation of the fluorescence yield for the K-shell,  $\omega_K$ , as a function of the atomic number of the sample, Z. The fluorescence yield is defined as  $\omega_X = \Gamma_X/\Gamma_{tot}$ . It is the ratio between the radiative and total transition probabilities,  $\Gamma$ , for the particular state (in addition the transition probabilities depend on the angular momentum quantum number, the number of electrons available for the transition and the excitation energy). It is close to 1

for heavy elements but it is only of a few percent for the light ones. The relative X-ray transition probability for the transition to K-shell ( $K_\alpha$  vs  $K_\beta$ ),  $k$ , is presented in **Figure 5.5b**. It shows that the probability of the  $K_\alpha$  emission decreases with the atomic number.

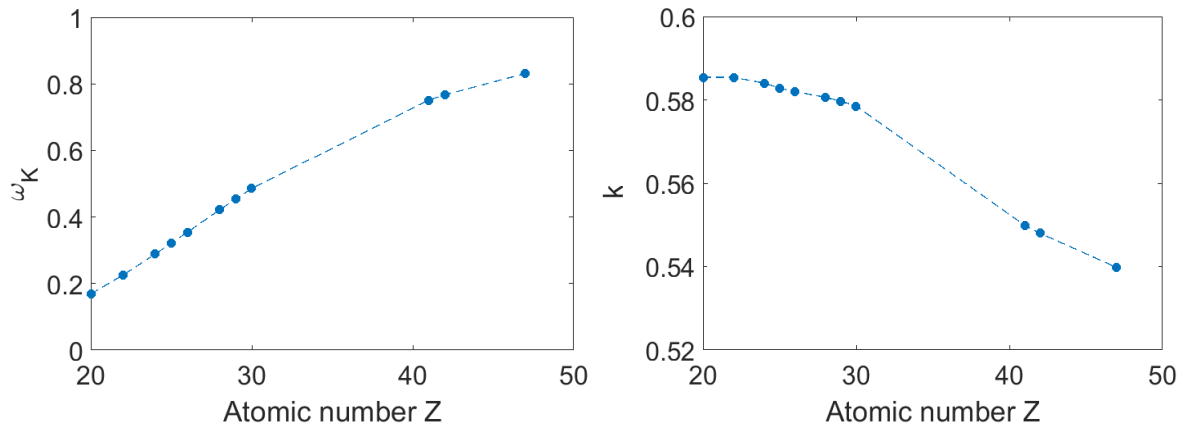


**Figure 5.5.** a) Fluorescence yield for the K-shell as a function of the atomic number b) probability of  $K_\alpha$  transitions a function of the atomic number. Values are taken from PIXE Data Library which is available from *the Radiation Safety Information Computational Center (RSICC) at Oak Ridge National Laboratory as DLC-246*.

### 5.2.2. Fluorescence cross-sections

**Figure 5.6** shows the PIXE X-ray  $K_\alpha$  cross-section for 6 different proton energies as functions of the sample atomic number. The values are taken from the *Radiation safety information computation center (RSICC) data library*. The PIXE cross-section decreases exponentially with  $Z$  for a given proton energy. For one fixed  $Z$ , the PIXE cross-section increases with the proton energy. When the proton velocity reaches the velocity of the electron in its orbit, the cross-section saturates. Consequently, the use of protons with several (< 4 MeV) MeV proton energies is optimal for the PIXE technique. Excitation with alpha particles (or heavier ions) requires higher energies to obtain the same efficiency.

We compare the XRF and PIXE cross-sections as a function of  $Z$  on **Figure 5.7**. The XRF cross-section data is taken from the XRAYLIB 2.3. The XRF cross-sections are given for three different X-ray energies: 8, 10, and 60 keV. They are indicated with squares. The PIXE ones are given for 4 MeV protons and indicated with dots.

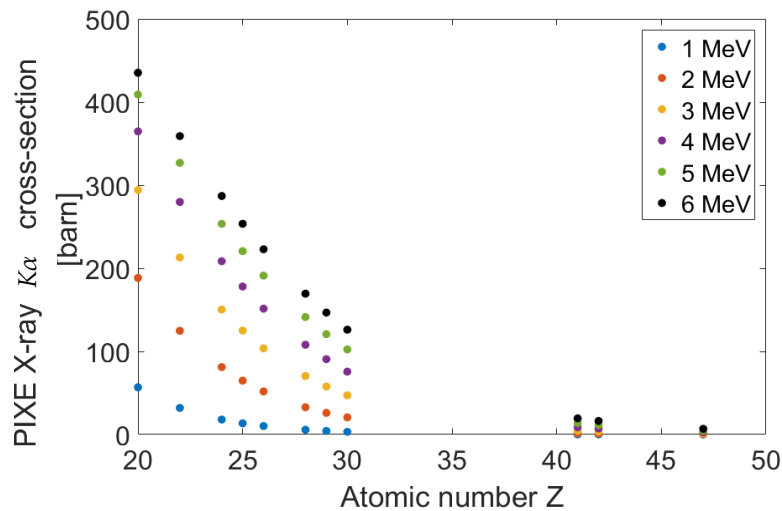


**Figure 5.6** PIXE X-ray  $K_{\alpha}$  cross-sections with different proton energies as function of the sample atomic number,  $Z$ . Values are taken from PIXE Data Library which is available from the Radiation Safety Information Computational Center (RSICC) at Oak Ridge National Laboratory as DLC-246.

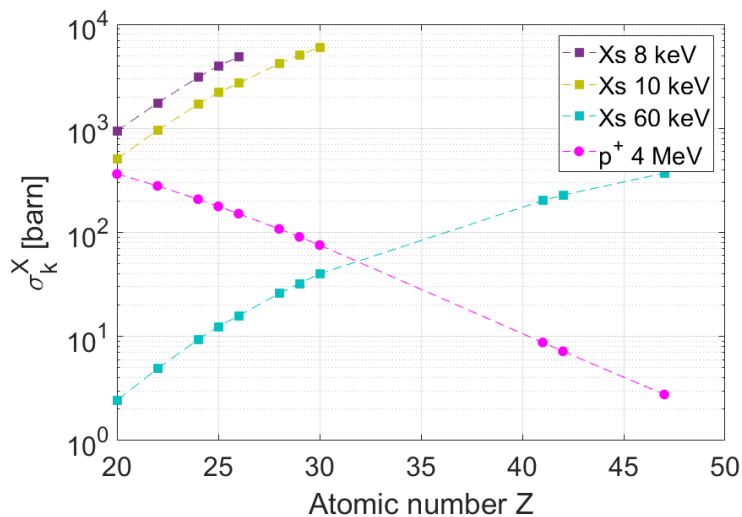


**Figure 5.7.** X-ray  $K_{\alpha}$  cross-sections as a function of  $Z$ . In purple squares, X-ray  $K_{\alpha}$  cross-sections induced by 8 keV X-rays, in green squares by 10 keV X-rays, in blue squares by 60 keV X-rays and in pink bullets by 4 MeV protons. XRF values are taken from XRAYLIB 2.3 data library.

One can observe that the XRF cross-sections increase with the atomic number for a given incident photon energy and decrease with the photon energy for a given atomic number. For *low* energy X-rays (e.g. 8 keV), the cross-sections are 3 orders of magnitude bigger than for *high* energy X-rays (e.g. 60 keV). However, *low* energy X-rays have not enough energy to produce XRF in all elements (the X-ray energy is smaller than the element-binding energy ( $K_B$ )). E.g. 8 keV X-rays can produce XRF in elements with  $Z < 28$ ,  $Z = 28$  being nickel. Since the Ni  $K_B$  is 8.33 keV, which is higher than the 8 keV, no XRF is produced. For 10 keV X-rays, the maximum  $Z$  is 30 (see **Table 5.2** for other elements). For higher atomic numbers ( $> 50$ ) the

XRF cross-section decreases. The PIXE cross-section for a 4 MeV proton is comparable with the XRF cross-section for 60 keV X-rays when  $Z = 32$ .

Element		$K_B$
Z	Name	(keV)
20	Ca	4.04
22	Ti	4.97
24	Cr	5.99
25	Mn	6.54
26	Fe	7.11
28	Ni	8.33
29	Cu	8.98
30	Zn	9.66
41	Nb	18.99
42	Mo	20.00
47	Ag	25.51

**Table 5.2** Electron binding energies, in keV, for some elements in their natural forms.

### 5.2.1. Conventional PIXE and XRF sources and detectors

Most PIXE sources are based on conventional (electrostatic or radio-frequency based) accelerators. The generated sources are monoenergetic particle (usually proton) beams.

Conventional XRF is usually accomplished using radioactive sources, X-ray tube or synchrotron X-ray sources as excitors.  $^{55}\text{Fe}$ ,  $^{109}\text{Cd}$  or  $^{241}\text{Am}$  are used as radioactive sources giving energies of (5.9 and 6.4) keV, (22.16, 24.84 and 8.03) keV and (59.6) keV respectively. The analysis range is from Al to Cr for K X-rays; from Ti to Ru for K X-rays and from Ta to U for L X-rays and Fe to Tm for K X-rays and Ta to U for L X-rays respectively. When using

X-ray tubes the complexity is bigger (compared to radioactive sources) but they are able to offer greater analytical flexibility. Depending on the applied voltage elements up to an atomic number of 87 (Fr) can be analyzed. Lately, synchrotron-based XRF is studied due to the brilliance of the beam, however, it is not always available for all studies.

There are two types of detection methods:

- *Wavelength dispersive X-ray spectroscopy* (WDS) which uses the reflection of X-rays off a dispersive crystal.
- *Energy dispersive X-ray spectroscopy* (EDS) which is based on semiconductor detectors, e.g. Si-Li detectors. Its performance is limited at low energies by the absorption due to the beryllium window in front of the silicon detector.

XRF detection and analysis is usually carried out with both methods. PIXE usually uses the second one. Hereinafter, we discuss the main differences between the PIXE and XRF techniques.

### 5.2.2. Background

When obtaining an X-ray spectrum, X-ray line transitions are observed on a continuous background, which is usually low compared with the characteristic peaks. In PIXE, there are 2 main background sources: *secondary electron Bremsstrahlung* (SEB) and spurious responses in the detector.

1. SEB is emitted when ionized electrons slow down in the sample. It only affects the lower energy part of the spectrum as the energy of the electrons from proton-electron collisions is about 6.5 keV for 3 MeV protons. The intensity of the secondary Bremsstrahlung is proportional to  $Z_{particle}^2$  and that it extends up to photon energies well above  $T_{max} = 4m_e M_{particle} E_{particle} / (m_e + M_{particle})^2$ . The background level in the higher energy part of the spectrum is mainly due to the Compton scattering of X-rays from the decay of excited nuclear states, e.g., 3 MeV protons on Al produce  $\gamma$ -transition of 170, 843 and 1013 keV.

An example of such background is shown in **Figure 5.8**.

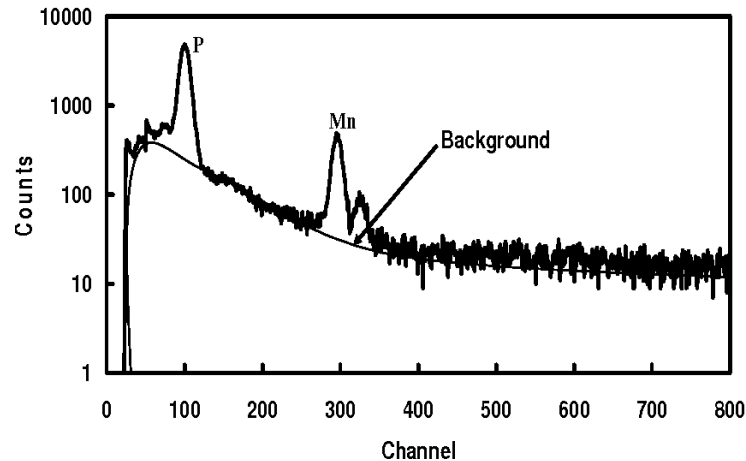


**Figure 5.8** X-ray spectrum of Manganese and Potassium for energy calibration. The figure is taken from [Kabir 2013].

2. The spurious responses are peaks artificially produced by the semiconductor detector and the most important ones are pile-ups, escape peaks and low energy tails. All of them complicate the spectrum analysis, in particular at high fluxes.

Pile-ups happen when two photons are detected simultaneously, giving a non-real peak at the sum of their energies (e.g. two Ca  $K_{\alpha}$  will give a peak at 7.38 keV, which can disturb a real Ni peak ( $K_{\alpha}$  energy = 7.48 keV)).

Escape peaks are caused by the emission of silicon  $K_{\alpha}$  X-rays from the detector near-surface regions. This causes a peak with an energy 1.7 keV below the energy of the primary peak (e.g. the escape peak of Ca will have an energy of  $3.69 - 1.7 = 1.99$  keV which is similar to the  $K_{\alpha}$  energy of P (2.01 keV)).

Low energy tails happen when various carrier trapping processes contribute to a long low energy tail on each peak.

In the conventional XRF technique, the possible background sources are the same as in the PIXE case except for the SEB, which is less important with X-rays. Instead, the background contribution is mostly due to the X-ray spectrum scattered by the sample, especially for unfiltered and broadband excitation spectrum sources. The Bremsstrahlung continuum from X-ray tubes leads to a high background level at high energies. The scattering of the characteristic lines from the sample is also observed.

### 5.2.3. Lower limits of detection

The detection limit depends on multiple factors: the origin of the sources, the elements on the sample (the matrix), its thickness, the installation, the detector, instrumentation related and so on. For example, if the detector is based on the WDS method, a high sensibility to very low atomic number elements is expected.

The most important factor is the cross-section dependencies with the atomic number, which are opposite for PIXE and XRF. For example, the fluorescence cross-section increases with the atomic number in XRF, while it decreases in PIXE. However, this cross-section decreases with the X-ray energy in XRF, and increases with the proton energy in PIXE. XRF can be more efficient (higher fluorescence yield) if the energy of excitation is not far from the absorption edge of the atom to be detected.

To measure the X-ray peak intensity in a standard spectrum, the peak is generally described by a Gaussian distribution. The smallest quantity of an element that can be detected depends on the ratio of the area of the characteristic peak to the background under the peak. This is called *minimum detectable limit* (MDL) and it is usually defined as  $3 \times \sqrt{\text{background within } 6\sigma \text{ of the Gaussian distribution}}$ .

In conventional PIXE, using 1-3 MeV protons, thick targets (e.g. > 20  $\mu\text{m}$  in a Cu sample for 2 MeV protons), the best sensitivities down to 0.1 ppm have been obtained for elements around  $Z = 40$ . For elements with  $Z$  far from 40, the sensitivities decreases to 100 ppm and for  $Z < 20$  the detection limit are larger than 100 ppm. In conventional XRF, for  $Z < 20$  they are usually very much higher (in the range of 10-100 ppm) than the PIXE ones, while for medium elements the detection limit can be one order of magnitude worse [Verma 2007]. The excitation of heavy elements may be easier by XRF than PIXE.

### 5.2.1. Penetration Depths

The penetration depths are different in PIXE and XRF. While XRF analytical depths are relatively large (few millimeters), PIXE analytical depths are smaller (dozens of micrometers). The depth depends on the particles and their energies. It also depends on the studied element.

### 5.2.2. Flexibility

For analysis at a well-defined position in a sample, PIXE spot-size can be easily adjustable to microns. Moreover, one can *easily* change the particle energy and it is possible to change the type of accelerated particle. The variation of energy allows depth-sensitive studies.

In the conventional XRF technique, the compactness of the radioisotope sources allows to manufacture a portable technique and the used X-ray energies can be chosen by selecting different radioisotopes. However, the  $r^{-2}$  dependence of the source intensity makes it very difficult to design an apparatus that allows a high lateral resolution [Neelmeijer 2000].

## 5.3. Laser-based analysis technique

A laser-based XRF and electron-induced fluorescence technique, based on moderate laser intensities ( $10^{16} - 10^{17}$  W/cm<sup>2</sup>) has been proposed recently to explore pigments [Valles Brozas 2016].

Additionally, laser-based proton sources, requiring lasers with an intensity  $I > 10^{18}$  W/cm<sup>2</sup>, have been used to investigate a laser-based PIXE diagnostic (laser-PIXE), both experimentally [Barberio 2018] and theoretically [Passoni 2019, Morabito 2019]. However, we cannot forget that in addition to ions, the ultra-intense laser-matter interaction produces photons X-rays. Therefore, it is necessary to evaluate both contributions to the induced fluorescence.

In this Chapter, we show that ultra-intense laser-matter interaction produces a versatile, nondestructive, fast analysis technique that allows, within a single sub-ns shot, to produce either laser-driven PIXE, laser-driven XRF, or both simultaneously. By simply changing the atomic number ( $Z$ ) of the laser interaction target, one can toggle between these techniques from shot to shot, in the same installation, with a delay of seconds (time to move from one target to the other). The dual contribution of both has the potential to improve the retrieval of constituents in materials. Moreover, the cross-comparison of the results obtained with both techniques in the same experimental environment enhances their reliability. In the following, we will name this technique *Laser-based X-ray and proton induced fluorescence* (laser-XPIF). The term *laser* will be omitted hereinafter to simplify the reading.

## 5.4. Experimental setup

The experiment is performed on the ALLS 100 TW laser facility. Using  $p$ -polarized laser pulses incident at an angle of  $20^\circ$  with respect to target-normal, the laser interaction is made at best focus with three different atomic number targets, namely foils of  $3\ \mu\text{m}$  aluminum ( $Z = 13$ ),  $5\ \mu\text{m}$  copper ( $Z = 29$ ) and  $5\ \mu\text{m}$  gold ( $Z = 79$ ) (purity 99.9%, purchased from Goodfellow). **Figure 5.9** and **Figure 5.10** show the experimental setup.

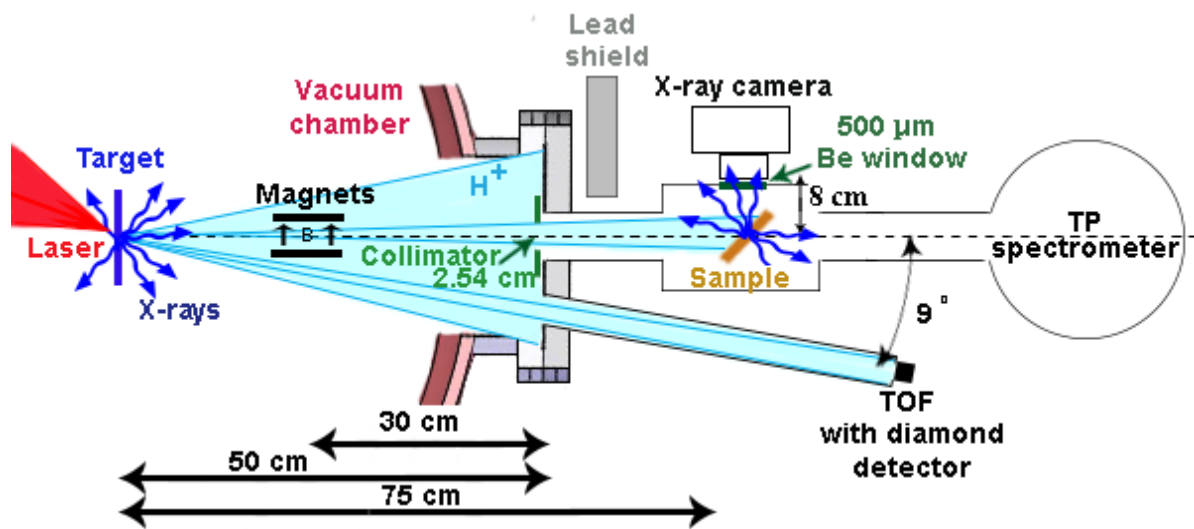


**Figure 5.9** Experimental setup. The interaction of the ALLS 100 TW laser with the solid target (represented in blue, on the left) accelerates several types of ions species (e.g. protons  $\text{H}^+$ ) and generates X-rays. The ions and X-rays propagate under vacuum to the sample (represented in orange, on the right) to be probed and to the ion detectors (the Thomson parabola (TP) and the time of flight (TOF)). The X-rays generated by the sample are analyzed by the X-ray camera.

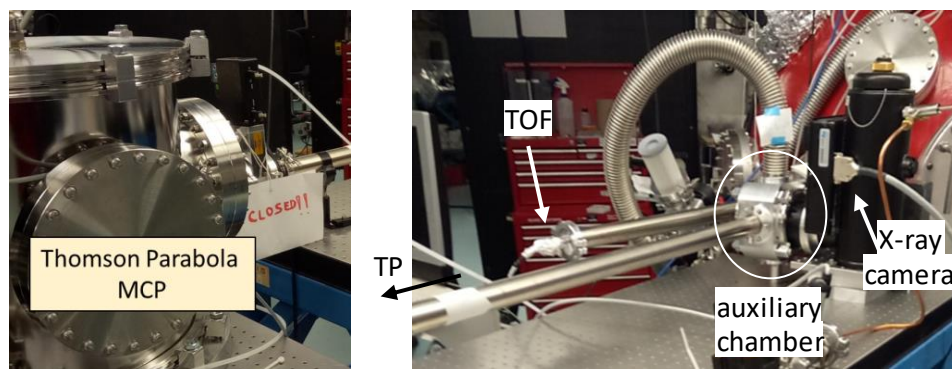


**Figure 5.10.** Picture of the experimental setup during the campaign.

The material sample to be analyzed using laser-based sources is positioned on-axis within a small auxiliary aluminum chamber connected to the main experimental chamber at 75 cm from the laser-matter interaction point. The sample is oriented at  $45^\circ$  with reference to the

proton cone-beam symmetry axis ( $0^\circ$  axis) such as to maximize detection efficiency. In order to deflect the electrons generated during the laser-matter interaction, magnets producing 0.1 T magnetic field at mid-distance are placed within the  $0^\circ$  axis at a distance of 20 cm. The presence of these magnets does not alter the proton energy distribution at  $0^\circ$ . In this setup geometry, the diameter of the proton beam is of 3.8 cm at the center of the auxiliary chamber, where the samples are placed. A collimator of diameter 2.54 cm is placed at a distance of 50 cm from the interaction target at  $0^\circ$  to avoid any interaction between the laser-based sources and the KF40 tube that connects the main chamber with the auxiliary chamber. This interaction could produce an undesired XPIF signal within our detector.

For measuring the X-ray production, an X-ray camera PI-LCX:1300 cooled with liquid nitrogen (1300x1340 pixels of 20  $\mu\text{m}$ ) is placed at a distance of 8 cm from the sample and at  $90^\circ$  with respect to the  $0^\circ$  proton axis. The quantum efficiency of the detector extends above 20 keV, allowing us to retrieve X-ray photon spectra by single-photon counting within a range from about 2.2 keV to 20 keV. The energy resolution of the camera can be calculated by using the Fano-limited resolution formula [Lumb 1987] and yields to about 0.2 keV for 8 keV. We have tested the camera by measuring X-rays of elements such as Ca ( $K_\alpha = 3.69$  keV and  $K_\beta = 4.01$  keV), up to Ag ( $K_\alpha = 22.16$  keV and  $K_\beta = 24.94$  keV).

The X-ray camera is placed outside the main chamber, shielded with lead bricks and far from the laser-interaction point to minimize the effect of strong *electro-magnetic pulses* (EMP) produced during the laser-matter interaction [Consoli 2020]. A 250  $\mu\text{m}$  thickness Be window of diameter 5.08 cm, which allows the transmission of nearly 90% of X-rays with 8 keV energy, is used to keep the camera in vacuum, protect it from visible light and reduce the background signal. An identical window is used to keep the vacuum in the auxiliary chamber.

### 5.4.1. Spectrum reconstruction

A precise measurement of the X-ray spectrum can be done by photon counting [Fourment 2009] as the camera has 1.74 Mega-pixel independent silicon layer detectors. If a *single photon event* (SPE) is detected, a number of counts,  $N_x$ , is obtained. SPE are events in which the charge is deposited only in a single pixel, with no charge spreading over the adjacent pixels.

The SPE events have a sharp energy resolution, as the reading noise comes from only one pixel. The pixel values are read at 100 kHz frequency in order to minimize the readout noise.

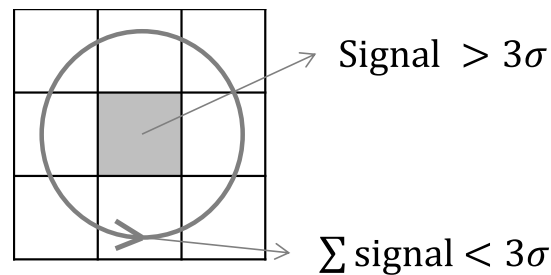


**Figure 5.11** Scheme of the SPE condition in our algorithm. We repeat this process for all the image pixels. The borders are not considered in the algorithm.  $\sigma$  is the standard deviation of the histogram from the acquisition when the laser is off. Only electronic noise is then measured.

The algorithm to select only SPE is the following: one must identify the *central* pixel of a single event, the one with the highest signal in the neighborhood and compare it with the sum over the signal included in the  $3 \times 3$  pixel cell around the central pixel. Due to the electronic noise, a threshold must be set, which is taken as  $3\sigma$ , where  $\sigma$  is the standard deviation of the camera background signal histogram (measured when the laser beam is off). Only the pixels that fulfilled this condition are used to build the spectra. Spectra are histograms of occurrence of the pixel content (channel). This procedure is illustrated in **Figure 5.11**.

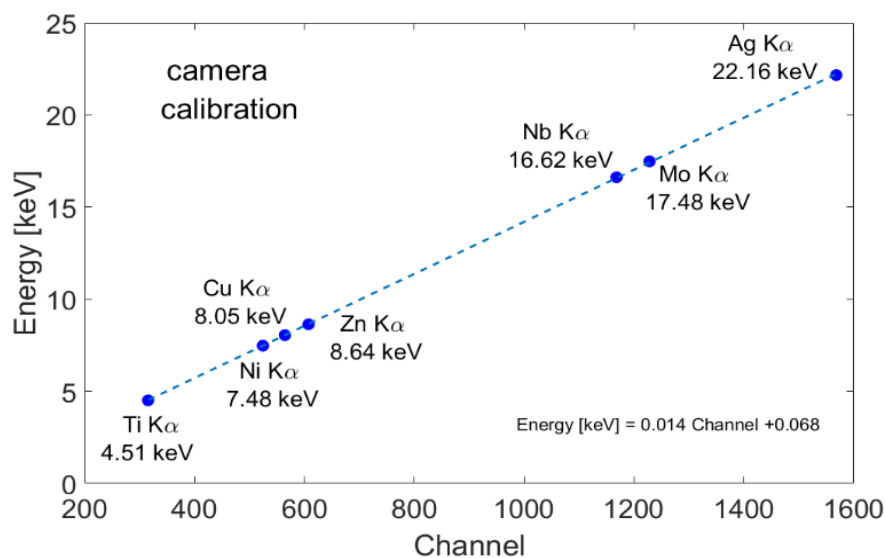


**Figure 5.12** Calibration of the camera with 7 different pure targets. The points are fitted with a linear curve:  $E(\text{Channel}) = \alpha_1 * \text{Channel} + \alpha_2$  where  $\alpha_1 = 0.01413$  with a confidence bound of (0.01403, 0.01423) and  $\alpha_2 = 0.06826$  with a confidence bound of (-0.02602, 0.1625).

The energy calibration channel-energy is done with 7 different pure targets (Ti, Ni, Cu, Zn, Nb, Mo, and Ag) which  $K_\alpha$  peaks are easily identified. **Figure 5.12** shows the linear dependence of the channel with the energy. The points are fitted with a linear curve:  $E(\text{Channel}) = \alpha_1 * \text{Channel} + \alpha_2$  where  $\alpha_1 = 0.01413$  with a confidence bound of (0.01403, 0.01423) and  $\alpha_2 = 0.06826$  with a confidence bound of (-0.02602, 0.1625).

For further analysis of the integrated peak areas, the SPE probability, the two 250  $\mu\text{m}$  thickness Be filters and the camera quantum efficiency are taken into account. **Figure 5.13** shows the evolution of the correction factor as a function of the X-ray energy. The recorded signal is divided by these corrections in order to obtain the emitted signal.

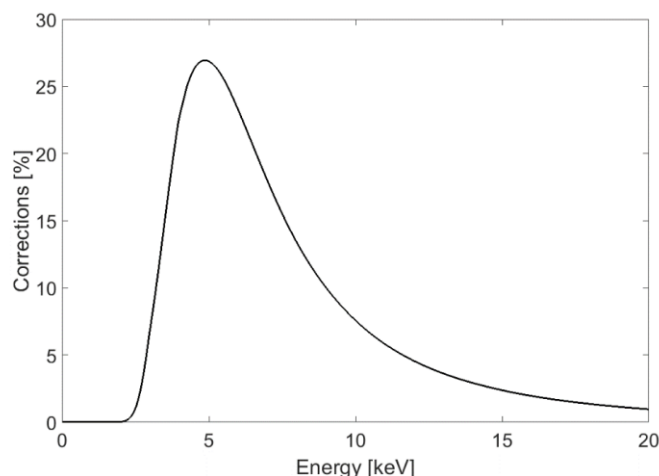


**Figure 5.13** Correction curve as a function of the energy taking into account the SPE probability, the two 250  $\mu\text{m}$  thickness Be windows and the camera quantum efficiency.

### 5.4.2. Particle diagnostics

Different ion diagnostics are used: a TP spectrometer, located at  $0^\circ$  with respect to the ion axis, using a 500  $\mu\text{m}$  pinhole and equipped with a MCP, as well as a TOF delay line equipped with a diamond detector positioned at  $9^\circ$ . This setup allows the sample to be inserted (or not) inside the auxiliary chamber before every shot using gate-valve isolations along with an independent pumping system. This allows to use either the TP or the XPIF setup on the  $0^\circ$  axis in a few minutes pumping time.

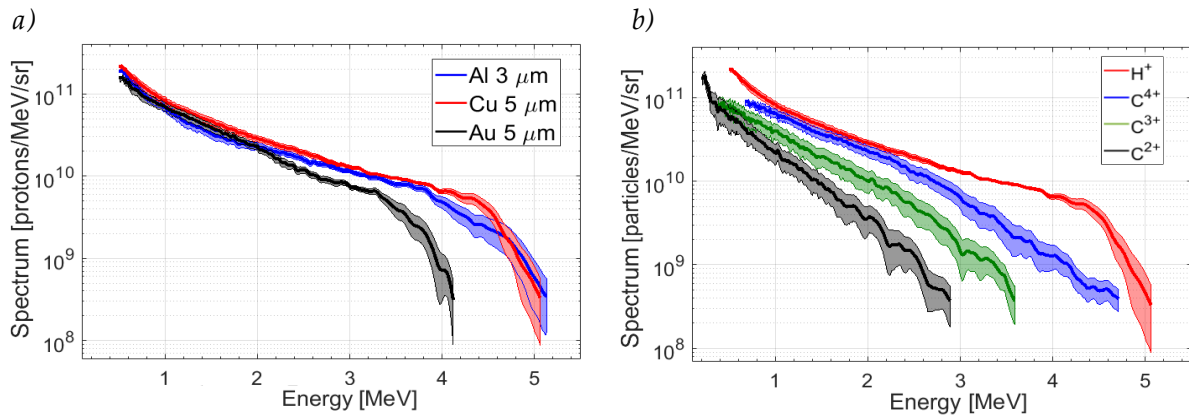


**Figure 5.14** *a)* Proton energy spectra as accelerated by an Al 3  $\mu\text{m}$  (blue), Cu 5  $\mu\text{m}$  (red) and Au 5  $\mu\text{m}$  (black) thickness targets obtained with the TP spectrometer at  $0^\circ$ . *b)* Particle spectra for different laser-accelerated ion species ( $\text{H}^+$  in red,  $\text{C}^{4+}$  in blue,  $\text{C}^{3+}$  in green and  $\text{C}^{2+}$  in black) as obtained by the TP spectrometer. Each spectrum is averaged over 10 shots and the uncertainties are calculated using the standard error of the mean.

Typical averaged ion spectra with their uncertainties, as obtained with the employed targets and measured using the  $0^\circ$  TP spectrometer are displayed in **Figure 5.14a**. About  $2 \times 10^{11}$  protons/sr in a continuous energy distribution up to a maximum proton energy of  $5.0 \pm 0.5$  MeV for Al and Cu targets and  $4.0 \pm 0.5$  MeV for Au targets are observed at  $0^\circ$ . A statistical (shot-to-shot) fluctuation of 15% in the central section of the spectrum around 3 MeV is found, as measured over 10 shots in an identical configuration.

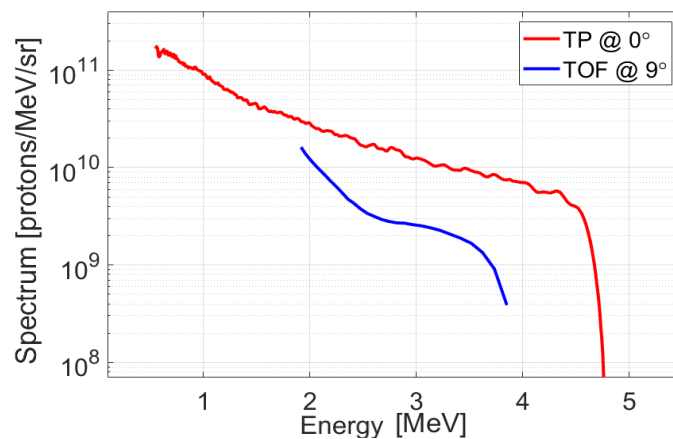


**Figure 5.15** TOF ( $9^\circ$  in blue) and TP ( $0^\circ$  in red) proton spectra as obtained for a Cu typical shot.

We employ simultaneously the TOF and TP when measuring the proton spectra. This configuration allows to cross-calibrate the two diagnostic systems [**Paper VII**] and to relate the proton spectra measured at  $9^\circ$  by the TOF line with the one measured at  $0^\circ$  by the TP spectrometer (see **Figure 5.15**). With this configuration, we can measure the main

characteristics of the proton beam impinging on the target shot-by-shot and in real-time, even if the sample is blocking the TP spectrometer. During the measurement, a 15  $\mu\text{m}$  aluminum filter is placed in front of the diamond detector to cut heavier ion contribution. Due to this filter, the minimum detectable proton energy by the TOF line is 1.8 MeV. Since the TOF line is placed at  $9^\circ$  degrees whereas the TP is on the target normal direction, the number of detected high-energy protons, as well the maximum detected energy, by the TOF is lower but both the spectra obtained by the TOF and TP follows the same trend.

Concerning other main ion species ( $\text{C}^{4+}$ ,  $\text{C}^{3+}$  and  $\text{C}^{2+}$ ) accelerated by TNSA mechanism (see **Figure 5.14b**), we find  $10^{11}$  particles/sr in a continuous distribution with a maximum energy of 4.7 MeV for  $\text{C}^{4+}$ , 3.6 MeV for  $\text{C}^{3+}$  and 2.9 MeV for  $\text{C}^{2+}$ , all of them with a statistical fluctuation of 55%.

To estimate the contribution of these heavy ions compared to protons in the PIXE process, we use the Monte Carlo simulation code called Geant4 [Allison 2016], a reference toolkit for the simulation of the passage of particles through matter (Geant4 simulations are not part of this thesis work). It used the low energy *emlivermore* Physics list [Bruker] to estimate the X-ray spectra resulting from the interaction of the particles (or X-ray beams later) with the samples. This program describes the passage of particles (or photons) through matter. It tracks the photons (or secondary particles) created in the different materials taking into account all physical processes. The X-ray energies deposited in the camera are stored on disk. The inputs of the simulation are the geometry of the detection set-up (which involves the size of the sample, its position relative to the source and to the CCD camera, the description of the camera components and filters) and the energy distribution of the incident particles. GEANT4 particle tracking CUTS are set to 1  $\mu\text{m}$ . The size of the beam on the target sample is defined by a collimator of 2.6 cm diameter placed 50 cm from the laser interaction target.

The results show that the heavy-ion contribution is negligible as the particle-induced X-ray emission signal is more than eight times smaller than the proton-induced one. **Figure 5.16** displays the Geant4 simulated number of counts in the Cr, Fe and Ni  $K_\alpha$  peak when irradiating the stainless steel sample with 3 MeV protons (blue) and 3 MeV carbon ions (red). The obtained values are then scaled with the measured number of 3 MeV protons and

carbons. The results show that the heavy-ion contribution is negligible as its PIXE signal is more than eight times smaller than the proton-induced PIXE signal.

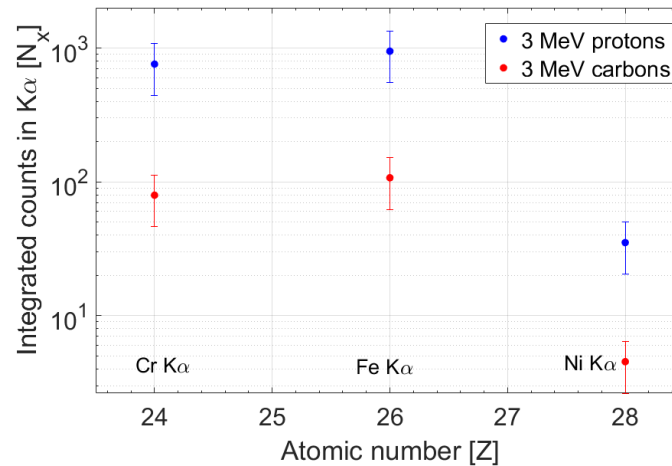


**Figure 5.16** Geant4 simulated number of counts in the Cr, Fe, and Ni  $K_{\alpha}$  peak when irradiating the stainless steel sample with 3 MeV protons (blue) and 3 MeV carbons (red) and scaled with the measured number of 3 MeV protons and carbons in the experiment.

### 5.4.3. X-ray diagnostics

As mentioned before, X-rays are also generated in the laser-matter interaction, and each laser-irradiated target emits its own characteristic atomic spectrum. **Table 5.3** shows the characteristic atomic X-ray energy lines for each of the laser-irradiated targets. The Bremsstrahlung background is present as well.

Element		X-ray energy lines (keV)					
Z		$K_{\alpha}$	$K_{\beta}$	$L_{\alpha}$	$L_{\beta}$	$M_{\alpha}$	$M_{\beta}$
13	Al	1.49	1.56				
29	Cu	8.05	8.90	0.93	0.95		
79	Au	68.81	77.98	9.71	11.44	2.12	2.20

**Table 5.3.** X-ray energy lines for each of the laser-irradiated targets used in the experiment.

Whenever the impinging X-ray energy is higher than the sample element-binding energy,  $B_K$  (**Table 5.2**), XRF can be produced in the sample. The versatility of the XPIF technique is based on this criterium: when we consider only characteristic line emission, given the detection range of ~2-20 keV and the use of Al ( $Z = 13$ ), Cu ( $Z = 29$ ) and Au ( $Z = 79$ )

interaction targets, we can produce XPIF signal with or without XRF contribution. In order to obtain a pure XRF contribution, strong enough magnets would need to be placed in between the laser-interaction target and the studied sample to deviate the laser-accelerated protons from their trajectory.

For low- $Z$  targets, such as Al: X-ray lines ( $K_\alpha = 1.49$  keV and  $K_\beta = 1.56$  keV) are not producing any XRF detectable by our diagnostic since the element with the lowest  $K_\alpha$  energy observable by the camera (Ca) has a binding energy  $B_K = 4.04$  keV ( $\text{Ca } B_K > \text{Al } K_\alpha \ \& \ K_\beta$ ). Bremsstrahlung can be neglected due to its  $Z^2$  dependency. No XRF contribution is expected.

On the other hand, for higher- $Z$  targets such as Cu: the Cu X-rays ( $K_\alpha = 8.05$  keV and  $K_\beta = 8.90$  keV) and Bremsstrahlung can produce inner-shell vacancies in elements up to Ni ( $Z = 28$ ), which has a binding energy of  $B_K = 8.33$  keV. In the case of Ni, the XRF can be only induced by the Cu  $K_\beta$  or the Bremsstrahlung, both energies are above the Ni  $B_K$  one. The Cu  $K_\alpha$  energy is not high enough to generate XRF with Ni element.

In the case of Au, XRF produced by  $L_\alpha$  (9.71 keV) and  $L_\beta$  (11.44 keV) and Bremsstrahlung is expected to contribute to the process. The higher  $L_\alpha$  and  $L_\beta$  energies are able to generate XRF in heavier elements than the Cu  $K_\alpha$  and  $K_\beta$ .

In the experiment, to estimate the amount of atomic X-rays that induce XRF in the samples for the Cu target, we proceed as follows:

- The X ray spectrum is measured by temporarily orienting the X ray camera towards the laser-matter interaction point, for technical constraints at an angle of  $6^\circ$ .
- Rayleigh scattering of Cu  $K_\alpha$  and  $K_\beta$  on pure samples (e.g. Mo, Zn and Ti) is studied using the Geant4 simulations. In the global photon calculation, the relative contributions between the subshell yield probabilities (i.e. between the  $K_\alpha$  and the  $K_\beta$ ) is taken into account. We make the assumption that this relative contribution did not change in the plasma state generated during the laser-target interaction and used the tabulated values [[Handbook 2009](#)]. Geant4 simulation results are scaled to the measured number of photons in order to compare the simulation and experimental results.

**Figure 5.17a** shows the X-ray sample spectra obtained in one single shot for Ti ( $Z = 22$ ), Zn ( $Z = 30$ ) and Mo ( $Z = 42$ ) when irradiated by the laser-based sources produced by a Cu interaction target (details will be discussed later), while **Figure 5.17b** shows the corresponding integrated measured number of counts in the Cu  $K_{\alpha}$  Rayleigh peak obtained with the three material samples (black dots). The simulation results (in red asterisks) match for a number of photons of  $(4.3 \pm 1.1) \times 10^{10}$  photons/sr, which is in reasonable agreement with the measured X-ray spectrum. This allows to verify the X-ray contribution produced during the interaction.

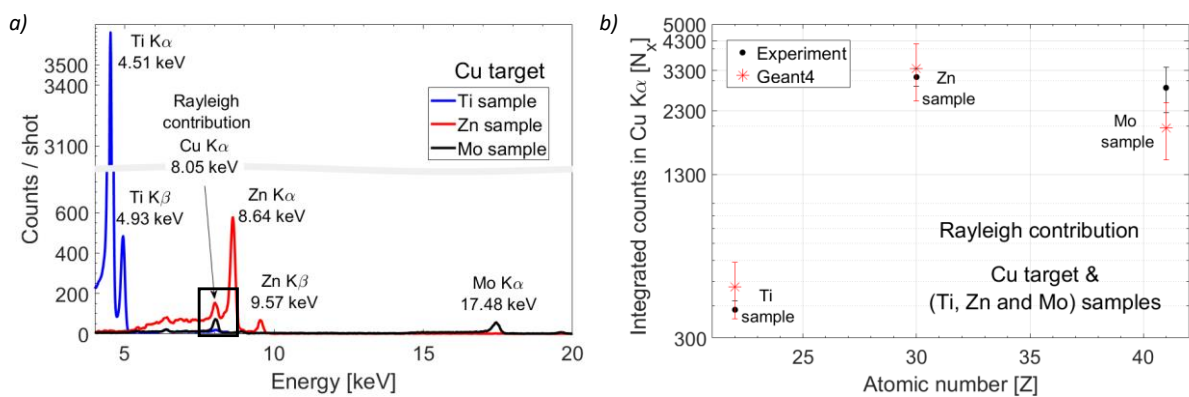


**Figure 5.17** *a)* X-ray spectra as obtained by the interaction of laser-based sources produced by a Cu target and a Ti, Zn and Mo samples. The Rayleigh contribution from the Cu X-rays is visible around 8 keV (see black box). *b)* Integrated number of counts in the Cu  $K_{\alpha}$  Rayleigh peak in Geant4 simulations when 8.05 keV photons are sent on the sample, scaled to  $4.3 \times 10^{10} \pm 1.1 \times 10^{10}$  incident photons/sr.

## 5.5. Results

### 5.5.1. PIXE and XRF contributions: XPIF technique

To study the XPIF technique and the contributions of either only protons or X-rays and protons, we irradiate a stainless steel sample (purchased from *McMaster-Carr*) and change the laser-interaction target from Al to Cu (from low to higher atomic number). The sample size is  $6 \times 5$  cm<sup>2</sup> and it has a thickness of 1.54 mm. It has been previously analyzed using *energy dispersive X-Ray* (EDX) spectroscopy, in conjunction with *scanning electron microscopy* (SEM) (LYRA3 TESCAM). The analysis reveals the following constituents:  $18.22 \pm 2.87$  % Cr,  $64.72 \pm 2.92$  % Fe,  $8.37 \pm 3.11$  % Ni,  $0.12 \pm 3.84$  % Ca (see **Figure 5.18a**).

**Figure 5.18b** shows the X-ray spectra obtained when irradiating in a single shot the same stainless steel sample using the source produced by an Al interaction target. This spectrum is depicting merely PIXE since line emission X-rays produced by the Al interaction target are not producing any detectable XRF and the contribution of the Bremsstrahlung in the Al source is negligible. One can observe the same peaks related to the elements observed by EDX, with the exception of the Ca signal that is not detected in our experiment when we are using an Al target as proton source. With an improvement of the proton spectra (an increase of the proton number and energy), we will be able to enhance the emitted X-ray yield.

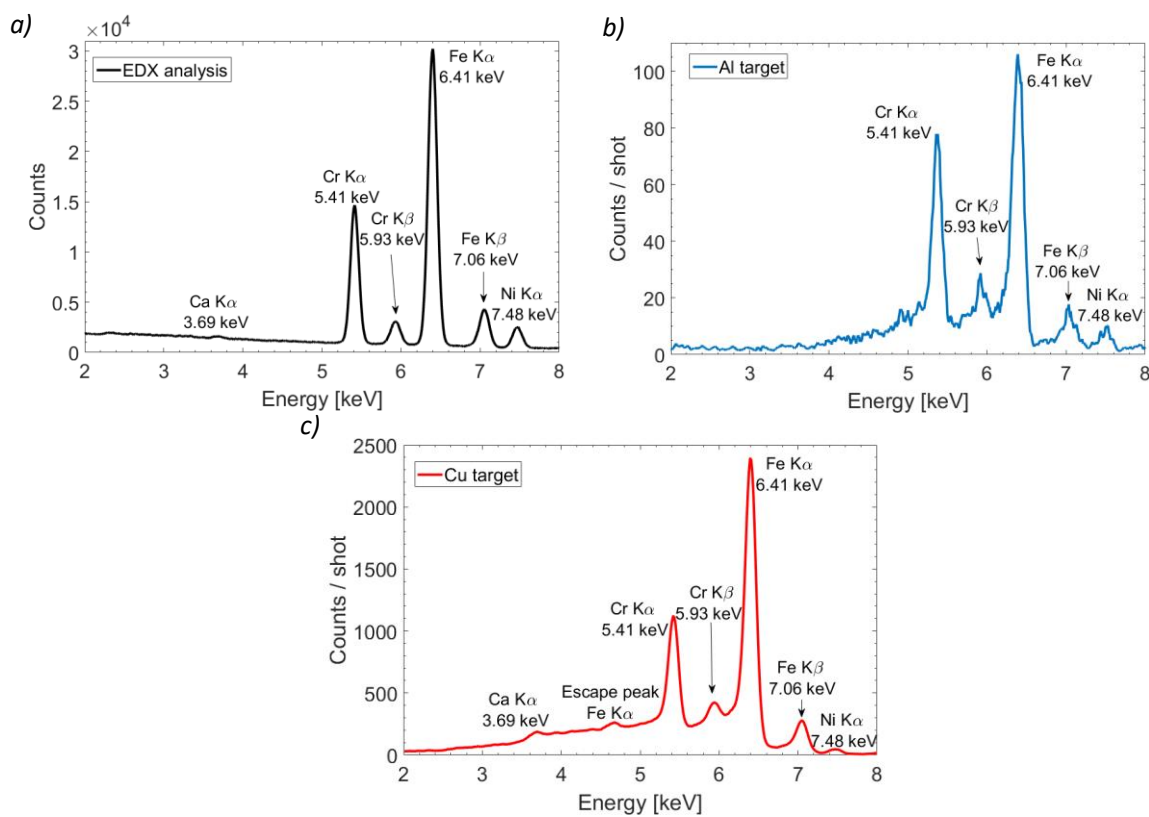


**Figure 5.18** Stainless steel sample analysis: *a*) EDX spectrum; *b*) and *c*) X-ray spectra obtained by a single shot irradiation, using the laser-based sources produced with a low Z (Al, blue) and high Z (Cu, red) target respectively

By simply changing the interaction target with a higher-Z target (a Cu target) there is an increase on the spectral intensity by almost 20 times (see **Figure 5.18c**). This allows revealing the Ca element, previously not detectable. We can also observe an escape peak from the Fe K $\alpha$  at 4.66 keV. This can be solved by increasing the distance from the sample to the camera or placing a suitable absorber in between them to lower the X-ray flux.

Since the protons spectra for an Al and Cu target are almost identical (see **Figure 5.14a**), one can conclude that the increase of the photon yield is solely due to the XRF contribution.

Geant4 simulations are performed in order to confirm the relative XRF and PIXE contributions using for the material sample the same composition as obtained by EDX. The simulation results are scaled using the measured proton spectra and the number of primary atomic X-rays generated in the laser-matter interaction: in the case of Al, only protons are considered and in the case of Cu, protons and X-rays. We consider that the proton spectra impinging the sample ( $1^\circ$  cone) is the same than the one impinging in the TP pinhole ( $0.01^\circ$  cone). **Figure 5.19** compares the integrated measured counts in the  $K_\alpha$  peak of the three major elements present in the sample (Cr, Fe and Ni) when the laser-interaction target is Al (blue dots) and Cu (red dots) to the corresponding Geant4 simulation results (asterisks).

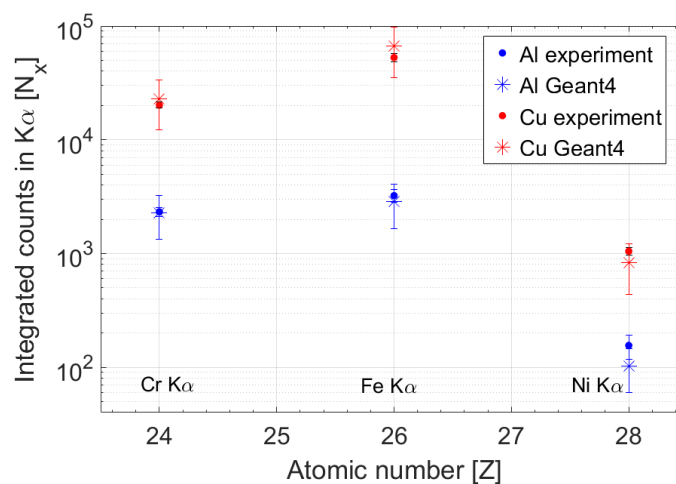


**Figure 5.19** Measured integrated number of counts in the respective Fe, Ni and Zn  $K_\alpha$  peaks (presented in dots) obtained from the spectra depicted in B and C. Geant4 simulation results are presented with asterisks.

One can note a good agreement between the experimental and numerical results, confirming that, depending on the type of laser-interaction target, the contribution of XRF can change. The uncertainties in the measured number of counts are mainly due to the undefined boundaries of the peaks within the spectra. The error bars in the Geant4 values, presented in asterisks, are incorporating the total uncertainty in the proton numbers, including the statistical fluctuations (see **Figure 5.14a**), the absolute calibration uncertainty and the uncertainty related to the kinetic energy indetermination for the TP.

### 5.5.2. Metallic samples

The XPIF technique is studied using Cu laser-interaction target for probing different pure metallic samples, including the pure (99.99%) elements Ti, Fe, Ni, Cu, Zn, Nb, and Mo (materials purchased at Goodfellow). Using a Cu interaction target, when probing elements with  $Z < 28$ , the detected signal is mostly due to XRF, while for heavier elements PIXE is dominant. For all samples, we observe in one single laser shot sufficient X-ray emission to clearly allow for a fingerprint of the material's element. **Figure 5.17a** shows the spectra of pure Ti, Zn, and Mo when the laser-interaction target is Cu.

The detected signal is lower for Mo than for Ti sample mainly for two reasons: firstly, the non-uniform efficiency of the camera for different X-ray photon energies, and secondly, the difference in the PIXE and XRF cross-sections. The same reasoning can be applied for the Ti and Zn signal. In **Figure 5.17a**, the Cu Rayleigh contribution is undoubtedly observed (see the black box), which helps to estimate the number of incident photons, as mentioned above. In our setup and with our sample sizes, a single shot irradiation provides an unambiguous readout spectrum. Several acquisitions of the same sample would have the benefit of decreasing the fluctuations in the photon counting statistics, especially if the sample had a small volume or if the irradiated surface is composed of more materials.

### 5.5.3. Minimum sample size

As next step, we test the minimal sample size that our setup is able to detect in a single shot. We irradiate different Ti pure samples with 38  $\mu\text{m}$  thickness and variable surface area sizes from 150 down to 9  $\text{mm}^2$ . (See **Figure 5.20**).

The choice of Ti is based on the fact that the camera's detection efficiency is optimal for the energy range of its characteristic X-ray emission. We find a linear dependence between the integrated number of counts in the Ti  $K_{\alpha}$  peak and the sample area, counts ranging from about  $5500 \pm 2400$  counts/shot for surfaces of  $150 \pm 8$   $\text{mm}^2$  down to about  $95 \pm 50$  counts/shot for surfaces of  $9 \pm 3$   $\text{mm}^2$ . The minimum detected quantity is defined as the MDL.

It should be noted that the X-ray signal depends on the element's individual interaction cross-sections and on the amount of noise generated in the interaction that could reduce the

signal-to-noise ratio. Moreover, it is necessary to take precautions concerning the Rayleigh scattering and the XPIF background.

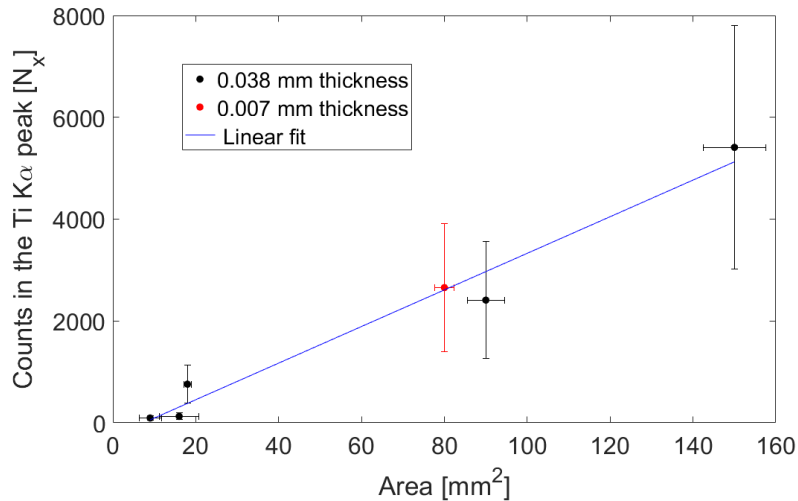


**Figure 5.20** Integrated number of counts in the Ti  $K_{\alpha}$  peak for different sample sizes using the laser-based sources produced by Cu or Au targets.

### 5.5.4. XPIF background

**Figure 5.26** shows the X-ray spectra obtained in one single shot using the laser-based sources produced by a Cu and Au interaction target when no sample is placed in the auxiliary chamber and the incident beams interact with the stainless steel components of the auxiliary chamber (e.g. the chamber windows).

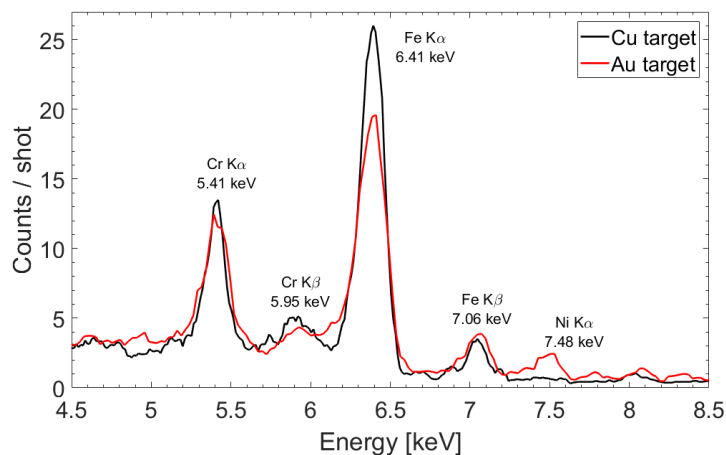


**Figure 5.21** XPIF background signal with no sample inside the auxiliary chamber.

One can observe that the XPIF background can be a problem when low amounts of counts are coming from the sample. The XPIF background is composed by undesired X-ray signal that lies within the sensitive energy detection range of the X-ray camera. E.g., the iron contained in stainless steel from the chamber windows could produce parasite signal at 6.41 keV. We strongly recommend not to use it in future campaigns. In this experiment, the XPIF background signal is subtracted from the sample signal. A high signal of Cr and Fe is observed. Some Ni signal is obtained in smaller quantity and only in the case of Au target (Ni  $K_{\alpha}$  is due to mostly due to XRF for Au target, but just due to PIXE in the case of Cu target).

### 5.5.5. Minimum detectable composition

In order to test the minimum detectable composition of a sample, we irradiate an Arsenic-doped silicon wafer (As:Si) of 0.5 mm thickness with a doping level of 20 ppm, i.e., 0.002 % (supplier *WaferPro*). To be able to optimize the analysis of elements with a  $Z > 28$ , we replace the Cu interaction target with an Au target. We observe that the resulting XPIF signal is similar to the one obtained with Cu target for elements with  $Z < 28$ .

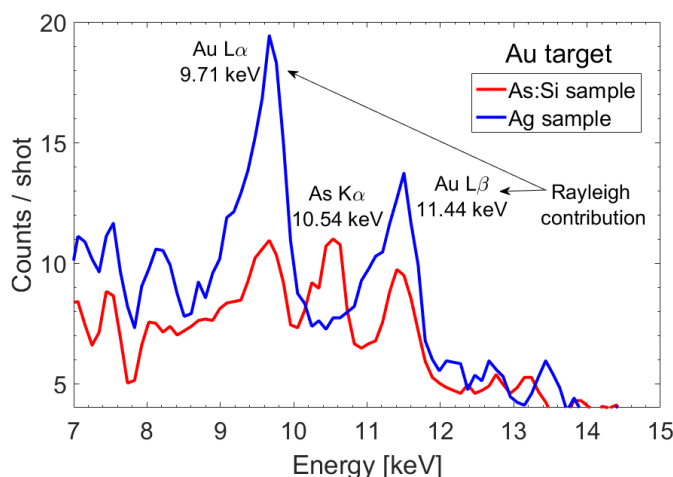


**Figure 5.22** X-ray spectra obtained when irradiating Arsenic doped Si wafer sample (red) using the laser-based sources produced with an Au laser-interaction target. and compared with an Ag sample (blue).

As shown in **Figure 5.22** (red line), it is possible to distinguish the Arsenic  $K_{\alpha}$  peak (10.54 keV), located in between the Rayleigh signal produced by the Au  $L_{\alpha}$  and  $K_{\beta}$ . To ensure that the two peaks nearby the peak located at 10.54 keV are due to Rayleigh signal, we compare the As:Si wafer spectrum with an Ag sample spectrum (blue line). We see that the

Rayleigh scattering peaks due to the Au lines are still present. For the Ag sample, the peaks are higher than for the case of the As:Si wafer since the Rayleigh scattering cross-section is bigger [Podgorsak 2010]. We are able to detect elements (in this case Arsenic) down to a level of 20 ppm.

### 5.5.6. Non-metallic samples

We test the efficiency of the XPIF technique also on non-metallic samples. **Figure 5.23** shows the spectrum obtained by a single irradiation of a watered green leaf with a surface of about 13 cm<sup>2</sup> (thickness 0.7 mm) coming from a *ficus* tree. In the spectrum, we can clearly see a fingerprint of Ca inside the sample, which is typical for green plants [Lucas 2011].

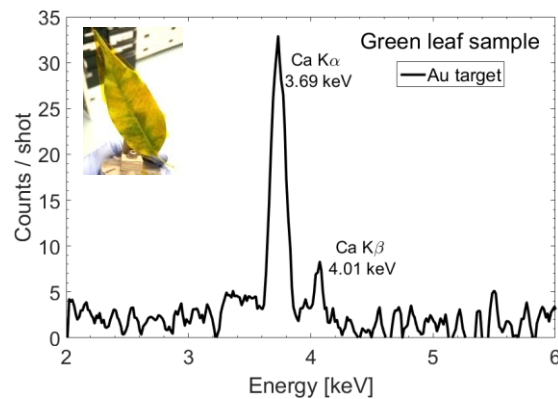


**Figure 5.23** X-ray spectra obtained when irradiating green leaf sample using the laser-based sources produced with an Au laser-interaction target.

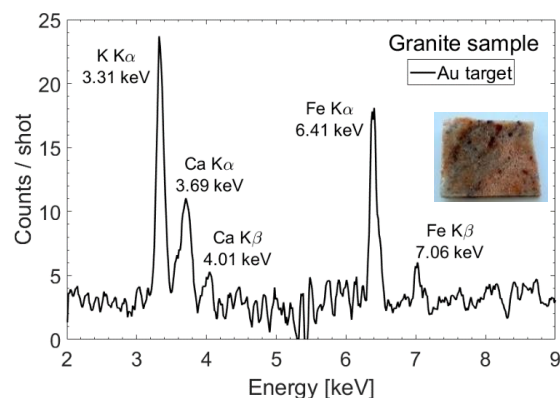


**Figure 5.24** X-ray spectra obtained when irradiating granite sample using the laser-based sources produced with an Au laser-interaction target.

Another example of non-metallic sample is the granite. Its non uniform surface makes the analysis harder. **Figure 5.24** shows the spectrum obtained by a single irradiation of a granite

sample with a surface of about 16 cm<sup>2</sup> (thickness 3 cm). In the spectrum, we can clearly see a fingerprint of potassium, calcium and iron contained inside the sample.

### 5.5.7. Volumetric probing

One of the advantages of the XPIF technique is the volumetric probing: it can analyze a depth up to few millimeters if using the XRF contribution and up to several micrometers using the PIXE one. **Figure 5.25a** shows the X-ray spectra as obtained when irradiating three different stacks using the laser-based sources produced by a Cu target. We use two-materials stacks consisting respectively of a 5, 10, and 20  $\mu\text{m}$  thickness pure Cu foil placed in front of a Ti substrate (thickness 0.5 mm). The surface of all stacks is 2 x 2 cm<sup>2</sup>. One can identify a clear fingerprint of titanium's  $K_{\alpha}$  and  $K_{\beta}$  lines up to a Cu foil thickness of 10  $\mu\text{m}$ , confirming the volumetric analysis of the sample. The Ti X-rays are attenuated by the Cu sample depending on its thickness and are almost fully attenuated for a thickness of 20  $\mu\text{m}$ .

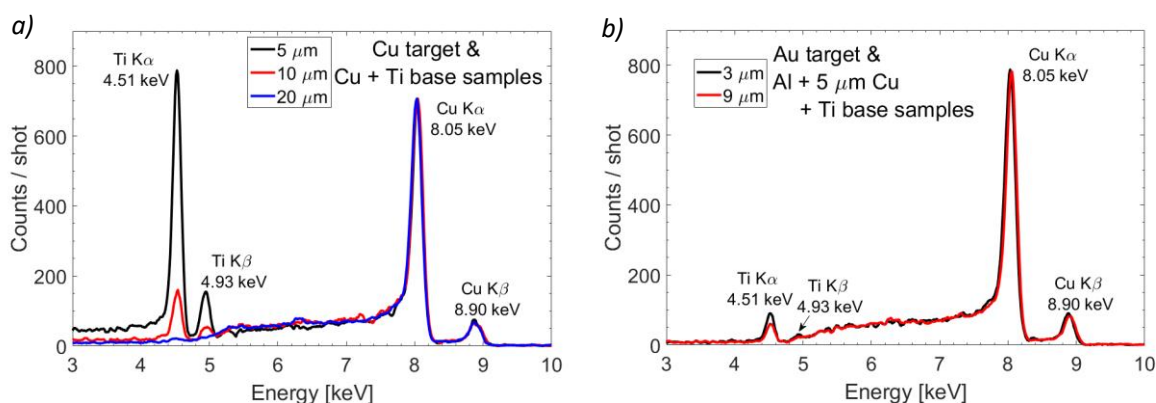


**Figure 5.25** X-ray spectra obtained when irradiating different stacks using the laser-based produced with a) Cu and b) Au laser-interaction target. In the a) case: 5, 10, and 20  $\mu\text{m}$  Cu layer on a Ti substrate. In the b) case: 3 and 9  $\mu\text{m}$  Al layer lying on a 5  $\mu\text{m}$  Cu layer on a Ti substrate.

We test the volumetric XPIF also using stacks of three elements (Al, Cu and Ti). **Figure 5.25b** shows the X-ray spectra using Au laser-interaction target. This time, the stacks are formed of a 3 or 9  $\mu\text{m}$  Al thickness sample, on top of a 5  $\mu\text{m}$  Cu sample followed by a Ti substrate (thickness 0.5 mm). The fingerprint of Al cannot be detected by the camera since its  $K_{\alpha}$  (1.49 keV) is not in the detection range (minimum threshold value of 2.2 keV). However, one can clearly observe the elements Ti and Cu when the corresponding foils are covered by a 3 and 9  $\mu\text{m}$  thickness Al foil.

### 5.5.8. Real-setting application: coins

Finally, as real-setting application of volumetric XPIF on compound samples, we irradiate different metallic coins.

The first coin is a Canadian quarter (25 cent, mint 2009, nickel-plated steel; 94% steel, 3.8% Cu, 2.2% Ni plating, diameter: 23.88 mm; thickness: 1.58 mm). The coin is made of several material layers, the external layer is 5  $\mu\text{m}$  Ni, which follows a 5  $\mu\text{m}$  Cu layer, on top of a 5  $\mu\text{m}$  Ni layer, before reaching the steel bulk. The second irradiated coin is an American penny (1 cent, mint 2000, diameter: 19.05 mm, thickness: 1.52 mm, copper-plated zinc: 97.5% Zn, 2.5% Cu). The American penny is made of a 20  $\mu\text{m}$  copper plating over a zinc core. As last coin, we irradiate an ancient Roman coin (Licinius I, Nicomedia mint 311-317 AD, bronze follis, 21.5 mm diameter, 3.41 g).

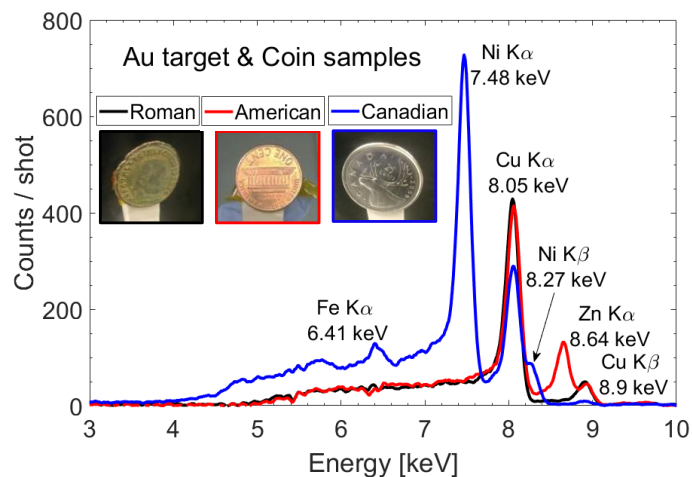


**Figure 5.26** X-ray spectra obtained when irradiating a Roman (black), American (red) and Canadian (blue) coin samples using the laser-based sources produced with Au target.

The results are shown in **Figure 5.26**. Concerning the Canadian quarter (blue line), one can clearly identify the peaks related to the constituting elements of the coin, including the main element of steel, iron. The second element contained in the alloy steel, carbon, is unfortunately not detectable by our diagnostic. Similarly, the second spectrum related to the American penny (red line) unambiguously reveals peaks related to the elements Cu and Zn, as expected. Finally, the spectrum related to the ancient Roman coin (black line) reveals the element Cu, bronze being an alloy consisting primarily of copper (~90%) and tin (Sn) (10%).

Unfortunately, the element Sn ( $K_{\alpha} = 25.27$  keV) is not detectable by our diagnostic (upper limit  $< 25$  keV).

One can notice that, in the case of the Canadian coin, the Ni  $K_{\alpha}$  peak is higher than the other peaks, even if there is only 2.2% Ni contribution in the coin. This is because the X-rays from Ni are not attenuated by any surface layer.

One can clearly assess that the XPIF is able to probe low-Z elements within tens of micrometer thickness and this within a single laser shot.

## 5.6. Conclusion

As demonstrated above, laser-matter interaction allows producing either PIXE or XRF or even both, depending on the need. By simply varying the atomic number of the laser interaction target, one can produce laser-driven PIXE, laser-driven XRF or the combination of both. Both techniques can be performed in the same installation within seconds or lower (depending on the target replacement system). The combination of both enhances the detection of elements. Moreover, the cross-comparison of the results obtained with both techniques in the same experimental environment enhances their reliability.



# CONCLUSION AND PERSPECTIVES

---

This thesis has presented two main works: the study of ion acceleration with gas-jet targets performed with the ENL group at CENBG, France; and the study of one application: a multi-element analysis technique in laser environments, which was done with the iPAT-LAB group at EMT-INRS in Canada.

## 6.1. Ion acceleration with gas-jet targets

Gas-jet targets were found to be a good alternative to replace solid targets for high repetition rate (HHR) experiments. They can be used to accelerate different ion species and they are debris free. Our goal was to produce gas density profiles with a maximum density of around  $10^{21} \text{ cm}^{-3}$  and minimum FWHM (of the order of  $100 \mu\text{m}$ ). Hence, supersonic gas nozzles were designed. It is important to note that commercial nozzles fulfilling these two requirements are not easy to find.

Three types of micrometric supersonic nozzles have been designed using CFD simulations: *conical nozzles*, *shock nozzles*, and *asymmetrical nozzles*. We deeply studied the optimization of the nozzle parameters for the two first types of nozzles. A comparison of their transversal and longitudinal density profiles has been done as well. The non-axisymmetric nozzles are more difficult to simulate as 3D CFD simulations are time-consuming.

In order to validate the results, the gas density profiles delivered by the *conical* nozzles were measured with a Mach-Zehnder interferometer using different gases. Information about 3D tomography with non-axisymmetric nozzles was reported as well. In all cases, a good agreement was found between the simulations and measurements, which validated the whole design procedure.

Rigorous characterization of the dynamics of the gas flux is mandatory to trigger the laser interaction at the maximum density of the gas-jet target. The evolution of the gas flux was measured by strioscopy. We observed the flow evolution of hydrogen, nitrogen and helium gases for different valve opening time durations. It takes several ms (110 ms for N<sub>2</sub> and ~60 ms for H<sub>2</sub> and He) to fill the nozzle reservoir volume and achieve the maximum density. In order to use these gas targets at HRR, the valve opening time duration ( $t_{open} = 40$  ms for H<sub>2</sub> and He and 80 ms for N<sub>2</sub>) will be reduced in the future by downsizing the nozzle reservoir volume.

Two experimental campaigns were performed at the LULI facility with the high-power infrared PICO2000 laser. In the first campaign, we studied *conical nozzles* of different sizes and *asymmetrical nozzles* to select the best design for ion acceleration. Most of the laser interactions were performed with pure hydrogen.

We observed interesting peaked structures in the case of *asymmetrical nozzles* with an energy of 3.9 MeV at 0°. However, the characterization of these nozzles is harder than for *conical nozzles* and their alignment was not precise enough due to mechanical constraints. This is why, although these targets might be promising, the *asymmetrical nozzles* were not further investigated.

In the 2<sup>nd</sup> campaign, *small conical nozzles* were used since they gave high proton fluxes with a good repeatability in the first campaign. Their alignment and characterization were easy, and a small quantity of gas was delivered into the vacuum chamber. The delivery of too much gas into the experimental chamber produced several *Thomson parabola* (TP) high-voltage break downs. During the second campaign, MS-IP were used as detectors to improve the detection signal-to-noise ratio. We gained one order of magnitude on the background level. However, the low energy protons below 0.7 MeV were not detectable

since they are stopped in the front protective layer of the MS-IP. In the first campaign, nozzle damage was observed after each shot. For the second one, we modified the *conical nozzles* to have a similar density profile but at a nozzle height of 400  $\mu\text{m}$  (instead of 200  $\mu\text{m}$ ).

In this campaign, we found that focusing the laser at the rising slope of the gas-jet density profile provides more energetic protons. We found as well that reducing the ASE level to the minimum achievable was an advantage for proton acceleration in the longitudinal direction. In summary, isotropic acceleration was observed with a flux of  $10^{11}$  protons/MeV/sr at low energies up to 1.5 MeV. Second structures with a constant flux of particles (plateau) were observed in the transverse direction. In the best conditions, a maximum energy of 6 MeV was reported in the longitudinal direction. Previously, using high-dense  $\text{H}_2$  targets, a maximum energy of only 0.8 MeV was obtained in the longitudinal direction [[Chen 2017](#)].

3D hydrodynamics simulations were used to understand the evolution of the gas-jet density profile due to the interaction with the laser ASE. The density profile was significantly modified and was no longer Gaussian. One side of the density profile was drastically transformed and a peak of approximately twice the original density was formed. The exact location of this peak was not well defined because it depends on the ASE duration which was not well measured in the experiment.

Once we calculated the shape of the target, 2D PIC simulations were performed to interpret the measured proton spectra and be able to explain the different acceleration mechanisms at play. Self-channeling, self-focusing, and multi-filamentation were found in the first ps of the simulation when the laser interacted with an under-dense plasma. This was the origin of the protons accelerated in the transversal directions. The protons in the longitudinal direction were accelerated due to the RPA-HB process, induced by a dramatic change of the density profile. The process accelerated protons to higher energy and created plateau structures in the spectra. Peaked structures at high energy were observed at different angles in several shots which were also found in the simulations.

Some laser shots were performed with a mixed  $\text{H}_2$  and He gas-jet target. In these cases, proton and helium emission at all angles were observed. About  $10^{12}$  protons were measured at the three most forward angles while the number of particles emitted at  $90^\circ$  is one order of

magnitude smaller. In the same shot, to the opposite,  $\text{He}^{2+}$  transverse emission seemed more important than the  $0^\circ$  one. Furthermore, almost no signal was observed at  $30^\circ$  which indicates a more collimated forward emission. These observations are consistent with the results reported in previous works.

### 6.1.1. Future approaches

In the future, an improvement of the gas-jet density profile is necessary in order to enhance the acceleration in one direction with well-defined energy distribution while avoiding the nozzle damage for HRR mode.

#### 6.1.1.1. How to avoid nozzle damage

The damage of the nozzle decreased from the first campaign to the second one, but we were not able to avoid it completely. **Figure 6.1** shows pictures of the nozzle taken with an optic microscope before (on the left) and after (on the right) the laser-matter interaction:

- **a)** and **b)** are pictures of the nozzle external surface on which the modification of even the external borders is visible. The surface around the nozzle exit is extremely affected.

- **c)** and **d)** is a magnification of the previous images. The nozzle exit diameter evolved from  $240\ \mu\text{m}$  to  $570\ \mu\text{m}$  and the rugosity of its walls is increased.

- **e)** and **f)** shows the nozzle throat diameter has increased from  $100\ \mu\text{m}$  to  $140\ \mu\text{m}$ .

This nozzle damage may be due to several phenomena. The first one is the extreme heat radiated from the plasma created in the laser-matter interaction. The second one is the bombardment of the nozzle by ionized plasma particles (e.g. hot electrons). The third one can be a strong electric current traveling inside the gas jet down to the nozzle throat.

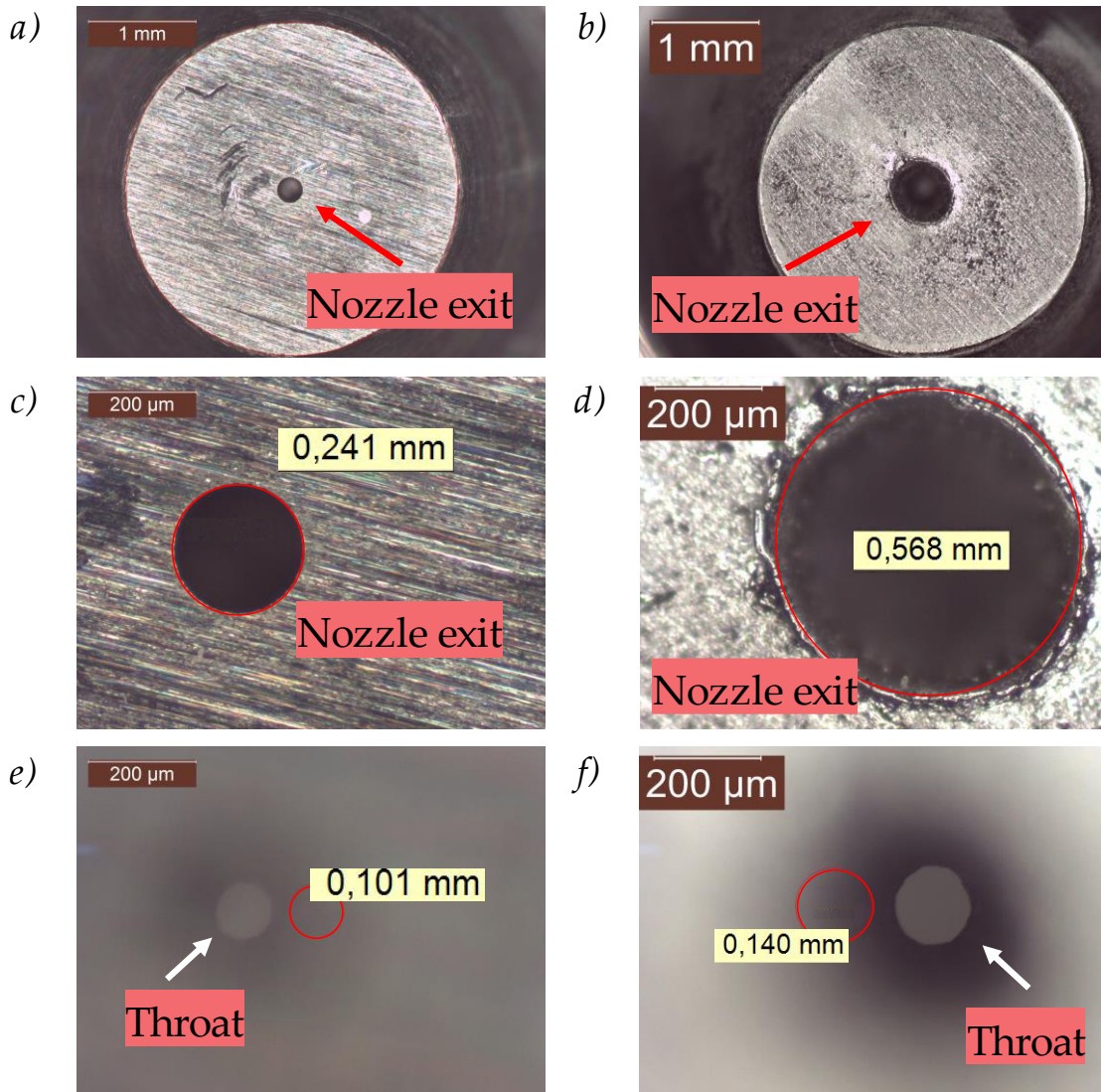


**Figure 6.1** On the left, pictures of the nozzle before the shot. On the right, pictures of the nozzle after one shot. *a)*, *b)*, *c)* and *d)* show the nozzle exit. *e)* and *f)* show the nozzle throat.

To solve this problem, two approaches are under investigation. The first one is designing new nozzles with much further interaction distances. The second one is the use of other materials besides stainless steel for the nozzle construction. E.g. using glass nozzles. Glass has a high resistance to heat and it is a dielectric (non-conductive) material.

In order to combine the two solutions, *shock nozzles* made in glass are already designed and their characterization is underway. **Figure 6.2a** shows a picture of the glass *shock nozzle* during the characterization. The red laser is illuminating the nozzle. **Figure 6.2b** shows the phase shift image from the *glass shock nozzle*. In this case, the focal point is found at  $z \sim 900 \mu\text{m}$ .

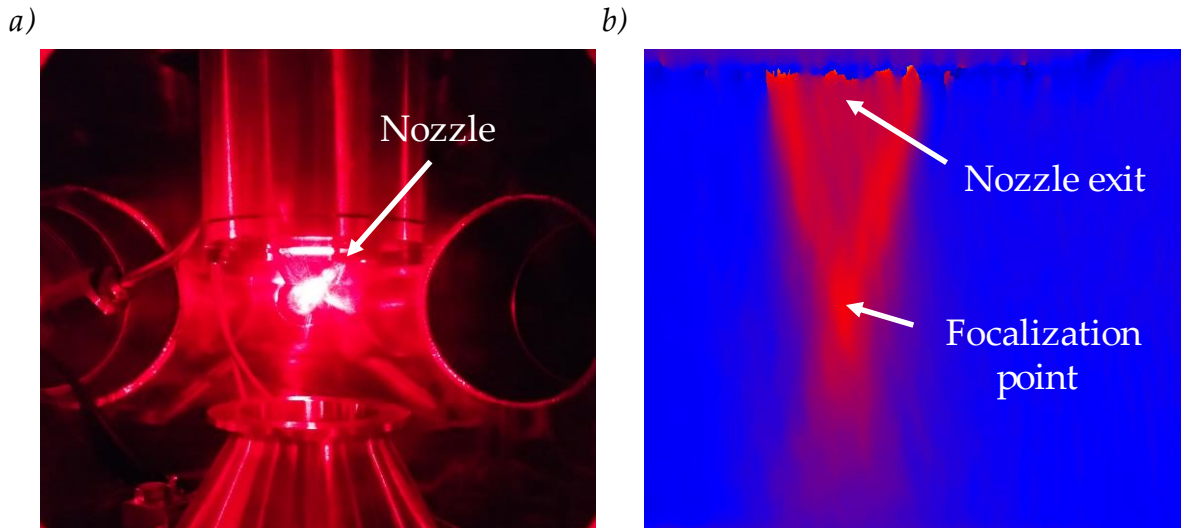


**Figure 6.2** *a)* Picture of the nozzle in the interferometer setup. The nozzle is illuminated by a red laser. *b)* Phase shift image by a glass made *shock nozzle*. The focal point is at  $z \sim 900 \mu\text{m}$ .

### 6.1.1.2. How to enhance the longitudinal proton acceleration: Plasma shaping

The control of the *wings* of the density profile is essential to enhance the acceleration in the longitudinal direction. In this thesis work, the laser interacts with an under-dense plasma and loses part of its energy before interacting with the maximum density of the target. As observed with the PIC simulations, the laser also filaments and bends so the ion acceleration is not always observed in the longitudinal direction. In order to avoid this, we propose to modify the target density profile by optical shaping. Plasma shaping of gas targets was first reported by Tresca *et al.* [2015].

Tresca *et al.* [2015] used optical plasma shaping in helium gas-jet targets using a  $\text{CO}_2$  laser. During the experiment, a high-intensity laser ( $I > 10^{16} \text{ W/cm}^2$ ) was sent to produce ion acceleration in a gas density profile modified by a low-energy laser prepulse ( $I < 10^{14} \text{ W/cm}^2$ ). First, they observed that with no prepulse ( $E = 150 \text{ mJ}$ ), no forward accelerated ions were observed. Second, when the main pulse arrives 25 ns after the prepulse, energetic ions with energies up to 1.5 MeV were reported. In this case, the main laser interacted with a peak density of  $6n_c$  and steep gradient ( $100 \mu\text{m}$ ). The prepulse had produced a blast wave and created a steep variable density gradient in the gas density profile. With a more intense prepulse (1.27 J), the blast wave induced by the prepulse

propagates too deep into the jet and no ion beam was observed. They also based their explanation on 2D PIC simulations. They explained that, as in our study, a collisionless shock due to the laser *piston* is generated in the steep plasma profile. Recently, a thorough hydrodynamical study of the modifications of the gas-jet target by laser prepulses has been published by [Passalidis 2020], which confirmed the experimental findings.

In our case, in order to improve the ion acceleration in the longitudinal direction using our designed gas-jet targets we propose to use a ps laser pulse with an excellent contrast in conjunction with a plasma target shaped by nanosecond laser pulses. To test this geometry, a GSI experiment was planned in March 2020 but delayed due to COVID-19.

**Figure 6.3** illustrates the planned setup. The gas jet flows along the  $z$ -axis and the main ps laser pulse is along the  $x$ -axis. One or two ns laser beams propagate along the  $y$ -axis in the low-density edge of the density profile at adjustable distances,  $b$ , from the target center. This is the main difference with Tresca *et al.*'s work, where the ns-beam and the ps-beam were copropagating. Consequently, the modification of the gas-jet density profiles will involve: higher maximum densities, smaller FWHM and sharper edges.

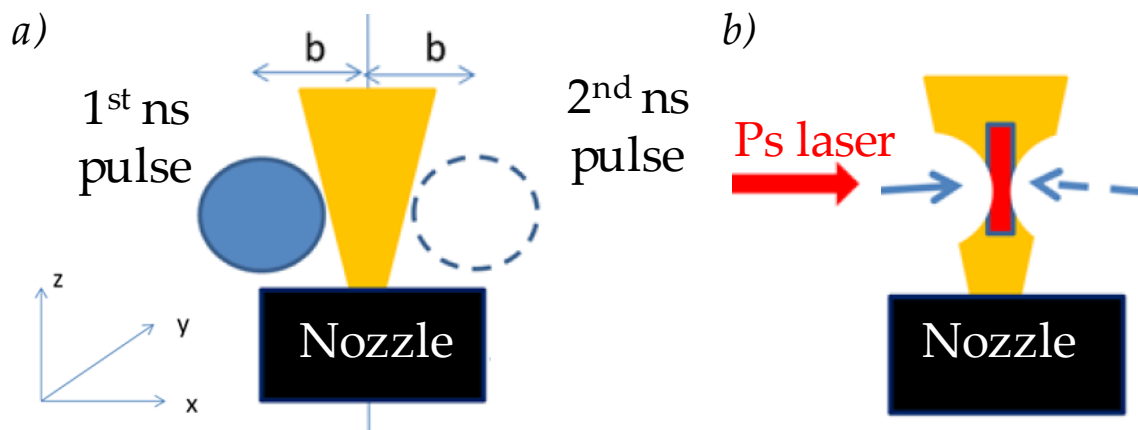


**Figure 6.3** *a)* Principle of the plasma laser-machining using one or two ns laser beams to shape the plasma profile before the arrival of the main ps laser pulse. *b)* The ps laser pulse arrives when the density profile is already modified.

2D hydrodynamic simulations with the code [Lefebvre 2019] were performed by P. Loiseau (CEA) to test quantitatively this laser-based plasma shaping scheme. Some of the results of these simulations are presented in **Figure 6.4** when two or one ns pulses are used. The plasma is heated along the  $y$ -axis due to the propagation of the ns beam(s). It is pushed in the

$x$ -axis by thermal pressure and converges towards the gas jet center at  $x = 0$ . The result is one or two sharp edges of high density ( $> 6n_c$ ).

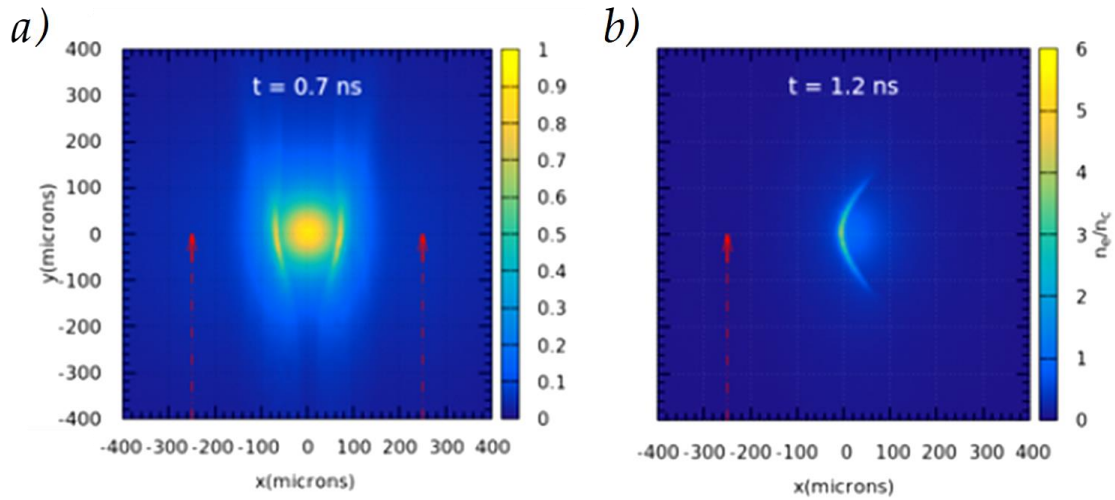


**Figure 6.4** 2D hydrodynamic simulations of the plasma shaping by a) two or b) one nanosecond lasers. The plasma electron density  $n_e/n_c$  is presented. Ns beams are propagating at  $-250$  and  $+250$   $\mu\text{m}$  along the  $y$ -axis.

With this type of sharp density profile, we expect to enhance the ion acceleration in the longitudinal direction. It can be due to a more controllable *hole boring* or even due to the *collisionless shock acceleration* obtaining more energetic protons than before. PIC simulations are already under investigation.

## 6.2. XPIF analysis technique

After three experimental campaigns performed at INRS-EMT with ALLS 100 TW laser to test laser-driven proton acceleration with solid targets in the new acceleration beamline, a first experimental campaign focusing on applications was done.

We showed, for the first time to our knowledge, experimentally and numerically (with Geant4 simulations) that the interaction of an intense laser with a solid target can produce XRF and PIXE. We found that the two analysis techniques can be implemented either simultaneously or individually within seconds by simply changing the interaction target type (different atomic numbers). We have used a stainless steel sample to verify this phenomenon. We found an increase of the spectra intensity when Cu target was used for the laser interaction in comparison with the signal obtained when Al target (low Z) was used.

We could confirm the relative XRF and PIXE contributions with Geant4 simulations, finding that the increase of the signal was due to the XRF contribution. Al X-ray lines do not produce any XRF detectable by our diagnostic.

We also studied the minimum sample size with different Ti pure samples. This technique allows to analyze not only large areas (the proton beam can have a spot size of several cms) but also small ones (e.g. down to 9 mm<sup>2</sup> in the case of Ti). We found as well that it was able to detect the arsenic in an arsenic-doped silicon wafer with a doping level of 20 ppm, giving the minimum detectable percent composition for this type of element. Moreover, we studied non-metallic samples, which spectrum were obtained in just one single irradiation. Finally, we studied the volumetric probing of different metallic stacks and different metallic coins. In this last case, we were able to identify the peaks related to the constituting element of each coin.

### **6.2.1. Future approaches**

#### **6.2.1.1. Quantitative analysis**

Quantitative analysis, which is important for some applications, is currently under investigation. Two options are available. The first one is the comparison of the sample response to the ones of known reference standards (e.g. *Micromatter* ones). The other one is to measure precisely the produced laser-based sources for an absolute quantitative analysis. For PIXE, it has been developed only for monochromatic ion sources and lately Passoni *et al.* [2019] extended the theory to arbitrary energy distributions.

#### **6.2.1.2. Air XPIF**

In the future, we plan to develop air-XPIF which is more adapted for delicate samples (for cultural heritage or biomedicine) which cannot be set under vacuum. The ion beam has to be extracted into air, which is commonly done at conventional accelerators.

### **6.2.1.3. PIXE at high laser repetition rate**

We plan to use high-repetition gas-jet targets to improve the statistics collected in the spectra with delicate samples, which need to be irradiated with low particle fluxes during several shots. However, with pure H<sub>2</sub> gas-jet target, the XRF contribution will be negligible.

In addition to that, if monochromatic laser-based proton sources are produced in the future with gas-jet targets due to CSA mechanism, quantitative volumetric analysis of the samples will be possible.

# BIBLIOGRAPHY

---

[Agostini 1979]

P. Agostini, F. Fabre, G. Mainfray, G. Petite and N.K. Rahman, *Free-free transitions following 6-photon ionization of xenon atoms*. Phys. Rev. Lett., vol. 42, 1127-1130 (1979).

[Allison 2016]

J. Allison, K. Amako, J. Apostolakis, P. Arce, M. Asai, T. Aso, E. Bagli, A. Bagulya, S. Banerjee, G. Barrand, B.R. Beck, A.G. Bogdanov, D. Brandt, J.M.C. Brown, H. Burkhardt, Ph. Canal, D. Cano-Ott, S. Chauvie, K. Cho, G.A.P. Cirrone, G. Cooperman, M.A. Cortés-Giraldo, G. Cosmo, G. Cuttone, G. Depaola, L. Desorgher, X. Dong, A. Dotti, V.D. Elvira, G. Folger, Z. Francis, A. Galoyan, L. Garnier, M. Gayer, K.L. Genser, V.M. Grichine, S. Guatelli, P. Guèye, P. Gumplinger, A.S. Howard, I. Hřivnáčová, S. Hwang, S. Incerti, A. Ivanchenko, V.N. Ivanchenko, F.W. Jones, S.Y. Jun, P. Kaitaniemi, N. Karakatsanis, M. Karamitros, M. Kelsey, A. Kimura, T. Koi, H. Kurashige, A. Lechner, S.B. Lee, F. Longo, M. Maire, D. Mancusi, A. Mantero, E. Mendoza, B. Morgan, K. Murakami, T. Nikitina, L. Pandola, P. Paprocki, J. Perl, I. Petrović, M.G. Pia, W. Pokorski, J.M. Quesada, M. Raine, M.A. Reis, A. Ribon, A. Ristić Fira, F. Romano, G. Russo, G. Santin, T. Sasaki, D. Sawkey, J.I. Shin, I.I. Strakovsky, A. Taborda, S. Tanaka, B. Tomé, T. Toshito, H.N. Tran, P.R. Truscott, L. Urban, V. Uzhinsky, J.M. Verbeke, M. Verderi, B.L. Wendt, H. Wenzel, D.H. Wright, D.M. Wright, T. Yamashita, J. Yarba, H. Yoshida, *Recent developments in Geant4*. Nucl. Instrum. Methods Phys. Res., A, vol. 835, 186-225 (2016).

[Anderson 1990]

J. D. Anderson, *Modern Compressible Flow*. Section 10.3, The McGraw-Hill Companies, Inc. (1990).

[ANSYS FLUENT]

ANSYS FLUENT® Academic Research Mechanical, Release 18.1.

[Antici 2017]

P. Antici, E. Boella, S. N. Chen, D. S. Andrews, M. Barberio, J. Böker, F. Cardelli, J. L. Feugeas, M. Glessner, P. Nicolai, L. Romagnani, M. Scisciò, M. Starodubtsev, O. Willi, J. C. Kieffer, V. Tikhonchuk, H. Pépin, L. O. Silva, E. d' Humières and J. Fuchs, *Acceleration of collimated 45 MeV*

protons by collisionless shocks driven in low-density, large-scale gradient plasmas by a 1020 W/cm<sup>2</sup>, 1  $\mu$ m laser. *Sci. Rep.*, vol. 7, 16463 (2017).

[Avizonis 1978]

P. V. Avizonis, B. D. O'Neil, and V. A. Hedin, *Intensity mapping optical aberrations*. *Appl. Opt.*, vol. 17, 10, 1527-1531 (1978).

[Barberio 2017]

M. Barberio, S. Veltri, M. Scisciò, P. Antici, *Laser-Accelerated Proton Beams as Diagnostics for Cultural Heritage*. *Sci. Rep.*, vol. 7, 40415 (2017).

[Barberio 2018]

M. Barberio, M. Scisciò, E. Skantzakis, P. Antici, *Carbon based nanostructured film materials for high-intense laser-matter interaction experiments*. *Adv. Eng. Mater.*, vol. 21, 1800777 (2018).

[Bespalov 1966]

V. I. Bespalov, and V.I. Talanov, *Filamentation structure of light beams in nonlinear liquids*. *JETP Lett.*, vol. 3, 307 (1966).

[Birdsall 1985]

C.K. Birdsall, and A.B. Langdon, *Plasma physics via computer simulation*. MacGraw-Hill, New York (1985).

[Bonnet 2013]

T. Bonnet, M. Comet, D. Denis-Petit, F. Gobet, F. Hannachi, M. Tarisien, M. Versteegen, and M. M. Aleonard, *Response functions of Fuji imaging plates to monoenergetic protons in the energy range 0.6–3.2 MeV*. *Rev. Sci. Instrum.*, vol. 84, 013508 (2013).

[Borghesi 2004]

M. Borghesi, A. J. Mackinnon, D. H. Campbell, D. G. Hicks, S. Kar, P.K. Patel, D. Price, L. Romagnani, A. Schiavi, and O. Willi, *Multi-MeV Proton Source Investigations in Ultraintense Laser-Foil Interactions*. *Phys. Rev. Lett.*, vol. 92, 055003 (2004).

[Borghesi 2014]

M. Borghesi, *Laser-driven ion acceleration: State of the art and emerging mechanisms*. *Nucl. Instrum. Methods Phys. Res. A*, vol. 740, 6-9 (2014).

[Born 1999]

M. Born, E. Wolf, A. B. Bhatia, P. C. Clemmow, D. Gabor, A. R. Stokes, A. M. Taylor, P. A. Wayman, and W. L. Wilcock, *Principles of Optics: Electromagnetic Theory of Propagation. Interference and Diffraction of Light*, 7th ed., Cambridge University Press (1999).

[Brunel 1987]

F. Brunel, *Not-so-resonant, resonant absorption*. Phys. Rev. Lett., vol. 59, 52-55 (1987).

[Bruker]

www.bruker.com/hhxf

[Bulanov 1992]

S.V. Bulanov, I.N. Inovenkov, V.I. Kirsanov, N.M. Naumova, and A.S. Sakharov, *Nonlinear depletion of ultrashort and relativistically strong laser pulses in an underdense plasma*. Phys. Fluids B, vol. 4, 1935-42 (1992).

[Burnett and Enright 1990]

N.H. Burnett and G.D. Enright, *Population inversion in the recombination of optically-ionized plasmas*. IEEE J. Quantum Electron, vol. 26, 1797 (1990).

[Ceccotti 2007]

T. Ceccotti, A. Lévy, H. Popescu, F. Résau, P. D'Oliveira, P. Monot, J.P. Geindre, E. Lefebvre, and Ph. Martin, *Proton acceleration with high-intensity ultrahigh-contrast laser pulses*. Phys. Rev. Lett., vol. 99, 185002 (2007).

[Chen 1984]

F.F. Chen, *Introduction to plasma physics and controlled fusion*. vol.1, Plasma Phys. (1984).

[Chen 2017]

S.N Chen, M. Vranic, T. Gangolf, E. Boella, P. Antici, M. Bailly-Grandvaux, P. Loiseau, H. Pépin, G. Revet, J. J. Santos, A. M. Schroer, M. Starodubtsev, O. Willi, L. O. Silva, E. d'Humières and J. Fuchs, *Collimated protons accelerated from an overdense gas jet irradiated by a 1 mm wavelength high-intensity short-pulse laser*. Sci. Rep., vol. 7, 20452322 (2017).

[Clark 2000]

E.L. Clark, K. Krushelnick, J.R. Davies, M. Zepf, M. Tatarakis, F.N. Beg, A. Machacek, P.A. Norreys, M.I.K. Santala, I. Watts, and A.E. Dangor, *Measurements of energetic proton transport through magnetized plasma from intense laser interactions with solids*. Phys. Rev. Lett., vol. 84, 670-673 (2000).

[Consoli 2020]

F. Consoli, V.T. Tikhonchuk, M. Bardon, P. Bradford, D.C. Carroll, J. Cikhardt, M. Cipriani, R. J. Clarke, T. Cowan, C.N. Danson, R. De Angelis, M. De Marco, J-L. Dubois, B. Etchessahar, A. Laso Garcia, D.I. Hillier, A. Honsa, W. Jiang, V. Kmetik, J. Krása, Y. LI, F. Lubrano, P. McKenna, J. Metzkes-Ng, A. Poyé, I. Prencipe, P. Rączka, R.A. Smith, R. Vrana, N.C. Woolsey, E. Zemaityte, Y. Zhang, Z. Zhang, B. Zielbauer and D. Neely, *Laser produced electromagnetic pulses: generation, detection and mitigation*. High Power Laser Sci. and Eng., vol. 8, e22 (2020).

[Constantin 1988]

P. Constantin, and C Foias, *Navier-Stokes equations*. Chicago IL, University of Chicagos Press, 199 (1988).

[Couperus 2016]

J.P. Couperus, A. Köhler, T.A.W. Wolterink, A Jochmann, O. Zarini, H.M.J. Bastiaens, K.J. Boller, A. Irman, and U.Schramm, *Tomographic characterization of gas-jet targets for laser wakefield acceleration*. Nucl. Instrum. Methods Phys. Res. A., vol. 830, 504–509 (2016).

[Cowan 2012]

T.E. Cowan, J. Fuchs, H. Ruhl, A. Kemp, P. Audebert, M. Roth, R. Stephens, I. Barton, A. Blazevic, E. Brambrink, J. Cobble, J. Fernández, J.-C. Gauthier, M. Geissel, M. Hegelich, J. Kaae, S. Karsch, G.P. Le Sage, S. Letzring, M. Manclossi, S. Meyroneinc, A. Newkirk, H. Pépin, and N. Renard-LeGalloudec, *Ultralow emittance, multi-MeV proton beams from a laser virtual-cathode plasma accelerator*. Phys. Rev. Lett., vol. 92, 204801 (2012).

[Cruz 2020]

J. Cruz, M. Manso, V. Corregidor, R.J.C. Silva, E. Figueiredo, M.L. Carvalho, L.C. Alves, *Surface analysis of corroded XV–XVI century copper coins by  $\mu$ -XRF and  $\mu$ -PIXE/ $\mu$ -EBS self-consistent analysis*. Mater. Charact., vol. 161, 110170 (2020).

[Daido 2012]

H. Daido, M. Nishiuchi and A. S. Pirozhkov, *Review of laser-driven ion sources and their applications*. Rep. Prog.Phys., vol. 75, 056401 (2012).

[De Angelis 2016]

R. De Angelis, F. Consoli, C. Verona, G. Di Giorgio, P. Andreoli, G. Cristofare, M. Cipriani, F. Ingenito, M. Marinelli, G. Verona-Rinate, *High performance diagnostics for Time of Flight and X-ray measurements in laser produced plasmas, based on fast diamond detectors*. J. Instrum., vol. 11 (2016).

[d’Humières 2010]

E. d’Humières J. L. Feugeas, P. Nicolai, S. Gaillard, T. Cowan, Y. Sentoku and V. Tikhonchuk, *Investigation of high intensity laser proton acceleration with underdense targets*. J. Phys.: Conf. Ser., vol. 244, 042023 (2010).

[Doria 2015]

D. Doria, S. Kar, H. Ahmed, A. Alejo, J. Fernandez, M. Cerchez, R. J. Gray, F. Hanton, D. A. MacLellan, P. McKenna, Z. Najmudin, D. Neely, L. Romagnani, J. A. Ruiz, G. Sarri, C. Scullion, M. Streeter, M. Swantusch, O. Willi, M. Zepf, and M. Borghesi, *Calibration of BAS-TR image plate response to high energy (3–300 MeV) carbon ions*. Rev. Sci. Instrum., vol. 86, 123302 (2015).

[Einstein 1905]

A. Einstein, *Über einen die Erzeugung und Verwandlung des Lichtes betreffenden heuristischen Gesichtspunkt*. *Annalen der Physik*, vol. 17, 132-148 (1905).

[Fiuza 2011]

F. Fiuza, R. A. Fonseca, L. O. Silva, J. Tonge, J. May, and W. B. Mori, *Three-dimensional simulations of laser-plasma interaction at ultrahigh intensities*. *IEEE Trans. Plasma Sci.*, vol. 39, 2618 (2011).

[Fiuza 2013]

F. Fiuza, A. Stockem, E. Boella, R.A. Fonseca, L.O. Silva, D. Haberberger, S. Tochitsky, W.B. Mori, and C. Joshi, *Ion acceleration from laser-driven electrostatic shocks*. *Phys. Plasmas*, vol. 20, 056304 (2013).

[Fourmaux 2013]

S. Fourmaux, S. Buffechoux, B. Albertazzi, D. Capelli, A. Lévy, S. Gnedyuk, L. Lecherbourg, P. Lassonde, S. Payeur, P. Antici, H. Pépin, R. S. Marjoribanks, J. Fuchs, and J. C. Kieffer, *Investigation of laser-driven proton acceleration using ultra-short, ultra-intense laser pulses*. *Phys. Plasma*, vol. 20, 013110 (2013).

[Fourment 2009]

C. Fourment, N. Arazam, C. Bonte, T. Caillaud, D. Descamps, F. Dorchies, M. Harmand, S. Hulin, S. Petit, and J. J. Santos, *Broadband, high dynamics and high resolution charge coupled device-based spectrometer in dynamic mode for multi-keV repetitive x-ray sources*. *Rev. Sci. Instrum.*, vol. 80, 083505 (2009).

[Fryxel 2000]

B. Fryxell, K. Olson, P. Ricker, F. X. Timmes, M. Zingale, D. Q. Lamb, P. MacNeice, R. Rosner, and H. Tufo, *FLASH: An adaptivemesh hydrodynamics code for modelling astrophysical thermonuclearflashes*. *Astrophys. J. Suppl. Ser.*, vol. 131, 273–334 (2000).

[Fuchs 2005]

J. Fuchs, P. Antici, E. d’Humières, E. Lefebvre, M. Borghesi, E. Brambrink, C. A. Cecchetti, M. Kaluza, V. Malka, M. Manclossi, S. Meyroneinc, P. Mora, J. Schreiber, T. Toncian, H. Pépin and P. Audebert, *Laser-driven proton scaling laws and new paths towards energy increase*. *Nat. Phys.*, vol. 2, 48-54 (2005).

[Gao 2017]

Y. Gao, J. Bin, D. Haffa, C. Kreuzer, J. Hartmann, M. Speicher, F. H. Lindner, T.M. Ostermayr, P. Hilz, T. F. Rösch, S. Lehrack, F. Englbrecht, S. Seufferling, M. Gilljohann, H. Ding, W. Ma, K. Parodi and J. Schreiber, *An automated, 0.5 Hz nano-foil target positioning system for intense laser plasma experiments*. *High Power Laser Sci. and Eng.*, vol. 5, 12 (2017).

[Gibbon 2005]

P. Gibbon, *Short pulse laser interactions with matter: An introduction*. Imperial College Press (2005).

[Gil 1989]

F. B. Gil, G. Barreira, M. F. Guerra and L. C. Alves, *Quantitative Elemental Analysis of Thick Samples by XRF and PIXE*. X-ray Spec., vol. 18, 147-164 (1989).

[Guerra 1998]

M. F. Guerra, *Analysis of Archaeological Metals. The Place of XRF and PIXE in the Determination of Technology and Provenance*. X-ray Spec. vol. 27, 73-80 (1998).

[Gwynne 2014]

D. Gwynne, S. Kar, D. Doria, H. Ahmed, M. Cerchez, J. Fernandez, R. J. Gray, J. S. Green, F. Hanton, D. A. MacLellan, P. McKenna, Z. Najmudin, D. Neely, J. A. Ruiz, A. Schiavi, M. Streeter, M. Swantusch, O. Willi, M. Zepf, and M. Borghesi, *Modified Thomson spectrometer design for high energy, multi-species ion sources*. Rev. Sci. Instrum., vol. 85, 033304 (2014).

[Haberberger 2012]

D. Haberberger, S. Tochitsky, F. Fiuza, C. Gong, R. A. Fonseca, L. O. Silva, W. B. Mori and C. Joshi, *Collisionless shocks in laser-produced plasma generate monoenergetic high-energy proton beams*. Nat. Phys., vol. 8, 9599 (2012).

[Handbook 2009]

Handbook of Modern Ion Beam Material Analysis (2009).

[Hecht 2002]

E. Hecht, *Optics*. Pearson Education Inc., fourth ed., vol. 38, 187 (2002).

[Hegelich 2002]

M. Hegelich, S. Karsch, G. Pretzler, K. Habs, K. Witte, W. Guenther, M. Allen, A. Blazevic, J. Fuchs, J.C. Gauthier, M. Geissel, P. Audebert, T. Cowan, and M. Roth, *MeV ion jets from short-pulse-laser interaction with thin foils*. Phys. Rev. Lett., vol. 89, 085002 (2002).

[Helle 2016]

M.H. Helle, D. F. Gordon, D. Kaganovich, Y. Chen, J. P. Palastro and A. Ting, *Laser-accelerated ions from a shock-compressed gas foil*. Phys. Rev. Lett., vol. 117, 165001 (2016).

[Higginson 2018]

A. Higginson, R. J. Gray, M. King, R. J. Dance, S. D. R. Williamson, N. M. H. Butler, R. Wilson, R. Capdessus, C. Armstrong, J. S. Green, S. J. Hawkes, P. Martin, W. Q. Wei, S. R. Mirfayzi, X. H. Yuan, S. Kar, M. Borghesi, R. J. Clarke, D. Neely and P. McKenna, *Near 100 keV protons via a laser-driven transparency-enhanced hybrid acceleration scheme*. Nat. Comm., vol. 9, 724 (2018).

[Hilz 2018]

P. Hilz, T.M. Ostermayr, A. Huebl, V. Bagnoud, B. Borm, M. Bussmann, M. Gallei, J. Gebhard, D. Haffa, J. Hartmann, T. Kluge, F.H. Lindner, P. Neumayr, C.G. Schaefer, U. Schramm, P.G. Thirolf, T.F. Rösch, F. Wagner, B. Zielbauer and J. Schreiber, *Isolated proton bunch acceleration by a petawatt laser pulse*. Nat. Comm., vol. 10, 10038 (2018).

[Hirschberg 2002]

A. Hirschberg, *Schlieren and shadowgraph techniques: Visualizing phenomena in transparent media: G.S. Settles* (Springer-Verlag, Berlin, Germany, 2001). Eur. J. Mech.: B/Fluids, vol. 21, 493 (2002).

[Kabir 2013]

M. H. Kabir, *Particle Induced X-ray Emission (PIXE): A Tool of Qualitative Elemental Analysis for Biological Sample*. Mat. Sci., vol. 39, 01-10 (2011).

[Kandidov 2009]

V. P. Kandidov, and E.P. Silaeva, *Self-focusing and multiple filamentation of laser light in disperse media*. J Russian Laser Res., vol. 30, 305 (2009).

[Karsch 2003]

S. Karsch, S. Düsterer, H. Schwoerer, F. Ewald, D. Habs, M. Hegelich, G. Pretzler, A. Pukhov, K. Witte and R. Sauerbrey, *High-Intensity Laser Induced Ion Acceleration from Heavy-Water Droplets*. Phys. Rev. Lett., vol. 91, 015001 (2003).

[Keldysh 1964]

L.V. Keldysh, *Ionization in the field of a strong electromagnetic wave*. Sov. Phys. JETP, vol. 20, 1307 (1964).

[Krushelnick 1997]

K. Krushelnick, A. Ting, C.I. Moore, H.R. Burris, E. Esarey, P. Sprangle, and M. Baine, *Plasma channel formation and guiding during high intensity short pulse laser plasma experiments*. Phys. Rev. Lett., vol. 78, 4047-4050 (1997).

[Krushelnick 1999]

K. Krushelnick, E. L. Clark, Z. Najmudin, M. Salvati, M. I. K. Santala, M. Tatarakis and A. E. Dangor, *Multi-MeV Ion Production from High-Intensity Laser Interactions with Underdense Plasmas*. Phys. Rev. Lett., vol. 83, 737 (1999).

[LasersAndOpt 2012]

Träger, *Handbook of Lasers and Optics*. Springer (2012).

[Lawson 1975]

J. D. Lawson, *Laser accelerators?*. RL-75-043 (1975).

[Lefebvre 2019]

E. Lefebvre, C. Bernard, S. ans Esnault, P. Gauthier, A. Grisol-let, P. Hoch, L. Jacquet, G. Kluth, S. Laffite, S. Liberatore, I. Marmajou, P.-E. Masson-Laborde, O. Morice, and J.-L. Willien, *Development and validation of the TROLL radiation-hydrodynamics code for 3D hohlraum calculations*. Nucl. Fusion, vol. 59, 032010 (2019).

[Lekki 2017]

J. Lekki, M. Matosz, C. Paluszkiwicz, E. Pięta, T. Pieprzyca, Z. Szklarz, and J. M. del Hoyo Meléndez, *Comparison of PIXE and XRF in the analysis of silver denarii of the early Piast*. J. Radioanal. Nucl. Chem., 314, 2309-2316 (2017).

[Lieberman 2005]

M.A. Lieberman, and A.J. Lichtenberg, *Principles of plasma discharges and material processing*. John Wiley & Sons, Inc, Hoboken, New Jersey (2005).

[Litvak 1970]

A.G. Litvak, *Finite-amplitude wave beams in a magnetoactive plasma*. Sov. Phys. JETP, vol. 30, 344-347 (1970).

[Liu 2013]

L. Liu, M. Chen, J. Zheng, Z.M. Sheng, and C.S. Liu, *Three dimensional effects on proton acceleration by intense laser solid target interaction*. Phys. Plasmas, vol. 20, 063107 (2013).

[Livingston 1962]

M.S. Livingston, J.P. Blewett, *Particle accelerators*. McGraw-Hill, NY (1962).

[Lucas 2011]

Y. Lucas, *The Role of Plants in Controlling Rates and Products of Weathering: Importance of Biological Pumping*. Annual Rev. Of Earth and Planetary Sci., 29, 135-163 (2011).

[Lumb 1987]

D. H. Lumb, E. G. Chowanietz, and A. Walls, *X-Ray Measurements Of Charge Diffusion Effects In EEV Ltd. Charge-Coupled Devices*. Opt. Eng., vol. 26, 773 (1987).

[Macchi 2013]

A. Macchi, M. Borghesi and M. Passoni, *Ion acceleration by superintense laser-plasma interaction*. Rev. Mod. Phys., vol. 85, 751793 (2013), and references therein.

[Mackinnon 2002]

A. J. Mackinnon, Y. Sentoku, P.K. Patel, D.W. Price, S. Hatchett, M.H. Key, C. Andersen, R. Snavely, and R.R. Freeman, *Enhancement of Proton Acceleration by Hot-Electron Recirculation in Thin Foils Irradiated by Ultraintense Laser Pulses*. Phys. Rev. Lett., vol. 88, 215006 (2002).

[Mackinnon 2006]

A. J. Mackinnon, P. K. Patel, M. Borghesi, R. C. Clarke, R. R. Freeman, H. Habara, S. P. Hatchett, D. Hey, D. G. Hicks, S. Kar, M. H. Key, J. A. King, K. Lancaster, D. Neely, A. Nikkro, P. A. Norreys, M. M. Notley, T. W. Phillips, L. Romagnani, R. A. Snavely, R. B. Stephens, and R. P. J. Town, *Proton Radiography of a Laser-Driven Implosion*. Phys. Rev. Lett., vol. 97, 045001 (2006).

[MacNeice 2000]

P. MacNeice, Kevin M. Olson, Clark Mobarry, Rosalinda de Fainchtein, Charles Packer, *PARAMESH: A parallel adaptive mesh refinement community toolkit*. Computer Phys. Comm., vol. 126, 3, 330-354 (2000).

[Mainfray 1991]

G. Mainfray, and C. Manus, *Multiphoton ionization of atoms*. Rep. Mod. Phys., vol. 54, 1333-1372 (1991).

[Maksimchuk 2000]

A. Maksimchuk, S. Gu, K. Flippo, K. Umstadter, and V. Yu. Bychenkov, *Forward ion acceleration in thin films driven by a high-intensity laser*. Phys. Rev. Lett., vol. 84, 4108-4111 (2000).

[Malka 2000]

V. Malka, C. Coulaud, J. P. Geindre, V. Lopez, Z. Najmudin, D. Neely, and F. Amiranoff, *Characterization of neutral density profile in a wide range of pressure of cylindrical pulsed gas jets*. Rev. Sci. Instrum., vol. 71, 2329-2333 (2000).

[Malka 2002]

V. Malka, S. Fritzler, E. Lefebvre, M.-M. Aleonard, F. Burgy, J.-P. Chambaret, J.-F. Chemin, K. Krushelnick, G. Malka, S. P. D. Mangles, Z. Najmudin, M. Pittman, J.-P. Rousseau, J.-N. Scheurer, B. Walton, A. E. Dangor, *Electron Acceleration by a Wake Field Forced by an Intense Ultrashort Laser Pulse*. Sci., vol. 298, 1596-1600 (2002).

[Malmqvist 1986]

K. G. Malmqvist, *Comparison between PIXE and XRF for applications in art and archaeology*. Nucl. Inst and Meth Phys. Reseach, B14, 86-92 (1986).

[Margarone 2016]

D. Margarone, A. Velyhan, J. Dostal, J. Ullschmied, J. P. Perin, D. Chatain, S. Garcia, P. Bonnay, T. Pisarczyk, R. Dudzak, M. Rosinski, J. Krasa, L. Giuffrida, J. Prokupek, V. Scuderi, J. Psikal, M. Kucharik, M. De Marco, J. Cikhardt, E. Krouscky, Z. Kalinowska, T. Chodukowski, G. A. P. Cirrone and G. Korn, *Proton Acceleration Driven by a Nanosecond Laser from a Cryogenic Thin Solid-Hydrogen Ribbon*. Phys. Rev. X, vol. 6, 041030 (2016).

[Marinelli 2013]

M. Marinelli, E. Milani, G. Prestopino, C. Verona, G. Verona-Rinati, M. Cutroneo, L. Torrisi, D. Margarone, A. Velyhan, J. Krasa and E. Drousky, *Analysis of laser-generated plasma ionizing radiation by synthetic single crystal diamond detectors*. Appl. Surf. Sci., vol. 272 (2013).

[Max 1974]

C.E. Max, J. Arons, and A.B. Langdon, *Self-modulation and self-focusing of electromagnetic waves in plasma*. Phys. Rev. Lett., vol. 33, 209-212 (1974).

[Millikan 1916]

R.A. Millikan, *Einstein's photoelectric equation and contact electromotive force*. Phys. Rev., vol. 7, 18-32 (1916).

[Mora 2005]

P. Mora, *Thin-foil expansion into a vacuum*. Phys. Rev. E, vol. 72, 056401 (2005).

[Morabito 2019]

A. Morabito, M. Scisciò, S. Veltri, M. Migliorati., P. Antici, *Design and optimization of a dedicated laser driven hybrid proton beam-line for cultural heritage applications*. Laser and Particle Beams, vol. 37, 354-363 (2019).

[Mori 2002]

M. Mori, E. Takahashi, and K. Kondo, *Image of second harmonic emission generated from ponderomotively excited plasma density gradient*. Phys. Plasmas, vol. 9, 2812 (2002).

[Mourou 2006]

G. A. Mourou, T. Tajima, and S. V. Bulanov, *Optics in the relativistic regime*. Rev. Mod. Phys., vol. 78 (2006) and references therein.

[Mourou and Tajima 2012]

G. Mourou and T. Tajima, *Exploring fundamental physics at the highest-intensity-laser frontier*, SPIE, 03 August (2012).

[Mulser and Bauer 2010]

P. Mulser, and D. Bauer, *High Power Laser-Matter Interaction*. Springer Tracts in Mod. Phys. (Springer, New York), vol. 238 (2010).

[Neelmeijer 2000]

C. Neelmeijer, I. Brissaud, T. Calligaro, G. Demortier, A. Hautajarvi, M. Mader, L. Martinot, M. Schreiner, T. Tuurnala and G. Weber, *Paintings, a Challenge for XRF and PIXE Analysis*. X-ray Spectrom., vol. 29, 101-110 (2000).

[Neutrino]

See <http://web.luli.polytechnique.fr/Neutrino/> for Neutrino, Alessandro Flacco and Tommaso Vinci.

[Obst 2017]

L. Obst, S. Göde, M. Rehwald, F-E. Brack, João Branco, S. Bock, M. Bussmann, T. E. Cowan, C. B. Curry, F. Fiuza, M. Gauthier, R. Gebhardt, U. Helbig, A. Huebl, U. Hübner, A. Irman, L. Kazak, J. B. Kim, T. Kluge, S. Kraft, M. Loeser, J. Metzkes, R. Mishra, C. Rödel, H-P. Schlenvoigt, M. Siebold, J. Tiggesbäumker, S. Wolter, T. Ziegler, U. Schramm, S. H. Glenzer and K. Zeil, *Efficient laser-driven proton acceleration from cylindrical and planar cryogenic hydrogen jets*. Sci. Rep., vol. 10, 1038 (2017).

[Ogura 2012]

K. Ogura, M. Nishiuchi, A.S. Pirozhkov, T. Tanimoto, A. Sagisaka, T.Zh. Esirkepov, M. Kando, T. Shizuma, T. Hayakawa, H. Kiriya, T. Shimomura, S. Kondo, S. Kanazawa, Y. Nakai, H. Sasao, F. Sasao, Y. Fukuda, H. Sakaki, M. Kanasaki, A. Yogo, S.V. Bulanov, P.R. Bolton, and K. Kondo, *Proton acceleration to 40 MeV using a high intensity, high contrast optical parametric chirped-pulse amplification/Ti:sapphire hybrid laser system*. Opt. Lett., vol. 37, 14, 2868-2870 (2012).

[Orban 2013]

C. Orban, M. Fatenejad, S. Chawla, S. Wilks and D. Lamb, *A Radiation-Hydrodynamics Code Comparison for Laser-Produced Plasmas: FLASH versus HYDRA and the Results of Validation experiments*. ArXiv (2013).

[Palmer 2011]

C.A.J. Palmer, N. P. Dover, I. Pogorelsky, M. Babzien, G. I. Dudnikova, M. Ispiriyani, M. N. Polyanskiy, J. Schreiber, P. Shkolnikov, V. Yakimenko and Z. Najmudin, *Monoenergetic Proton Beams Accelerated by a Radiation Pressure Driven Shock*. Phys. Rev. Lett., vol. 106, 014801 (2011).

[Passalidis 2020]

S. Passalidis, O.C. Ettliger, G.S. Hicks, N.P. Dover, Z. Najmudin, E.P. Benis, E. Kaselouris, N.A. Papadogiannis, M. Tatarakis, and V. Dimitriou, *Hydrodynamic computational modelling and simulations of collisional shock waves in gas jet targets*. High Power Laser Sci. and Eng., vol. 8, e7 (2020).

[Passoni 2019]

M. Passoni, L. Fedeli, and F. Mirani, *Superintense Laser-driven Ion Beam Analysis*. Sci. Rep., vol. 9, 9202 (2019).

[Passoni 2010]

M. Passoni, L. Bertagna<sup>1</sup> and A. Zani, *Target normal sheath acceleration: theory, comparison with experiments and future perspectives*, New J. Phys., vol. 12 045012 (2010).

[Peck 1977]

E. R. Peck and S. Huang, *Refractivity and dispersion of hydrogen in the visible and near infrared*. J. Opt. Soc. Am., vol. 67, 1550–1554 (1977).

[Pegoraro 2005]

F. Pegoraro, T. Zh. Esirkepov, and S.V. Bulanov, *Special relativity in action in laser produced plasmas*. Phys. Lett. A, vol. 347, 133-42 (2005).

[Photonics 2016]

V. Degiorgio, I. Cristiani, *Photonics, A short Course*. Springer (2016).

[Plaisir 2010]

*Etudes expérimentales de l'accélération de particules avec des lasers ultra-intenses; Applications à des expériences de physique nucléaire dans les plasmas lasers*. Thèse de l'Université de Bordeaux (2010).

[Podgorsak 2010]

E. B. Podgorsak, *Radiation Physics for Medical Physicists*. Second Edition, Springer. 329-336 (2010).

[Poole 2014]

P. L. Poole, C. D. Andereck, D. W. Schumacher, R. L. Daskalova, S. Feister, K. M. George, C. Willis, K. U. Akli and E. A. Chowdhury, *Liquid crystal films as on-demand, variable thickness (50–5000 nm) targets for intense lasers*. Phys. Plasmas., vol. 21, 063109 (2014).

[Reyes-Herrera 2015]

J. Reyes-Herrera, J. Miranda, O.G. de Lucio, *Simultaneous PIXE and XRF elemental analysis of atmospheric aerosols*. Microch. J., vol. 120, 40-44 (2015).

[Robson 2007]

L. Robson, P.T. Simpson, P. McKenna, K.W.D. Ledingham, R.J. Clarke, T. McCanny, D. Neely, O. Lundh, F. Lindau, C. G. Wahlström, M. Zepf, *Scaling of proton acceleration driven by petawatt-laser-plasma interactions*. Nat. Phys., vol. 3, 58, 58-62 (2007).

[Roth 2001]

M. Roth, T. E. Cowan, M. H. Key, S. P. Hatchett, C. Brown, W. Fountain, J. Johnson, D. M. Pennington, R. A. Snavely, S. C. Wilks, K. Yasuike, H. Ruhl, F. Pegoraro, S. V. Bulanov, E. M. Campbell, M. D. Perry, and H. Powell, *Fast Ignition by Intense Laser-Accelerated Proton Beams*. Phys. Rev. Lett., vol. 86, 436 (2001).

[Roth 2016]

M. Roth, and M. Schollmeier, *Ion Acceleration-Target Normal Sheath Acceleration*. Proceedings of the CAS-CERN Acc. School: Plasma Wake Acc., Geneva Switzerland, 23-29 (1016).

[Salvadori 2020]

M. Salvadori, F. Consoli, C. Verona, M. Cipriani, M. P. Anania, P. L. Andreoli, P. Antici, F. Bisesto, G. Costa, G. Cristofari, R. De Angelis, G. Di Giorgio, M. Ferrario, M. Galletti, D. Giulietti, M. Migliorati, R. Pompili and A. Zigler, *Accurate spectra for high energy ions by advanced time-of-flight diamond-detector schemes in experiments with high energy and intensity lasers*. Submitted to Sci. Rep. (2020).

[Sarachik and Schappert 1970]

E.S. Sarachik, and G.T. Schappert, *Classical theory of the scattering of intense laser radiation by free electrons*. Phys. Rev. D, vol. 1, 2738-2753 (1970).

[Sarkisov 1999]

G. S. Sarkisov, V. Yu. Bychenkov, V. N. Novikov, V. T. Tikhonchuk, A. Maksimchuk, S.-Y. Chen, R. Wagner, G. Mourou, and D. Umstadter, *Self-focusing, channel formation, and high-energy ion generation in interaction of an intense short laser pulse with a He jet*. Phys. Rev. E. vol. 59, 7042 (1999).

[Sawada 2015]

H. Sawada, Y Sentoku, A Bass, B Griffin, R Pandit, F Beg, H Chen, H McLean, A J Link, P K Patel and Y Ping, *Characterization of intense laser-produced fast electrons using hard x-rays via bremsstrahlung*. J. Phys. B: At. Mol. Opt. Phys., vol. 48, 224008 (2015).

[Schlegel 2009]

T. Schlegel, N. Naumova, V.T. Tikhonchuk, C. Labaune, I.V. Sokolov, and G. Mourou, *Relativistic laser piston model: Ponderomotive ion acceleration in dense plasmas using ultraintense laser pulses*. Phys. Plasmas, vol. 16, 083103 (2009).

[Schmid 2012]

K. Schmid and L. Veisz, *Supersonic gas jets for laser-plasma experiments*. Rev. Sci. Instrum., vol. 83, 053304 (2012).

[Schnurer 2005]

M. Schnurer, S. Ter-Avetisyan, S. Busch, E. Risse, M.P. Kalachnikov, W. Sandner and P.V. Nickles, *Ion acceleration with ultrafast laser driven water droplets*. Cambridge University Press, 0263-0346005 (2005).

[Schwoerer 2006]

H. Schwoerer, S. Pfoth, O. Jaeckel, K.U. Amthor, b. Liesfeld, W. Ziegler, R. Sauerbrey, K.W.D. Ledingham, and T. Esirkepov, *Laser-plasma acceleration of quasi-monoenergetic protons from microstructured targets*. Nat. (London), vol. 439, 445-448 (2006).

[Seggern 1992]

H. von Seggern, *X-ray imaging with photostimulable phosphors*. Nucl. Instrum. Meth. A, vol. 322, 3; 467-471 (1992).

[Seibert and Boone 2005]

J.A. Seibert, J.M. Boone, *X-ray imaging physics for nuclear medicine technologists. Part 2: X-ray interactions and image formation*. J. Nucl. Medicine Tech., vol. 33, 3-18 (2005).

[Sentoky 2008]

Y. Sentoku and A.J. Kemp, *Numerical Methods for Particle Simulations at Extreme Densities and Temperatures: Weighted Particles, Relativistic Collisions and Reduced Currents*. J. Comp. Phys., vol. 227 (14), p. 6846-6861 (2008).

[SketchUp]

[www.sketchup.com](http://www.sketchup.com)

[Silva 2004]

L.O. Silva M. Marti, J. R. Davies and R. A. Fonseca, *Proton Shock Acceleration in Laser-Plasma Interactions*. Phys. Rev. Lett., vol. 92, 015002 (2004).

[Snavely 2000]

R.A. Snavely, M.H. Key, S.P. Hatchett, T.E. Cowan, M. Roth, T.W. Phillips, M.A. Stoyer, E.A. Henry, T.C. Sangster, M.S. Singh, S.C. Wilks, A. MacKinnon, A. Offenberger, D.M. Pennington, K. Yasuike, A.B. Kangdon, B.F. Lasinski, J. Johnson, M.D. Perry, and E.M. Campbell, *Intense high-energy proton beams from Petawatt-laser irradiation of solids*. Phys. Rev. Lett., vol. 85, 2945-2948 (2000).

[Sprangle 1987]

P. Sprangle, C.-M. Tang, and E. Esarey, *Relativistic self-focusing of short-pulse radiation beams in plasmas*. IEEE Trans. Plasma Sci., vol. 15, 145-153 (1987).

[Stamper 1985]

J. A. Stamper, R. H. Lehmberg, A. Schmitt, M. J. Herbst, F. C. Young, J. H. Gardner, and S. P. Obenschain, *Evidence in the second-harmonic emission for self-focusing of a laser pulse in a plasma*. Phys. Fluids, vol. 28, 2563 (1985).

[Stone 2004]

J. A. Stone and A. Stejskal, *Using helium as a standard of refractive index: Correcting errors in a gas refractometer*. Metrologia, vol. 41, 189 (2004).

[Strickland 1985]

D. Strickland and G. Mourou, *Compression of amplified chirped optical pulses*. Opt. Commun., vol. 56, 219 (1985).

[Sylla 2013]

F. Sylla, A. Flacco, S. Kahaly, M. Veltcheva, A. Lifschitz, V. Malka, E. d'Humières, I Andriyash and V. Tikhonchuk, *Short Intense Laser Pulse Collapse in Near-Critical Plasma*. Phys. Rev. Lett., vol. 110, 085001 (2013).

[Tajima 1979]

T. Tajima and J.M. Dawson, *Laser electron accelerator*. Phys. Rev. Lett., vol. 43, 267 (1979).

[Teng 2001]

L. Teng, *Particle Accelerators: Outlook for the Twenty-first century*. 2<sup>nd</sup> Asian Particle Acc. Conference, p. 926 (2001).

[Ter-Avetisyan 2004]

S. Ter-Avetisyan, M. Schnurer, S. Busch, E. Risse, P.V. Nickles and W. Sandner, *Spectral Dips in Ion Emission Emerging from Ultrashort Laser-Driven Plasmas*. Phys. Rev. Lett., vol. 93, 155006 (2004).

[Tresca 2015]

O. Tresca, N. P. Dover, N. Cook, C. Maharjan, M. N. Polyanskiy, Z. Najmudin, P. Shkolnikov, and I. Pogorelsky, *Spectral Modification of Shock Accelerated Ions Using a Hydrodynamically Shaped Gas Target*. Phys. Rev. Lett., vol. 115, 094802 (2015).

[Tarisien 2011]

M. Tarisien, C. Plaisir, F. Gobet, F. Hannachi, M.M. Aleonard and A. Rebi, *NATALIE: A 32 detector integrated acquisition system to characterize laser produced energetic particles with nuclear techniques*. Rev. Sci. Instrum., vol. 82, 023302 (2011).

[Valle Brozas 2016]

F. Valle Brozas, A. Crego, L. Roso and A. Peralta Conde. *Laser-based X-ray and electron source for X-ray fluorescence studies*. Appl. Phys. B 122, 220 (2016).

[Verma 2007]

H.R. Verma, *Atomic and Nuclear Analytical Methods*. Springer (2007).

[Verona 2015]

C. Verona, G. Magrin, P. Solevi, V. Grilj, M. Jaksic, R. Mayer, M. Marinelli and G. Verona-Rinati, *Spectroscopic properties and radiation damage investigation of a diamond based Schottky diode for ion-beam therapy microdosimetry*. J. Appl. Phys., vol. 118 184503 (2015).

[Volkov 1935]

D.M. Volkov, *Über eine Klasse von Lösungen der Dirac'schen Gleichung*. Z. Phys., vol. 94, 250-260 (1935).

[Volpe 2011]

L. R Jafer, B Vauzour, Ph Nicolai, J J Santos, F Dorchies, C Fourment, S Hulin, C Regan, F Perez, S Baton, K Lancaster, M Galimberti, R Heathcote, M Tolley, Ch Spindloe, W Nazarov, P Koester, L Labate, L A Gizzi, C Benedetti, A Sgattoni, M Richetta, J Pasley, F N Beg, S Chawla, D P Higginson, A G MacPhee and D Batani, *Proton radiography of cylindrical laser-driven implosions*. Plasma Phys. Control. Fusion, vol. 53, 032003 (2011).

[Wagner 2016]

F. Wagner, O. Deppert, C. Brabetz, P. Fiala, A. Kleinschmidt, P. Poth, V.A. Schanz, A. Tebartz, B. Zielbauer, M. Roth, T. Stohlker, and V.L.R. Bagnoud, *Maximum Proton Energy above 85 MeV from the Relativistic Interaction of Laser Pulses with Micrometer Thick Targets*. Phys. Rev. Lett, vol. 116, 205002 (2016).

[Wei 2004]

M.S. Wei, S. P. D. Mangles, Z. Najmudin, B. Walton, A. Gopal, M. Tatarakis, A. E. Dangor, E. L. Clark, R.G. Evans, S. Fritzler, R. J. Clarke, C. Hernandez-Gomez, D. Neely, W. Mori, M. Tzoufras and K. Krushelnick, *Ion Acceleration by Collisionless Shocks in High-Intensity-Laser-Underdense-Plasma Interaction*. Phys. Rev. Lett., vol. 93, 155003 (2004).

[Wilcox 2006]

D.C. Wilcox, *Turbulence Modeling for CFD*. 3rd ed. DCW Industries (2006).

[Wilks 1992]

S.C. Wilks, W.L. Kruer, M. Tabak and A. B. Langdon, *Absorption of ultra-intense laser pulses*. Phys. Rev. Lett., vol. 69, 1383 (1992).

[Wilks 1997]

S.C. Wilks and W.L. Kruer, *Absorption of ultrashort, ultra-intense laser light by solids and overdense plasmas*. IEEE J. Quant. Elec., vol. 33, 1954-1968 (1997).

[Wilks 2001]

S.C. Wilks, A.B. Langdon, T.E. Cowan, M. Roth, M. Singh, S. Hatchett, M.H. Key, D. Pennington, A. MacKinnon, and R.A. Snavely, *Energetic proton generation in ultra-intense laser-solid interactions*. Phys. Plasmas, vol. 8, 542 (2001).

[Williams and Bird 1989]

J.S. Williams and J.R. Bird, *Ion Beams for Materials Analysis*. Academic Press (1989).

[Willingale 2006]

L. Willingale, S. P. D. Mangles, P. M. Nilson, R. J. Clarke, A. E. Dangor, M. C. Kaluza, S. Karsch, K. L. Lancaster, W. B. Mori, Z. Najmudin, J. Schreiber, A. G. R. Thomas, M. S. Wei and K. Krushelnick, *Collimated Multi-MeV Ion Beams from High-Intensity Laser Interactions with Underdense Plasma*. Phys. Rev. Lett., vol. 96, 245002 (2006).

[Zhang 2007]

X. Zhang, B. Shen, M.Y. Yu, X. Li, Z. Jin, F. Wang, and M. Wen, *Effect of the plasma temperature on electrostatic shock generation and ion acceleration by laser*. Phys. Plasmas, vol. 14, 113108 (2007).

[Zhang 2009]

X. Zhang, B. Shen, L. Lin, F. Wang, Z. Jin, X. Li, M. Wen, and J.R. Cary, *Ion acceleration with mixed solid targets interacting with circularly polarized lasers*. Phys. Rev. ST Accel. Beams, vol. 12, 021-301 (2009).

[Zhizhan 1983]

X. Zhizhan, X. Yuguang, Y. Guangyu, Z. Yanzhen, Y. Jiajin, and P. H. Y. Lee, *Second-harmonic emission from laser-plasma interactions*. J. Appl. Phys., vol. 54, 4902 (1983).

[Ziegler 2008]

J. Ziegler, J. Biersack, and M. Ziegler, *Stopping and Range of ions in Matter*. SRIM Co. Chester, MD (2008).